Direct Photons in Heavy-Ion Collisions

Dissertation

zur Erlangung des Doktorgrades

der Naturwissenschaften

vorgelegt beim Fachbereich Physik

der Johann Wolfgang Goethe -Universität

in Frankfurt am Main

von

Björn Bäuchle

aus Frankfurt am Main

Frankfurt 2010

D 30

Direct Photons in Heavy-Ion Collisions

vom Fachbereich Physik der
Johann Wolfgang Goethe-Universität
als Dissertation angenommen.

Dekan: Michael Huth
Gutachter: Marcus Bleicher, Horst Stöcker
Datum der Disputation: 13. Dezember 2010

Diese Arbeit beruht auf folgenden Publikationen:

- "Hybrid model calculations of direct photons in high-energy nuclear collisions" [Bäu10]
- "Direct photon calculations in heavy-ion collisions at $\sqrt{s_{\mathsf{NN}}}$ = 62.4 - 200 GeV in a (3+1) dimensional hybrid approach" [Bäu10a]
- "Transport and hydrodynamic calculations of direct photons at FAIR" [Bäu10b]
- "Direct photon emission from hadronic sources: Hydrodynamics vs. Transport theory" [Bäu09]
- "Direct photon emission in Heavy Ion Collisions from Microscopic Transport Theory and Fluid Dynamics" [Bäu10c]
- "Calculations of direct photon emission in heavy ion collisions at $\sqrt{s_{\mathsf{NN}}}$ = 200 GeV" [Bäu10d]
- "Direct Photons from a Hybrid Approach – Exploring the parameter space" [Bäu10e]

Contents

1 Introduction **1**

2 Direct Photons **11**
2.1 Direct photon experiments 11
2.2 Photon emission sources 11
2.3 Photon measurement 13
2.3.1 Direct photon extraction 13
2.4 Calculations of direct photons 15

3 Model **17**
3.1 Transport Models 17
3.1.1 UrQMD 18
3.2 Hydrodynamic Models 20
3.2.1 SHASTA 22
3.3 Hybrid Model 23
3.3.1 Early Stage 24
3.3.2 Intermediate Stage 25
3.3.3 Late Stage 25
3.4 Equations of State 27
3.5 Photon emission sources 36
3.5.1 Photon emission from the Transport Phase 36
3.5.2 Photon emission from the Hydrodynamic Phase 43
3.5.3 Photon emission from primordial pQCD scatterings . . . 45

4 Numerical Tests and Investigations **49**
4.1 Rates from transport and hydrodynamics 49
4.2 String ends 49
4.3 ρ-meson width 52
4.4 Comparison to previous works with UrQMD 52
4.5 Exploring the parameter space 54
4.5.1 Transport $\rightarrow$ hydrodynamics 55
4.5.2 Hydrodynamics $\rightarrow$ transport 55

5 Results **61**
5.1 Photons at FAIR: CBM 61
5.2 Photons at SPS: WA98 64
5.3 Photons at RHIC: PHENIX 68
5.4 Collective Patterns 74

6 Channel decomposition **81**
6.1 Hadronic channels 81
6.2 Partonic contribution 86

7 Time emission patterns **89**
7.1 Emission stages 89
7.2 High-$p_\perp$ emission 96
7.3 Emission times 97

8 Baryon number density **113**

9 Summary **119**

A Kinetic variables in $2 \leftrightarrow 2$ scatterings **123**
A.1 Mandelstam variables 123
A.2 Lorentz-Transformations 125

B Photons from Hydrodynamics **129**

C Conventions and Units **135**
C.1 Natural Units 135
C.2 Einstein notation 136
C.3 Coordinate systems and indices 136
C.4 Accelerator parameters 137

D Bibliography **139**

E Acknowledgements **153**

F Zusammenfassung **155**
F.1 Einführung 155
F.2 Das Modell 156
F.3 Ergebnisse 157
F.4 Schlussfolgerungen 159

G Index **161**

H Lebenslauf **163**
H.1 Meine Akademischen Lehrer 163
H.2 Lebenslauf 164

List of Figures

1.1 Particles in Standard Model 2
1.2 Phase Diagram of Strongly Interacting Matter 4

2.1 Photon sources in Heavy-Ion collisions 12

3.1 Cross-sections $\pi + \pi$ in UrQMD (resonance / string / PYTHIA) 19
3.2 Spectra in UrQMD with and without PYTHIA 20
3.3 Speed of sound in HG-EoS 27
3.4 Degree of deconfinement in χ-EoS 28
3.5 Speed of sound in χ-EoS 29
3.6 Degree of deconfinement in BM-EoS 30
3.7 Speed of sound in BM-EoS 31
3.8 Initial temperature profiles 32
3.9 Distribution of transition points with gradual transition 33
3.10 Distribution of QGP-content of the hydrodynamic system 34
3.11 Distribution of temperatures in hydrodynamic calculations 35
3.12 Photon production Feynman-diagrams 37
3.13 Photon production cross-sections 42
3.14 Thermal rates with and without form factor at $T = 170$ MeV . . 46
3.15 Comparison of hadronic vs. partonic thermal rates 47
3.16 Integrated thermal rates vs. temperature 47

4.1 Comparison of UrQMD box calculations to thermal rates 50
4.2 Comparison of UrQMD and HG-EoS hybrid (common channels only) 50
4.3 Comparison of calculations with and without string contribution 51
4.4 Impact of taking into account the ρ-spectal function 53
4.5 Comparison to calculations by Dumitru *et al.* 54
4.6 Effect of changing start time for hydrodynamics t_{start} 56
4.7 Effect of changing the critical energy density for the transition to transport calculation $\varepsilon_{\mathsf{crit}}$ 58
4.8 Effect of transferring the whole system at the same time 59

5.1 Direct photon spectra in U+U at $E_{\mathsf{lab}} = 35$ AGeV 62

5.2 Photon emission from the intermediate stage at $E_{\mathsf{lab}} = 35$ AGeV 63
5.3 Direct photon spectra in central Pb+Pb at $E_{\mathsf{lab}} = 158$ AGeV . . 65
5.4 Direct photon spectra at $E_{\mathsf{lab}} = 158$ AGeV including prompt photons 66
5.5 Direct photons in peripheral Pb+Pb-collisions at $E_{\mathsf{lab}} = 158$ AGeV 67
5.6 Direct photons from pQCD, cascade and BM-EoS calculations at $\sqrt{s_{\mathsf{NN}}} = 200$ GeV 69
5.7 Direct photons from central Au+Au at $\sqrt{s_{\mathsf{NN}}} = 200$ GeV 70
5.8 Direct photons in Au+Au and Cu+Cu at $\sqrt{s_{\mathsf{NN}}} = 62.4$ GeV, $\sqrt{s_{\mathsf{NN}}} = 130$ GeV and $\sqrt{s_{\mathsf{NN}}} = 200$ GeV 72
5.9 $v_2(p_\perp)$ at $E_{\mathsf{lab}} = 35$ AGeV 75
5.10 $v_2(p_\perp)$ at $E_{\mathsf{lab}} = 158$ AGeV 76
5.11 $v_2(p_\perp)$ at $\sqrt{s_{\mathsf{NN}}} = 62.4$ GeV 78
5.12 $v_2(p_\perp)$ at $\sqrt{s_{\mathsf{NN}}} = 130$ GeV 79
5.13 $v_2(p_\perp)$ at $\sqrt{s_{\mathsf{NN}}} = 200$ GeV 80

6.1 Channel decomposition in transport calculations 82
6.2 Relative contributions of hadronic channels: HG-EoS 83
6.3 Relative contributions of hadronic channels: χ-EoS 84
6.4 Relative contributions of hadronic channels: BM-EoS 85
6.5 Contributions of QGP and pQCD to photon spectra with χ-EoS 87
6.6 Contributions of QGP and pQCD to photon spectra with BM-EoS 88

7.1 Contribution of the different stages at $E_{\mathsf{lab}} = 35$ AGeV 90
7.2 Contribution of the different stages at $E_{\mathsf{lab}} = 158$ AGeV 92
7.3 Contribution of the different stages at $E_{\mathsf{lab}} = 158$ AGeV with isochronous transition 93
7.4 Contribution of the different stages in Au+Au at $\sqrt{s_{\mathsf{NN}}} = 200$ GeV 94
7.5 High-$p_\perp$ photon spectra at $E_{\mathsf{lab}} = 158$ AGeV 96
7.6 High-$q_\perp^{\mathsf{coll}}$ photon spectra at $E_{\mathsf{lab}} = 158$ AGeV 97
7.7 High-$\sqrt{s_{\mathsf{coll}}}$ photon spectra at $E_{\mathsf{lab}} = 158$ AGeV 98
7.8 Average photon emission times in UrQMD at $E_{\mathsf{lab}} = 35$ AGeV . 99
7.9 Emission time distribution in UrQMD at $E_{\mathsf{lab}} = 35$ AGeV 99
7.10 Fraction of photons emitted at various times at $E_{\mathsf{lab}} = 35$ AGeV 100
7.11 Average photon emission times in UrQMD at $E_{\mathsf{lab}} = 158$ AGeV . 101
7.12 Emission time distribution in UrQMD at $E_{\mathsf{lab}} = 158$ AGeV . . . 102
7.13 Fraction of photons emitted at various times at $E_{\mathsf{lab}} = 158$ AGeV 102
7.14 Average photon emission times in UrQMD at $\sqrt{s_{\mathsf{NN}}} = 62.4$ GeV 103
7.15 Emission time distribution in UrQMD at $\sqrt{s_{\mathsf{NN}}} = 62.4$ GeV . . . 104
7.16 Fraction of photons emitted at various times at $\sqrt{s_{\mathsf{NN}}} = 62.4$ GeV 106
7.17 Average photon emission times in UrQMD at $\sqrt{s_{\mathsf{NN}}} = 130$ GeV . 107
7.18 Emission time distribution in UrQMD at $\sqrt{s_{\mathsf{NN}}} = 130$ GeV . . . 108
7.19 Fraction of photons emitted at various times at $\sqrt{s_{\mathsf{NN}}} = 130$ GeV 109
7.20 Average photon emission times in UrQMD at $\sqrt{s_{\mathsf{NN}}} = 200$ GeV . 110

7.21 Emission time distribution in UrQMD at $\sqrt{s_{\mathsf{NN}}} = 200$ GeV . . . 111
7.22 Fraction of photons emitted at various times at $\sqrt{s_{\mathsf{NN}}} = 200$ GeV 112

8.1 Number of photons from given ρ_{B} at $E_{\mathsf{lab}} = 35$ AGeV 114
8.2 Number of photons from given ρ_{B} at $E_{\mathsf{lab}} = 158$ AGeV 115
8.3 Number of photons from given ρ_{B} at $\sqrt{s_{\mathsf{NN}}} = 62.4$ GeV 116
8.4 Number of photons from given ρ_{B} at $\sqrt{s_{\mathsf{NN}}} = 130$ GeV 117
8.5 Number of photons from given ρ_{B} at $\sqrt{s_{\mathsf{NN}}} = 200$ GeV 118

A.1 Schematic view of a $2 \leftrightarrow 2$-scattering 123
A.2 Rotation of momenta 127

B.1 Possible $\vec{p}$ for constant $p^\mu u_\mu$ 130
B.2 Surface of the $p^\mu u_\mu$-ellipsoid 131
B.3 Various distributions on the $p^\mu u_\mu$-ellipsoid 132
B.4 Monte-Carlo efficiency 133

List of Tables

3.1 Overview of the Equations of State 30
3.2 Parametrisations of the thermal rates 44

5.1 Thermal fit to the calculations at $E_{\mathsf{lab}} = 35$ AGeV 62
5.2 Centrality classes in PHENIX-data 68
5.3 Thermal fits to cascade-calculations at $\sqrt{s_{\mathsf{NN}}} = 200$ GeV 71
5.4 Thermal fits to calculations at RHIC (Au+Au) 73
5.5 Thermal fits to calculations at RHIC (Cu+Cu) 74

7.1 Transition times in hybrid calculations 95

C.1 Conversions between E_{lab} and $\sqrt{s_{\mathsf{NN}}}$ 137

Chapter 1

Introduction

Knowledge about the matter surrounding us has always been of greatest interest for humankind. Discoveries of smaller substructures of matter have led to technological advances and, ultimately, to the development of technologies that allow to survey even smaller structures.

While the limit of direct observation has been reached with the invention and perfection of light microscopy, non-optical means for the exploration of small structures have been around since the introduction of electron microscopy in the 1930s.

One obstacle that has to be overcome when probing small structures is that the wavelength of the probe has to be smaller than or comparable to the size of the structure, and by a fundamental principle of quantum mechanics, the de Broglie-relation, the requirement for short wavelengths means a requirement for high-momentum and therefore high-energy probes. Additionally, in quantum mechanical systems macroscopic concepts such as the position of a particle lose their classical meaning and observation can only be statistical.

Parallel to the discovery that small structures require high energies, particle creation from energy has been found to be possible in the framework of special relativity at the beginning of the 20^{th} century. After passing a certain threshold energy, the investigation of small structures is therefore always connected with the production of new particles and with the discovery of new particle species.

After a multitude of experimental discoveries and theoretical formulations, the standard model of particle physics has been formulated in the late 1960s. It describes all phenomena observed in particle physics to high precision, but is incompatible with gravitation. In the standard model, 12 elementary fermionic particles and 4 different bosons exist (see Figure 1.1). The bosons mediate the electroweak- and strong forces. Of the 12 fermions, only the up-quarks, down-quarks and electrons are relevant for the chemical elements that surround us. In exotic astrophysical objects, strange quarks and electron neutrinos may also be significant.

The matter present on earth is composed of atoms, which are made up of

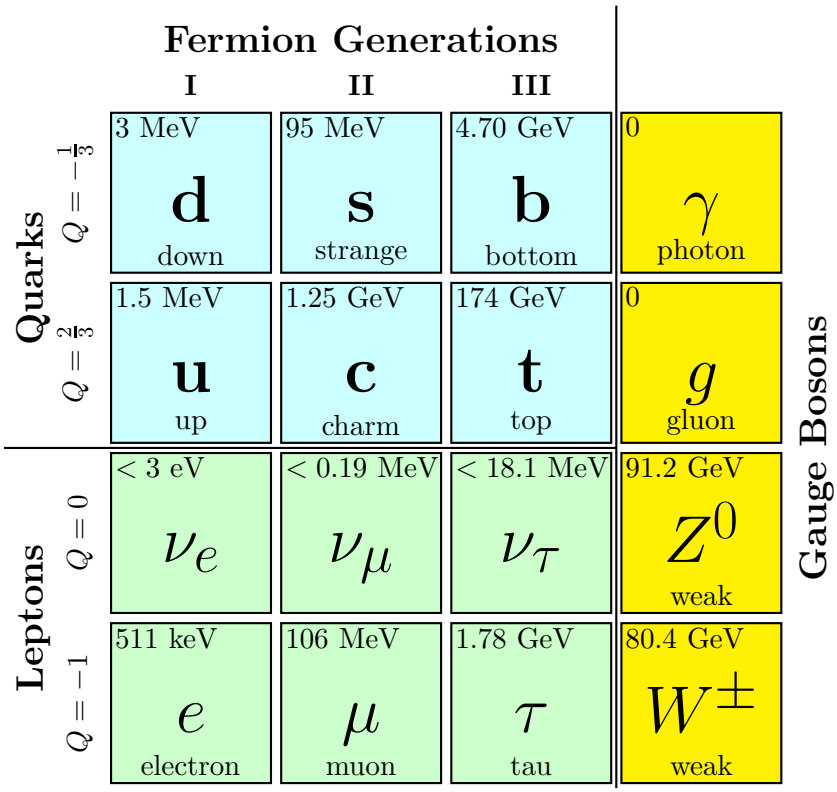

Figure 1.1: The particle species in the standard model of particle physics. The number in the upper left corner of each frame is the mass.

a massive, small, positively charged nucleus and the electron shell which in the atom's ground state neutralises the electric charge of the nucleus. The nucleus itself consists of protons and neutrons with masses of $m_p \approx m_n = 0.938$ GeV. From the schematic in Figure 1.1, it is clear that these are not themselves elementary particles. Instead, they are built up from three quarks each, which are bound by gluons.

The interaction between quarks and gluons is described by Quantum Chromodynamics (QCD). QCD is flavour-symmetric, i.e. it does not distinguish between the six different quark species up, down, strange, charm, bottom and top. Moreover, an additional $SU(3)_C$-symmetry is present in QCD, whose degrees of freedom are, by analogy to the human perception of colours, called colours: There are three elementary colours (red, green and blue), each with a complementary colour (cyan, magenta and yellow, respectively). If either each colour is accompanied by its complementary colour or all three colours are present, the resulting sensation is that of an uncoloured object. The same applies to QCD and its three independent charges: QCD-neutral objects can be built from QCD-charged objects by either neutralising any charge with its anti-charge or

by using each of the three charges. In QCD, quarks carry one colour-charge and gluons carry a combination of colour and anti-colour. All other elementary particles carry no colour charge and therefore do not interact strongly. $SU(3)_{\mathsf{C}}$ is an unbroken symmetry.

The Lagrangian density of QCD reads

$$\mathcal{L}_{\mathsf{QCD}} = \sum_{f\in\mathsf{flav.}} \sum_{\mathsf{a,b}=1}^{3} \bar{\Psi}_f^{\mathsf{a}} \left(\imath\gamma^\mu \partial_\mu \delta^{\mathsf{ab}} - g\gamma^\mu \sum_{c=1}^{8} A_{\mu,\mathsf{c}} (\lambda^{\mathsf{c}})_{\mathsf{ab}} - m_f \right) \Psi_f^{\mathsf{b}} - \frac{1}{2}\mathsf{Tr}\left(\mathcal{F}^{\mu\nu}\mathcal{F}_{\mu\nu}\right) \quad , \quad (1.1)$$

where Ψ_f^{a} are the dirac-spinors of the quarks with flavour f, mass m_f and colour a, g is the strong coupling constant, A_{c}^{μ} is the gluon field, λ^{c} are the 3×3 Gell-Mann-matrices and $\mathcal{F}^{\mu\nu} = \lambda^{\mathsf{c}} F_{\mathsf{c}}^{\mu\nu}$ is the gluon field-strength tensor, in which $F_{\mathsf{c}}^{\mu\nu} = \partial^\mu A_{\mathsf{c}}^{\nu} - \partial^\nu A_{\mathsf{c}}^{\mu}$ is defined analogously to QED. The trace runs over the colour indices introduced into $\mathcal{F}$ by λ^{c}.

Three prominent effects of QCD emerge from this Lagrangian: a) confinement, which means that free colour charges cannot exist, b) spontaneous chiral symmetry breaking, which generates an additional mass of $m_\chi \approx 0.3$ GeV to all bound quarks, and c) asympotic freedom, which means that unlike the coupling constants of electromagnetic and weak interactions, the effective coupling of the strong interaction decreases as a function of momentum transfer, so that at high energies the strong force is actually weak. At low momentum transfers $Q^2 \approx \Lambda^2_{\mathsf{QCD}} \approx 0.2^2$ GeV^2, the coupling constant is too large for perturbation theory to be usable, so that first principle calculations of dynamic systems are not feasible. In this regime, effective models have to be employed. In order to gain a deeper understanding of QCD matter, strong interactions may be observed in small systems, where above all perturbative processes can be examined, and in large systems, where collective properties of strongly interacting systems can be probed.

The study of collective behaviour of strongly interacting matter may give insight to the phase diagram of QCD. In the phase structure of QCD, various phases are expected (see Figure 1.2): At low temperatures T and low chemical potentials μ_{B}, a hadron gas (HG) consisting mainly of pions, is present. At very high temperatures, quarks and gluons are supposed to be moving freely, this state of deconfined matter is called the Quark-Gluon-Plasma QGP [Har96, Bas99]. At zero chemical potential, the transition between HG and QGP has been determined to be a cross-over by lattice gauge simulations [Aok06, De08] and is expected to happen at a critical temperature of $T_{\mathsf{C}} \approx 170$ MeV [Bor10]. Unfortunately, lattice gauge theory loses its applicability at finite chemical potential, so that it cannot reliably be used to predict the phase structure in this regime. Therefore, the phase diagram has to be explored by comparing experimental results to predictions of effective models that incorporate different phase structures. A first order liquid-gas phase transition at very low temperatures close

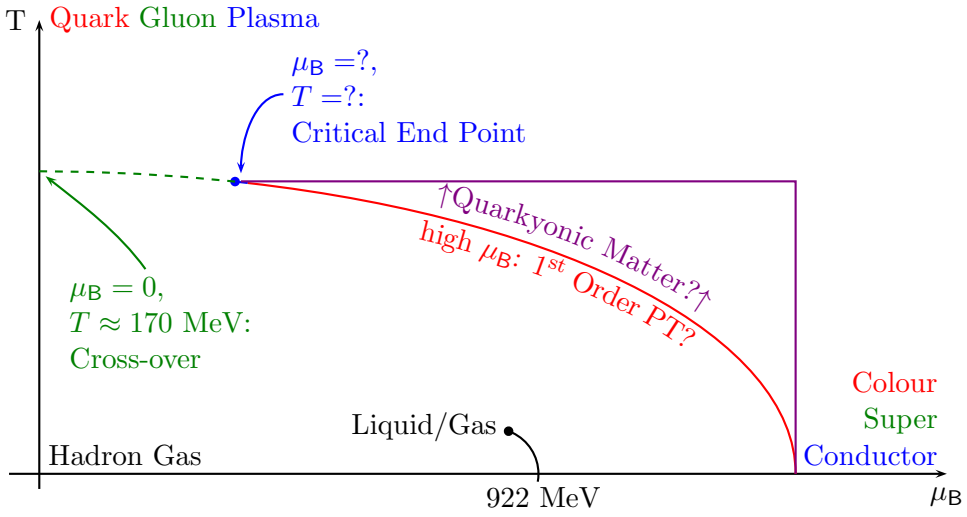

Figure 1.2: Schematic Phase Diagram of strongly interacting Matter.

to the nuclear ground state has been established by experiments several decades ago, while the remaining structure is far from being well-established.

At low temperatures and high chemical potentials, quarks are expected to bind similarly to Cooper pairs in electric superconductors and form colour super conducting phases [Ris04]. The densities needed for the creation of this state of matter are not reachable in experiments, but colour super conductivity may be realised in compact stellar objects like neutron stars. The transition to deconfined matter is expected to be a first order phase transition at low temperatures. Since it has been determined to be a cross-over at high temperatures, a critical endpoint where the first order phase transition ends should be present. In the region above the phase transition line, at intermediately high chemical potentials and temperatures, a new state of Quarkyonic Matter has been proposed [Mcl07].

At or near the transition to deconfined matter, the spontaneously broken part of chiral symmetry is expected to be restored, while the much smaller explicit breaking from the bare quark masses remains. The exact effects of this transition are dependent on the exact theory used to describe this phenomenon. A lot of research is being focused on the behaviour of meson spectral functions in hot and dense matter. Current theories, though, are inconclusive as to what the effect of chiral symmetry restauration on pole masses and widths of the mesons would be.

The hot, deconfined phase of QCD is currently not present in the universe. However, after the big bang, the cooling universe must have passed the relevant temperature regime. In all probability, it did so at low chemical potential. Since the transition from the primodial QGP to a hadron gas is where all baryons have been created, the investigation of that transition can give answers in the quest of understanding the nature of the early universe.

In order to investigate the phase diagram of nuclear matter in experiments, large nuclei (heavy ions) such as lead (Pb), gold (Au) and uranium (U) are collided. If a sufficiently large fraction of the matter that is created in those collisions thermalises at least locally, the terms temperature and chemical potential can in principle be used to describe it. Unfortunately, the created "fireball", thermalised or not, expands explosively into vacuum and therefore cools and dilutes very quickly, so that temperature and chemical potential are not constant over any extended period of time. Also, after a short time $t_{\mathsf{fireball}} \approx 10^{-22}$ s thermal equilibrium and collective behaviour are no longer present. Therefore, only indirect observations about the hot and dense matter can be made, because only the decay products of the fireball are detectable. Besides the question what kind of matter has been created and what its thermodynamic properties are, the underlying requirement that a thermodynamic system has been created has to be investigated. For that, the size of the colliding system can be varied, either by using smaller nuclei such as copper (Cu) or Indium (In) or by triggering on different centralities of the nucleus-nucleus collisions. Here, central collisions mean that the nuclei collide head-on, while in peripheral collisions only the outer nucleons participate in the reaction. The remaining nucleons continue on their trajectory unscathed. Thus, nucleons are divided into participants and spectators.

The region of the phase diagram that can be probed in a heavy-ion collision is mainly dependent on the initial collision energy [Cle98, Cle06, Dum06]. While higher energies lead to higher temperatures, they also lead to smaller baryochemical potentials, because the baryons are not stopped to form a part of the thermalised system, but continue on their original trajectories. In the largest heavy-ion accelerators, we therefore expect the matter to thermalise in the deconfined QGP-phase and cool and hadronise via the cross-over phase transition region. This is certainly the case for the Large Hadron Collider (CERN-LHC), whose heavy-ion program (Pb+Pb at up to $\sqrt{s_{\mathsf{NN}}} = 5.5$ TeV) is expected to start in the next winter 2010/2011. At top energies at the Relativistic Heavy Ion Collider (BNL-RHIC), the collision of Au+Au nuclei at $\sqrt{s_{\mathsf{NN}}} = 200$ GeV is also expected to follow the same phase diagram trajectory. Evidence for the creation of a strongly coupled deconfined phase, the sQGP, has been put forward by the experiments after the discovery of strong jet quenching and large elliptic flow [PHENIX03, PHENIX04, STAR05, Bac05, BRAHMS05, PHENIX05].

At lower energies that are accessible in the fixed-target experiments at the Super Proton Synchrotron (CERN-SPS, Pb+Pb at $E_{\mathsf{lab}} = 158$ AGeV), it is questionable if the temperatures reached are high enough to cross the phase transition line, although the step in the mean transverse mass excitation function of protons, kaons and pions and the enhanced K^+/π^+-ratio have been cited by the collaborations at SPS as indicators that a QGP has actually been formed [NA49-08]. However, as discussed above, the chemical potentials at low beam energies may be sufficiently high so that the system may be close to the critical point, whose exact position is not known.

The search for this critical end point is the main motivation for current and planned experimental heavy-ion programs of the SHINE-experiment at the SPS [NA61-07] and the CBM-experiment at the Facility for Antiproton and Ion Reserach (FAIR) [CBM05]. The current low-energy run at RHIC also addresses this issue [STAR09, STAR10]. All of these programs plan to systematically investigate excitation functions of various observables, foremost fluctuations, which are expected to show non-monotonous behaviour around the critical point. Therefore, they will vary the initial collision energy in a large range. While FAIR will investigate the low energy regime $E_{\mathsf{lab}} \leq 35$ AGeV ($\sqrt{s_{\mathsf{NN}}} \approx 8.2$ GeV), RHIC will investigate the high energy regime, reaching down to $\sqrt{s_{\mathsf{NN}}} \geq 5$ GeV ($E_{\mathsf{lab}} \approx 12.3$ AGeV). The SHINE-heavy-ion program aims at collision energies between $E_{\mathsf{lab}} = 20$ AGeV and $E_{\mathsf{lab}} = 80$ AGeV. Thus, the energy regime interesting in the quest for the critical point will be covered by different experiments.

On the theoretical side, the major problem with the description of heavy-ion collisions is the difficulty to describe the time evolution of the produced matter. As pointed out above, this is, up to now, not possible from first principle Quantum Chromodynamics (QCD). One has to rely on well-developed dynamical models to describe the space-time evolution of the nuclear interactions in the hot and dense stage of the reaction. A well-established approach to explore the dynamics of heavy-ion reactions is relativistic transport theory [Ehe95, Gei97, Bas98, Ble99, Mol05, Xu05, Lin05, Bur05, Bas07]. In this kind of microscopic description, the hadronic and/or partonic stage of the collision is described under certain approximations. Most transport models, for instance, cannot describe collisions with more than two incoming particles, which restricts the applicability to low particle densities, where multi-particle interactions are less important. Some attempts to include multi-particle interactions do exist [Bar01, Cas02, Xu05, Lar07, Ble07, Ble08], but this field of study is still rather new. The coupling of a partonic phase with a hadronic phase poses another challenge on transport models, because the microscopic details of that transition are not well known. Another complication in the transport approach is that all microscopic scatterings are explicitly treated in the model and therefore the cross-sections for all processes must be known or extrapolated. However, for many processes high quality experimental data are not available, and therefore a large fraction of the cross-sections have to be calculated or parametrised by additional models. Transport theory is explained in more detail in Section 3.1.

Relativistic, (non-)viscous fluid- or hydrodynamics is a different approach to explore the space-time evolution of a heavy-ion collision [Cle85, Mcl86, Von86, Kat88, Sri91, Sri96, Sri92, Sri92a, Cle93, Ris95, Hir02, Huo02, Huo02a, Kol03, Non07, Fro07]. It constitutes a macroscopic description of the matter that is created, assuming that at every time and in every place the matter is in local thermal equilibrium. This assumption can only be true if the matter is sufficiently dense, so in the late stages of a heavy-ion collision hydrodynamics loses applicability. In addition, the requirement of local thermal equilibrium restricts the starting time of the hydrodynamic model. One advantage is that in the

dense stages, hydrodynamics can propagate any kind of matter, and also allows for transitions between two types of matter, e.g. QGP and hadron gas, if an appropriate Equation of State (EoS) is provided. Hydrodynamics can therefore be used to study hadronic and partonic matter in one common framework.

The restrictions of these kinds of models can be relaxed as well. By introducing viscosity and heat conductivity, perfect thermal equilibrium does not have to be present at any point. However, even with second order corrections the matter has to be close to equilibrium [Bai06, Dus08, Son08].

Input to solve the hydrodynamic differential equations are the boundaries, i.e. the initial state (the distributions of all relevant densities and currents at the time the evolution starts), the Equation of State providing the pressure as function of the energy and baryon number densities that describes the behaviour of the matter that is considered, and the freeze-out hypersurface. Ideal hydrodynamics is examined more closely in Section 3.2.

Other models that are used in heavy-ion collisions often focus on more detailed problems. The production of heavy quarks, for instance, can only happen when the typical energy scale of the elementary collisions is sufficiently high. This is only the case at the beginning of the heavy-ion reaction. Usually, for the calculation of the yields of heavy quarks, one uses perturbative QCD (pQCD)-calculations of the initial nucleon-nucleon interactions and neglects the effects of early interactions of the medium. pQCD-processes are also an important source for photon emission, see Chapter 2.

A lot of approaches try to model the interaction of high-$p_\perp$ particles produced in these initial pQCD-processes (hard particles) with the thermal, soft (low-$p_\perp$) medium and try to determine the mechanisms of energy loss and absorption [Wan92, Bai97, Bai97a, Gyu00] which has been one of the key findings from the experiments at RHIC [STAR05].

As pointed out above, a heavy-ion collision is too small and too short-lived to be observed directly. All information about the fireball has to be inferred from the momentum distributions of the stable or meta-stable particles that are emitted by the heavy-ion reaction. One obstacle that arises from this limitation is that the bulk part of particles is emitted at the late stages of the reaction and therefore most single particles carry only indirect information about the early stage, where the energy density is highest.

In order to gain information about the early part of a heavy-ion collision, one has several options: i) look for multi-particle correlations which may have been created very early and may have survived subsequent scatterings, at least in a statistical average, ii) use particles whose production mechanism is well-known and investigate how their final distribution differs from the expected distribution, or iii) examine particles that are created in the hot and dense phase and leave the system unscathed.

Let us examine these possibilities: multi-particle correlations (i) give insight to collective behaviour like flow patterns of the medium and can therefore, among other things, help answering the question whether the matter created

can be thought of as a collective medium at all. Particles whose production mechanism is well-known (ii) must be created independently from the medium that may be formed, i.e. the energy scale for creation must be higher than what is available in the medium. This includes high-$p_\perp$ jets and heavy quarks. The production of both can be calculated in pQCD or measured directly in elementary proton-proton collisions and then scaled with the number of elementary proton-proton collisions. The scaling, though, is model-dependent and varies with the assumption about the geometry of the initial nuclei [Won84, Ian03], and proton-proton collisions themselves may start to show effects of a medium at LHC-energies [CMS10, Shu10].

Option (iii) has the advantage that single-particle information is available directly from the hot and dense parts of the fireball evolution. Particles that do not interact strongly, but electromagnetically, are perfect for these investigations. Their production cross-section is, albeit suppressed with respect to hadronic production cross-sections, large enough to be detectable, and the detection can be done largely with the same methods as the detection of hadrons.

Three different electromagnetic probes are available: The charged leptons (muons μ and electrons e) and photons γ. Leptons are usually used to reconstruct hadronic decays, but $q\bar{q}$-annihilations in initial nucleon-nucleon scatterings (the Drell-Yan process [Dre70]) also contribute to the spectrum. Since lepton number is conserved, they can only be produced associated with their respective anti-particle or together with a neutrino, which escapes detection. Associated pairs of leptons and anti-leptons, dileptons, are used to study spectral functions of decaying particles [Bro91, Sch06]. This way, possible in-medium modifications of the spectral function due to e.g. chiral restauration may be detectable.

Single leptons, on the other hand, are mostly used to measure the semi-leptonic decays of heavy quarks and thus give complementary information to that reconstructed from hadronic decays. The undetected neutrinos from such decays carry only a small fraction of the mother particle's momentum and do not significantly alter the measurement.

Photons have the advantage that they can be produced in pairs and as single particles, because they carry no conserved quantum number except spin. The idea to use them to probe the matter has been put forward some 30 years ago by Feinberg, Shuryak and others [Fei76, Shu78, Hal82, Sin83, Hwa85, Sta86].

The aim of this work is to present calculations of direct photon emission with the current version of UrQMD (u3.3) with pure transport calculations and transport + hydrodynamic hybrid calculations. After a review of the state of the art in both direct photon experiments and theory in Chapter 2, the model for the fireball evolution and for photon emission out of it will be presented in Chapter 3 and its numerical properties and parameters tested in Chapter 4. In Chapter 5, transverse momentum spectra and elliptic flow coefficients for direct photons are presented. Detailed analyses on photon emitting channels, photon emission times and bayron number densities at photon emission sources follow

in Chapters 6, 7 and 8, respectively. The results and their implications are summarised in Chapter 9.

Chapter 2

Direct Photons

2.1 Direct photon experiments

In the history of heavy-ion physics, seven experiments have been trying to extract direct photon yields. At the SPS, Helios was the first experiment to publish upper limits for direct photon yields [HELIOS90], followed by the WA80 [WA80-91, WA80-96] and CERES [CERES96] collaborations. The WA93 collaboration only measured inclusive photon spectra [WA93-94]. Direct photon measurements have first been available from the WA98 collaboration [WA98-00, WA98-00a, WA98-04]. At RHIC, the PHENIX collaboration has published various results on direct photon spectra [PHENIX05a, PHENIX05b, PHENIX06, PHENIX07, PHENIX10, PHENIX09, PHENIX10a, PHENIX10b]. The STAR collaboration at RHIC has published photon-hadron azimuthal two-particle correlation data [STAR09a], their analysis of direct photon spectra is still ongoing. The ALICE experiment at the LHC plans to measure direct photon spectra in Pb+Pb collisions [ALICE08].

2.2 Photon emission sources

There are several different sources of photon production in heavy-ion collisions. A schematic overview of them is given in Figure 2.1. The foremost distinction is being made between decay photons and direct photons. Hadronic decays make up the overwhelming part of all photons, most dominantly the decays $\pi^0 \to \gamma\gamma$, $\pi^0 \to \gamma e^+ e^-$, $\eta \to \gamma\gamma$ and $\omega \to \pi^0\gamma$ [WA98-00]. Direct photons are all those photons that do not come from hadronic decays. They may come from hard (pQCD-) processes, processes that happen before thermalisation or otherwise out of equilibrium, and from thermal scatterings.

Hard photon emission may come from quark-gluon compton scattering $qg \to \gamma q$ and annihilation $q\bar{q} \to \gamma g$. These processes happen at the initial nucleon-nucleon scatterings, are not affected by the medium and constitute the prompt photon contribution. Hard photons may also come from bremsstrahlung $qg \to$

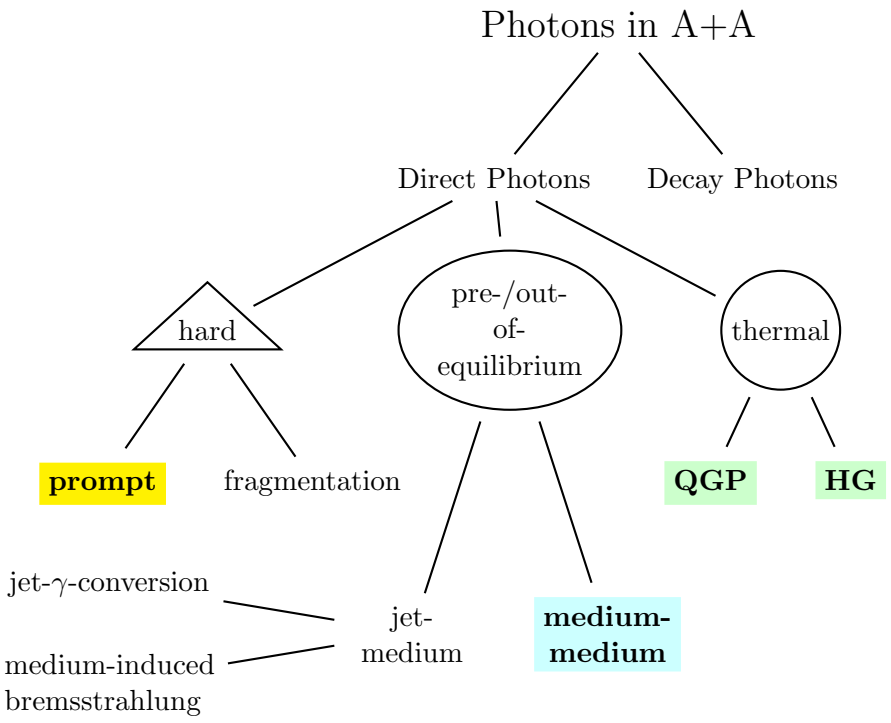

Figure 2.1: Schematic overview of the different photon emission sources in heavy-ion collisions. In this work, the shaded contributions are examined.

$gq^* \rightarrow gq + \gamma$ and fragmentation $qg \rightarrow qg^* \rightarrow q + \gamma X$. Those processes are influenced by the medium [Gal09].

Processes out of equilibrium include interactions of jets with a thermalised medium as well as collisions among soft particles that are not yet thermalised. In the former, the processes discussed above reappear, e.g. Compton scattering $q_{\mathsf{hard}} + g_{\mathsf{QGP}} \rightarrow \gamma + q$ and annihilation $q_{\mathsf{hard}} + \bar{q}_{\mathsf{QGP}} \rightarrow \gamma + g$, but additionally, a quark jet may emit a photon instead of a gluon in one of its scatterings through the medium. In non-thermalised soft collisions, the same processes as in thermalised systems may appear.

In partonic thermalised systems, photon sources are annihilation and bremsstrahlung, as before, and additionally any $2 \leftrightarrow 2$-scatterings of quarks, antiquarks and gluons that may happen in the medium. In hadronic systems, the major photon sources are collisions of the π, ρ, K and η-mesons.

In the framework of this work, non-thermalised partonic systems cannot be described, and neither partonic jets. Photon emission from jet-fragmentation, jet-bremsstrahlung and jet-γ-conversion can therefore not be included. Prompt photons are calculable from pQCD from the initial nucleon-nucleon collisions without the knowledge of the partonic system that is formed later and therefore

are included.

2.3 Photon measurement

In contrast to electrons, photons are not charged. Therefore, the only means of measuring them is electromagnetic calorimetry. We will discuss two types of electromagnetic calorimeters: homogeneous calorimeters and sampling calorimeters. In both types, the photons decay in e^+e^- pairs, which produce less energetic photons by bremsstrahlung. The calorimeter material has a short radiation length X_0. Within one radiation length, the probability of pair creation from one photon is $1 - \mathrm{e}^{-7/9} \approx 54$ % and the average energy loss of an electron is $1 - \mathrm{e}^{-1} \approx 63$ % of its initial energy. After enough steps of pair creation and bremsstrahlung, the energy loss by ionisation of the detector is equal to the energy loss by bremsstrahlung, and the shower stops. Then, the low-energy photons are detected by a photomultiplier tube (PMT). The shower shape can be used to disentangle hadronic particles from electromagnetic particles, because the nuclear interaction length λ is large compared to the radiation length X_0. Therefore, hadronic showers are usually deeper and broader.

A homogeneous calorimeter consists of one large lead-glass Čerenkov radiator. Here, the number of Čerenkov photons is proportional to the initial photon energy. They propagate to the PMT with wavelength-dependent attenuation. Also, some photons leak through the PMT. Thus, non-linear acceptance effects occur.

In sampling calorimeters, a material that creates showers (e.g. lead) is alternately layered with a scintillator material (e.g. POPOP[1]), and the produced light is collected with optical fibers through the whole tower (one pixel). In contrast to the homogeneous calorimeters, the deposited energy is proportional to the initial photon energy in this kind of detector.

The problem with each of these detectors is that the materials needed are usually both very heavy and very expensive. Therefore, photon measurements usually have a much lower coverage than hadronic or charged particle measurements [ALICE08].

2.3.1 Direct photon extraction

From the inclusive photon spectra, direct photon spectra need to be extracted by experiments. For this, several methods are available.

Subtraction method In the subtraction method, the basic idea is to measure the inclusive photon spectrum, determine the number of π^0 and η mesons with high accuracy by invariant mass analysis and extrapolate the yield of other particles that decay to photons by the assumption of $m_\perp$-scaling,

[1] 1,4-bis(5-phenyloxazol-2-yl) benzene

i.e. that the ratio of the yield at the same $m_\perp$ is constant. The photons from those meson decays are then subtracted from the inclusive spectrum. In order to account for systematic errors, the double ratio R is introduced, with

$$\gamma^{\mathsf{direct}} = (1 - R^{-1})\gamma^{\mathsf{all}} \quad . \tag{2.1}$$

R is defined as

$$R = \frac{\gamma^{\mathsf{all}}}{\gamma^{\mathsf{background}}} = \frac{\left(\gamma^{\mathsf{all}}/\pi^0\right)_{\mathsf{measured}}}{\left(\gamma^{\mathsf{all}}/\pi^0\right)_{\mathsf{calculated}}} \tag{2.2}$$

and is the photon-to-π^0-ratio as measured, divided by the photon-to-π^0-ratio as calculated from the number of π^0 mesons assuming there are no other photon sources. This method relies on the assumption that the number of π^0 mesons can be measured with high accuracy and that the signal-to-background ratio (direct photons vs. decay photons) is sufficiently high. The subtraction method has been successfully used by the WA98 and PHENIX collaborations [WA98-00, PHENIX05b].

Hanbury Brown and Twiss analysis HBT-analyses use quantum interference effects to determine lifetime and size of an object too remote (like stars) or too small (like heavy-ion reactions) to be directly observed [Han56, Gol60, Zaj84]. Following the realisation that π^0 mesons, which decay after $c\tau \approx 25 \cdot 10^6$ fm, have a two-particle correlation function too narrow to experimentally resolve, the complete measurable two-photon correlation is composed from direct photons (other decay photons are subtracted similarly). Its magnitude can then be used to extract the direct photon yield. Unfortunately, this method only works for very small $p_\perp < 300$ MeV and has only been successfully tried by the WA98 collaboration [WA98-04].

Extrapolation from dileptons Any process that produces real (i.e. massless) photons can also produce virtual, massive photons γ^* which decay into dileptons. The connection between the number of photons $\mathsf{d}N_\gamma$ and dileptons $\mathsf{d}N_{ee}$ with an invariant mass of M is given by [Lic95]

$$\frac{\mathsf{d}^2 N_{ee}}{\mathsf{d}M} = \frac{2\alpha}{3\pi}\frac{1}{M}\sqrt{1 - \frac{4m_e^2}{M^2}}\left(1 + \frac{2m_e^2}{M^2}\right) S\mathsf{d}N_\gamma \quad , \tag{2.3}$$

where α is the fine structure constant and S is a process dependent factor which for $M \to 0$ and $M \ll p_\perp$ goes to 1, and is 0 for dileptons from hadronic decays if $M > m_{\mathsf{had}}$. The low-mass dilepton spectrum is contaminated by dileptons from the π^0-Dalitz decay, so that the limit $M \ll p_\perp$ has to be exploited. Since the dilepton mass has to be greater than at least M_{π^0}, but preferrably also greater than M_η, the reach to low $p_\perp$ is limited to approximately $p_\perp = 1$ GeV. Still, the PHENIX collaboration could extend the $p_\perp$ range of direct photon measurement

with this method compared to the "traditional" subtraction method (see above) [PHENIX10, PHENIX10a].

2.4 Calculations of direct photons

In the past, direct photon calculations have been done in different frameworks. A previous version of UrQMD has been used by Dumitru *et al.* [Dum95, Dum98, Dum97]. For a comparison with that work, see Section 4.4. Also, HSD [Ehe96] has been used to extract direct and decay photon yields by Bratkovskaya *et al.* [Bra08], and Li *et al.* [Li97] have published calculations using the AMPT model.

Various hydrodynamic models have been used for direct photon calculations. Among those were Kapusta *et al.* [Kap91], Srivastava, Sinha *et al.* [Sri91, Sri96, Sri92, Sri92a, Sri98, Sri01], Turbide *et al.* [Tur04, Tur05], Liu *et al.* [Liu09, Liu09a], Bass [Bas07] and Dusling [Dus10, Dus09].

Calculations of pQCD photon emission are available from Gordon and Vogelsang [Gor93], Wong *et al.* [Won98], Aurenche *et al.* [Aur87, Aur87a, Aur88, Aur98, Aur99, Aur00], the CTEQ-805 Collaboration [Apa99] and others, e.g. [Bai92, Hus95, Pap00].

Comprehensive reviews about direct photon calculations can be found in [Owe87, Gal02, Gal09].

Chapter 3

Model

3.1 Transport Models

One of the tools used to describe heavy-ion physics is transport theory. In transport theory, particles or one-particle distribution functions $f(x,p) = \frac{\mathrm{d}N}{\mathrm{d}^3x\mathrm{d}^3p}$ are propagated according to the Boltzmann-Equation [Ehe96]

$$\begin{aligned}&\left[\left(p_\mu - U_{i\mu} - \{p_\nu - U_{i\nu}\}\,\partial_\mu^p U_i{}^\nu - \{M_i + U_i\}\,\partial_\mu^p U_i\right)\partial_x^\mu\right.\\&\left.+\left(\{p_\nu - U_{i\nu}\}\,\partial_\mu^x U_i{}^\nu - \{M_i + U_i\}\,\partial_\mu^x U_i\right)\partial_p^\mu\right] f_i\,(x,p) = \mathcal{C}\,(f_i, f_j, \ldots) \quad , \quad (3.1)\end{aligned}$$

where $\mathcal{C}\,(f_i, f_j, \ldots)$ is the full collision term describing collisions between particle species i and all other particle species $f_j, \ldots$. M_i is the mass of the particle species i and $U_i{}^\mu$ and U_i are the real parts of the vector and scalar hadron self-energies. In cases where the interaction between particles consists only of collisions (no potential), Equation (3.1) simplifies to

$$p^\mu \partial_\mu f_i\,(x,p) = \mathcal{C}\,(f_i, f_j, \ldots) \quad . \quad (3.2)$$

In numerical implementations of the Boltzmann-Equation, the particle distribution functions are usually represented by a number of classical test particles whose initial momenta and positions are distributed according to $f\,(x,p)$. While a large number of test particles allows for a smooth representation of f, a small number of test particles allows for the study of event-by-event fluctuations.

From Equation (3.2), it can be seen that transport codes propagate particles on classical trajectories, i.e. in the absence of potentials on straight lines. However, the collision probability, encoded in the collision term $\mathcal{C}$, is usually calculated with, or at least inspired by, quantum mechanics.

The collision term $\mathcal{C}$ in Equation (3.2) usually consists of an incoherent addition of the partial collision terms of all sub-processes that are implemented. For collisions with two incoming particles and two outgoing particles $2 \leftrightarrow 2$, the

collision term according to Uehling-Uhlenbeck can be written as

$$\mathcal{C}_{22}(p) = \int \frac{\mathsf{d}^3p_1}{E_1}\frac{\mathsf{d}^3p'}{E'}\frac{\mathsf{d}^3p_1'}{E_1'}\sigma\left(ab\to cd\right)\delta^{(4)}\left(p^\mu + p_1^\mu - p'^\mu - p_1'^\mu\right) \cdot\Big\{f(p')f(p_1')\left[1+af(p)\right]\left[1+af(p_1)\right] - f(p)f(p_1)\left[1+af(p')\right]\left[1+af(p_1')\right]\Big\} \quad . \tag{3.3}$$

Here, a is the quantum factor ($a=+1$ for fermions, $a=-1$ for bosons and $a=0$ for classical particles) and $\sigma(ab\to cd)$ is the cross-section for this particular process.

Transport models need to assume that the particles have a large mean free path λ_{mfp}, so that subsequent scatterings can be considered incoherent and quantum interferences can therefore be ignored. Also, in dense systems, multiparticle interactions become important, i.e. interactions with three or more incoming particles. While those can be described by transport models [Grä09, Xu05], their implementation poses a big numerical challenge.

3.1.1 The Ultra-relativistic Quantum Molecular Dynamics Model

The Ultra-relativistic Quantum Molecular Dynamics (UrQMD) model has been developed at Frankfurt University more than ten years ago [Bas98, Ble99]. In standard setup, UrQMD calculates hadronic collisions with one test particle per real particle and without potential. The inclusion of potential terms is negligible at ultrarelativistic energies $E_{\mathsf{lab}} \gtrsim 1$ GeV, where the typical energy scale is much larger than the typical binding energy.

Nuclei are initialised according to a coordinate-space Woods-Saxon-distribution in UrQMD. All calculations in this thesis are done with spherically symmetric nuclei. In the case of the collisions of uranium nuclei, which have an eccentricity of $\epsilon = 0.27$, this provides an intrinsic averaging over different possible alignments of the projectile and target nucleus. It turns out that for untriggered collisions (i.e. without selection on the alignment of the nuclei) the results are not sensitive to this choice.

UrQMD includes all hadronic particle species that are included in the Particle Data Book [Ams08] and have a pole mass $m < 2.25$ GeV. In cases in which the cross-sections of processes are not experimentally known, the cross-sections are determined via one of the following principles:

Isospin-symmetry The cross-sections of all hadrons with the same isospin are considered to be equal, if the channels are not forbidden by conservation laws, e.g., $\sigma\left(\pi^+\pi^0\to\rho^+\right) = \sigma\left(\pi^-\pi^0\to\rho^-\right) = \sigma\left(\pi^+\pi^-\to\rho^0\right)$.

Detailed Balance If the matrix-element $|\mathcal{M}|^2$ of scatterings is independent of the mandelstam variables, it is also independent of the permutation of external particles, i.e. $|\mathcal{M}\left(AB\to CD\right)|^2 = |\mathcal{M}\left(AD\to BC\right)|^2 =$

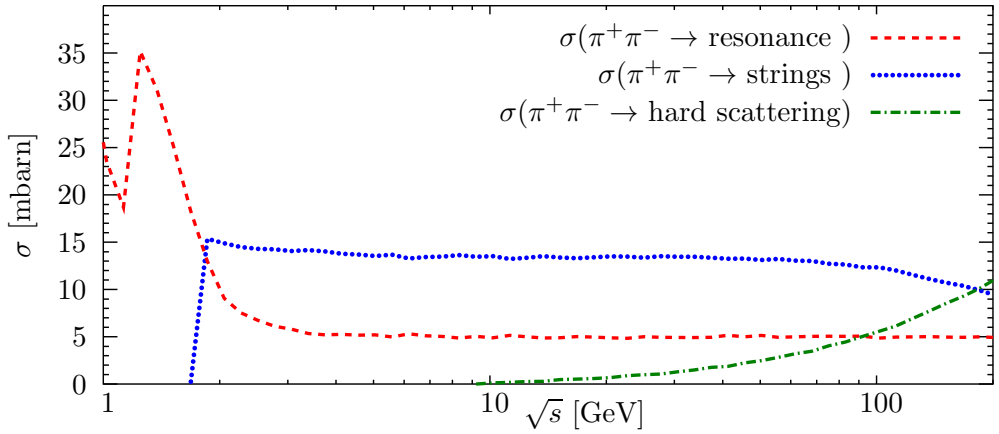

Figure 3.1: UrQMD-cross-sections for $\pi^+\pi^-$-collisions as function of center-of-mass energy. We show the resonant hadronic cross-section (dashed line), the cross-section for the formation of strings (dotted line) and for hard scatterings via PYTHIA (dash-dotted line). The peak at the ρ-meson pole mass has been cut out for better visibility.

$|\mathcal{M}(CD \to AB)|^2 = \ldots$. Therefore, the cross-sections of those processes can be calculated if one of them is known.

Additive Quark Model If all else fails, the additive quark model (AQM) is used. Here, the valence quark content of the hadrons is used to determine the cross-sections.

Unstable particles in UrQMD are assigned a mass according to their vacuum spectral function and are then propagated on shell with this mass. No in-medium modification is present.

Inelastic collisions at low center-of-mass energies $\sqrt{s_{\mathsf{coll}}}$ excite hadronic resonances, which are themselves treated as particles and propagated accordingly. At higher $\sqrt{s_{\mathsf{coll}}}$, the resonance model is no longer suited to describe the collisions, because the hadron spectrum starts to be a continuum and particle production is very much forward-peaked and therefore less isotropic. In this region, the LUND string model [And83, And86] is employed [Sch93, Win96].

At very high center-of-mass energies $\sqrt{s_{\mathsf{coll}}}$ and high momentum transfers $t > 1.5$ GeV^2, UrQMD models hard interactions via PYTHIA v6.4 [Sjö06]. Figure 3.1 shows the total cross-sections of resonant hadronic interactions, string excitation and (hard) PYTHIA-scatterings as a function of the center-of-mass energy of the collision $\sqrt{s_{\mathsf{coll}}}$. The contribution of hard scatterings to the total $\pi^+\pi^-$ cross-section at the highest SPS-energies ($\sqrt{s} \approx 17.3$ GeV) is about 4 %, and at top RHIC energies ($\sqrt{s_{\mathsf{NN}}} = 200$ GeV), it is the largest contribution with approximately 43 %. Figure 3.2 shows a comparison between charged particle spectra from proton-proton collisions calculated in UrQMD with and without

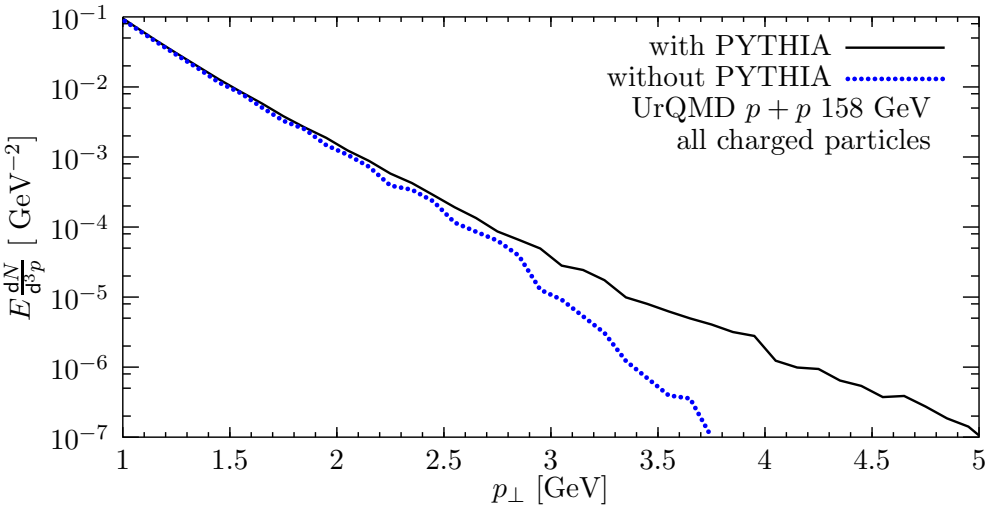

Figure 3.2: Charged particle spectra from proton-proton collisions at $E_{\mathsf{lab}} = 158$ AGeV calculated with UrQMD with (solid line) and without (dotted line) PYTHIA.

the PYTHIA contribution.

The collision criterion in UrQMD is a geometrical interpretation of the quantum-mechanical cross-section σ. The cross-section is considered to be the transverse area of a particle with radius $r = \sqrt{\sigma/\pi}$. The minimal distance between two particles must be less than $d < 2r = 2\sqrt{\sigma/\pi}$ in order for them to interact.

Due to the uncertainty principle, $\Delta E \Delta t \geq \hbar/2$, the duration of the formation of a particle with given energy has some uncertainty. Therefore, particles that are formed from a string are assigned a formation time t_{form} during which they cannot interact.

Furthermore, when a string is produced, the leading quarks or diquarks are considered to be hadrons and can interact with different particles, although their cross-section is reduced to 1/3 (for quarks) or 2/3 (for diquarks) of the usual cross-section.

3.2 Hydrodynamic Models

Hydrodynamics is a different effective model for the description of matter. Like transport theory, it is based on the Boltzmann-Equation (see Equation (3.2)). Unlike in transport theory, only the first and second moment of the Boltzmann-Equation are considered, so that the remaining equations represent the conservation of energy density and net baryon number density. In relativistic formulation,

the five Equations of Motion in (ideal) hydrodynamics are:

$$\partial_\mu T^{\mu\nu} = 0 \quad , \tag{3.4a}$$
$$\partial_\mu N_i^\mu = 0 \quad , \tag{3.4b}$$

with

$$T^{\mu\nu}(x) = \int \frac{\mathsf{d}^3 p}{p^0} p^\mu p^\nu \sum_i f_i(x,p) \quad , \tag{3.5a}$$
$$N_i^\mu(x) = \int \frac{\mathsf{d}^3 p}{p^0} p^\mu f_i(x,p) \quad . \tag{3.5b}$$

In the following, we consider only systems with a common particle distribution function for all particles, so that the index i can be dropped from Equation (3.5). The energy-momentum-tensor $T^{\mu\nu}$ and the particle number density N^μ can be decomposed with respect to an arbitrary normalised, time-like 4-vector u^μ. To see this, we define a projection operator $\Delta^{\mu\nu}$ which projects onto the three-space orthogonal to u^μ:

$$\Delta^{\mu\nu} = g^{\mu\nu} - u^\mu u^\nu \quad . \tag{3.6}$$

Now, we are able to decompose the particle number density and the energy-momentum tensor in the general form:

$$N^\mu = \rho u^\mu + q^\mu \tag{3.7a}$$
$$T^{\mu\nu} = \varepsilon u^\mu u^\nu - P\Delta^{\mu\nu} + W^\mu u^\nu + W^\nu u^\mu + \pi^{\mu\nu} \quad . \tag{3.7b}$$

If we boost to the frame where $u^\mu = (1, \vec{0})$, we can give meaning to the arising quantities:

$$\rho = N^\mu u_\mu \qquad \text{charge density} \tag{3.8a}$$
$$q^\mu = \Delta^{\mu\nu} N_\nu \qquad \text{charge flow} \tag{3.8b}$$
$$\varepsilon = u_\mu T^{\mu\nu} u_\nu \qquad \text{energy density} \tag{3.8c}$$
$$P = -\frac{1}{3}\Delta^{\mu\nu} T_{\mu\nu} \qquad \text{isotropic pressure} \tag{3.8d}$$
$$W^\mu = \Delta^{\mu\alpha} T_{\alpha\beta} u^\beta \qquad \text{energy flow} \tag{3.8e}$$
$$\pi^{\mu\nu} = \left[\frac{1}{2}\left(\Delta^\mu{}_\alpha \Delta^\nu{}_\beta + \Delta^\nu{}_\alpha \Delta^\mu{}_\beta\right) - \frac{1}{3}\Delta^{\mu\nu}\Delta_{\alpha\beta}\right] T^{\alpha\beta} \qquad \text{stress tensor} \tag{3.8f}$$

The vectors q^μ and W^μ have three independent parameters each, and the traceless tensor $\pi^{\mu\nu}$ has five, so that the number of independent quantities remains 14 ($n, \varepsilon, P, q^\mu, W^\mu, \pi^{\mu\nu}$).

To add physical meaning to the Lorentz frame, we can connect u^μ to the flow velocity of the particles or of the energy:

$$u^\mu_{\mathsf{E}} = \frac{N^\mu}{\sqrt{N^\nu N_\nu}} \qquad \text{Eckart frame} \tag{3.9a}$$
$$u^\mu_{\mathsf{L}} = \frac{T^{\mu\nu} u_\nu}{\sqrt{u_\alpha T^{\alpha\beta} T_{\beta\gamma} u^\gamma}} \qquad \text{Landau frame} \tag{3.9b}$$

In the Eckart frame, the charge flow q^μ vanishes, while in the Landau frame the energy flow W^μ vanishes.

Solving the full hydrodynamic equations in a closed form is still impossible, so one must either find additional equations or further simplifications. In ideal hydrodynamics, one assumes that the phase space distribution function is given by the local thermal equilibrium distribution

$$f(x,p) = \frac{g}{(2\pi)^3} \frac{1}{\exp \frac{p^\nu u_\nu - \mu}{T} + a} \quad , \tag{3.10}$$

where T and μ are the local temperature and chemical potential, a is the quantum factor and u^ν is the local fluid flow. With this assumption and Equation (3.5), one can derive that the energy and the particle number flow in the same direction $u^\mu_{\mathsf{E}} = u^\mu_{\mathsf{L}} = u^\mu$. From this, it follows that the charge flow and energy flow vanish $q^\mu = W^\mu = 0$. Additionally, one can show that with this assumption the stress tensor must vanish, $\pi^{\mu\nu} = 0$. Thus, one is left with 6 unkowns $\rho, \varepsilon, P, u^\mu$. Inserting these results into Equation (3.8), we obtain

$$T^{\mu\nu}(x) = [\varepsilon(x) + P(x)]\, u^\mu(x) u^\nu(x) - P(x) g^{\mu\nu} \tag{3.11}$$

$$N^\mu(x) = \rho(x) u^\mu(x) \quad . \tag{3.12}$$

In order to close the system of equations, one additional equation is needed. Usually, a relationship between the pressure P and the energy- and particle densities ε, ρ is employed, the so-called Equation of State $P = P(\varepsilon, \rho)$ (EoS). All information about the medium that is to be described is encoded in the EoS. Of special interest for the evolution is the speed of sound c_{S}, because it connects the pressure P and energy density ε

$$c^2_{\mathsf{S}} = \frac{\partial P}{\partial \varepsilon} \quad . \tag{3.13}$$

It should be noted that although $P(\varepsilon, \rho)$ closes the system of hydrodynamic equations, it is not sufficient to calculate arbitrary thermodynamic quantities such as chemical potential μ_{B}, temperature T or entropy density s. Parametrising $P = P(T, \mu)$, however, allows the determination of any thermodynamic quantity.

In hydrodynamics, information about single particles have been integrated over, so that it is a theory for bulk matter rather than for individual particles. Collective behaviour, on the other hand, can be described very well and is extractable easier from a hydrodynamic simulation than from a transport calculation.

3.2.1 The SHASTA-model

The SHarp And Smooth Transport Algorithm SHASTA is a numerical implementation of the relativistic ideal hydrodynamic Equations of Motion [Bor73].

This algorithm works with a Eulerian grid, which means that the matter is distributed into cells whose position is fixed in coordinate space. An alternative is the use of Lagrangian cells that co-move with the fluid. In this case, though, the cells will be highly deformed by the evolution of the medium, which increases the computational complexity of the problem.

In the implementation used for this work [Ris95a, Ris95], the grid is formulated in cartesian coordinates (t, x, y, z). In order to prevent numerical instabilities, the cell sizes in space are equal $\Delta x = \Delta y = \Delta z$ and the time step is $\Delta t = 0.4\Delta x$.

SHASTA solves the hydrodynamic Equations of Motion with a flux-corrected transport algorithm. Here, the densities are first transported and diffused to the next time step with second-order accuracy, and in a separate step, the diffusion introduced during the transport is estimated and subtracted from the time-advanced quantities. That last step must not introduce create new maxima or minima in the propagated densities. Therefore, the naïve antidiffusion fluxes are replaced by "flux corrected" antidiffusion fluxes in which this is ensured.

In cases where the propagation algorithm violates the relativistic constraint $\varepsilon \geq |\vec{m}|$, i.e. that the energy density must be larger then the modulus of the momentum density vector, the momentum density $\vec{m}$ is simply restricted not to be larger than ε. The algorithm is stable enough so that the effect of this on global energy and momentum conservation is negligible.

Introducing second-order accuracy over numerically cheaper first order calculations is necessary to prevent overshoots at shock fronts. The algorithm is explicit, i.e. all quantities at a given time only depend on quantities at earlier times. The exact calculation of transported quantities and their diffusion can be found in Section 3.1 of Rischke *et al.* [Ris95a].

3.3 Hybrid Model

In version 3.3, UrQMD (see Section 3.1.1) has been extended beyond the standard transport model. The SHASTA hydrodynamic algorithm can now be used to calculate the high-density part of the evolution [Pet08, Pet09]. The main motivation behind this work is the combination of two successful models for the description of heavy-ion collisions.

In the early phase of the collision the matter is very far out of equilibrium, both chemically and kinetically. Hence, the matter cannot be described in a hydrodynamic model.

After some time, local equilibrium is reached, together with typically high energy- and baryon number densities. In this regime, the applicability of a transport model with only binary collisions may not be justified, so that the description with a hydrodynamic model better fits the characteristics of the system. Also, new states of matter can be implemented easily into a hydrodynamic model without the need to know all microscopic details of the state and – espe-

cially – the transition to this state. This can be achieved simply by varying the Equation of State of the matter.

The assumption of local thermal equilibrium requires the matter to be sufficiently dense, so that an expanding system, as is present in heavy-ion collisions, will at some point evolve to a state where hydrodynamics is no longer applicable. Here, transport theory can step in again to model the dilute matter at the late stages of the evolution.

All calculations with the hybrid model are done on an event-by-event basis, so that fluctuations are naturally taken into account and preserved throughout the calculation. The hybrid model has previously been used for various investigations of hadronic probes, such as strangeness [Pet09a, Ste09], $\langle m_\perp \rangle$ [Pet09b], elliptic flow [Pet09c] and HBT [Li09], as well as dileptons [San10].

3.3.1 Early Stage

As indicated above, the non-equilibrium early stage of a collision is calculated with UrQMD. After some time t_{start}, which depends on the system and the initial collision energy, the matter is transferred to a hydrodynamic description. In standard setup, it is chosen so that the incoming nuclear flow densities may have been absorbed to form a locally kinetically equilibrated matter. We assume the time for this to happen to be the time when the two Lorentz-contracted nuclei have passed through each other. Given the mass of a nucleon m_{N}, the initial collision energy E_{lab} and the radius of the nuclei R, this gives a start time of

$$t_{\mathsf{start}} = 2R\sqrt{\frac{2m_{\mathsf{N}}}{E_{\mathsf{lab}}}} \quad . \tag{3.14}$$

At high energies, this criterion yields starting times which are much smaller than $t_{\mathsf{start}} = 0.6$ fm. For both lead-lead and gold-gold collisions, this is the case for $\sqrt{s_{\mathsf{NN}}} > 40$ GeV. Since even at higher center-of-mass energy thermalisation takes some time, the minimal time for the first transition is set to $t_{\mathsf{start,min}} = 0.6$ fm. In the forward and backward regions of the collision, the matter has had less proper time $\tau = \sqrt{t^2 - z^2}$ to equilibrate, so that the degree of equilibration is expected to deteriorate as one goes away from mid-rapidity particles. While this is no serious problem at smaller energies, it presents a numerical challenge at RHIC-energies. To counter this effect, we exclude all particles from the hydrodynamic phase whose rapidity is $|y| > 2$ at the time of the transition in calculations of RHIC-systems.

At the computational time t_{start}, all particles that have interacted or are newly produced are mapped onto the 3-dimensional spatial grid of the hydrodynamic calculation. In order to stabilise the numerics, the baryon number, energy and momentum of each particle are represented by a Gaussian distribution with a width of $\sigma = 1$ fm, so that e.g. the momentum density m^μ of a particle with

momentum p^μ at position $\vec{x}^0$ reads

$$m^\mu(x,y,z) = \frac{1}{(2\pi)^{3/2}} \frac{\gamma_z}{\sigma^3} p^\mu \exp\left[-\frac{(\vec{x}_\perp - \vec{x}_\perp^0)^2 + (\gamma_z(z-z^0))^2}{2\sigma^2} \right] \quad . \tag{3.15}$$

In this Equation, $\gamma_z = \sqrt{1-\beta_z^2}^{-1}$ is the Lorentz-factor in beam direction, which accounts for the Lorentz-contraction of the nuclei in that direction [Vog08]. The total baryon- and momentum-densities ρ_B and m^μ in each cell are obtained by summing the contribution of all particles.

Particles that have not interacted are considered spectators. Those and the particles that are excluded due to their high rapidity (see above) are propagated in the transport part.

3.3.2 Intermediate Stage

Once the transition from transport to hydrodynamics is complete and all thermodynamic quantities have been calculated from the Equation of State, the matter is propagated according to the hydrodynamic Equations of Motion in the rest frame, which read

$$\begin{aligned} \partial_t \varepsilon_\mathsf{cf} + \nabla_i(\varepsilon_\mathsf{cf} v_i) &= -\nabla_i(P v_i) && \text{(3.16a)} \\ \partial_t m_i + \nabla_i(m_j v_j) &= -\nabla_i P && \text{(3.16b)} \\ \partial_t \rho_\mathsf{cf} + \nabla_i(\rho_\mathsf{cf} v_i) &= 0 && \text{(3.16c)} \end{aligned}$$

with the momentum density $m^\mu_\mathsf{cf} = (\varepsilon_\mathsf{cf}, m_i)$, the net baryon number density ρ_cf and the fluid flow velocity v_i, all given in the computational frame. The Equations are solved on a 200^3 cell grid with $\Delta x = 0.2$ fm and time steps of $\Delta t = 0.08$ fm. In RHIC-calculations, the cell size and time step have been reduced to $(\Delta x, \Delta t) = (0.1, 0.04)$ fm, to account for the strong Lorentz-contraction.

In some cases, the matter expands further than the hydrodynamic grid. If so, the overflowing parts of the system are lost. Therefore, if more than 0.01 % of the initial energy are lost, the matter is transferred to a grid with larger cell size $\Delta x' = 2\Delta x$ and a correspondingly increased time step $\Delta t' = 2\Delta t$. In this procedure, the quantities m^μ and ρ_B of $2^3 = 8$ neighbouring cells are averaged over and the intensive quantities P, T and μ_B are calculated from the Equation of State.

3.3.3 Late Stage

As the matter evolves, it expands into vacuum and dilutes. When a critical energy density $\varepsilon_\mathsf{crit}$ is reached, the matter is transferred back to the transport description. Two scenarios for this transition are available, the isochronous and the gradual transition.

Isochronous transition In calculations with the isochronous transition, the whole system is described with hydrodynamics until the energy density of every cell is smaller than $\varepsilon_{\mathsf{crit}}$. Then, particles are created with the procedure described below. In this scenario, it is possible that parts of the system have already diluted far below $\varepsilon_{\mathsf{crit}}$, so that the applicability of hydrodynamics may be questioned.

Gradual transition The other alternative is the gradual transition. Here, parts of the system can be transferred to the transport description individually. The transition proceeds in transverse "slices" of the thickness of one cell, each of which is transferred as soon as all cells of that slice meet the transition criterion. The distribution of transition times t_{trans} in hybrid calculations is presented in Section 3.4 (Figure 3.9).

In both scenarios, the transition is performed using an implementation of the Cooper-Frye equation [Coo74] which links the phase space distribution function $f(x,p)$ along a hypersurface σ to a momentum-space distribution $\mathsf{d}N/\mathsf{d}^3p$

$$E\frac{\mathsf{d}N}{\mathsf{d}^3p} = \int_\sigma \mathsf{d}\sigma_\mu p^\mu f(x,p) \quad . \tag{3.17}$$

In both scenarios, the normal vector on the hypersurface is assumed to be $\mathsf{d}\sigma^\mu = (\mathsf{d}^3x, \vec{0})$ and since the matter is assumed to be in perfect local equilibrium, the distribution function is taken as in Equation (3.10). Temperature T and chemical potential μ_{B} are calculated from ε and ρ_{B} via the Equation of State. Since this calculation goes from energy and baryon numbers (or their densities) via temperature and potential back to energies and baryon numbers (distributed among the particles), it is important that the Equation of State has the same degrees of freedom at the transition as does the transport calculation, so that both quantities are conserved during the procedure. The low-temperature part of each Equation of State is therefore fixed to be an ideal gas of massive hadrons.

The implementation of the transition is based on a Monte Carlo sampling of Equation (3.17) and proceeds in several steps. First, the number of particles of each species is calculated. Newly formed particles are assigned a random isospin, but in order to assure total conservation of electric charge, isospins that would increase the difference between the present charge and the aspired total charge are exponentially suppressed. Then, the four-momenta of the particles are generated using the rejection method on Equation (3.17).

The procedure is done in 5 steps. In the first step, particles are produced until the total energy matches that of the fluid, but all except strange particles are discarded. This guarantees the correct strangeness-to-energy ratio to be present in the final particle spectra. Subsequently, anti-strange particles are produced in the same way until the total strangeness is zero. Those two steps are repeated very similarly by producing first (non-strange) anti-baryons and then filling up the baryon number by producing (non-strange) baryons. After this step, the total strangeness and baryon number have been fixed. In order to

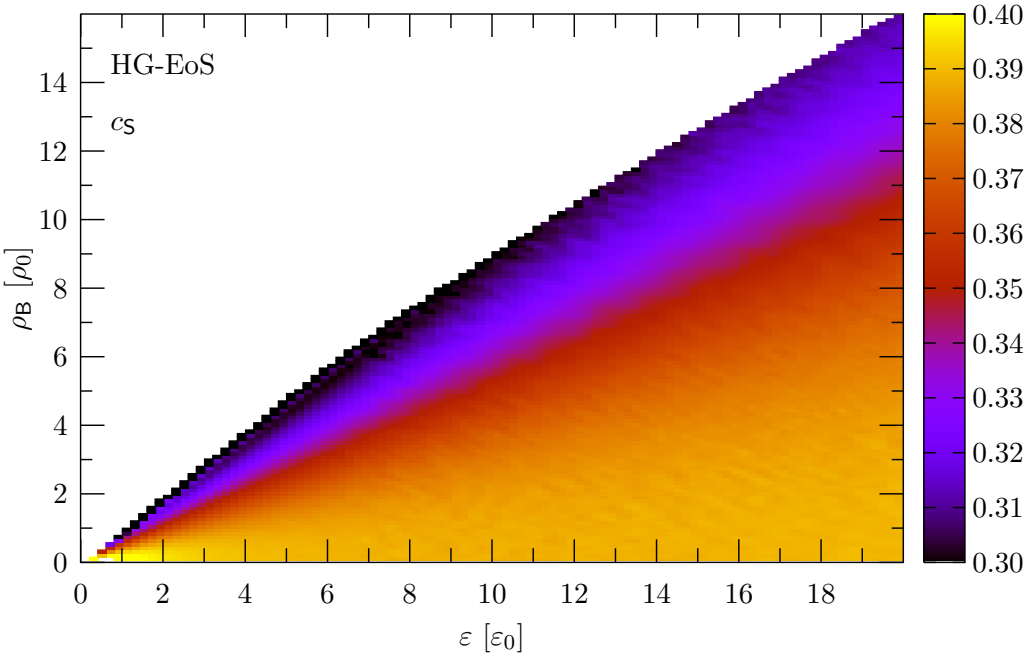

Figure 3.3: Speed of sound c_S in calculations with HG-EoS as a function of energy density ε and baryon density ρ_B, both given as multiples of their ground state values.

fix the energy, mesons are now produced until the total energy of all adopted particles matches that of the fluid [Ste10].

3.4 Equations of State

The hydrodynamic caculations presented in this work have been done with three different Equations of State.

Hadron Gas EoS For the base line calculations, the Hadron Gas Equation of State (HG-EoS) [Zsc02] has been used. In it, the same (hadronic) degrees of freedom as in the transport phase are present, i.e. all non-charmed hadronic particle species from the Particle Data Book up to $m = 2.25$ GeV. String dynamics is not included. They resemble a massive ideal gas. No phase transition is present in this scenario. Therefore, it allows to directly compare the impact of the different kinetic descriptions of the matter (the particle-based transport description vs. the density-based hydrodynamic description) on the observables. Figure 3.3 visualises the speed of sound c_S that is present in calculations with this EoS.

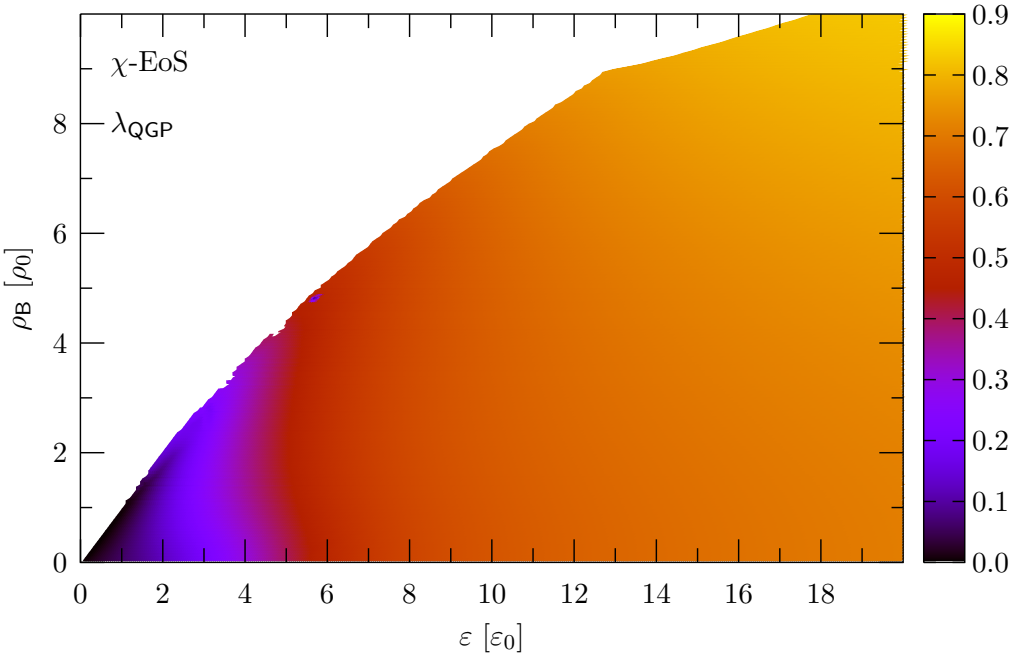

Figure 3.4: Degree of deconfinement λ_{QGP} in calculations with χ-EoS as a function of energy density ε and baryon density ρ_{B}, both given as multiples of their ground state values.

Chiral EoS In the Chiral Equation of State χ-EoS [Ste09a, Ste09b], a rapid cross-over between a hadronic gas and a chirally restored phase is implemented. The χ-EoS bases on a hadronic $SU(3)$-Lagrangian that incorporates the scalar, pseudo-scalar, vector and axial vector multiplets and the lowest baryon-octet of $SU(3)_{\mathsf{fl}}$ [Pap99]. At high temperatures, the Wilson loop is finite, so that deconfinement is present. The critical temperature for the phase transition at $\mu_{\mathsf{B}} = 0$ is at $T_{\mathsf{C}} = 180$ MeV. Figure 3.4 shows the degree of deconfinement as a function of ε and ρ_{B}, Figure 3.5 shows the speed of sound as a function of the same variables.

Bag Model EoS A massless gas of Quarks and Gluons is coupled to a non-strange ($SU(2)_{\mathsf{fl}}$) Walecka-like hadron gas in the Bag Model Equation of State (BM-EoS) [Ris95]. In this EoS, the only phase structure is a strong first order phase transition with large latent heat between the Quark-Gluon-Plasma and the hadron gas. The transition temperature at $\mu_{\mathsf{B}} = 0$ is $T_{\mathsf{C}} = 169$ MeV. Figures 3.6 and 3.7 show the fraction of QGP λ_{QGP} and the speed of sound c_{S} as function of ε and ρ_{B}.

An overview over the main characteristics of each EoS is given in Table 3.1. The initial temperature distribution at $z = 0$ in a sample central lead-lead collision is shown in Figure 3.8 for a calculation with Bag Model Equation of

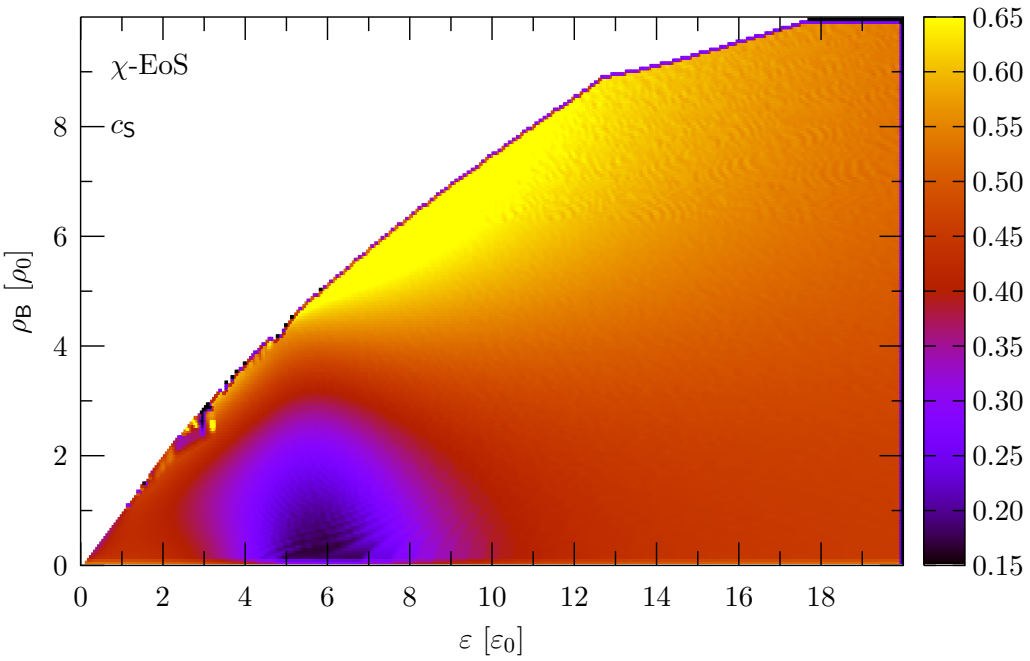

Figure 3.5: Speed of sound c_S in calculations with χ-EoS as a function of energy density ε and baryon density ρ_B, both given as multiples of their ground state values.

State (left part) and Hadron Gas Equation of State (right part). Here, the irregular shape of a single event is visible.

Let us investigate the behaviour of the various Equations of State in hybrid calculations. Figure 3.9 shows the distributions of the times at which the sytem is transferred from hydrodynamics to transport t_{trans} as a function of the position z for all three Equations of State for central ($b = 0$ fm) lead-lead collisions at $E_{lab} = 35$ AGeV, $E_{lab} = 158$ AGeV and $\sqrt{s_{NN}} = 200$ GeV for calculations with the gradual transition scenario. We can observe that the transition times at the center of the system (small $|z|$) is indeed lower than in the forward- and backward region. The difference between the transition times with HG-EoS (solid lines) and χ-EoS (dashed lines) is very small, while calculations with BM-EoS (dotted lines) remain in the intermediate stage much longer. Especially the forward and backward regions take very long to dilute enough to match the transition criterion. In calculations with an isochronous transition, in which the densest cell determines the length of the hydrodynamic calculation, a large part of the hadronic gas is calculated with hydrodynamics.

The relative amount of partonic and hadronic matter can be seen in Figure 3.10. Here, the fraction of the system, weighted by the energy density, that exists at a certain QGP-fraction λ_{QGP} is shown as function of λ_{QGP}. It confirms the picture that most of the evolution with BM-EoS is hadronic. Almost 54 %

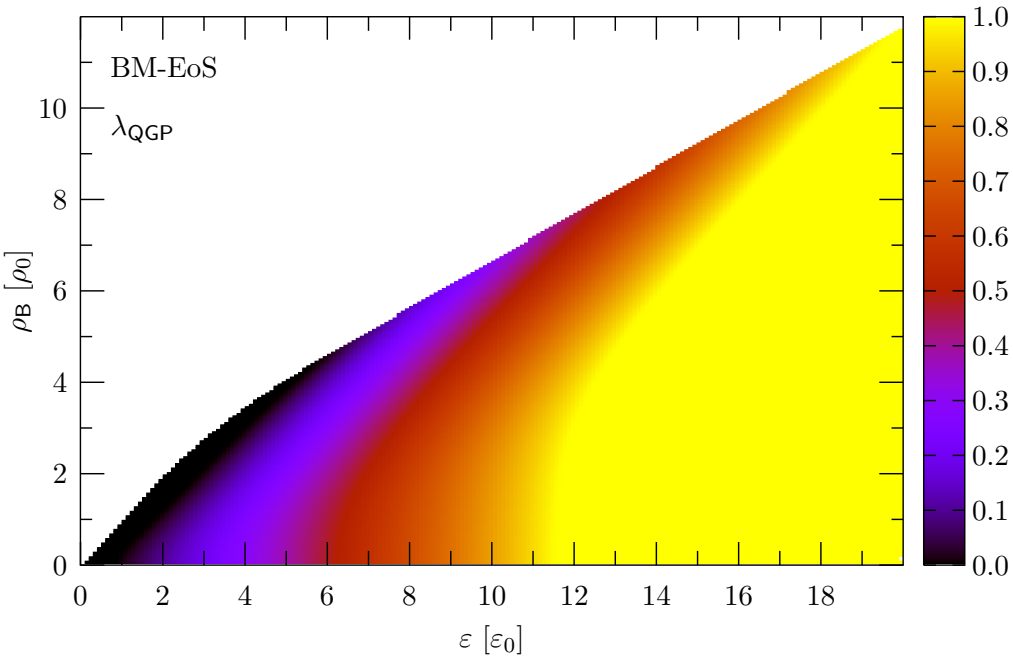

Figure 3.6: Degree of deconfinement λ_{QGP} in calculations with BM-EoS as a function of energy density ε and baryon density ρ_{B}, both given as multiples of their ground state values.

Name	Abbr.	ϵ_{crit}	Note
Hadron Gas	HG-EoS	$5\epsilon_0$	Same d.o.f. as UrQMD
Chiral	χ-EoS	$7\epsilon_0$	Cross-over to chirally restored and deconfined matter
Bag Model	BM-EoS	$5\epsilon_0$	First order Phase Transition to Quark-Gluon-Plasma

Table 3.1: Overview of the Equations of State and the critical energy densities for the mapping from hydrodynamics to transport theory. $\epsilon_0 = 146$ MeV/fm^3 is the nuclear ground state energy density.

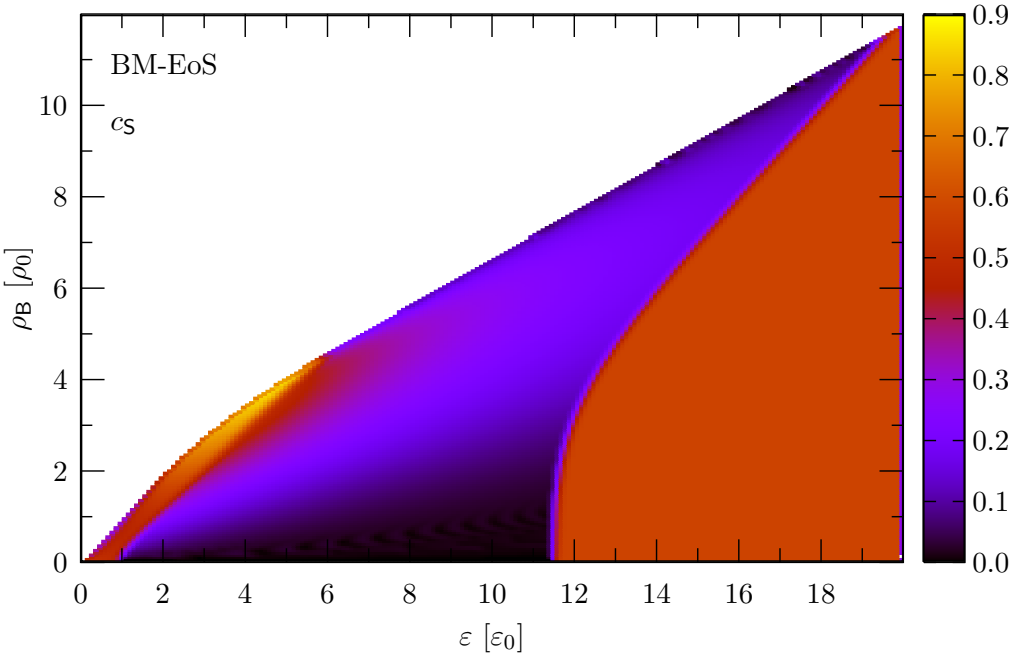

Figure 3.7: Speed of sound c_S in calculations with BM-EoS as a function of energy density ε and baryon density ρ_B, both given as multiples of their ground state values.

of the system at $E_{lab} = 35$ AGeV (uppermost panel) is in the purely hadronic phase ($\lambda_{QGP} < 2$ %). While this ratio decreases with increasing energy, still 26 % percent of the matter are in this phase at top RHIC-energy $\sqrt{s_{NN}} = 200$ GeV. In comparison, only a small part of about 2 % is in the purely partonic phase ($\lambda_{QGP} > 98$ %). The remaining part of the evolving matter is in the mixed phase. In calculations with the Chiral EoS, the matter does not reach the purely partonic state, as was expected from Figure 3.4. The biggest part of the matter is in the range $60 < \lambda_{QGP} < 80$ %. Since λ_{QGP} drops to zero only at very low temperatures, the system never leaves the mixed phase.

To estimate the temperature profile of the matter, we can also look at the distribution of temperatures in the fireball. In Figure 3.11, the space-time volume of the collisions, multiplied with the integrated photon emission rates (see Figure 3.16) is shown. Please note that this Figure does not take into account the different values λ_{QGP}, nor the energy distribution of the emitted photons. The sharp peak visible in calculations with BM-EoS (dotted lines) at all energies shows the actual temperature at which the phase transition happens, and from the shift of this peak with the energy one can see that the phase transition happens at higher baryochemical potential, as is expected. The Figure shows that both in calculations with BM-EoS and χ-EoS, most photons come from the phase transition region, which is much broader in the case of χ-EoS.

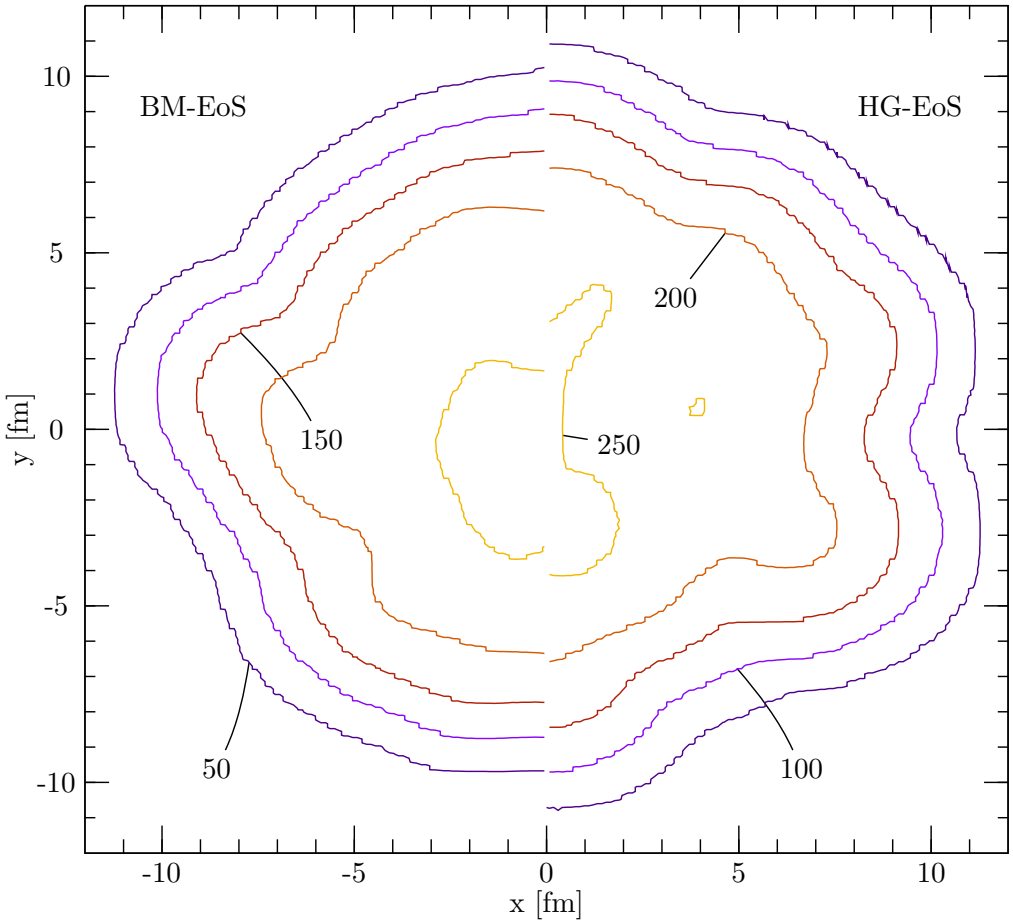

Figure 3.8: Temperature profiles in central Pb+Pb-collisions at $E_{\mathsf{lab}} = 158$ AGeV directly after the first transition, calculated with the BM-EoS (left half) and HG-EoS (right half). The lines are isotherms, going from $T = 50$ MeV at the outermost line to $T = 250$ MeV at the innermost.

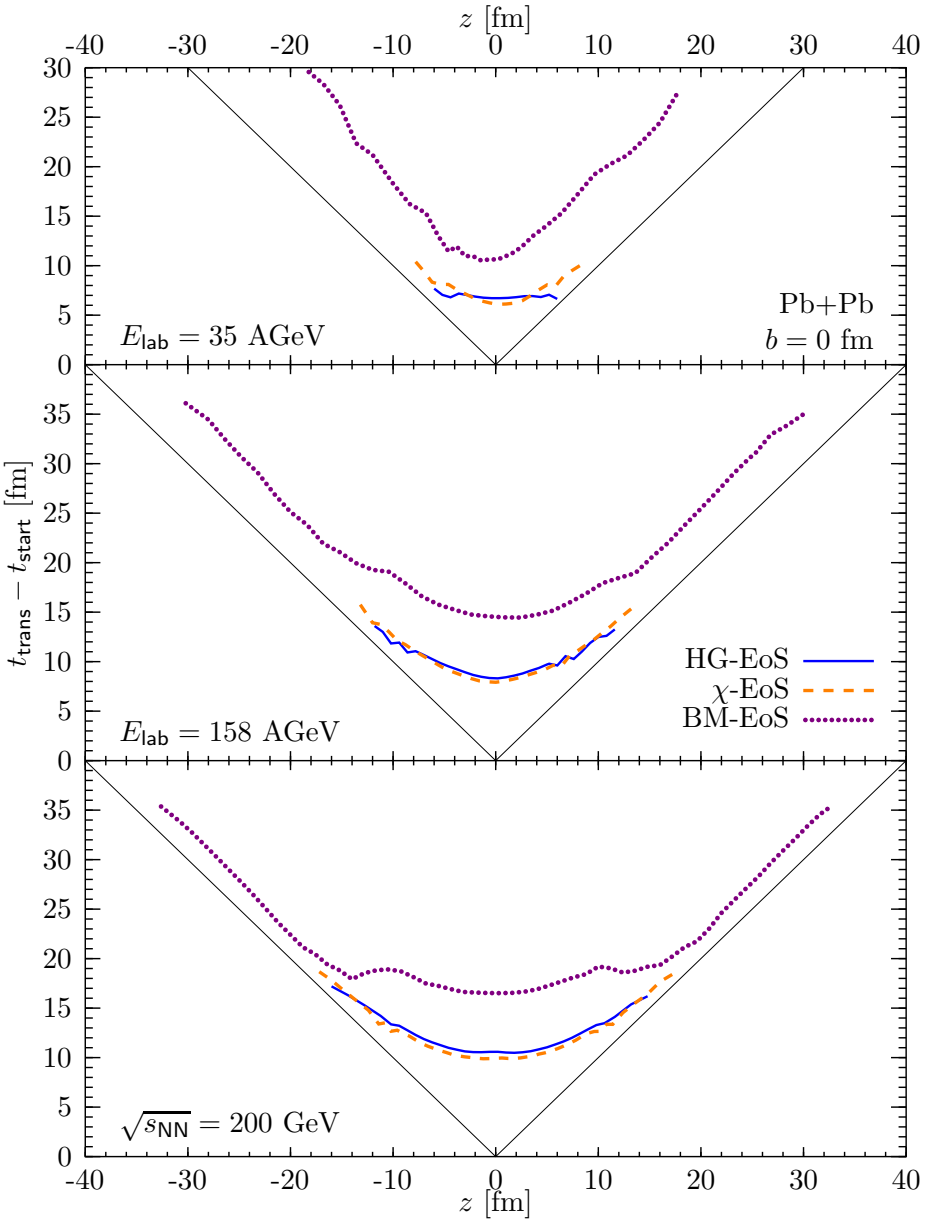

Figure 3.9: Distribution of transition times in gradual transition hybrid calculations at $E_{\mathsf{lab}} = 35$ AGeV (top), $E_{\mathsf{lab}} = 158$ AGeV (middle) and $\sqrt{s_{\mathsf{NN}}} = 200$ GeV (bottom) for HG-EoS (solid lines), χ-EoS (dashed lines) and BM-EoS (dotted lines) calculations. The solid lines represent the light cone $t = |z|$.

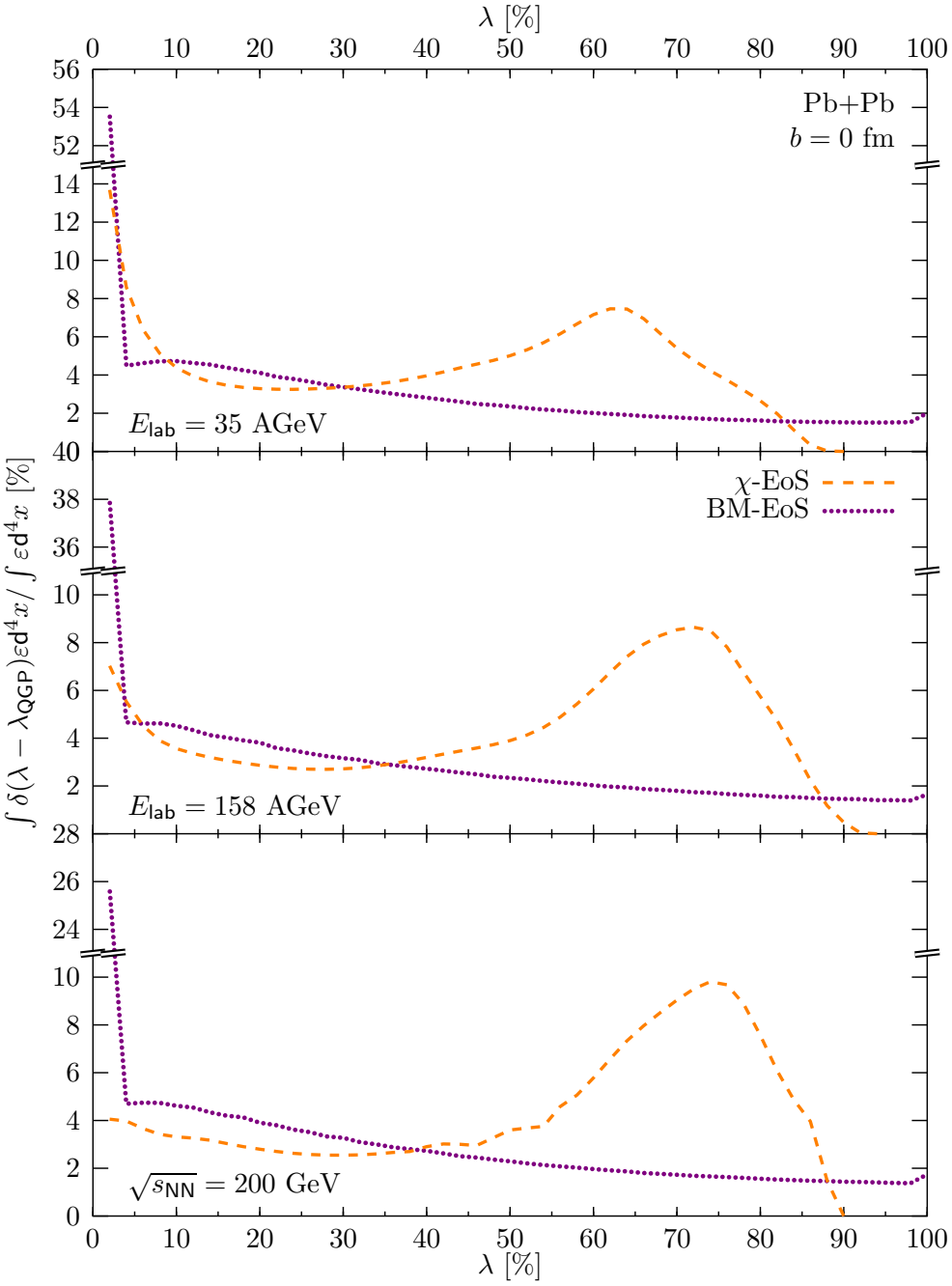

Figure 3.10: Distribution of matter with given QGP-fraction in the intermediate stage of hybrid model calculations with χ-EoS (dashed lines) and BM-EoS (dotted lines) in Pb+Pb-calculations at $E_{\mathsf{lab}} = 35$ AGeV (top), $E_{\mathsf{lab}} = 158$ AGeV (middle) and $\sqrt{s_{\mathsf{NN}}} = 200$ GeV (bottom).

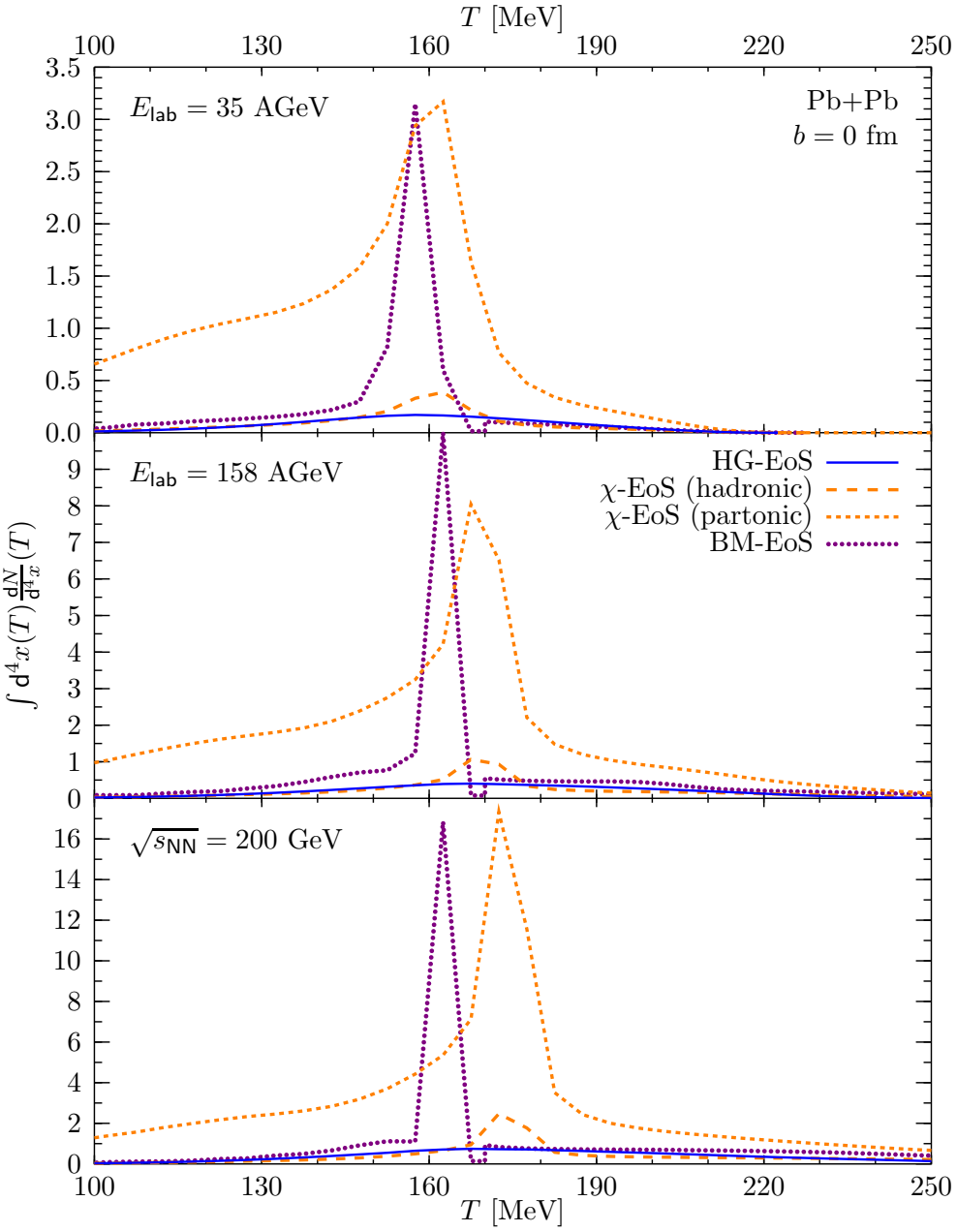

Figure 3.11: Space-time volume occupied by given temperatures in intermediate stage of hybrid model calculations with HG-EoS (solid lines) χ-EoS (dashed lines) and BM-EoS (dotted lines) in Pb+Pb-calculations at $E_{\mathsf{lab}} = 35$ AGeV (top), $E_{\mathsf{lab}} = 158$ AGeV (middle) and $\sqrt{s_{\mathsf{NN}}} = 200$ GeV (bottom). The results are weighted with the photon emission rates (HG-EoS: hadronic, χ-EoS: separately hadronic (long dashes) and partonic (short dashes), BM-EoS: hadronic for $T < 170$ MeV, partonic above).

3.5 Photon emission sources

Photon emission is calculated perturbatively in both parts of the model, hydrodynamics and transport, because the evolution of the underlying event is not altered by the emission of photons due to their very small emission probability. The channels considered for photon emission may differ between the hybrid approach and the binary scattering model. Emission from a Quark-Gluon-Plasma can only happen in the hydrodynamic phase, and only if the Equation of State used has partonic degrees of freedom. Photons from baryonic interactions are neglected. Emission of hard photons from early pQCD-scatterings of nucleons is calculated separately and incoherently added to the simulated spectra.

3.5.1 Photon emission from the Transport Phase

In the transport part of the (hybrid) model, each scattering is examined and the cross-section for photon emission is calculated. Here, we employ the well-established cross-sections from Kapusta *et al.* [Kap91] and Xiong *et al.* [Xio92]. Kapusta and collaborators based their calculations on the photon self-energy derived from a Lagrange density involving the pion, ρ and photon-fields

$$\mathcal{L} = |D_\mu \Phi|^2 - m_\pi^2 |\Phi|^2 - \frac{1}{4}\rho_{\mu\nu}\rho^{\mu\nu} + \frac{1}{2}m_\rho^2 \rho_\mu \rho^\mu - \frac{1}{4}F_{\mu\nu}F^{\mu\nu} \quad . \tag{3.18}$$

Here, Φ is the pion field, $\rho_{\mu\nu} = \partial_\mu \rho_\nu - \partial_\nu \rho_\mu$ and $F_{\mu\nu} = \partial_\mu A_\nu - \partial_\nu A_\mu$ are the ρ and photon field-strength tensors and $D_\mu = \partial_\mu - \imath e A_\mu - \imath g_\rho \rho_\mu$ is the covariant derivative. The ρ decay constant g_ρ is calculated from the total width $\Gamma^\rho_{\mathsf{tot}}$ of the ρ meson:

$$g_\rho^2 = 48\pi \frac{\Gamma^\rho_{\mathsf{tot}} m_\rho^2}{\left(\sqrt{m_\rho^2 - 4m_\pi^2}\right)^3} \quad . \tag{3.19}$$

All scatterings during the transport phase are examined in order to obtain direct photon spectra. For every scattering that may produce photons, the corresponding fraction of a photon,

$$N_\gamma = \frac{\sigma_{\mathsf{em}}}{\sigma_{\mathsf{tot}}} \quad , \tag{3.20}$$

is produced. Here, σ_{tot} is the sum of the total hadronic cross-section for a collision with these ingoing particles (as provided by UrQMD) and the electromagnetic cross-section σ_{em} as calculated by the aforementioned formulæ. In order to obtain the correct angular distribution of the produced photons and to enhance statistics, for each scattering many fractional photons are created that populate all kinematically allowed momentum transfers t. In this procedure, each photon is given a weight $\Delta N_\gamma^{\mathsf{t}}$ according to

$$\Delta N_\gamma^{\mathsf{t}} = \frac{\frac{\mathsf{d}\sigma_{\mathsf{em}}}{\mathsf{d}t}(s,t)\Delta t}{\sigma_{\mathsf{tot}}(s)} \quad , \tag{3.21}$$

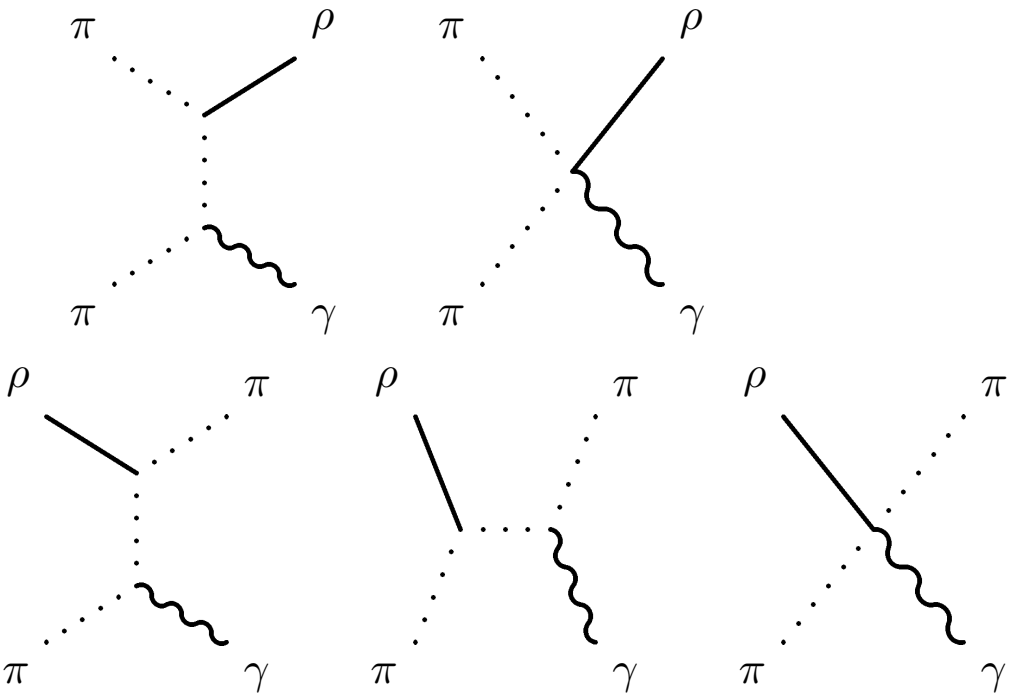

Figure 3.12: Some of the Feynman diagrams taken into account for the calculation of cross-sections (taken from [Kap91]).

and the photons are distributed evenly in the azimuthal angle φ. The integral $\sigma_{\mathsf{em}}(s) = \int \mathsf{d}\sigma_{\mathsf{em}}/\mathsf{d}t\mathsf{d}t$ is performed analytically for each channel.

Photon emission is considered from the following channels:

$$\pi^{\pm} + \pi^{\mp} \rightarrow \gamma + \rho^0 \quad , \tag{3.22a}$$
$$\pi^{\pm} + \pi^0 \rightarrow \gamma + \rho^{\pm} \quad , \tag{3.22b}$$
$$\pi^{\pm} + \rho^0 \rightarrow \gamma + \pi^{\pm} \quad , \tag{3.22c}$$
$$\pi^{\pm} + \rho^{\mp} \rightarrow \gamma + \pi^0 \quad , \tag{3.22d}$$
$$\pi^0 + \rho^{\pm} \rightarrow \gamma + \pi^{\pm} \quad , \tag{3.22e}$$
$$\pi^{\pm} + \pi^{\mp} \rightarrow \gamma + \eta \quad , \tag{3.22f}$$
$$\pi^{\pm} + \eta \rightarrow \gamma + \pi^{\pm} \quad , \tag{3.22g}$$
$$\pi^{\pm} + \pi^{\mp} \rightarrow \gamma + \gamma \quad . \tag{3.22h}$$

The cross-sections calculated correspond to the Feynman diagrams shown in Figure 3.12.

The differential cross-sections of these processes are

$$\frac{\mathsf{d}\sigma}{\mathsf{d}t}\left(\pi^{\pm}\pi^{\mp}\to\gamma\rho^{0}\right)=\frac{\alpha g_{\rho}^{2}}{4sp_{\mathsf{c.m.}}^{2}}\left\{2-(m_{\rho}^{2}-4m_{\pi}^{2})\left[\frac{s-2m_{\pi}^{2}}{s-m_{\rho}^{2}}\frac{1}{t-m_{\pi}^{2}}+\frac{m_{\pi}^{2}}{(t-m_{\pi}^{2})^{2}}+(t\leftrightarrow u)\right]\right\} \tag{3.23a}$$

$$\frac{\mathsf{d}\sigma}{\mathsf{d}t}\left(\pi^{\pm}\pi^{0}\to\gamma\rho^{\pm}\right)=-\frac{\alpha g_{\rho}^{2}}{16sp_{\mathsf{c.m.}}^{2}}\left[\frac{(s-2m_{\rho}^{2})(t-m_{\pi}^{2})^{2}}{m_{\rho}^{2}(s-m_{\rho}^{2})^{2}}+\frac{(s-6m_{\rho}^{2})(t-m_{\pi}^{2})}{m_{\rho}^{2}(s-m_{\rho}^{2})}+\frac{4s(m_{\rho}^{2}-4m_{\pi}^{2})}{(s-m_{\rho}^{2})^{2}}+\frac{4(m_{\rho}^{2}-4m_{\pi}^{2})}{t-m_{\pi}^{2}}\left(\frac{s}{s-m_{\rho}^{2}}+\frac{m_{\pi}^{2}}{t-m_{\pi}^{2}}\right)+\frac{m_{\pi}^{2}}{m_{\rho}^{2}}-\frac{9}{2}+(t\leftrightarrow u)\right] \tag{3.23b}$$

$$\frac{\mathsf{d}\sigma}{\mathsf{d}t}\left(\pi^{\pm}\rho^{0}\to\gamma\pi^{\pm}\right)=\frac{\alpha g_{\rho}^{2}}{12sp_{\mathsf{c.m.}}^{2}}\left[2-\frac{s(m_{\rho}^{2}-4m_{\pi}^{2})}{(s-m_{\pi}^{2})^{2}}-\frac{(m_{\rho}^{2}-4m_{\pi}^{2})}{t-m_{\pi}^{2}}\cdot\left(\frac{s-m_{\rho}^{2}+m_{\pi}^{2}}{(s-m_{\pi}^{2})(t-m_{\pi}^{2})}+\frac{m_{\pi}^{2}}{(t-m_{\pi}^{2})}\right)\right] \tag{3.23c}$$

$$\frac{\mathsf{d}\sigma}{\mathsf{d}t}(\pi^{\pm}\rho^{\mp}\to\gamma\pi^{0})=-\frac{\alpha g_{\rho}^{2}}{48sp_{\mathsf{c.m.}}^{2}}\left\{4(m_{\rho}^{2}-4m_{\pi}^{2})\left[\frac{t}{(t-m_{\pi}^{2})^{2}}+\frac{u}{(u-m_{\rho}^{2})^{2}}-\frac{m_{\rho}^{2}}{s-m_{\pi}^{2}}\left(\frac{1}{t-m_{\pi}^{2}}+\frac{1}{u-m_{\rho}^{2}}\right)\right]+\left(3+\frac{s-m_{\pi}^{2}}{m_{\rho}^{2}}\right)\frac{s-m_{\pi}^{2}}{u-m_{\rho}^{2}}-\frac{1}{2}+\frac{s}{m_{\rho}^{2}}-\left(\frac{s-m_{\pi}^{2}}{u-m_{\rho}^{2}}\right)^{2}\right\} \tag{3.23d}$$

$$\frac{\mathsf{d}\sigma}{\mathsf{d}t}\left(\pi^{0}\rho^{\pm}\to\gamma\pi^{\pm}\right)=\frac{\alpha g_{\rho}^{2}}{48sp_{\mathsf{c.m.}}^{2}}\left[\frac{9}{2}-\frac{s}{m_{\rho}^{2}}-\frac{4s(m_{\rho}^{2}-4m_{\pi}^{2})}{(s-m_{\pi}^{2})^{2}}+\frac{(s-m_{\pi}^{2})^{2}-4m_{\rho}^{2}(m_{\rho}^{2}-4m_{\pi}^{2})}{(u-m_{\rho}^{2})^{2}}+\frac{1}{u-m_{\rho}^{2}}\left(5(s-m_{\pi}^{2})-\frac{(s-m_{\pi}^{2})^{2}}{m_{\rho}^{2}}-\frac{4(m_{\rho}^{2}-4m_{\pi}^{2})(s-m_{\pi}^{2}+m_{\rho}^{2})}{s-m_{\pi}^{2}}\right)\right] \tag{3.23e}$$

$$\frac{\mathsf{d}\sigma}{\mathsf{d}t}\left(\pi^{\pm}\pi^{\mp}\to\gamma\eta\right)\quad=\quad\frac{\pi\alpha A\left|f_{\pi}(s)\right|^{2}}{16m_{\eta}^{2}m_{\rho}^{4}sp_{\mathsf{c.m.}}^{2}}\left[s(u-m_{\pi}^{2})(t-m_{\pi}^{2})-m_{\pi}^{2}(s-m_{\eta}^{2})^{2}\right] \tag{3.23f}$$

$$\frac{\mathsf{d}\sigma}{\mathsf{d}t}\left(\pi^{\pm}\eta\to\gamma\pi^{\pm}\right) = \frac{\pi\alpha A\left|f_{\pi}(u)\right|^{2}}{16m_{\eta}^{2}m_{\rho}^{4}sp_{\mathsf{c.m.}}^{2}}\left[u(s-m_{\pi}^{2})(t-m_{\pi}^{2})-m_{\pi}^{2}(u-m_{\eta}^{2})^{2}\right] \tag{3.23g}$$

$$\frac{\mathsf{d}\sigma}{\mathsf{d}t}\left(\pi^{\pm}\pi^{\mp}\to\gamma\gamma\right)=\frac{2\pi\alpha^{2}}{sp_{\mathsf{c.m.}}^{2}}\left[1+2m_{\pi}^{2}\left(\frac{1}{t-m_{\pi}^{2}}+\frac{1}{u-m_{\pi}^{2}}\right)+2m_{\pi}^{4}\left(\frac{1}{t-m_{\pi}^{2}}+\frac{1}{u-m_{\pi}^{2}}\right)^{2}\right] \tag{3.23h}$$

In these equations, $t=(p_{\pi}-p_{\gamma})^{2}$ is always the momentum transfer from the pion to the photon and $p_{\mathsf{c.m.}}$ is the three-momentum of the incoming particles in the center-of-mass frame (see Appendix A.1 for a detailed explanation of all the kinematic variables and their connections). The value of A is, consistent with [Kap91], $A=g_{\eta\rho\rho}^{2}g_{\rho}^{2}/4\pi\gamma_{\rho}^{2}=4.7$, and the pion electromagnetic form factor is

$$F_{\pi}(s)=\frac{m_{\rho}^{4}}{(s-m_{\rho}^{2})+\Gamma_{\rho}^{2}m_{\rho}^{2}} \quad .$$

In their 1992 paper, Xiong *et al.* [Xio92] calculate the cross-section for the formation of an intermediate a_1-meson during $\pi\rho$-scattering, averaged over all possible charge combinations:

$$\frac{\mathsf{d}\sigma}{\mathsf{d}t}\left(\pi\rho\to a_{1}\to\gamma\pi\right) = \frac{\pi^{2}\sqrt{s}}{2p_{\mathsf{c.m.}}^{3}(s-m_{\pi})^{2}}\frac{\Gamma_{a_{1}\to\pi\rho}\Gamma_{a_{1}\to\gamma\pi}}{(\sqrt{s}-m_{a_{1}})^{2}+(\Gamma_{a_{1}\to\pi\rho}+\Gamma_{a_{1}\to\gamma\pi})^{2}/4} \quad . \tag{3.23i}$$

This channel is not included in Kapusta *et al.* Xiong *et al.* obtain this from a Lagrange-density involving only the pion-, photon-, ρ- and a_1-fields

$$\mathcal{L}=G_{\rho}a_{1}^{\mu}(g_{\mu\nu}(p_{\pi}\cdot p_{\rho})-p_{\pi\mu}p_{\rho_{\nu}})\rho^{\nu}\Phi+G_{\rho}\frac{e}{g_{\rho}}a_{1}^{\mu}(g_{\mu\nu}(p_{\pi}\cdot p_{\gamma})-p_{\pi\mu}p_{\gamma_{\nu}})A^{\nu}\Phi \quad , \tag{3.24}$$

where $G_{\rho}=14.8\ \mathrm{GeV}^{-1}$. The partial widths of the a_1, $\Gamma_{a_1\to\pi\rho}$ and $\Gamma_{a_1\to\gamma\pi}$, are estimated to be

$$\Gamma_{a_{1}\to\pi\rho} = \frac{G_{\rho}^{2}p_{\mathsf{c.m.}}}{24\pi m_{a_{1}}^{2}}\left\{\frac{m_{\rho}^{2}}{4s}\left[s-(m_{\rho}^{2}-m_{\pi}^{2})\right]+\frac{1}{2}(s-m_{\rho}^{2}-m_{\pi}^{2})\right\} \tag{3.25a}$$

and

$$\Gamma_{a_{1}\to\gamma\pi} = \frac{G_{\rho}^{2}\alpha p_{\mathsf{c.m.}}}{12g_{\rho}^{2}m_{a_{1}}^{2}}(s-m_{\pi}^{2}) \quad . \tag{3.25b}$$

The integration over the cross-sections listed above yield the following results:

$$\sigma\left(\pi^{\pm}\pi^{\mp}\to\gamma\rho^{0}\right)=\frac{\alpha g_{\rho}^{2}}{4sp_{\mathsf{c.m.}}^{2}}\left\{2\Delta t-(m_{\rho}^{2}-4m_{\pi}^{2})\left[\frac{s-2m_{\pi}^{2}}{s-m_{\rho}^{2}}\ln\frac{(t_{-}-m_{\pi}^{2})}{(t_{+}-m_{\pi}^{2})}\right.\right.$$
$$\left.\left.+\frac{m_{\pi}^{2}\Delta t}{(m_{\pi}^{2}-t_{+})(m_{\pi}^{2}-t_{-})}+(t_{\pm}\leftrightarrow u_{\mp})\right]\right\} \quad (3.26a)$$

$$\sigma\left(\pi^{\pm}\pi^{0}\to\gamma\rho^{\pm}\right)=-\frac{\alpha g_{\rho}^{2}}{16sp_{\mathsf{c.m.}}^{2}}\left[\frac{s-2m_{\rho}^{2}}{m_{\rho}^{2}(s-m_{\rho}^{2})^{2}}\frac{1}{3}(t_{-}^{3}-t_{+}^{3})\right.$$
$$+\frac{s-6m_{\rho}^{2}}{m_{\rho}^{2}(s-m_{\rho}^{2})}\frac{1}{2}(t_{-}^{2}-t_{+}^{2})+\left(\frac{4s(m_{\rho}^{2}-4m_{\pi}^{2})}{(s-m_{\rho}^{2})^{2}}+\frac{m_{\pi}^{2}}{m_{\rho}^{2}}-\frac{9}{2}\right)\Delta t$$
$$\left.+\frac{4s(m_{\rho}^{2}-4m_{\pi}^{2})}{(s-m_{\rho}^{2})}\ln\frac{t_{-}-m_{\pi}^{2}}{t_{+}-m_{\pi}^{2}}+\frac{4m_{\pi}^{2}(m_{\rho}^{2}-4m_{\pi}^{2})\Delta t}{(m_{\pi}^{2}-t_{+})(m_{\pi}^{2}-t_{-})}+(t_{\pm}\leftrightarrow u_{\mp})\right] \quad (3.26b)$$

$$\sigma\left(\pi^{\pm}\rho^{0}\to\gamma\pi^{\pm}\right)=\frac{\alpha g_{\rho}^{2}}{12sp_{\mathsf{c.m.}}^{2}}\left[2\Delta t-\frac{s(m_{\rho}^{2}-4m_{\pi}^{2})}{(s-m_{\pi}^{2})^{2}}\Delta t-(m_{\rho}^{2}-4m_{\pi}^{2})\right.$$
$$\left.\cdot\left(\frac{s-m_{\rho}^{2}+m_{\pi}^{2}}{s-m_{\pi}^{2}}\ln\frac{t_{-}-m_{\pi}^{2}}{t_{+}-m_{\pi}^{2}}+\frac{m_{\pi}^{2}\Delta t}{(m_{\pi}^{2}-t_{+})(m_{\pi}^{2}-t_{-})}\right)\right] \quad (3.26c)$$

$$\sigma(\pi^{\pm}\rho^{\mp}\to\gamma\pi^{0})=-\frac{\alpha g_{\rho}^{2}}{48sp_{\mathsf{c.m.}}^{2}}\left\{4(m_{\rho}^{2}-4m_{\pi}^{2})\left[\frac{m_{\pi}^{2}\Delta t}{(u_{+}-m_{\rho}^{2})(u_{-}-m_{\rho}^{2})}\right.\right.$$
$$+\frac{m_{\pi}^{2}\Delta t}{(t_{+}-m_{\pi}^{2})(t_{-}-m_{\pi}^{2})}+\ln\frac{u_{+}-m_{\rho}^{2}}{u_{-}-m_{\rho}^{2}}+\ln\frac{t_{-}-m_{\pi}^{2}}{t_{+}-m_{\pi}^{2}}$$
$$\left.-\frac{m_{\rho}^{2}}{s-m_{\pi}^{2}}\left(\ln\frac{t_{-}-m_{\pi}^{2}}{t_{+}-m_{\pi}^{2}}+\ln\frac{u_{+}-m_{\rho}^{2}}{u_{-}-m_{\rho}^{2}}\right)\right]+(s-m_{\pi}^{2})\left(3+\frac{s-m_{\pi}^{2}}{m_{\rho}^{2}}\right)$$
$$\left.\cdot\ln\frac{u_{+}-m_{\rho}^{2}}{u_{-}-m_{\rho}^{2}}+\Delta t\left(\frac{s}{m_{\rho}^{2}}-\frac{1}{2}-\frac{(s-m_{\pi}^{2})^{2}}{(u_{+}-m_{\rho}^{2})(u_{-}-m_{\rho}^{2})}\right)\right\} \quad (3.26d)$$

$$\sigma\left(\pi^{0}\rho^{\pm}\to\gamma\pi^{\pm}\right)=\frac{\alpha g_{\rho}^{2}}{48sp_{\mathsf{c.m.}}^{2}}\left[\Delta t\left(\frac{9}{2}-\frac{s}{m_{\rho}^{2}}-\frac{4s(m_{\rho}^{2}-4m_{\pi}^{2})}{(s-m_{\pi}^{2})^{2}}\right.\right.$$
$$\left.+\frac{(s-m_{\pi}^{2})^{2}-4m_{\rho}^{2}(m_{\rho}^{2}-4m_{\pi}^{2})}{(u_{+}-m_{\rho}^{2})(u_{-}-m_{\rho}^{2})}\right)+\left(5(s-m_{\pi}^{2})-\frac{(s-m_{\pi}^{2})^{2}}{m_{\rho}^{2}}\right.$$
$$\left.\left.-\frac{4(m_{\rho}^{2}-4m_{\pi}^{2})(s-m_{\pi}^{2}+m_{\rho}^{2})}{s-m_{\pi}^{2}}\right)\ln\frac{u_{+}-m_{\rho}^{2}}{u_{-}-m_{\rho}^{2}}\right] \quad (3.26e)$$

$$\sigma\left(\pi^{\pm}\pi^{\mp}\to\gamma\eta\right)=\frac{\pi\alpha A\left|F_{\pi}(s)\right|^{2}}{16m_{\eta}^{2}m_{\rho}^{4}sp_{\mathsf{c.m.}}^{2}}\Big[(2m_{\pi}^{2}+m_{\eta}^{2}-s)\frac{s}{2}(t_{+}^{2}-t_{-}^{2}) -\frac{s}{3}(t_{+}^{3}-t_{-}^{3})-m_{\pi}^{2}\left(m_{\eta}^{4}+s(m_{\pi}^{2}-m_{\eta}^{2})\right)\Big] \quad (3.26f)$$

$$\begin{aligned}\sigma\left(\pi^{\pm}\eta\to\gamma\pi^{\pm}\right)=\frac{\pi\alpha A}{16m_{\eta}^{2}sp_{\mathsf{c.m.}}^{2}}\Big\{&-m_{\pi}^{2}\left[(t_{-}+u_{-})(s-m_{\pi}^{2})+(2m_{\pi}^{2}-s)^{2}\right]I_{0}\\&+\left[(s-m_{\pi}^{2})(m_{\pi}^{2}+t_{-}+u_{-})-2m_{\pi}^{2}(s-2m_{\pi}^{2})\right]\left[(t_{-}+u_{-}-m_{\rho}^{2})I_{0}+\frac{1}{2}I_{1}\right]\\&-s\left[\Delta t+(t_{-}+u_{-}-m_{\rho}^{2})I_{1}+(t_{-}+u_{-}-m_{\rho}^{2})^{2}I_{0}-m_{\rho}^{2}\Gamma_{\rho}^{2}I_{0}\right]\Big\}\end{aligned} \quad (3.26g)$$

$$\sigma\left(\pi^{\pm}\pi^{\mp}\to\gamma\gamma\right)=\frac{2\pi\alpha^{2}}{sp_{\mathsf{c.m.}}^{2}}\Big\{\Delta t+2m_{\pi}^{2}\Big[\left(1-\frac{2m_{\pi}^{2}}{s}\right)\ln\frac{t_{-}-m_{\pi}^{2}}{t_{+}-m_{\pi}^{2}} +\frac{m_{\pi}^{2}\Delta t}{(t_{-}-m_{\pi}^{2})(t_{+}-m_{\pi}^{2})}+(t_{\pm}\leftrightarrow u_{\mp})\Big]\Big\} \quad (3.26h)$$

$$\sigma\left(\pi\rho\to a_{1}\to\gamma\pi\right) \qquad = \qquad 4p_{1}\omega\frac{\mathsf{d}\sigma}{\mathsf{d}t}\left(\pi\rho\to a_{1}\to\gamma\pi\right) \quad (3.26i)$$

In those equations, $t_{\pm}$ are the minimal and maximal allowed momentum transfers, and $u_{\pm}$ is defined correspondingly. Δt is a shorthand for $t_{-}-t_{+}$. See also Appendix A.1. In the cross-section $\pi^{\pm}\eta\to\gamma\pi^{\pm}$ (Equation (3.26g)), the following notations have been used for simplicity:

$$I_{0} = \frac{1}{m_{\rho}\Gamma_{\rho}}\left[\operatorname{atan}\left(\frac{u_{+}-m_{\rho}^{2}}{m_{\rho}\Gamma_{\rho}}\right)-\operatorname{atan}\left(\frac{u_{-}-m_{\rho}^{2}}{m_{\rho}\Gamma_{\rho}}\right)\right] \quad \text{and} \quad (3.27a)$$

$$I_{1} = \ln\left(\frac{(u_{-}-m_{\rho}^{2})^{2}+m_{\rho}^{2}\Gamma_{\rho}^{2}}{(u_{+}-m_{\rho}^{2})^{2}+m_{\rho}^{2}\Gamma_{\rho}^{2}}\right) \quad . \quad (3.27b)$$

Since the width of the ρ-meson is not negligible, its mass distribution has to be taken into account. For the processes with a ρ-meson in the initial state, the actual mass $m_{\rho}=\sqrt{p_{\mu}p^{\mu}}$ of the incoming meson is used for the calculation of the cross-section. If there is a ρ-meson in the final state, then first the mass of the ρ is chosen randomly according to a Breit-Wigner distribution $A(M)$ with

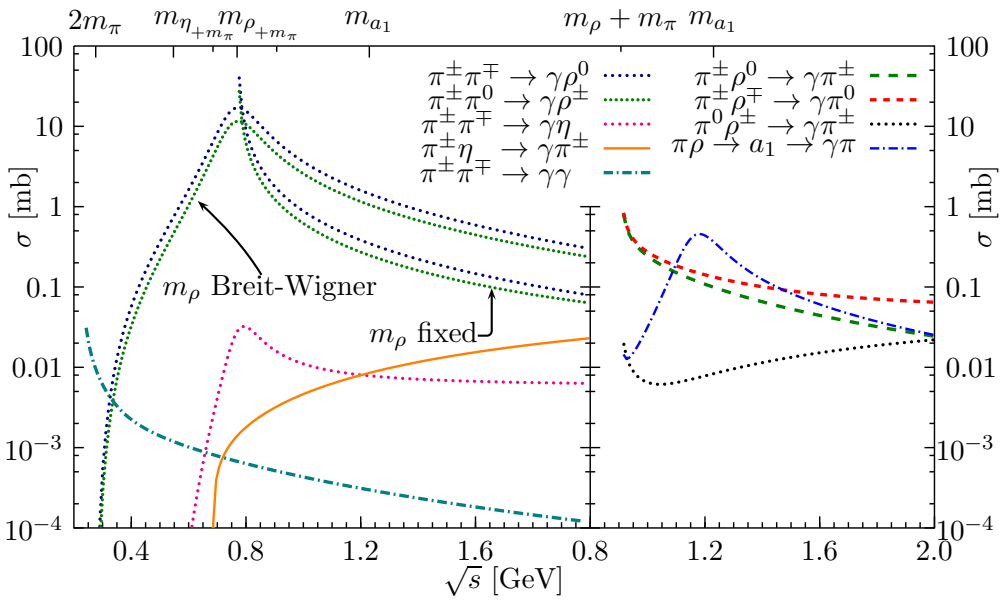

Figure 3.13: Cross-sections for all included channels as a function of $\sqrt{s}$. For visibility, the cross-sections for all processes $\pi\rho \to \gamma\pi$ are shown separately. They have been calculated with a ρ mass $m_\rho = 0.769$ GeV. The left plot shows the cross-sections for $\pi\pi \to \gamma\rho$ both for fixed ρ mass ($m_\rho = 0.769$ GeV, labelled "m_ρ fixed") and for variable ρ mass (labelled "m_ρ Breit-Wigner").

mass-dependent width (see [Bas98])

$$A(M) = \frac{\Gamma(M)M^2}{\left(M^2 - m_\rho^2\right)^2 + M^2\Gamma(M)^2} \quad , \tag{3.28}$$

$$\Gamma(M) = \Gamma(m_\rho)\left(\frac{m_\rho}{M}\right)^2 \sqrt{\left(\frac{M^2 - 4m_\pi^2}{m_\rho^2 - 4m_\pi^2}\right)^3} F(M) \quad , \tag{3.29}$$

$$F(M) = 1.2\left(1 + 0.2\frac{M^2 - 4m_\pi^2}{m_\rho^2 - 4m_\pi^2}\right)^{-1} \quad . \tag{3.30}$$

This mass is then used for all further calculations of this process. The total electromagnetic cross-section is calculated as the average over the mass

$$\sigma_{\mathsf{el}}(s) = \left(\int_{2m_\pi}^{\infty} A(M)dM\right)^{-1} \int_{2m_\pi}^{\sqrt{s}} dM\sigma(s,M)A(M) \tag{3.31}$$

Figure 3.13 shows the cross-sections of the channels listed above as a function of $\sqrt{s}$.

3.5.2 Photon emission from the Hydrodynamic Phase

In the hydrodynamic phase photons are produced fractionally from every cell on the hydrodynamic grid whose temperature is above a threshold $T_{\mathsf{thr}} = 30$ MeV using the parametrisations by Turbide, Rapp and Gale [Tur04]. They use an effective non-linear σ-model Lagrange density in which the vector and axial vector fields are implemented as massive gauge fields of the chiral $U(3)_{\mathsf{L}} \times U(3)_{\mathsf{R}}$ symmetry to obtain the rates:

$$\begin{aligned}\mathcal{L} = \frac{1}{8}F_\pi^2 \mathsf{Tr} D_\mu U D^\mu U^\dagger + \frac{1}{8}F_\pi^2 \mathsf{Tr} M(U + U^\dagger - 2) - \frac{1}{2}\mathsf{Tr}\left(F^{\mathsf{L}}_{\mu\nu}F^{\mathsf{L}\mu\nu} + F^{\mathsf{R}}_{\mu\nu}F^{\mathsf{R}\mu\nu}\right) \\ + m_0^2 \mathsf{Tr}\left(A^{\mathsf{L}}_\mu A^{\mathsf{L}\mu} + A^{\mathsf{R}}_\mu A^{\mathsf{R}\mu}\right) + \gamma \mathsf{Tr} F^{\mathsf{L}}_{\mu\nu} U F^{\mathsf{R}\mu\nu} U^\dagger \\ - \imath\xi \mathsf{Tr}\left(D_\mu U D_\nu U^\dagger F^{\mathsf{L}\mu\nu} + D_\mu U^\dagger D_\nu U F^{\mathsf{R}\mu\nu}\right) \quad (3.32)\end{aligned}$$

In Equation (3.32), the following relations have been used:

$$U = \exp\left(\frac{2\imath}{F_\pi}\sum_i \frac{\phi_i \lambda_i}{\sqrt{2}}\right) \quad , \quad (3.33a)$$

$$A^{\mathsf{L/R}}_\mu = \frac{1}{2}(V_\mu \pm A_\mu) \quad , \quad (3.33b)$$

$$F^{\mathsf{L/R}}_{\mu\nu} = \partial_\mu A^{\mathsf{L/R}}_\nu - \partial_\nu A^{\mathsf{L/R}}_\mu - \imath g_0 \left[A^{\mathsf{L/R}}_\mu, A^{\mathsf{L/R}}_\nu\right] \quad , \quad (3.33c)$$

$$D_\mu U = \partial_\mu U - \imath g_0 A^{\mathsf{L}}_\mu U + \imath g_0 U A^{\mathsf{R}}_\mu \quad , \quad (3.33d)$$

$$M = \frac{2}{3}\left[m_K^2 + \frac{1}{2}m_\pi^2\right] - \frac{2}{\sqrt{3}}(m_K^2 - m_\pi^2)\lambda_8 \quad . \quad (3.33e)$$

Here, $F_\pi = 135$ MeV and ϕ_i, A^μ and V^μ are the pseudo-scalar, vector and axial vector meson matrices, respectively. For more details on the ansatz and values for the parameters g_0, γ, ξ and m_0, the reader is referred to [Tur04].

As mentioned earlier, the processes calculated by Turbide *et al.* differ from those considered by Kapusta *et al.* Only the processes $\pi\pi \to \gamma\rho$ and $\pi\rho \to \gamma\pi$ are therefore common in both models. The rate of Turbide *et al.* for $\pi\rho \to \gamma\pi$ directly includes the process with an intermediate a_1-meson.

To simplify the calculations, all photon rates in [Tur04] are parametrised by the general form

$$E\frac{\mathsf{d}R}{\mathsf{d}^3p} = E\frac{\mathsf{d}N}{\mathsf{d}^4x\mathsf{d}^3p} = T^A \exp\left(\frac{B}{(2ET)^C} - D\frac{E}{T}\right) \quad , \quad (3.34)$$

where B, C and D are linear functions of some power of the temperature T: $B(T) = B_1 + B_2 T^{B_3}$. The parameter set can be found in Table 3.2.

Following [Arl03] and [Liu09b], we introduce a hadronic form factor according to

$$F(\bar{t}) = \left(\frac{2\Lambda^2}{2\Lambda^2 - \bar{t}}\right)^2 \quad , \quad (3.35)$$

	$\pi\pi \to \gamma\rho$	$\pi\rho \to \gamma\pi$	$\pi K^* \to \gamma K$	$\pi K \to \gamma K^*$	$\rho K \to \gamma K$	$K^* K \to \gamma\pi$
A	-5.0	2.8	3.75	-3.0	3.5	3.7
B_1	5.328	-0.727	-0.35	1.51	-0.634	-1.0299
B_2	-9.314	-1.461	0.0	-5.4018	-0.9386	-6.096
B_3	-0.584	2.3094	–	-0.6864	1.551	1.889
C_1	-0.088	0.86	1.05	-0.07	1.01	0.975
C_2	0.0	0.0	0.0	0.0	0.0	-1.613
C_3	–	–	–	–	–	2.162
D_1	0.8998	0.9957	3.2222	0.91	1.164	0.96
D_2	-0.3189	-0.566	-2.2893	0.0	-0.568	0.0
D_3	0.721	1.4094	0.03435	–	0.5397	–
X	π	π	K	K	K	K

Table 3.2: The values used in the parametrisations of the photon emission rates (see text). The last line ("X") states which meson is supposed to be transferred in the exchange.

which enters the rates quadrupled. Here, $\Lambda = 1$ GeV is taken to be the typical hadronic scale and $\bar{t}$ the average momentum transfer $\bar{t} = -2Em_{\mathsf{X}}$, with X being the meson that is exchanged in the t-channel (see Table 3.2, last line).

In the Quark-Gluon-Plasma, the rate used is taken from [Arn01]. They computed the full leading-order result as

$$E\frac{dR}{d^3p} = \sum_{i=1}^{N_f} q_i^2 \frac{\alpha_{\mathsf{em}}\alpha_{\mathsf{S}}}{2\pi^2} T^2 \frac{1}{e^x+1} \cdot \left(\ln\left(\frac{\sqrt{3}}{g}\right) + \frac{1}{2}\ln(2x) + C_{22}(x) + C_{\mathsf{brems}}(x) + C_{\mathsf{ann}}(x) \right) , \quad (3.36)$$

and give convenient parametrisations for the contribution of $2 \leftrightarrow 2$-, bremsstrahlung- and annihilation-processes (C_{22}, C_{brems} and C_{ann}, respectively)

$$C_{22}(x) = 0.041x^{-1} - 0.3615 + 1.01\exp(-1.35x) \quad , \quad (3.37a)$$

$$C_{\mathsf{brems}}(x) + C_{\mathsf{ann}}(x) = \sqrt{1+\frac{N_f}{6}} \left[\frac{0.548\ln\left(12.28+\frac{1}{x}\right)}{x^{\frac{3}{2}}} + \frac{0.133x}{\sqrt{1+\frac{x}{16.27}}} \right] \quad . \quad (3.37b)$$

In Equation (3.36) and Equation (3.37), $x = {}^{E}/_{T}$, q_i is the charge of quark-flavour i, α_{em} and $\alpha_{\mathsf{S}} = {}^{g^2}/_{4\pi}$ are the electromagnetic and QCD coupling constants, respectively. In our calculations, we use $N_{\mathsf{f}} = 3$, and therefore $\sum_i q_i^2 =$

2/3. The temperature dependence of α_S is taken from [Liu09b] as

$$\alpha_S(T) = \frac{6\pi}{(33 - 2N_f)\ln\left(\frac{8T}{T_C}\right)} \quad , \tag{3.38}$$

and the critical temperature at $\mu_B = 0$ to be $T_C = 170$ MeV.

Figure 3.14 shows all hadronic rates with and without form factor. In Figure 3.15, the sum of all hadronic rates is compared to the QGP-rate at $T = 170$ MeV. The integrated rates as a function of temperature (divided by T^3) are shown in Figure 3.16. From these Figures, it is clear that partonic emission is strongly enhanced with respect to the hadronic channels at equal temperatures. Even at the phase transition temperature T_C of the BM-EoS, the partonic rate is about 7.5 times higher than the hadronic rate, so that a QGP-fraction of $\lambda_{QGP} = 0.15$ is enough for the QGP-emission to dominate.

The calculation procedure for direct photons from the hydrodynamic phase is explained in detail in Appendix B.

3.5.3 Photon emission from primordial pQCD scatterings

At high transverse momenta, a major contribution to the photon yield is the emission of photons from hard pQCD-scatterings of the partons in the incoming nucleons. In the intermediate and low $p_\perp$-regions, the contribution may be comparable to or smaller than the yield from other sources.

For calculations at SPS-energies, we apply the results extracted by Turbide *et al.* [Tur04]. They first scale the photon spectrum from proton-proton collisions by the number of binary collisions in Pb+Pb-collisions, and then add a Gaussian-shaped additional $k_\perp$-smearing to the result. The width of the Gaussian is obtained by fitting this procedure to the data from proton-nucleus collisions. The results shown here are obtained with $\langle \Delta k_\perp^2 \rangle = 0.2$ GeV^2.

For comparison, we also show pQCD spectra obtained earlier by Gale [Gal02] following Wong *et al.* [Won98]. They follow the same procedure as explained above. The authors of [Gal02] obtain a higher intrinsic transverse parton momentum of $\langle \Delta k_\perp^2 \rangle = 0.9$ GeV^2, yet lower spectra.

In order to compare our calculations to experimental data in Figures 5.4 and 5.5, we use the newer calculations by Turbide *et al.* [Tur04].

At the higher energies available at RHIC (see e.g. Figure 5.6), the smearing effect outlined above is negligible. The spectra predicted by NLO-pQCD calculations from Gordon and Vogelsang [Gor93] fit the experimental data from the PHENIX-collaboration [PHENIX05b] rather well at high $p_\perp$. Therefore, the pQCD contributions from [Gor93], directly scaled by the number of binary collisions $\langle N_{coll} \rangle$, are added to the soft photons calculated here.

In the case of FAIR-experiments ($E_{lab} = 35$ AGeV), the contribution of pQCD-scatterings to the overall photon spectra is negligible, so that no calculations need to be added to the spectra.

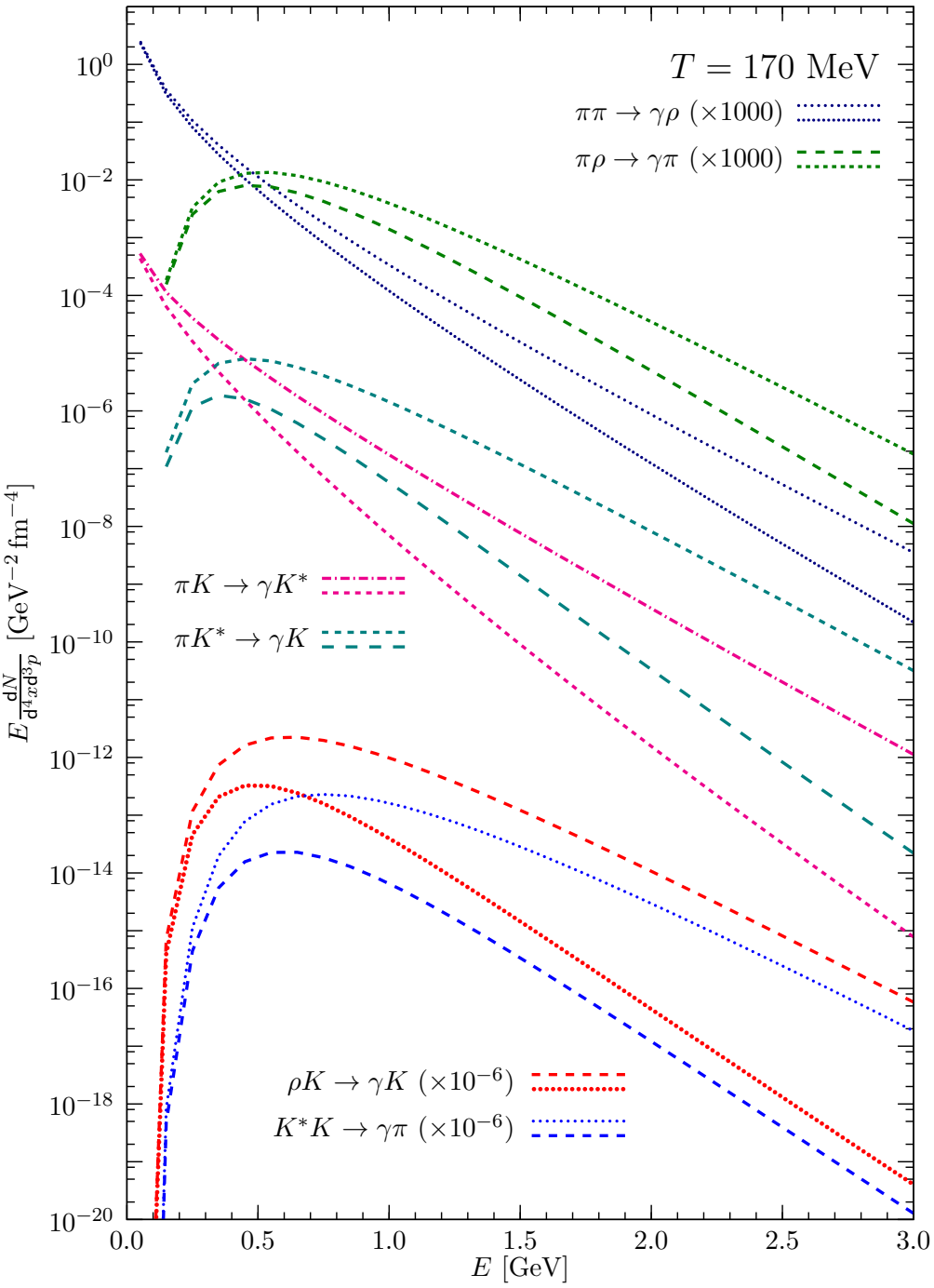

Figure 3.14: Rates of all processes considered in the hydrodynamic phase with a Hadron Gas EoS with form factor (upper lines) and without form factor (lower lines). For better visibility, some rates have been scaled by factors of 10^3 ($\pi\pi \to \gamma\rho$ and $\pi\rho \to \gamma\pi$) and 10^{-6} ($\rho K \to \gamma K$ and $K^*K \to \gamma\pi$), respectively.

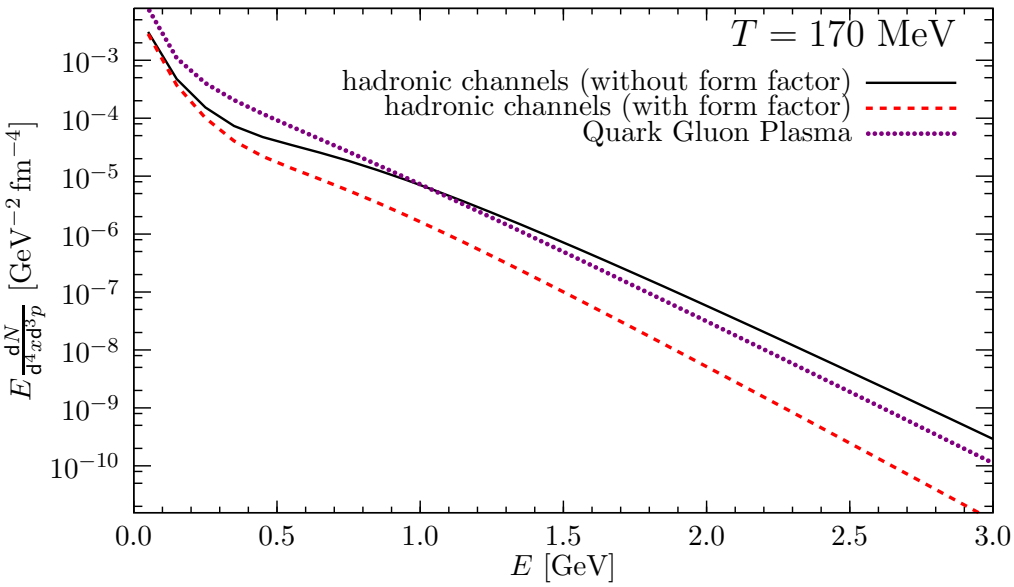

Figure 3.15: Thermal rates: Comparison between the sum of all hadronic contributions shown above (with form factor, dashed line and without form factor, solid line) to the contribution of Quark-Gluon-Plasma (dash-dotted line).

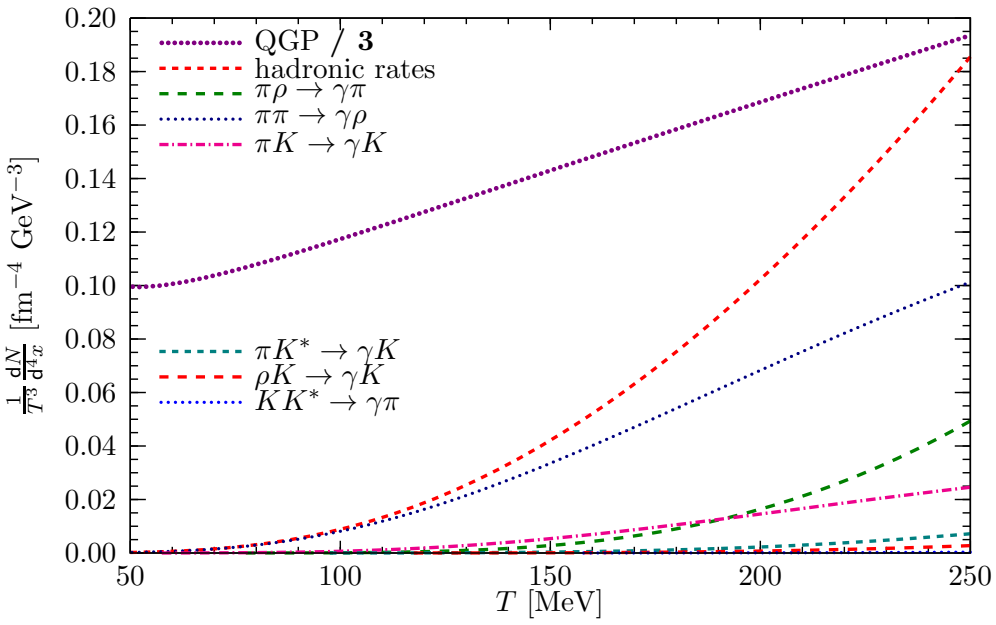

Figure 3.16: Energy-integrated thermal rates (w/ form factor) for temperatures $50 < T < 250$ MeV, divided by T^3. The QGP-emission rate (dash-dotted line) is scaled down by a factor of 3.

Chapter 4

Numerical Tests and Investigations

4.1 Rates from transport and hydrodynamics

Before comparing photon spectra from complex nucleus-nucleus collisions between cascade- and hybrid model, we check if both approaches give similar results for the setup of a fully thermalised box.

I.e., we perform UrQMD calculations in a box [Bel98], allowing only π-, ρ- and a_1-mesons to be present and to scatter. When the matter in the box has reached thermal and chemical equilibrium, the rate of photon emission is extracted based on the microscopic scatterings with the procedure described in Section 3.5.1. Next, we compare the microscopic rates to the hydrodynamic rates from Equation (3.34) with the parameters from Table 3.2. Since the available rates in the cascade and hydrodynamic models differ, as pointed out above, we restrict the comparison to the common rates $\pi\pi \to \gamma\rho$ and $\pi\rho \to \gamma\pi$. The cascade-rates are explicitly summed over all charge combinations.

Figure 4.1 shows the comparison of the rates at a temperature $T = 150$ MeV. It can be seen that the microscopically obtained rates agree very well with the thermodynamic rates. We can compare this to the spectra obtained from a realistic system. In Figure 4.2, we show a comparison of hybrid model calculations with HG-EoS and transport-calculations using only common channels. One observes that the direct photon spectrum is not sensitive to the change in the underlying dynamics (e.g. finite viscosities vs. ideal fluid) and indicates that even the two-body collision dynamic in UrQMD drives the system into equilibrium in the $\pi - \rho - a_1$ channel.

4.2 String ends

In UrQMD, the leading particles from a string have a reduced cross-section during their formation time (see Section 3.1.1) For all other purposes, they are

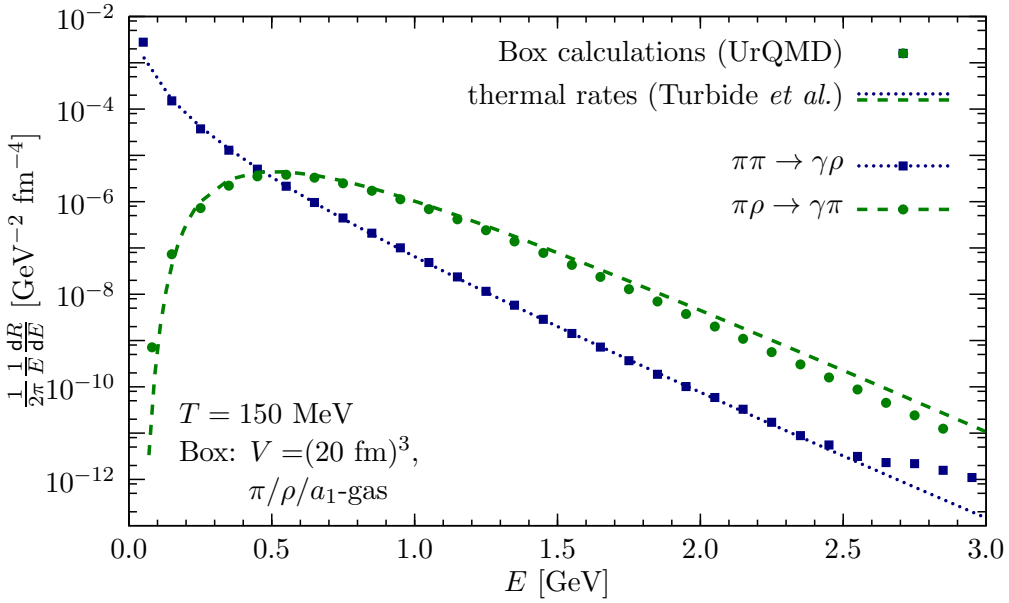

Figure 4.1: Comparisons between the rates from [Tur04] (lines) and box calculations restricted to a π, ρ, a_1-system (points) with UrQMD at $T = 150$ MeV.

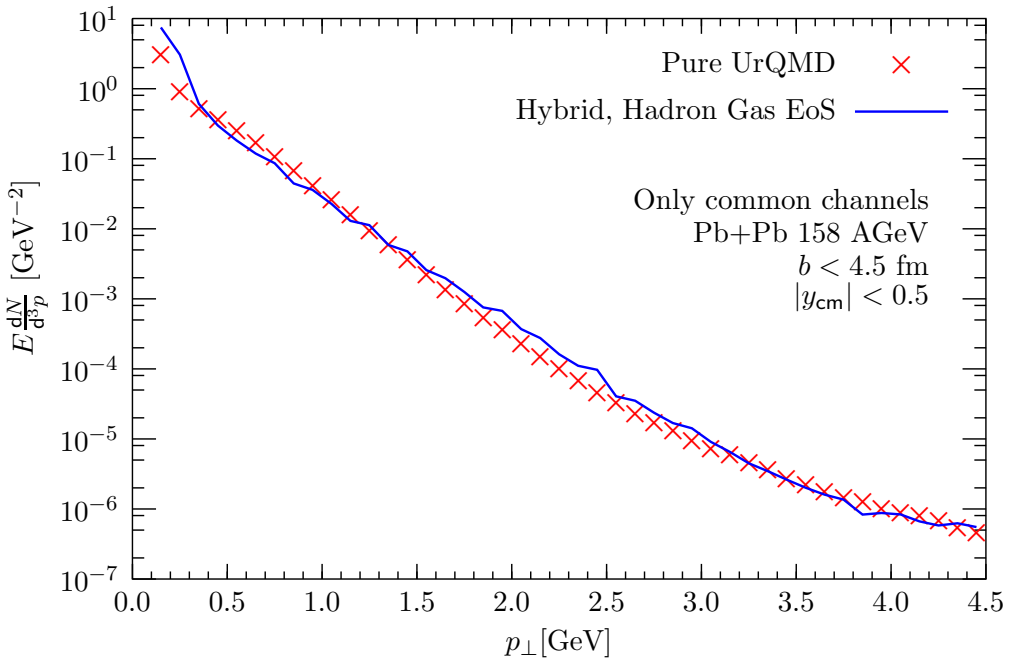

Figure 4.2: Comparison of direct photon spectra from the hybrid model with HG-EoS (solid line) and transport model (crosses), using only common channels.

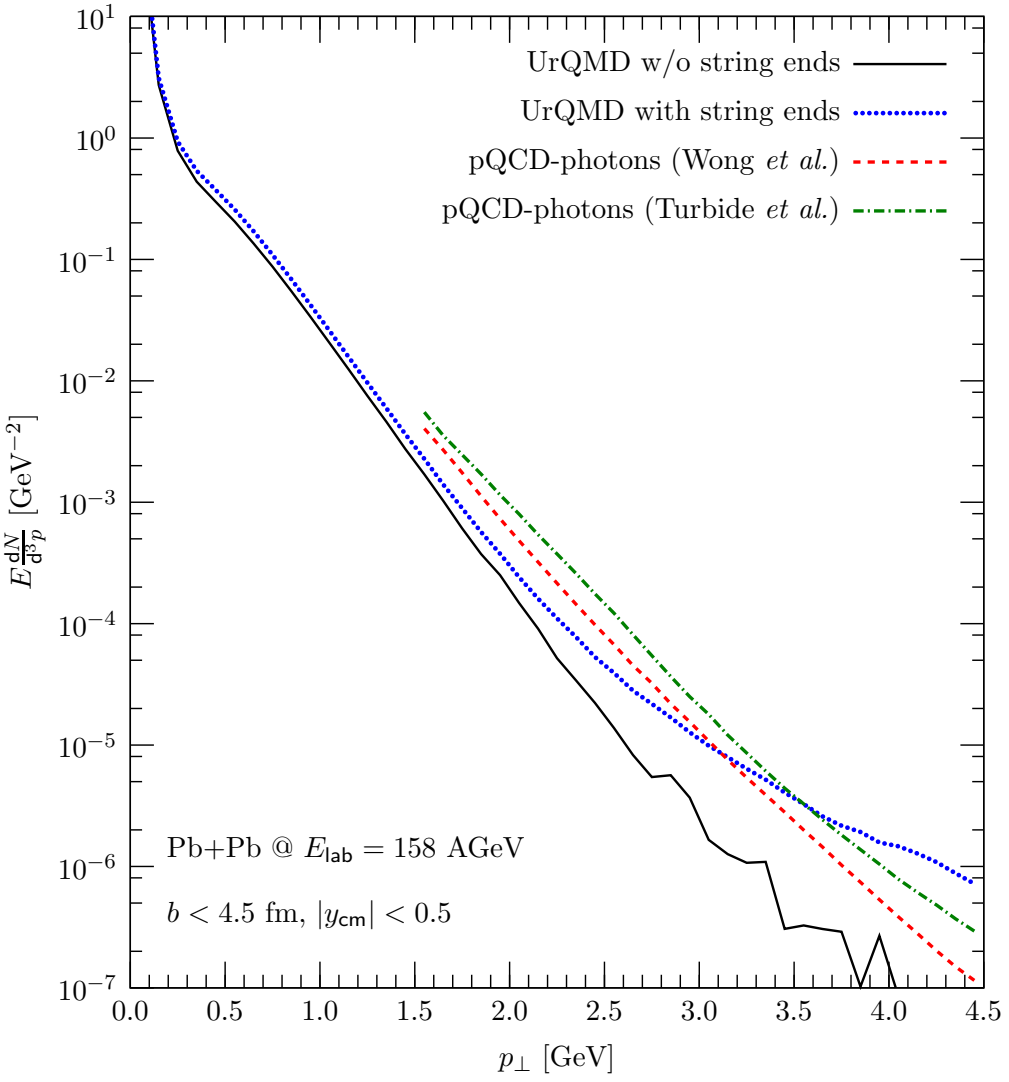

Figure 4.3: UrQMD calculation. Total yields of photons with (dotted line) and without (solid line) the contributions from colliding string ends. For comparison, the pQCD-spectra from Wong *et al.* [Won98] (dashed line) and Turbide *et al.* [Tur04] (dashed-dotted line) are shown.

treated as hadrons. Hadronic scatterings of the string ends happen typically at high center-of-mass energies $\sqrt{s}$. Collisions from string ends can only produce photons if the collision of fully formed hadrons of the same type would produce photons. Thus, their contribution is treated as an addition to the prompt contribution from primordial nucleus-nucleus interactions. Photons from those collisions contribute significantly to the spectra at high transverse momenta. Since these particles are not fully formed hadrons, but effectively represent quarks or di-quarks, a hadronic treatment of those processes is questionable.

The effects of including the photons from colliding string ends, i.e. interactions of leading (di-)quarks, in the calculation is studied for a system at $E_{\mathsf{lab}} = 158$ AGeV (top SPS-energy) in Figure 4.3. The spectrum obtained by neglecting the collision of string ends is exponential and does not exhibit a flattening at high transverse photon momenta (cmp. Figure 5.3). The inclusion of (di-)quark scatterings, however, leads to a strong increase of the photon yield at high $p_\perp$. The contribution of pQCD-photons at this collision energy to the inclusive spectrum starts to be significant already at relatively low transverse photon momenta $p_\perp \approx 1$ GeV, although the magnitude of the contribution differs between the different parametrisations in [Tur04] and [Won98].

4.3 ρ-meson width

Earlier, we discussed the handling of the ρ-meson's finite width. Figure 4.4 shows the effects of following the calculation outlined there. In both channels, $\pi^\pm\pi^\mp \to \gamma\rho^0$ and $\pi^\pm\pi^0 \to \gamma\rho^\pm$, the yield is about 10 % higher for ρs produced at their pole mass, and only at very low momenta this excess becomes as large as 40 %.

This behaviour can be explained by kinematic arguments: The by far highest scattering rate in $\pi + \pi$-collisions is at $\sqrt{s} \approx m_\rho^0$. Here, the photon cross-section with fixed pole mass is much higher than the extended calculation with variable ρ mass. At all other center-of-mass energies, the extended model gives a higher cross-section, but these comparatively rare processes provide only a minor contribution to the spectrum. The processes at low $\sqrt{s}$ will contribute primarily to the low-$p_\perp$-region, because the production of the ρ-meson consumes most of the available energy. Therefore, the enhancement in the model is most pronounced at low $p_\perp$.

4.4 Comparison to previous works with UrQMD

As mentioned in Section 2.4, UrQMD has been used previously in order to obtain direct photon spectra [Dum98]. The authors calculated transverse momentum spectra for central ($b = 0$ fm) Pb+Pb-collisions at $E_{\mathsf{lab}} = 160$ AGeV. Limiting ourselves to the same conditions, we can compare our work to that of Dumitru *et al.* In Figure 4.5, we compare results from the current UrQMD-version 3.3 to

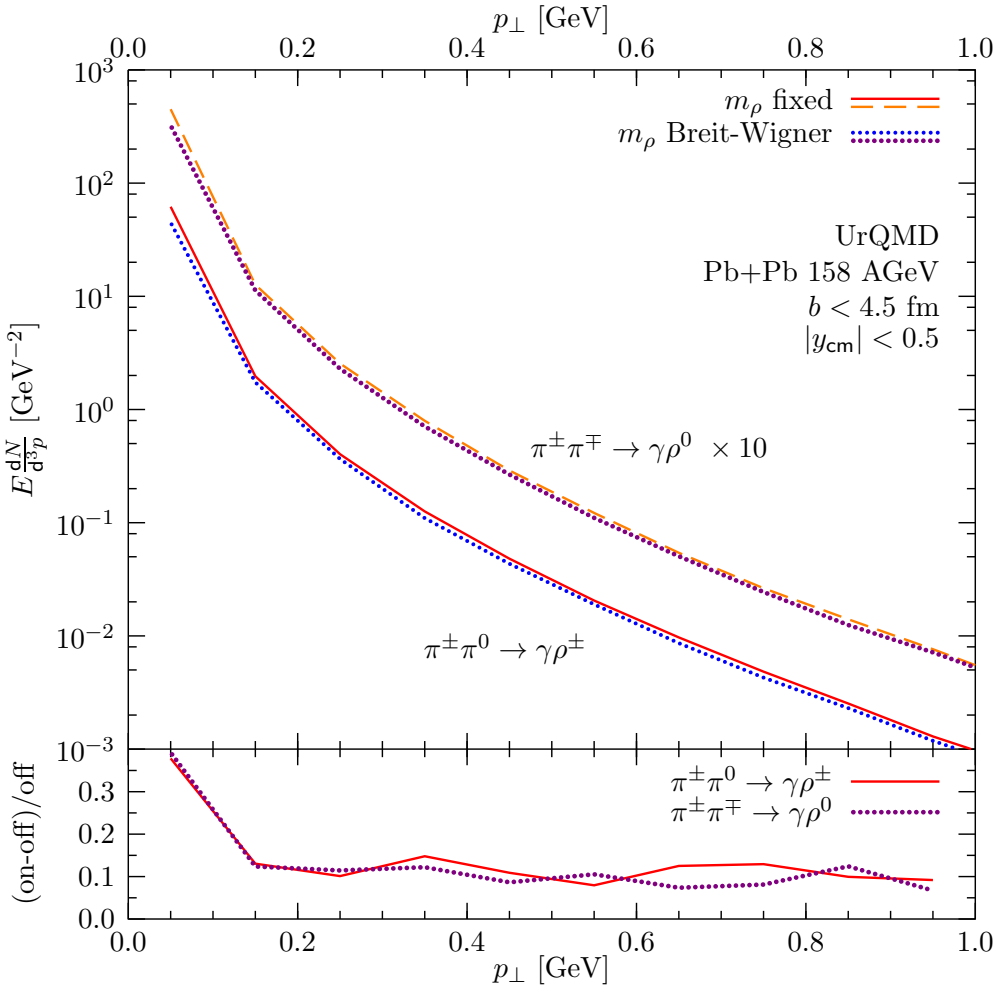

Figure 4.4: UrQMD calculation. Photon spectra from collisions that produce a ρ meson in the final state for the production of ρ mesons at its pole-mass (solid and dashed lines) and for the production of ρ mesons according to a Breit-Wigner-mass distribution (dotted and dash-dotted lines).

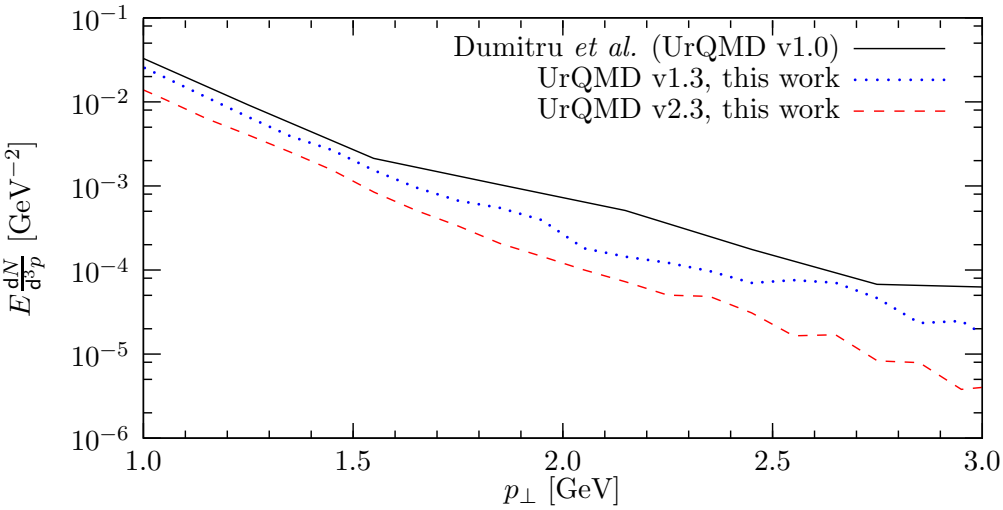

Figure 4.5: Comparison of the current model (dashed line) to calculations from Dumitru *et al.* ([Dum98], solid line). For further comparison, we apply our model to an earlier UrQMD version (dotted line).

those obtained with the earlier versions 1.3 (using our own photon-analysis) and 1.0 (taken from [Dum98]). The older UrQMD-versions yield significantly higher photon spectra at intermediate $p_\perp$.

We can identify two changes in UrQMD that lead to this behaviour. Between versions 1.0 (used by Dumitru *et al.*) and 1.3, the angular distributions of various processes have been improved. Since the collisions of pions with a high difference in rapidity provide significant contributions to the spectra from [Dum98], the improved angular distributions reduce the photon production cross-section. Furthermore, in versions prior to 2.3, the number of pions has been unphysically high [Pet08a]. The correction of this leads to fewer collisions involving pions and hence to a further reduction of the spectra.

4.5 Exploring the parameter space

The hybrid approach introduces a set of new parameters whose influence on the direct photon spectra will be studied in the following Section. Since the collision systems considered in this thesis (gold, lead and uranium nuclei) have very similar sizes, the dependence of the collision system on photonic observables is not studied and all calculations in this Section are done for central ($b < 5$ fm) lead-lead collisions. We will change the time for the first transition t_{start}, the critical energy density for the second transition $\varepsilon_{\mathsf{crit}}$ and the scenario for the second transition (gradual vs. isochronous). During each of these changes, the other two parameters are kept at their default values.

4.5.1 Transport → hydrodynamics

At the transition from transport calculation to the hydrodynamic description all particles and their momenta are transformed to baryon number-, energy- and momentum densities (see Section 3.3.1). In this process, the system is forced into local thermal equilibrium, because in ideal hydrodynamics only perfectly equilibrated matter can be described. The time t_{start} at which this transition happens is, in standard setup, when the initial nuclei have passed through each other (cmp. Equation (3.14)). This number depends on the radii of the incoming nuclei as well as the initial collision energy. We investigate the changing of this parameter from $\frac{1}{4}\,t_0$ to $4\,t_0$, with t_0 being the standard value. At high energies, this time is too short to allow even for partial thermalisation. As pointed out before, the minimal time for switching to the hydrodynamic description has been set to $t_{\mathsf{start}} = 0.6$ fm, which is $0.41\,t_0$ for Pb+Pb-collisions at top SPS-energies ($E_{\mathsf{lab}} = 158$ AGeV) and more than $4\,t_0$ at $\sqrt{s_{\mathsf{NN}}} = 200$ GeV. Therefore, the latter energy has been omitted from this investigation.

Figure 4.6 shows the invariant direct photon yields from calculations with varying start time of the hydrodynamic description, divided by the value from standard calculations (with $t_{\mathsf{start}} = t_0$). From left to right, the panels show the ratios at $0.5 < p_\perp < 1.5$ GeV, $1.5 < p_\perp < 2.5$ GeV and $2.5 < p_\perp < 3.5$ GeV. Each panel shows the ratios for $E_{\mathsf{lab}} = 158$ AGeV, scaled by 10^3, $E_{\mathsf{lab}} = 45$ AGeV, scaled by 10^2 (middle curves) and $E_{\mathsf{lab}} = 8$ AGeV, scaled by 1/10 (lower curves). At $E_{\mathsf{lab}} = 8$ AGeV and late switching times $t_{\mathsf{start}} > 2\,t_0$, the whole system has an energy density below or close to the threshold for switching back to transport calculations $\varepsilon = 5\varepsilon_0$, so that the hydrodynamic calculation only runs for a very short time. The yield of direct photons is maximal in calculations with $t_{\mathsf{start}} \approx 0.75\,t_0$ for all systems and is about 1.5 to 2 times larger than in standard parameter calculations. In calculations with large t_{start} values, most of the high-density evolution of the system takes place in the transport phase. Here, chemical equilibration is reached only after some time, so that especially the $\pi\rho \to \gamma\pi$-channel, which dominates the hadronic sources, is suppressed by the lack of ρ-mesons in the unequilibrated cascade calculation with respect to the equilibrated hydrodynamic calculation. Hence, the direct photon yield is suppressed by a factor of approximately 10 in calculations with large t_{start}. By geometrical arguments, reasonable values for t_{start} are in the range from $t_{\mathsf{start}} = 0.5\,t_0$ (complete overlap of the nuclei) to $t_{\mathsf{start}} \gtrsim 1\,t_0$ (complete pass-through), and in this range, the deviations are less than a factor of 3.

4.5.2 Hydrodynamics → transport

At the transition from hydrodynamics to transport, the densities have to be translated back to particles. Here, the system remains in thermal equilibrium. Besides the criterion when this happens, the details of this transition can also be changed. Usually, the transition happens when the system has di-

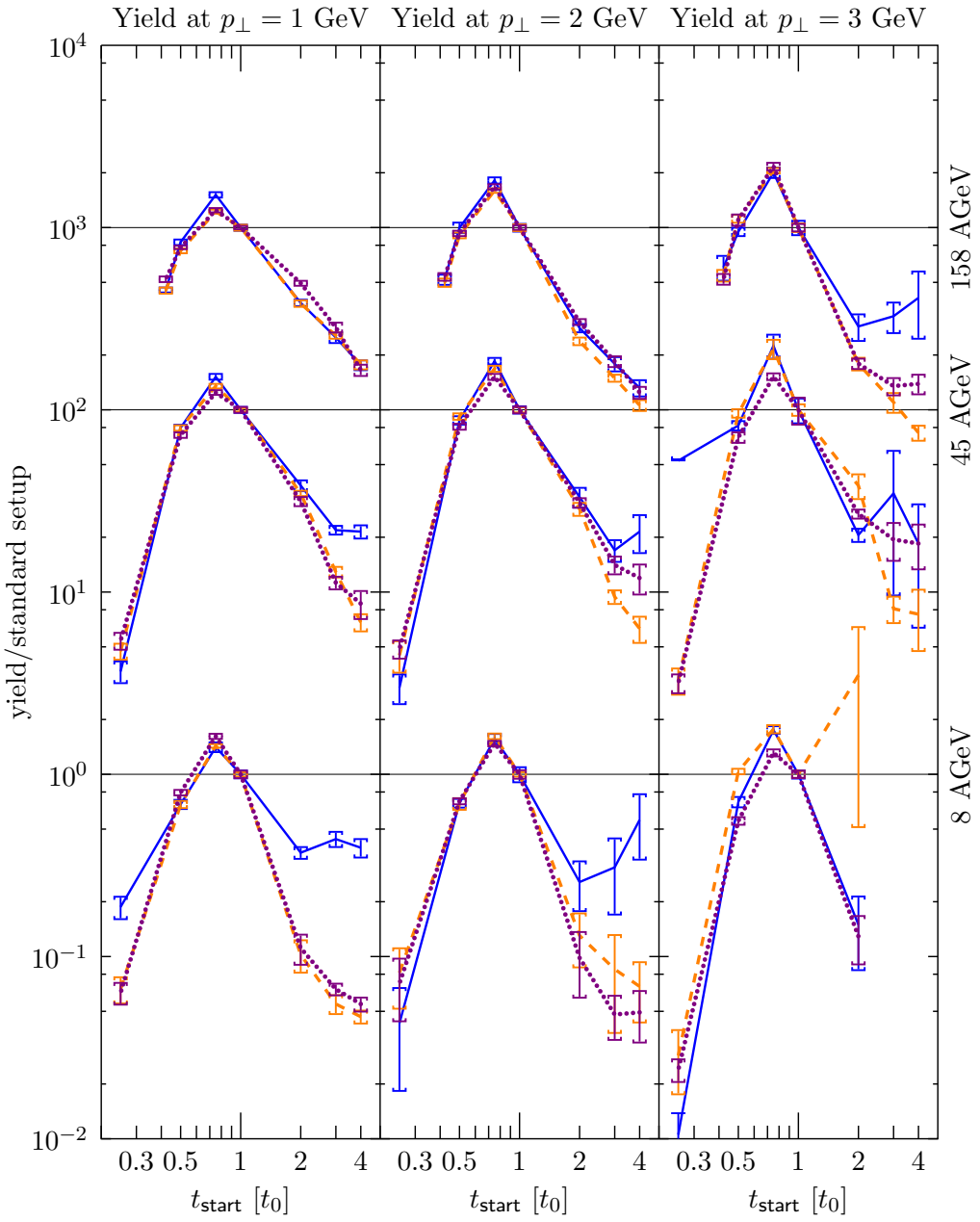

Figure 4.6: Ratio of invariant direct photon yield of calculations with varying start time of the hydrodynamic description to calculations with standard parameters ($t_{\mathsf{start}} = t_0$). The left panel shows the ratio at $0.5 < p_\perp < 1.5$ GeV, the middle panel at $1.5 < p_\perp < 2.5$ GeV and the right panel shows the ratio at $2.5 < p_\perp < 3.5$ GeV. Each panel shows the yields for $E_{\mathsf{lab}} = 158$ AGeV, scaled by 10^3 (upper curves), $E_{\mathsf{lab}} = 45$ AGeV, scaled by 10^2 (middle curves) and $E_{\mathsf{lab}} = 8$ AGeV (lower curves) for HG-EoS calculations (solid lines), χ-EoS calculations (dashed lines) and BM-EoS calculations (dotted lines).

luted below $\varepsilon = 5\varepsilon_0$ (or $\varepsilon = 7\varepsilon_0$ for χ-EoS calculations, see Table 3.1), where $\varepsilon_0 = 146$ MeV/fm^3 is the nuclear ground state energy density. This number is varied between $\varepsilon_{\mathsf{crit}} = 2.5\varepsilon_0$ and $\varepsilon_{\mathsf{crit}} = 10\varepsilon_0$. The scenario for the transition can either be that the criterion must be met by the part of the system that has the same z-coordinate (along the beam axis), whereafter this slice is transferred to the transport calculation. This is the default **gradual** scenario. The other scenario, called **isochronous** scenario, requires the criterion to be met by the whole system, after which it is transferred to the transport calculation instantaneously (for details on both approaches, refer to Section 3.3.3).

The investigation shown in Figure 4.7 varies the critical energy density $\varepsilon_{\mathsf{crit}}$ below which the system is described by transport calculations from $\varepsilon_{\mathsf{crit}} = 2\varepsilon_0$, where the applicability of hydrodynamics seems very questionable, to $\varepsilon_{\mathsf{crit}} = 10\varepsilon_0$, where the use of a transport calculation might be questioned. We find a slight decrease of the photon spectra as the threshold is raised, consistent with the findings above. This behaviour is present in nearly all systems; deviations from it are not significant.

The influence of changing the transition scenario is investigated in Figure 4.8. The yield in the gradual transition scenario is very similar to the yield in the isochronous transition scenario, albeit a small increase on the order of 10-30 % is visible in most of the calculations. Since in the isochronous transition scenario the fraction of the system calculated with hydrodynamics is larger than in the gradual transition scenario, this is also consistent with the investigations on $\varepsilon_{\mathsf{crit}}$ and t_{start}.

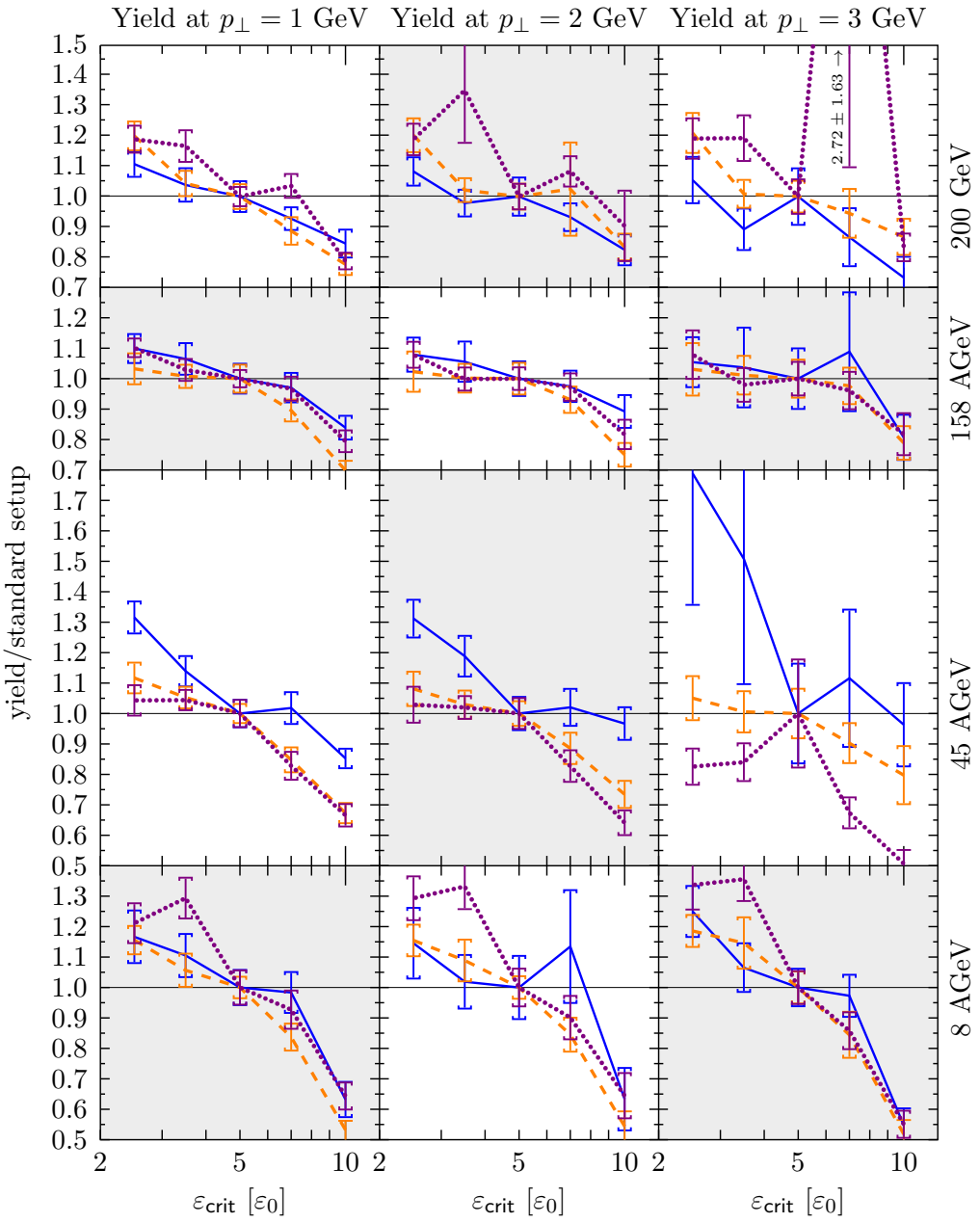

Figure 4.7: Ratio of invariant direct photon yield of calculations with varying critical energy density for the transition from hydrodynamic description to transport description to calculations with standard parameters ($\varepsilon_{\mathsf{crit}} = 5\varepsilon_0$). The left panels shows the yield at $0.5 < p_\perp < 1.5$ GeV, the middle panels at $1.5 < p_\perp < 2.5$ GeV and the right panel shows the yield at $2.5 < p_\perp < 3.5$ GeV. The panels show (upper to lower) the results for $\sqrt{s_{\mathsf{NN}}} = 200$ GeV, $E_{\mathsf{lab}} = 158$ AGeV, $E_{\mathsf{lab}} = 45$ AGeV and $E_{\mathsf{lab}} = 8$ AGeV for HG-EoS calculations (solid lines), χ-EoS calculations (dashed lines) and BM-EoS calculations (dotted lines).

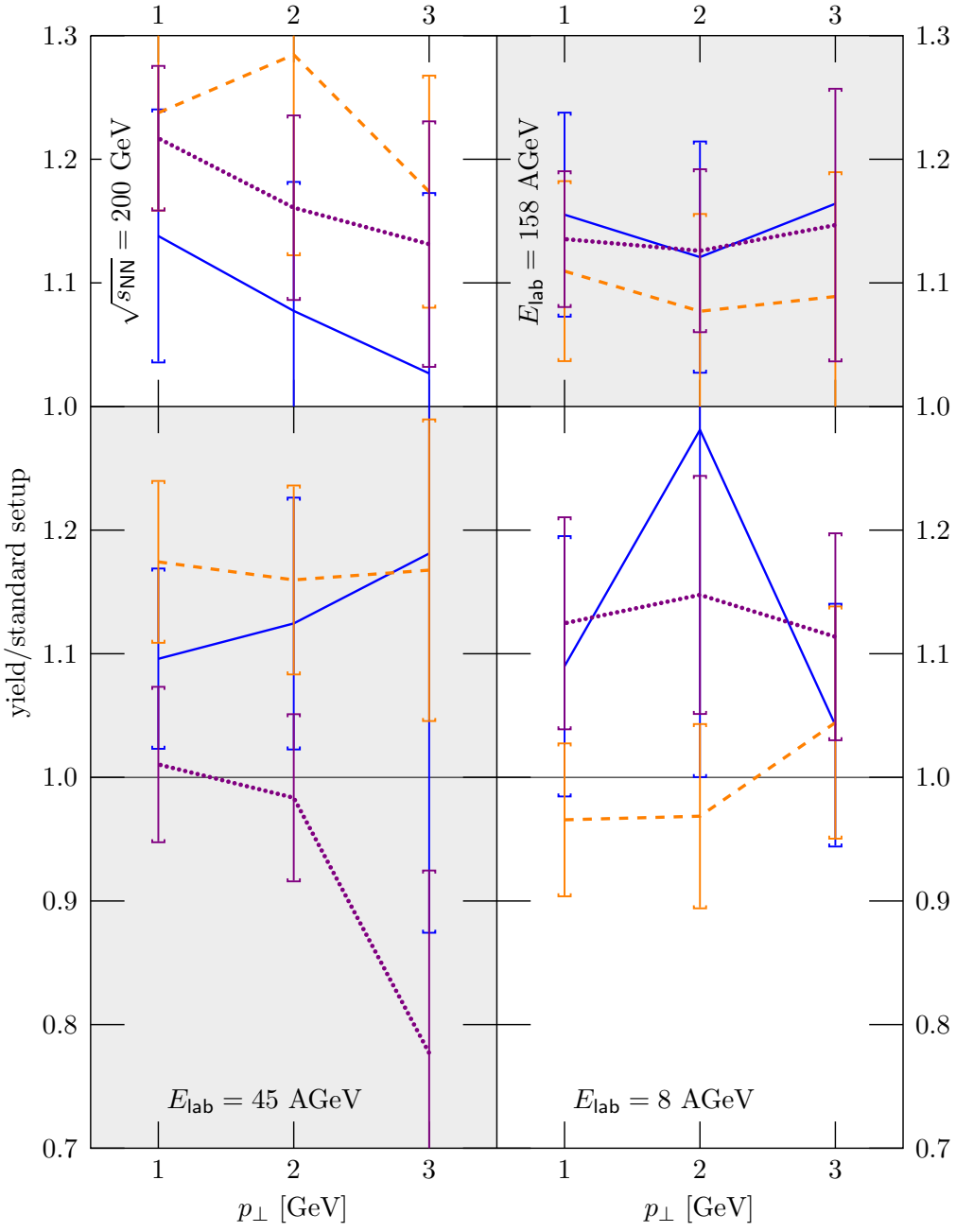

Figure 4.8: Ratio of invariant direct photon yields in calculations with isochronous transition scenario and gradual transition scenario. The panels show the ratios at $\sqrt{s_{\mathsf{NN}}} = 200$ GeV (upper left), $E_{\mathsf{lab}} = 158$ AGeV (upper right), $E_{\mathsf{lab}} = 45$ AGeV (lower left) and $E_{\mathsf{lab}} = 8$ AGeV (lower right) for HG-EoS calculations (solid lines), χ-EoS calculations (dashed lines) and BM-EoS calculations (dotted lines).

Chapter 5

Results

In the following Chapter, we will present the direct photon spectra and elliptic flow results obtained with our model for systems that have been or will be measured in direct photon experiments and, where available, compare our calculations to experimental data. In Chapters 6, 7 and 8, we will investigate the calculations more thoroughly.

5.1 Photons at FAIR: CBM

At the Facility for Antiproton and Ion Research FAIR, which is under construction and planned to start operations later this decade, the experiment CBM is expected to measure direct photon spectra in collisions of Uranium-Uranium-nuclei at $E_{\mathsf{lab}} = 35$ AGeV. Since centrality cuts that will be used for data from this experiment are not yet known, we calculate events with impact parameters of $b < 5$ fm and only take into account photons with a center-of-mass rapidity $|y_{\mathsf{cm}}| < 0.5$.

We compare the overall direct photon spectra calculated with the various Equations of State and with the transport-only approach. From Figure 5.1, one can clearly see that the transport-only (crosses) and HG-EoS (solid line) calculations give very similar results. The BM-EoS and χ-EoS calculations, on the other hand, yield significantly higher spectra than both hadronic calculations.

In order to understand this difference, we can look at the intermediate stages and investigate the contribution of hadronic and partonic direct photon emissions to the spectra from χ-EoS and BM-EoS hybrid calculations. In Figure 5.2, we show the total contributions of the intermediate stages and the part of it that comes from hadronic sources (in case of the χ- and BM-EoS-calculations). We note that the hadronic contributions are very similar in all cases, and that the excess observed in calculations with partonic degrees of freedom comes from the partonic part of the system. The ratio between hadronic and partonic sources is investigated in more detail in Section 6.2.

What is eye-catching with the spectra is that despite the obvious differences

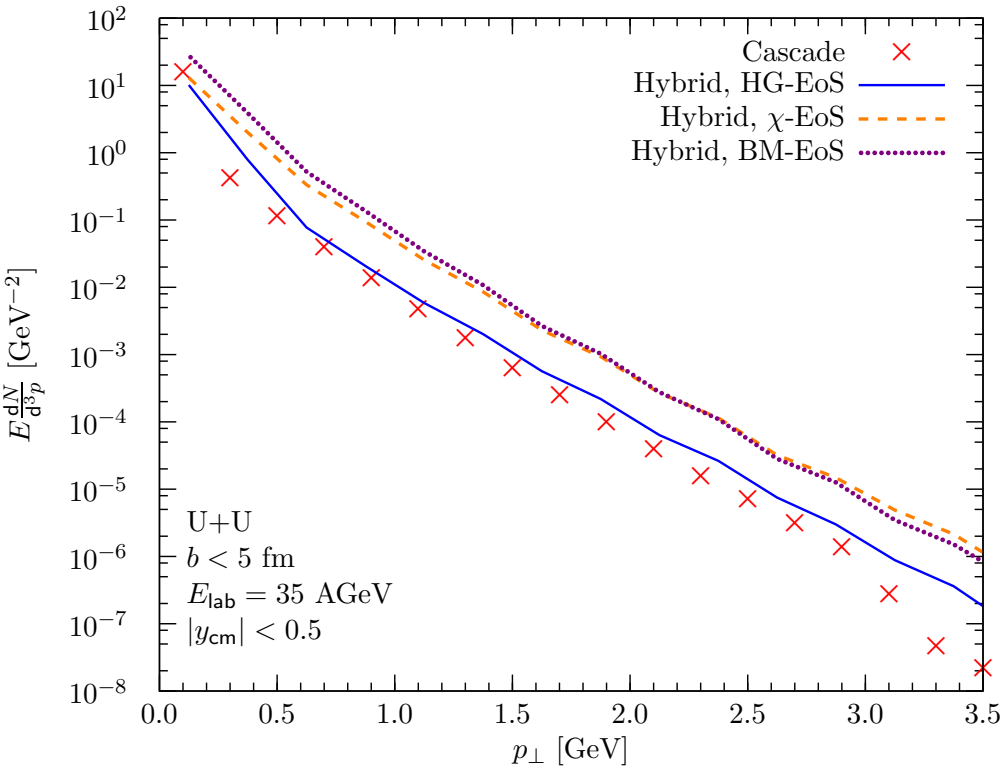

Figure 5.1: Overall direct photon spectra from central U+U-collisions. Calculations in pure cascade mode are shown as crosses, hybrid calculations with HG-EoS are shown as solid line, χ-EoS-hybrid calculations as dashed line and BM-EoS-hybrid calculations are shown as dotted line.

Calculation	T_{slope} [MeV]	A [GeV^{-2}]	χ^2/d.o.f.
Transport	198.0±6.6	2.09±0.74	0.559
HG-EoS	203.5±8.0	2.98±1.16	0.532
χ-EoS	214.8±6.1	7.57±2.02	0.249
BM-EoS	200.8±5.8	15.39±4.45	0.291

Table 5.1: Results of exponential fits to the spectra in the range $0 < p_\perp < 3.5$ GeV. The fit function is $f(p_\perp) = A \exp\left(-\frac{p_\perp}{T_{\mathsf{slope}}}\right)$.

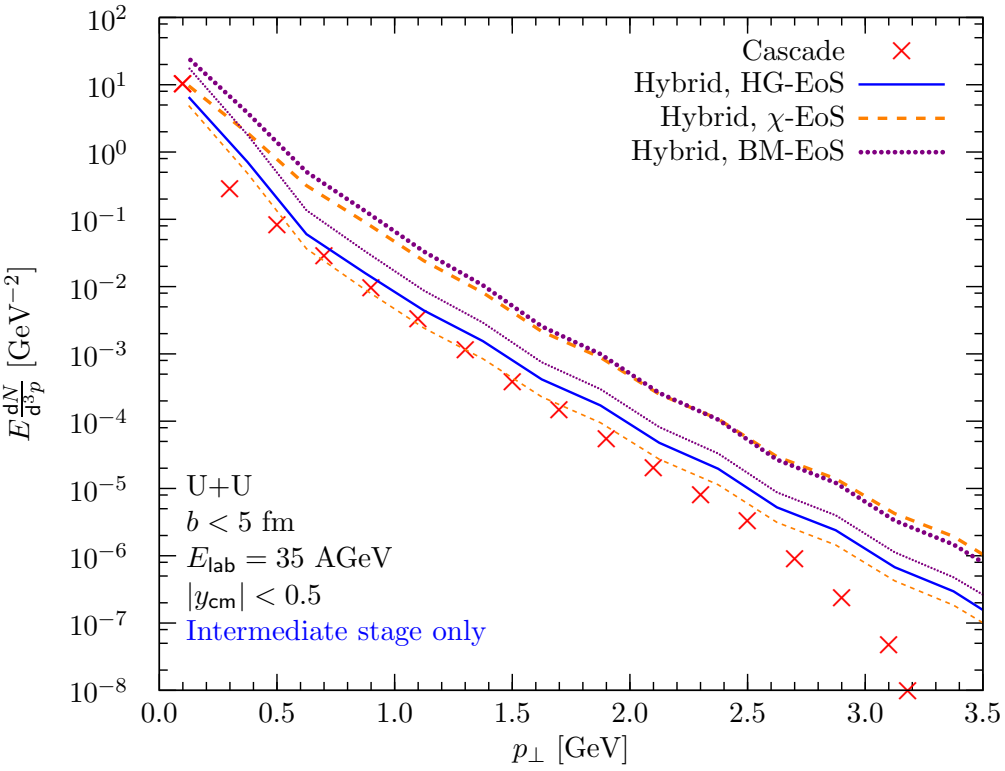

Figure 5.2: Comparison of the contributions of the intermediate stages for all variations of the model at $E_{\mathsf{lab}} = 35$ AGeV: Calculations in pure cascade mode are shown as crosses, hybrid calculations with HG-EoS are shown as solid line, χ-EoS-hybrid calculations as dashed line and BM-EoS-hybrid calculations are shown as dotted line. In addition, the hadronic contributions to the intermediate-stage emissions in χ-Eos and BM-EoS are shown in thin lines.

in magnitude, the slopes of the spectra are very similar. Indeed, a closer anaylsis reveals all inverse slope parameters to be about $T_{\mathsf{slope}} = 200$ MeV, with only the χ-EoS calculations being significantly higher (see Table 5.1).

5.2 Photons at SPS: WA98

The experiment WA98 published data on direct photon spectra in lead-lead collisions at $E_{\mathsf{lab}} = 158$ AGeV [WA98-00, WA98-00a]. They quote data points in two different centrality bins: central collisions with $b < 4.5$ fm and peripheral collisions with $b > 12.5$ fm, their acceptance in center-of-mass rapidity is $|y_{\mathsf{cm}}| < 0.5$. We compare the data set from central collisions to transport and hybrid model calculations with gradual transition with all EoS and hybrid calculations with isochronous transition with HG- and BM-EoS in Figure 5.3.

The calculations show a big difference between calculations with partonic degrees of freedom (BM-EoS, dotted lines, and χ-EoS, dashed line) and those with only hadronic degrees of freedom (HG-EoS, solid lines, and cascade, crosses). While the latter clearly undershoot the data, the calculations with a partonic phase fit the data very well. The choice of the transition scenario (gradual transition, thick lines vs. isochronous transition, thin lines) is investigated for HG-EoS and BM-EoS calculations and shown not to make a difference (compare Section 4.5.2). The calculation without intermediate hydrodynamic phase shows a significant deviation from an exponential spectrum at high transverse momentum. In Figure 4.3, it has been shown that collisions from string ends are responsible for this behaviour. Section 7.2 examines the direct photon emission at high $p_\perp$ more closely.

Those calculations lack the contribution from prompt photons that are emitted from initial pQCD-scatterings of nucleons. After adding the pQCD-spectra as extracted by Turbide *et al.* [Tur04], we obtain Figure 5.4. Now, the picture is less clear: While the hadronic+pQCD calculations fit the data, the partonic calculations slightly overpredict the data.

The data set for peripheral ($b > 12.5$ fm) collisions is only compared to cascade calculations and prompt photon emission in Figure 5.5, because the applicability of hydrodynamics is limited to central collisions. Since the system created in those collisions is very small, no big thermal or hadronic contribution to the direct photon yield is expected. However, the intrinsic transverse momentum of partons is not affected by the centrality of the collision, so that we scale the pQCD-spectra used for central collisions by the ratio of the number of binary collisions in central and peripheral collisions $\langle N_{\mathsf{bin}}^{\mathsf{per}} \rangle / \langle N_{\mathsf{bin}}^{\mathsf{cen}} \rangle = 118/8440$.

We find that at such peripheral collisions the hadronic contribution is indeed highly suppressed with respect to the prompt photon contribution and is negligible in the overall direct photon spectrum. The prompt photon contribution, on the other hand, is sufficient to explain the data published by the WA98 collaboration.

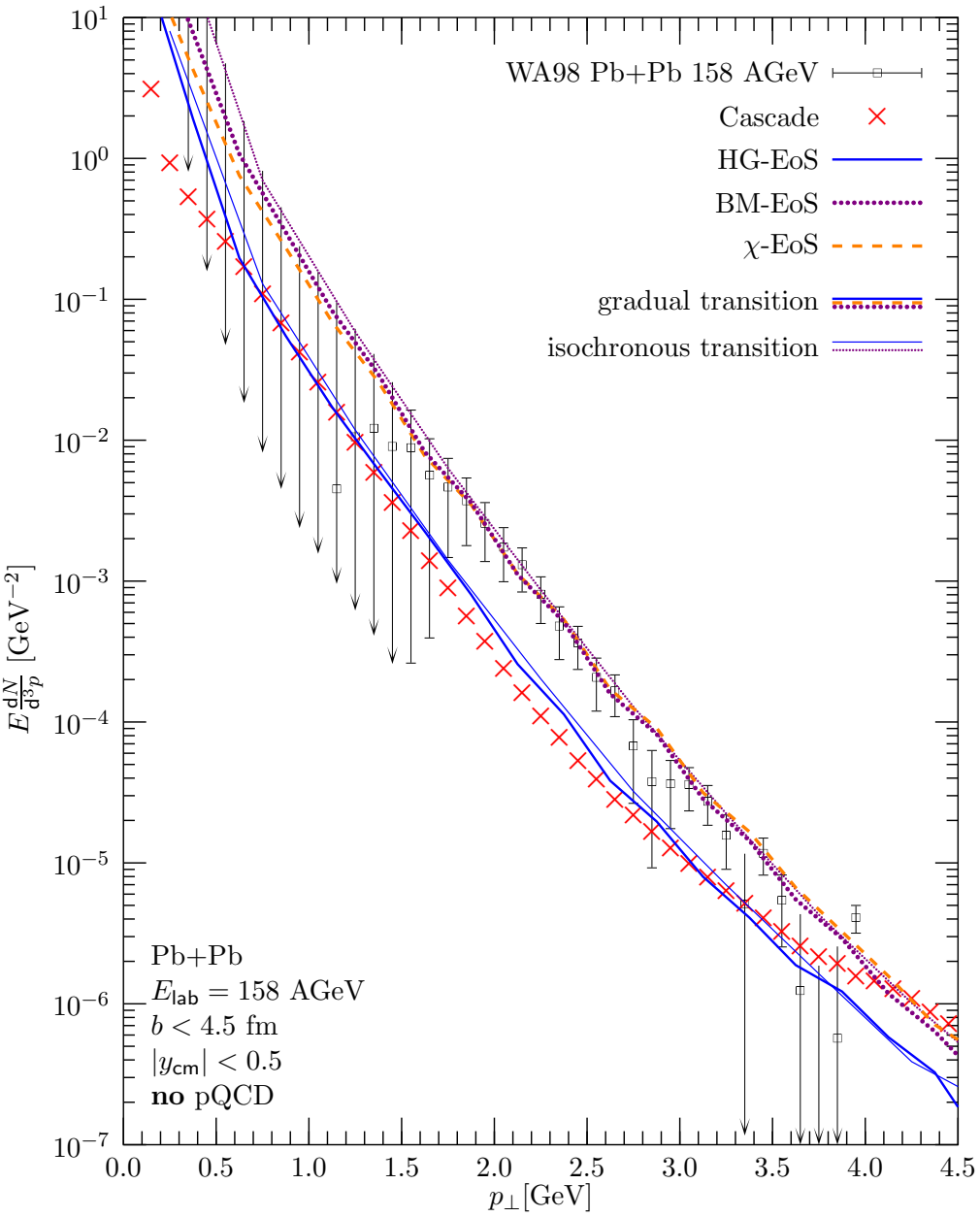

Figure 5.3: Comparison of the direct photon spectra from all variations of the model to the experimental data by the WA98-collaboration [WA98-00]. Calculations without intermediate hydrodynamic stage (pure cascade mode, crosses), hybrid calculations with HG-EoS (solid lines), χ-EoS (dashed line) and BM-EoS (dotted lines) are shown. HG-EoS- and BM-EoS-calculations are shown with gradual transition scenario (thick lines) and isochronous transition scenario (thin lines), χ-EoS calculations are only shown for the gradual scenario.

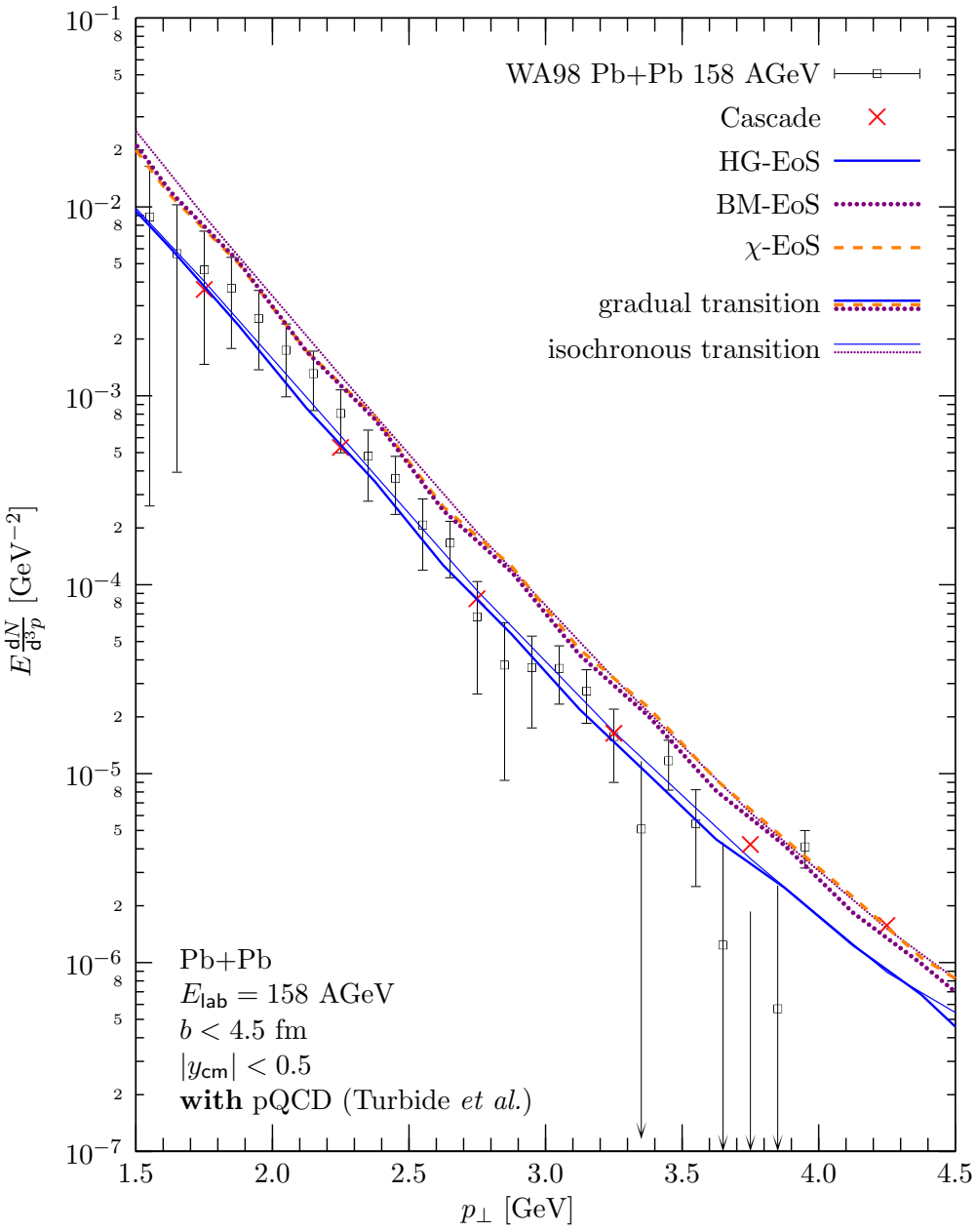

Figure 5.4: Comparison of the direct photon spectra from all variations of the model to the experimental data by the WA98-collaboration [WA98-00]. The calculations include prompt photon contribution as exctracted by Turbide *et al.* [Tur04]. Calculations without intermediate hydrodynamic stage (pure cascade mode, crosses), hybrid calculations with HG-EoS (solid lines), χ-EoS (dashed line) and BM-EoS (dotted lines) are shown. HG-EoS- and BM-EoS-calculations are shown with gradual transition scenario (thick lines) and isochronous transition scenario (thin lines), χ-EoS calculations are only shown for the gradual scenario.

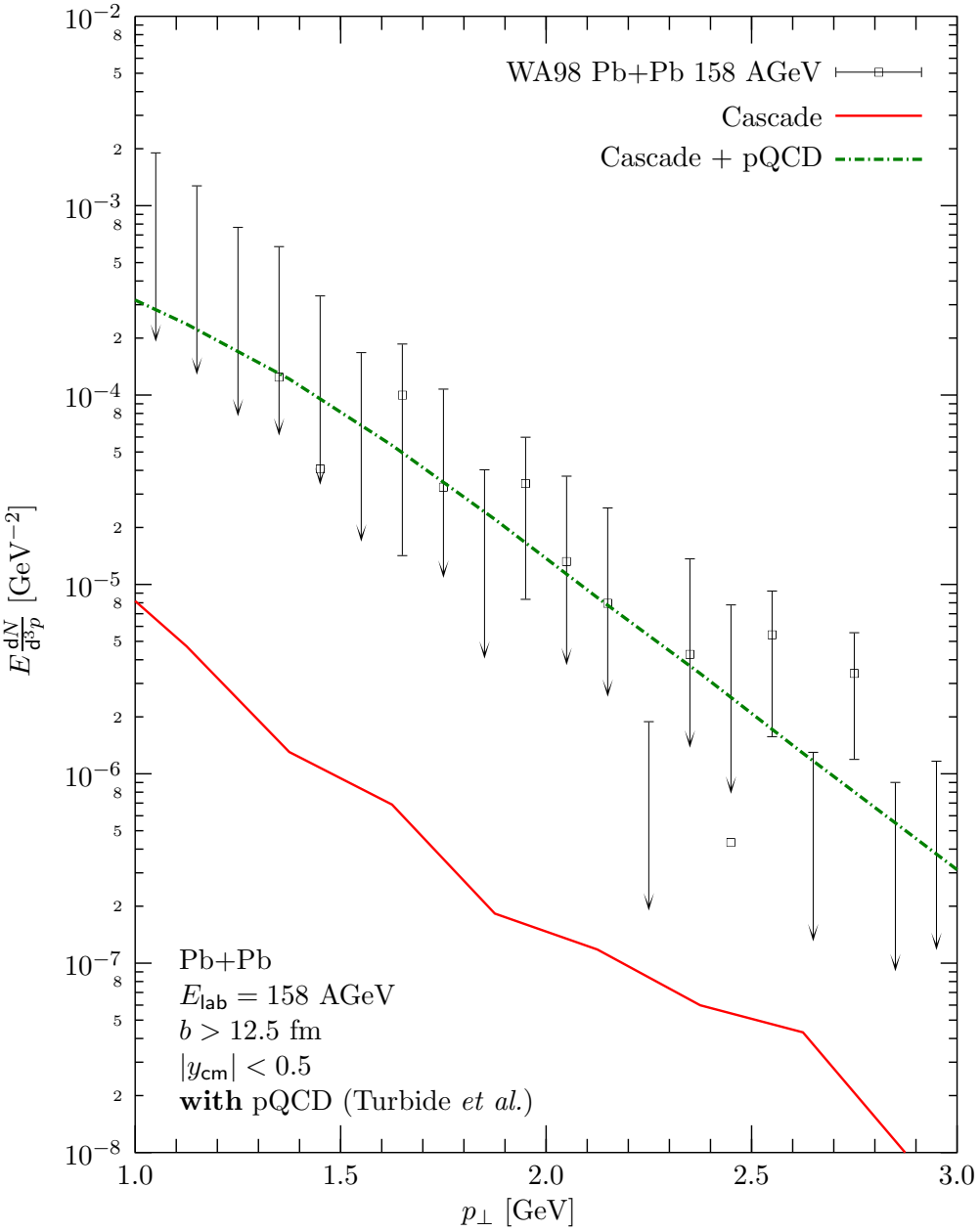

Figure 5.5: Comparison of the direct photon spectra from cascade calculations with (dotted line) and without (solid line) prompt photon contribution to experimental data by the WA98-collaboration [WA98-00] for peripheral ($b > 12.5$ fm) Pb+Pb-collisions at $E_{\mathsf{lab}} = 158$ AGeV. The prompt photon data are taken from Turbide *et al.* [Tur04] and scaled with $\langle N_{\mathsf{bin}} \rangle$.

Centrality	Au+Au			Cu+Cu	
	b_{min} [fm]	b_{max} [fm]	$\langle N_{\mathsf{bin}} \rangle$	b_{min} [fm]	b_{max} [fm]
00%-10%	0.0	4.1	955.4	0.0	2.8
10%-20%	4.1	6.2	602.6	2.8	4.4
20%-30%	6.2	7.8	373.8	4.4	5.5
30%-40%	7.8	9.1	219.8	5.5	6.4
40%-50%	9.1	10.2	120.3	6.4	7.3
50%-60%	10.2	11.2	61.0	7.3	8.0
60%-92%	11.2	14.1	8.4	—	—

Table 5.2: Centrality classes and their corresponding impact parameters and average number of binary collisions in PHENIX-data.

5.3 Photons at RHIC: PHENIX

At the Relativistic Heavy-Ion Collider (RHIC), the PHENIX experiment has measured direct photon spectra in gold-gold collisions at $\sqrt{s_{\mathsf{NN}}} = 200$ GeV [PHENIX05b, PHENIX10]. Other observables have been published for gold-gold and copper-copper collisions at this energy, at $\sqrt{s_{\mathsf{NN}}} = 62.4$ GeV, $\sqrt{s_{\mathsf{NN}}} = 130$ GeV and also at lower energies. In the following, direct photon calculations will be presented for the three mentioned energies and both systems at different centrality bins. The PHENIX-collaboration usually quotes centrality classes by the percentage of collisions that are more central (e.g., 0-10 % means all collisions for which less than 10 % of all collisions are more central). The corresponding impact parameters b and average number of binary collisions $\langle N_{\mathsf{bin}} \rangle$ have been obtained from [Büs10] and are quoted in Table 5.2. For simplicity, the divisions made at $\sqrt{s_{\mathsf{NN}}} = 200$ GeV are also used at the lower energies. In bins larger than what is quoted in that table, $\langle N_{\mathsf{bin}} \rangle$ is calculated as the average of the values for $\langle N_{\mathsf{bin}} \rangle$ in the sub-bins, weighted with the size of that bin.

The comparison between direct photon spectra at low and intermediate transverse momentum $p_\perp$ from cascade calculations and data from the PHENIX collaboration [PHENIX05b] for Au+Au-collisions at $\sqrt{s_{\mathsf{NN}}} = 200$ GeV is shown in Figure 5.6. One clearly observes that the hadronic transport model (full lines) does not saturate the upper limits of the experimental data. In all centrality bins, the prompt photon yield is significantly larger than predicted by the hadronic cascade. The ratio between pQCD and hadronic contributions is fairly constant among the centrality bins. For comparison, Figure 5.6 also shows the spectra obtained with the hybrid model using the Bag Model EoS (BM-EoS) for the two most central bins, 0-10% and 10-20%, which agree nicely with the data. Thermal fits to the low-$p_\perp$-parts of the cascade spectra show inverse slope parameters of $T_{\mathsf{slope}} \approx 235$ MeV throughout the centrality bins, see Table 5.3.

A more detailed exploration of the low-$p_\perp$-part of the direct photon calculation is shown in Figure 5.7. Here, the low-$p_\perp$-data obtained by extrapolating

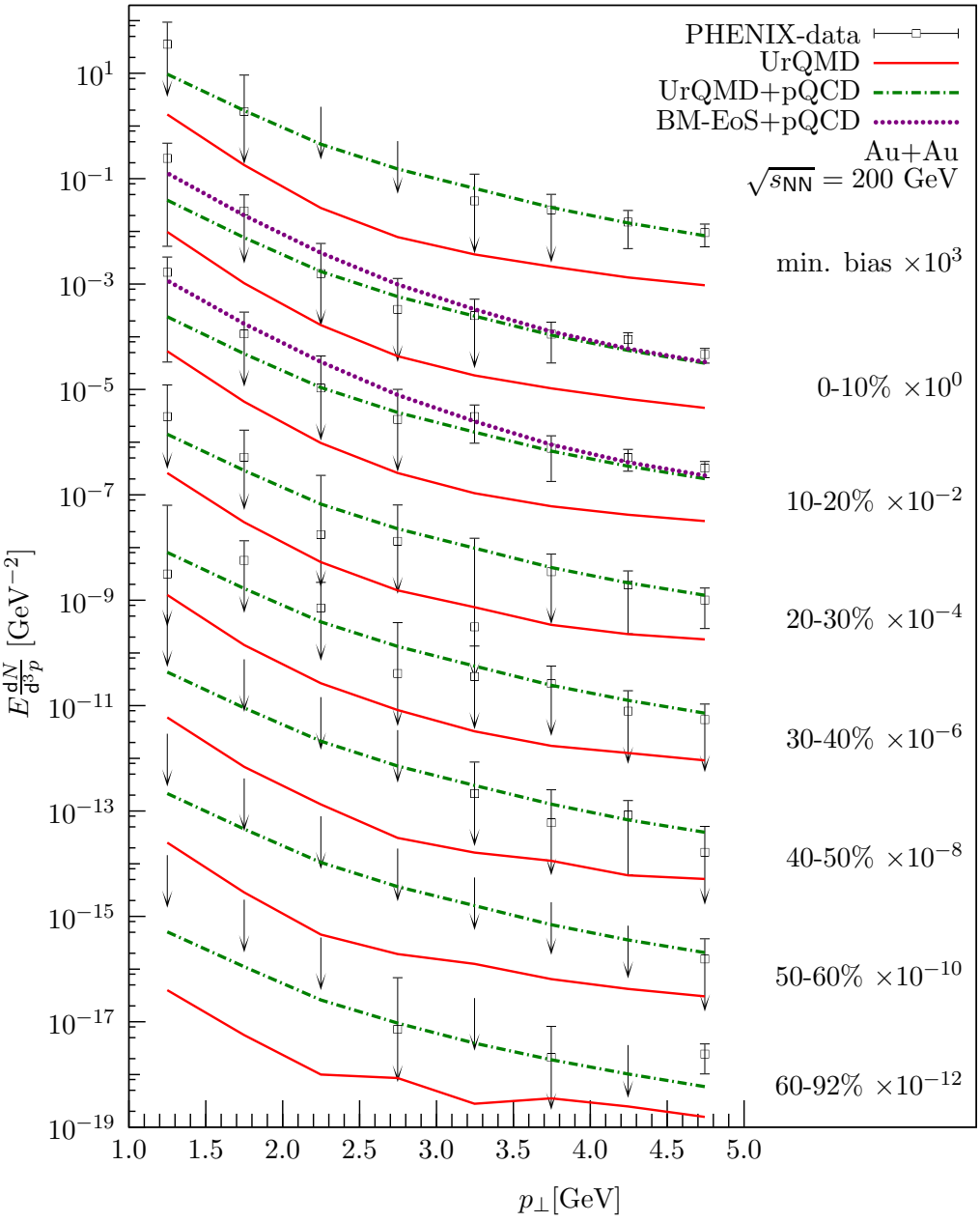

Figure 5.6: Comparison of the data from the PHENIX-collaboration [PHENIX05b] (squares) to cascade calculations (solid lines) for central to peripheral collisions. The dashed-dotted lines show the sum of pQCD-calculations [Gor93, PHENIX05b] and the cascade contribution. For the most central collisions, 00-10% and 10-20%, the spectra from hybrid calculations with the BM-EoS plus pQCD-contribution are shown (dotted lines).

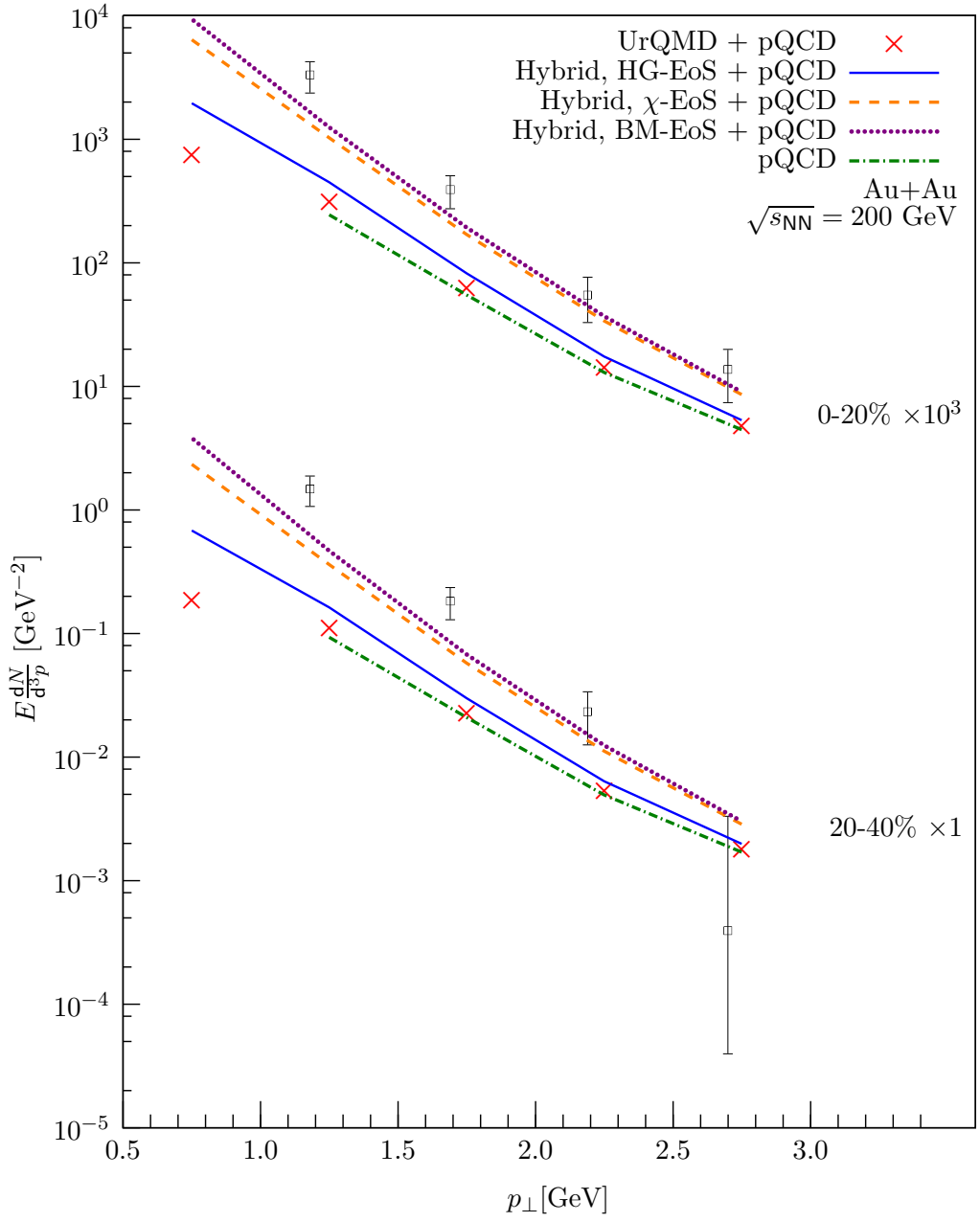

Figure 5.7: Comparison of data from the PHENIX-collaboration [PHENIX10] (squares) to cascade caculations (crosses) and hybrid model calculations with HG-EoS (solid lines), χ-EoS (dashed lines) and BM-EoS (dotted lines) for central (0-20 %) and mid-central (20-40 %) Au+Au-collisions at $\sqrt{s_{\mathrm{NN}}} = 200$ GeV. The contributions from initial pQCD-scatterings [Gor93, PHENIX10] (dash-dotted lines) have been added to all spectra. The spectra from central collisions have been scaled by a factor of 10^3 to enhance readability.

Centrality	T_{slope} [MeV]	A [GeV^{-2}]	χ^2/d.o.f.
00%-10%	231.9± 9.4	2.39±0.67	0.038
00%-92%	231.4± 8.5	0.41±0.11	0.032
10%-20%	234.0±10.0	1.26±0.37	0.041
20%-30%	239.0±11.4	0.56±0.18	0.049
30%-40%	239.0±13.1	0.27±0.10	0.065
40%-50%	243.0±13.4	0.12±0.04	0.064
50%-60%	235.4± 8.8	$(5.64\pm1.43)\cdot10^{-2}$	0.032
60%-92%	250.5±11.8	$(6.91\pm2.08)\cdot10^{-3}$	0.044

Table 5.3: Fit results for the low-$p_\perp$-part ($p_\perp < 2.5$ GeV) of the cascade calculations of Au+Au-collisions at $\sqrt{s_{\mathsf{NN}}} = 200$ GeV(see Figure 5.6). The fit function is $f(p_\perp) = A \exp\left(-\frac{p_\perp}{T_{\mathsf{slope}}}\right)$.

the dilepton yield to zero invariant mass [PHENIX10] for central (0-20%) and mid-central (20-40%) are shown in comparison to cascade calculations (crosses) and hybrid calculations with Hadron Gas EoS (HG-EoS, solid lines), Chiral EoS (χ-EoS, dashed lines) and Bag Model EoS (BM-EoS, dotted lines) and prompt (pQCD) photon calculations. All calculated spectra include the $\langle N_{\mathsf{bin}}\rangle$-scaled prompt photon contribution.

In both centrality bins, the direct photon spectra obtained with the BM-EoS and χ-EoS, which include a phase transition to a deconfined state of matter, are significantly higher than the hadronic HG-EoS-calculations and agree with the measured data.

A similar picture presents itself in Au+Au-collisions at lower initial collision energy $\sqrt{s_{\mathsf{NN}}} = 62.4$ GeV and $\sqrt{s_{\mathsf{NN}}} = 130$ GeV, shown in the upper panels of Figure 5.8. The cascade calulations have been omitted from the Figure for clarity.

Thermal fits to the spectra (see Table 5.4) show inverse slope parameters in the range from $233 < T_{\mathsf{slope}} < 262$ MeV, with the cascade calculations showing the smallest and the χ-EoS hybrid calculations showing the largest values of T_{slope}. HG-EoS and BM-EoS calculations show similar inverse slope parameters. The integrated yield A is highest in BM-EoS hybrid calculations. The spectra from the hybrid calculations are rather similar for the different beam energies.

Hybrid model calculations for central (0-20%) and mid-central (20-40%) Cu+Cu-collisions are shown in the lower panels of Figure 5.8 for all EoS. The thermal fits (see Table 5.5) again show no significant energy dependence of inverse slope parameter T_{slope} or yield A. We observe a clear ordering of the total yield between the Equations of State, with yield from the BM-EoS calculations being higher than that of the χ-EoS, and both yields exceeding that of HG-EoS calculations. However, the inverse slope parameters are similar in HG-EoS and χ-EoS calculations but significantly lower in BM-EoS calculations.

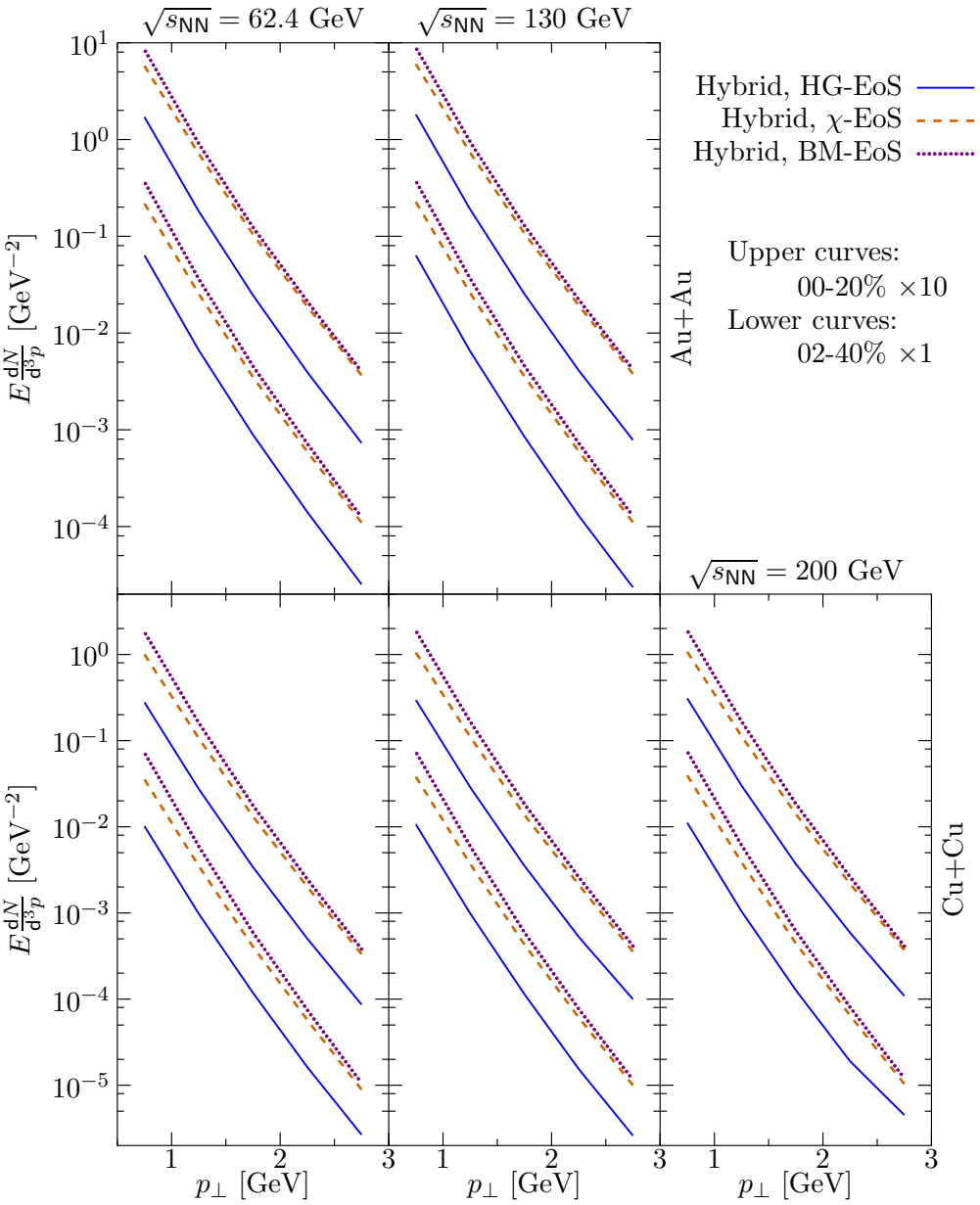

Figure 5.8: Direct photon spectra calculated with the hybrid model and HG-EoS (solid lines), χ-EoS (dashed lines) and BM-EoS (dotted lines) without prompt photon contribution. The panels show from left to right calculations for $\sqrt{s_{\mathrm{NN}}} =$ 62.4 GeV, $\sqrt{s_{\mathrm{NN}}} = 130$ GeV and $\sqrt{s_{\mathrm{NN}}} = 200$ GeV. The upper panels show calculations for Au+Au-collisions, while the lower panels show calculations for Cu+Cu-collisions. In each panel, the upper curves are central collisions (0-20%) and the lower curves are mid-central collisions (20-40%).

$\sqrt{s_{\mathsf{NN}}}$	EoS	centr.	T_{slope} [MeV]	A [GeV^{-2}]	$\frac{\chi^2}{\text{d.o.f.}}$
200	Transport	0-20%	232.5± 9.8	1.65±0.48	0.041
200	HG-EoS	0-20%	246.7± 8.6	3.63±0.83	0.025
200	χ-EoS	0-20%	261.9± 8.7	10.13±2.05	0.020
200	BM-EoS	0-20%	251.4± 9.7	16.37±4.03	0.029
200	Transport	20-40%	237.3±12.1	0.38±0.13	0.057
200	HG-EoS	20-40%	243.4± 8.3	1.32±0.30	0.025
200	χ-EoS	20-40%	253.0± 8.0	4.11±0.82	0.020
200	BM-EoS	20-40%	240.6± 9.0	7.61±1.90	0.030
130	Transport	0-20%	232.5± 9.1	$(9.87\pm2.67)^{*}$	0.035
130	HG-EoS	0-20%	246.3± 8.5	3.42±0.66	0.024
130	χ-EoS	0-20%	261.2± 8.5	9.67±1.93	0.019
130	BM-EoS	0-20%	250.2± 9.6	15.84±3.88	0.039
130	Transport	20-40%	257.2±11.3	$(5.48\pm1.50)^{+}$	0.036
130	HG-EoS	20-40%	242.4± 7.6	1.26±0.26	0.021
130	χ-EoS	20-40%	252.7± 7.9	4.01±0.80	0.019
130	BM-EoS	20-40%	240.6± 8.8	7.46±1.82	0.029
62.4	Transport	0-20%	242.1±13.5	$(5.29\pm1.95)^{*}$	0.066
62.4	HG-EoS	0-20%	247.3± 8.1	3.19±0.67	0.022
62.4	χ-EoS	0-20%	261.8± 8.2	9.24±1.78	0.018
62.4	BM-EoS	0-20%	250.3± 9.5	15.13±3.65	0.028
62.4	Transport	20-40%	232.8± 9.4	$(4.18\pm1.16)^{+}$	0.038
62.4	HG-EoS	20-40%	245.8± 8.0	1.21±0.26	0.022
62.4	χ-EoS	20-40%	253.9± 7.7	3.82±0.73	0.018
62.4	BM-EoS	20-40%	240.8± 8.6	7.33±1.74	0.028

*: $\times 10^{-2}$, $^{+}$: $\times 10^{-3}$

Table 5.4: Fit results for the low-$p_\perp$-part ($p_\perp < 2.5$ GeV) of the spectra from central (0-20%) and mid-central (20-40%) Au+Au-collisions. The fit function is $f(p_\perp) = A \exp\left(-\frac{p_\perp}{T_{\mathsf{slope}}}\right)$. The data are shown in Figure 5.7 (for $\sqrt{s_{\mathsf{NN}}} =$ 200 GeV) and Figure 5.8 ($\sqrt{s_{\mathsf{NN}}} =$ 62.4 GeV, upper left panel and $\sqrt{s_{\mathsf{NN}}} =$ 130 GeV, upper central panel).

$\sqrt{s_{\mathsf{NN}}}$	EoS	centr.	T_{slope} [MeV]	A [GeV^{-2}]	$\frac{\chi^2}{\mathsf{d.o.f.}}$
200	HG-EoS	0-20%	252.0± 9.6	(4.84±1.38)$^{\times}$	0.057
200	χ-EoS	0-20%	251.5± 7.3	1.77±0.39	0.033
200	BM-EoS	0-20%	237.7± 7.8	3.61±0.94	0.047
200	HG-EoS	20-40%	254.6±13.2	(1.61±0.62)$^{\times}$	0.103
200	χ-EoS	20-40%	242.9± 7.0	(7.25±1.63)$^{\times}$	0.036
200	BM-EoS	20-40%	229.2± 7.5	1.60±0.43	0.051
130	HG-EoS	0-20%	250.0± 9.3	(4.78±1.35)$^{\times}$	0.056
130	χ-EoS	0-20%	250.9± 7.1	1.76±0.37	0.031
130	BM-EoS	0-20%	238.1± 7.9	3.56±0.93	0.048
130	HG-EoS	20-40%	240.4± 7.7	(1.99±0.50)$^{\times}$	0.044
130	χ-EoS	20-40%	242.8± 7.1	(6.99±1.59)$^{\times}$	0.036
130	BM-EoS	20-40%	228.5± 7.7	1.58±0.44	0.054
62.4	HG-EoS	0-20%	248.2± 7.7	(4.71±1.11)$^{\times}$	0.039
62.4	χ-EoS	0-20%	250.2± 6.8	1.71±0.35	0.029
62.4	BM-EoS	0-20%	236.8± 7.4	3.52±0.88	0.044
62.4	HG-EoS	20-40%	242.8± 6.9	(1.87±0.41)$^{\times}$	0.034
62.4	χ-EoS	20-40%	241.7± 6.3	(6.71±1.37)$^{\times}$	0.029
62.4	BM-EoS	20-40%	227.0± 6.7	1.62±0.40	0.042

$^{\times}$: $\times 10^{-1}$

Table 5.5: Fit results for the low-$p_\perp$-part ($p_\perp < 2.5$ GeV) of the spectra from central (0-20%) and mid-central (20-40%) Cu+Cu-collisions. The fit function is $f(p_\perp) = A \exp\left(-\frac{p_\perp}{T_{\mathsf{slope}}}\right)$. The data are shown in Figure 5.8, lower panels.

5.4 Collective Patterns

If the bulk matter in heavy-ion reactions shows signs of collective behaviour, those should reflect in flow patterns of hadronic probes. Of special interest is the second coefficient of the fourier transformed azimuthal particle distribution v_2, the so-called elliptic flow coefficient

$$\frac{\mathsf{d}N}{\mathsf{d}\varphi} = \frac{1}{2\pi}\frac{\mathsf{d}N}{p_\perp \mathsf{d}p_\perp}\left(1 + 2\sum_{n=1}^{\infty} v_n \cos\left(n\varphi\right)\right) \quad , \tag{5.1}$$

$$v_2 = \left\langle \frac{p_x^2 - p_y^2}{p_x^2 + p_y^2} \right\rangle \quad . \tag{5.2}$$

v_2 of light hadronic particles is expected to be very large if the system behaves collectively. Elliptic flow of heavy probes (hadrons with charm or beauty) can give insight in the interaction between the bulk medium and those particles. They are produced only in early scatterings of incoming nucleons, much like prompt photons, and have a flat distribution in the azimuthal angle. If their interaction with the bulk is strong enough, they will approach kinetic equilibrium

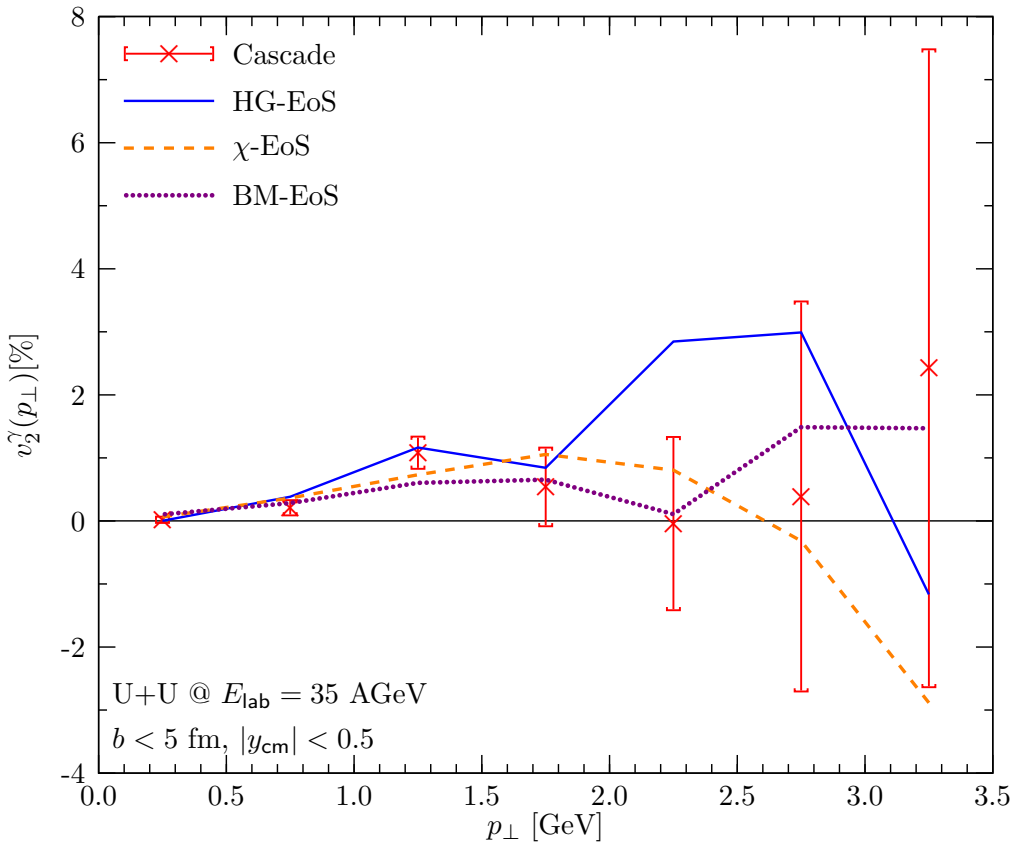

Figure 5.9: Elliptic flow parameter v_2 as a function of photon transverse momentum in U+U-collisions at $E_{lab} = 35$ AGeV for transport calculations (crosses) and hybrid model calculations with HG-EoS (solid line), χ-EoS (dashed line) and BM-EoS (dotted line). For visibility, the error bars have been omitted from the hybrid calculations and are only shown for the cascade calculation.

with the underlying medium and exhibit the same flow pattern as the lighter particles.

In the case of photons, the scattering rate between the photons and the medium is negligible, so that the elliptic flow of photons is frozen at the time the photons are created. As discussed above, the elliptic flow coefficient of prompt photons is zero $v_2^{prompt} = 0$, but elliptic flow of photons from thermal interactions may show a resemblance of the flow pattern of the underlying medium. The azimuthal distributions from inclusive direct photon measurements, which are dominated by decay photons from π^0- and η-mesons, show the same behaviour as these particles.

We will investigate the elliptic flow pattern of direct thermal photons in the hybrid- and pure cascade calculations. The elliptic flow of hadronic probes has been investigated with the same model in [Pet09c].

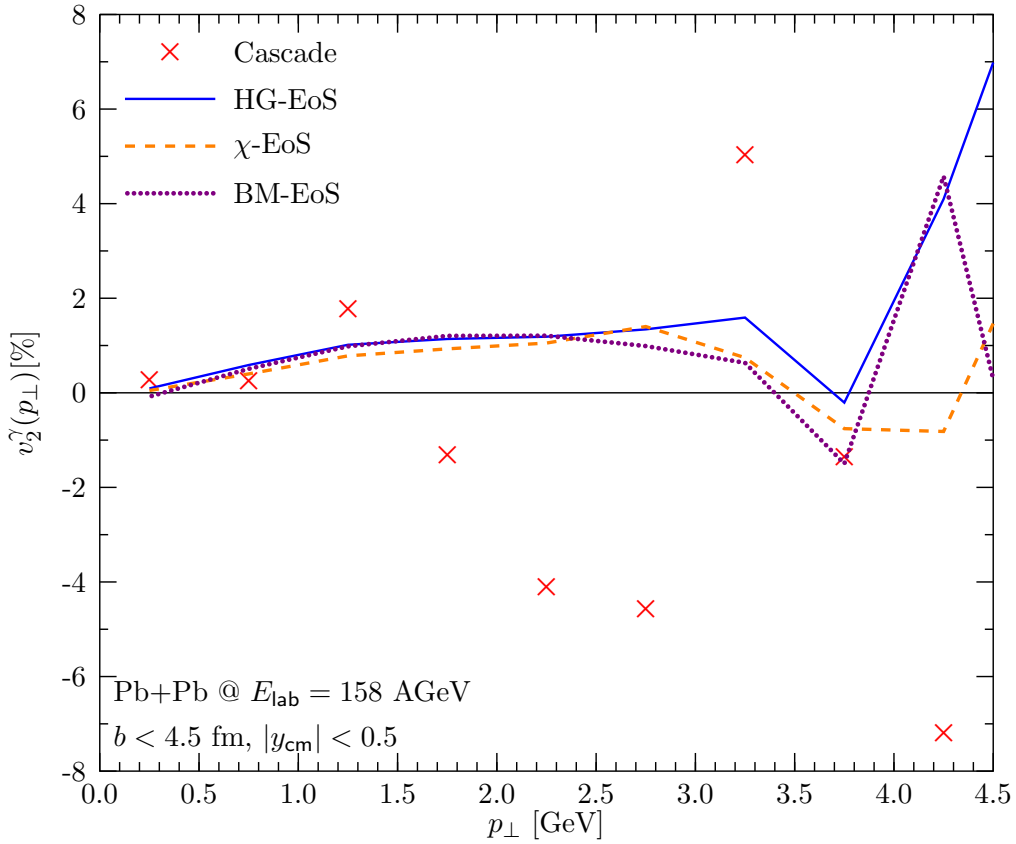

Figure 5.10: Elliptic flow parameter v_2 as a function of photon transverse momentum in Pb+Pb-collisions at E_{lab} = 158 AGeV for transport calculations (crosses) and hybrid model calculations with HG-EoS (solid line), χ-EoS (dashed line) and BM-EoS (dotted line).

From the azimuthal distribution of emitted direct photons the elliptic flow parameter v_2 has been calculated as a function of direct photon transverse momentum $p_\perp$ at $E_{lab} = 35$ AGeV (see Figure 5.9) for all hybrid calculations with all Equations of State and for pure cascade calculations. All calculations agree very well and show small positive values at small $p_\perp$, which are compatible with $v_2 = 0$, i.e. the direct photon emission is azimuthally isotropic. This is consistent with the observations that the boost of the collisions that produce photons do not significantly influence the photon spectra (see Section 7.2). For better visibility in the Figure, the error bars are only shown for the cascade calculation; the error bars of the hybrid calculations have similar magnitudes. This might allow to disentangle hadronic contributions to the photons from the direct photons.

For Pb+Pb-collisions at $E_{lab} = 158$ AGeV, see Figure 5.10, the picture is very similar. Although v_2 is still compatible with zero, all hybrid calculations yield a positive value at intermediate transverse momentum $1 < p_\perp < 3$ GeV. The

elliptic flow from transport calculations fluctuates strongly, so that no conclusive picture can be drawn. Error estimates for the data in Figure 5.10 are not shown; the errors are in the same order as the errors in the calculations for $E_{\mathsf{lab}} = 35$ AGeV (see Figure 5.9).

At RHIC-energies ($\sqrt{s_{\mathsf{NN}}} = 62.4$ GeV, see Figure 5.11, $\sqrt{s_{\mathsf{NN}}} = 130$ GeV, see Figure 5.12, and $\sqrt{s_{\mathsf{NN}}} = 200$ GeV, see Figure 5.12), the elliptic flow coefficient has been calculated for gold-gold collisions and copper-copper collisions in the 20 % most central collisions and in mid-central collisions (20-40 % most central). At intermediate $p_\perp$, v_2 turns significantly positive in most systems. In calculations of Au+Au-collisions with χ-EoS, the absolute value of v_2 at small and intermediate $p_\perp$ is smaller than that of calculations with HG-EoS and BM-EoS. In Cu+Cu-collisions, the elliptic flow of photons is less pronounced and on the order of $v_2^\gamma \approx 1$ %. At high transverse momentum, the elliptic flow approaches zero again, and the error bars and fluctuations become very large. The fluctuation is larger in the small system of Cu+Cu collisions and in mid-central collisions. The cascade calculations follow a similar trend, giving positive values at low $p_\perp$, but they return to values compatible with zero at lower transverse momenta than the hybrid model calculations do.

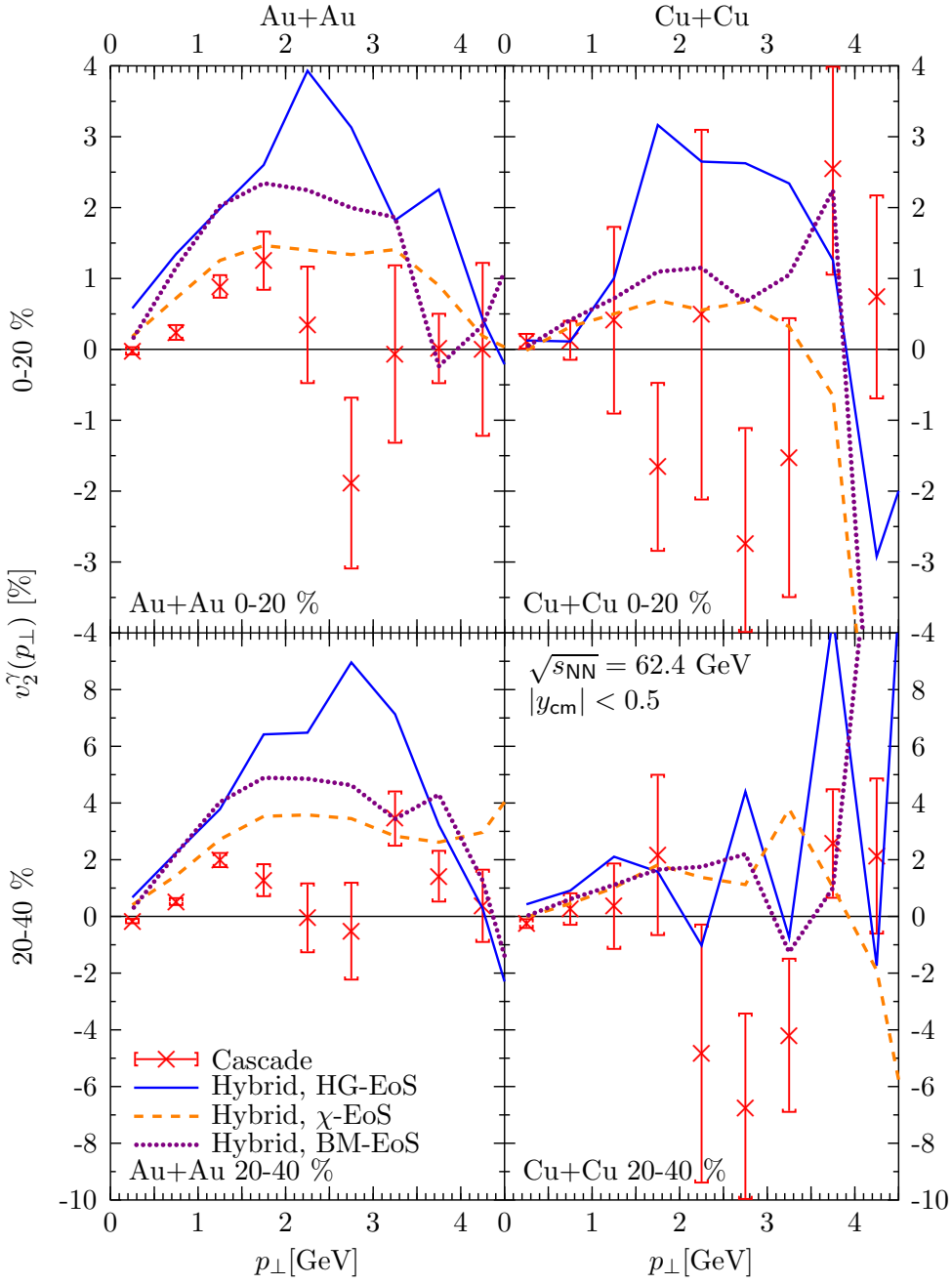

Figure 5.11: Elliptic flow parameter v_2 as a function of photon transverse momentum in central (0-20 %, upper panels) and mid-central (20-40 %, lower panels) Au+Au-collisions (left panels) and Cu+Cu-collisions (right panels) at $\sqrt{s_{NN}}$ = 62.4 GeV for hybrid model calculations with HG-EoS (solid line), χ-EoS (dashed line) and BM-EoS (dotted line).

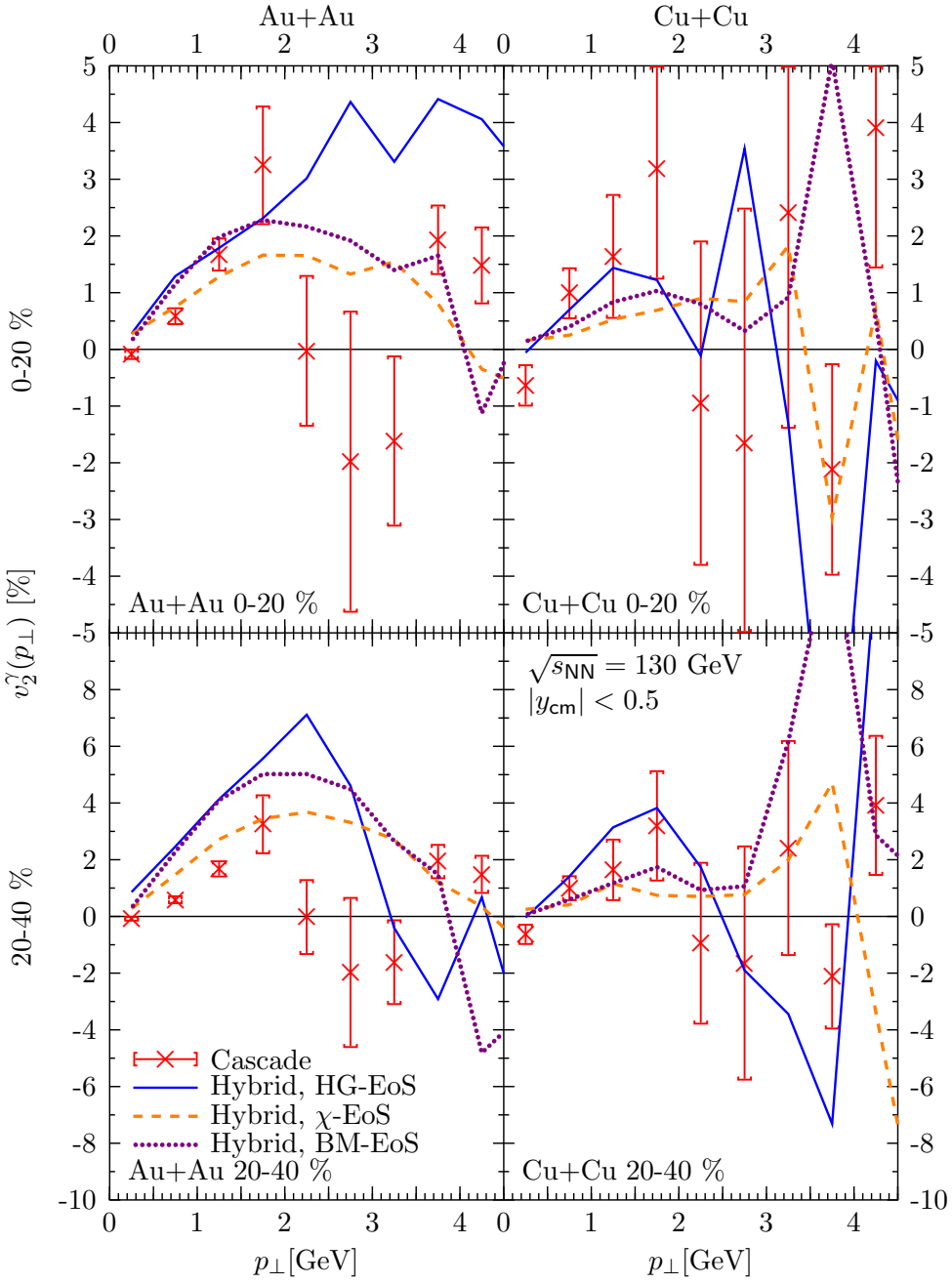

Figure 5.12: Elliptic flow parameter v_2 as a function of photon transverse momentum in central (0-20 %, upper panels) and mid-central (20-40 %, lower panels) Au+Au-collisions (left panels) and Cu+Cu-collisions (right panels) at $\sqrt{s_{NN}} = 130$ GeV for hybrid model calculations with HG-EoS (solid line), χ-EoS (dashed line) and BM-EoS (dotted line).

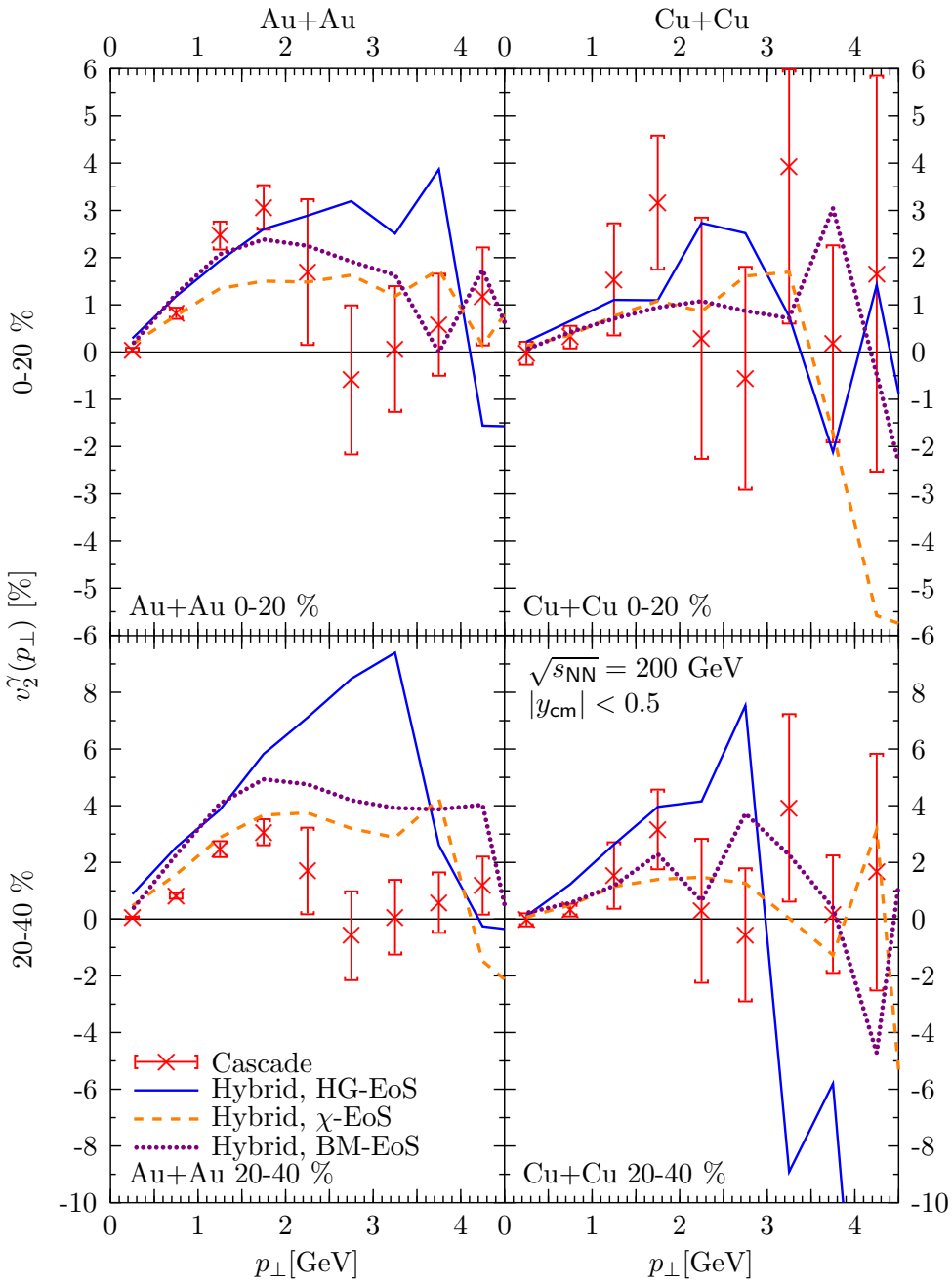

Figure 5.13: Elliptic flow parameter v_2 as a function of photon transverse momentum in central (0-20 %, upper panels) and mid-central (20-40 %, lower panels) Au+Au-collisions (left panels) and Cu+Cu-collisions (right panels) at $\sqrt{s_{\mathsf{NN}}} = 200$ GeV for transport calculations (crosses) and hybrid model calculations with HG-EoS (solid line), χ-EoS (dashed line) and BM-EoS (dotted line).

Chapter 6

Channel decomposition

6.1 Hadronic channels

Let us now look at the channel decomposition of the direct photon spectra. The relative contributions of the hadronic channels is similar in all calculations. Figure 6.1 shows the spectrum obtained with transport calculations from lead-lead collisions at $E_{\mathsf{lab}} = 158$ AGeV. At intermediate $p_\perp (0.5 < p_\perp < 3$ GeV), the process $\pi\rho \to \gamma\pi$ dominates the spectrum of direct photons, while at low $p_\perp < 0.5$ GeV, the process $\pi\pi \to \gamma\rho$ is more pronounced. This behaviour is already clear from the thermal rates, compare Figures 3.14 and 4.1.

At high $p_\perp$, however, where collisions at high center-of-mass energy $\sqrt{s_{\mathsf{coll}}}$ dominate, all channels contribute to the final spectra in similar amounts.

Figure 6.2 shows the relative contributions of the hadronic channels to hybrid model calculations with HG-EoS at top FAIR-, top SPS- and top RHIC-energies (U+U at $E_{\mathsf{lab}} = 35$ AGeV, Pb+Pb at $E_{\mathsf{lab}} = 158$ AGeV and Au+Au at $\sqrt{s_{\mathsf{NN}}} = 200$ GeV, respectively). Channels that differ only by the charges of the particles have been combined, as well as all particles with two π in the initial state (i.e., $\pi\pi \to \gamma\rho$, $\pi\pi \to \gamma\eta$ and $\pi\pi \to \gamma\gamma$), which have been combined to $\pi\pi \to \gamma X$ (dotted line). Furthermore, particles with a strange meson and an initial resonance, i.e. $K\rho \to \gamma K$, $K^*\pi \to \gamma K$, $K^*K \to \gamma\pi$ have been combined to K-resonance (short-dashed line).

The picture at low $p_\perp$is very consistent throughout the calculations and the same as described above. However, at high $p_\perp$, a clear dependence on the beam energy is visible. The calculation with low beam energy $E_{\mathsf{lab}} = 35$ AGeV does not show a decrease of the relative $\pi\rho$-contribution. At these low beam energies, the large contributions of $\pi\pi$- and $\pi\eta$-collisions from high-$\sqrt{s_{\mathsf{coll}}}$-collisions (see above), are very much suppressed and therefore do not contribute much to the direct photon spectrum, so that the $\pi\rho$-contribution remains the dominating channel.

For reference, the relative contributions of the hadronic channels to the hadronic cocktail in calculations with χ-EoS and BM-EoS have been shown

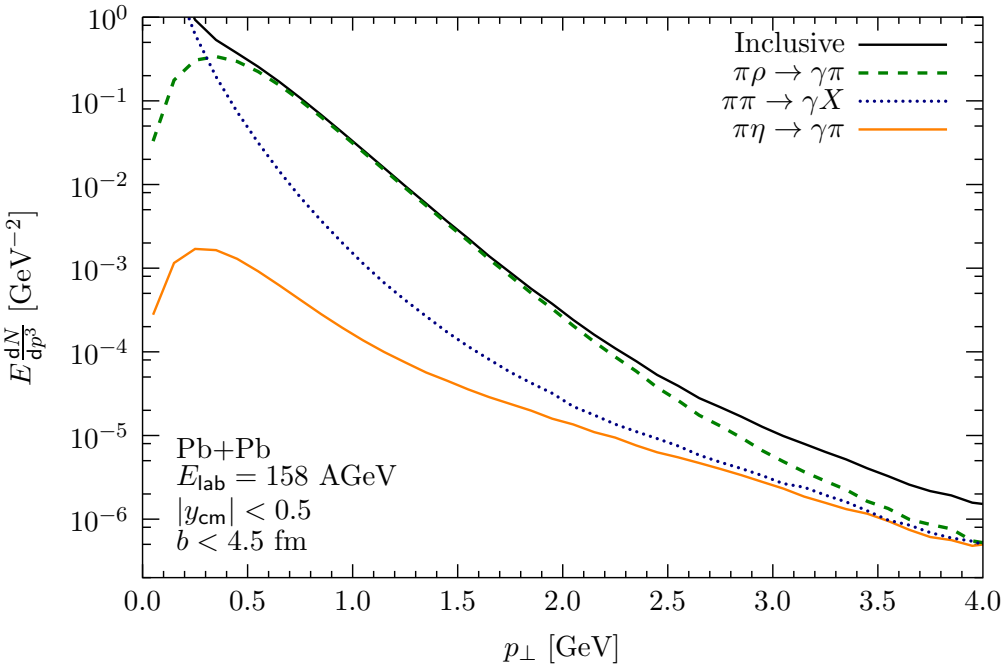

Figure 6.1: Contributions of the different channels $\pi\rho \to \gamma\pi$ (dashed line), $\pi\pi \to \gamma X$ (dotted line) and $\pi\eta \to \gamma\pi$ (light solid line) to the overall spectrum (dark solid line) for transport calculations of Pb+Pb-collisions at $E_{\mathsf{lab}} = 158$ AGeV.

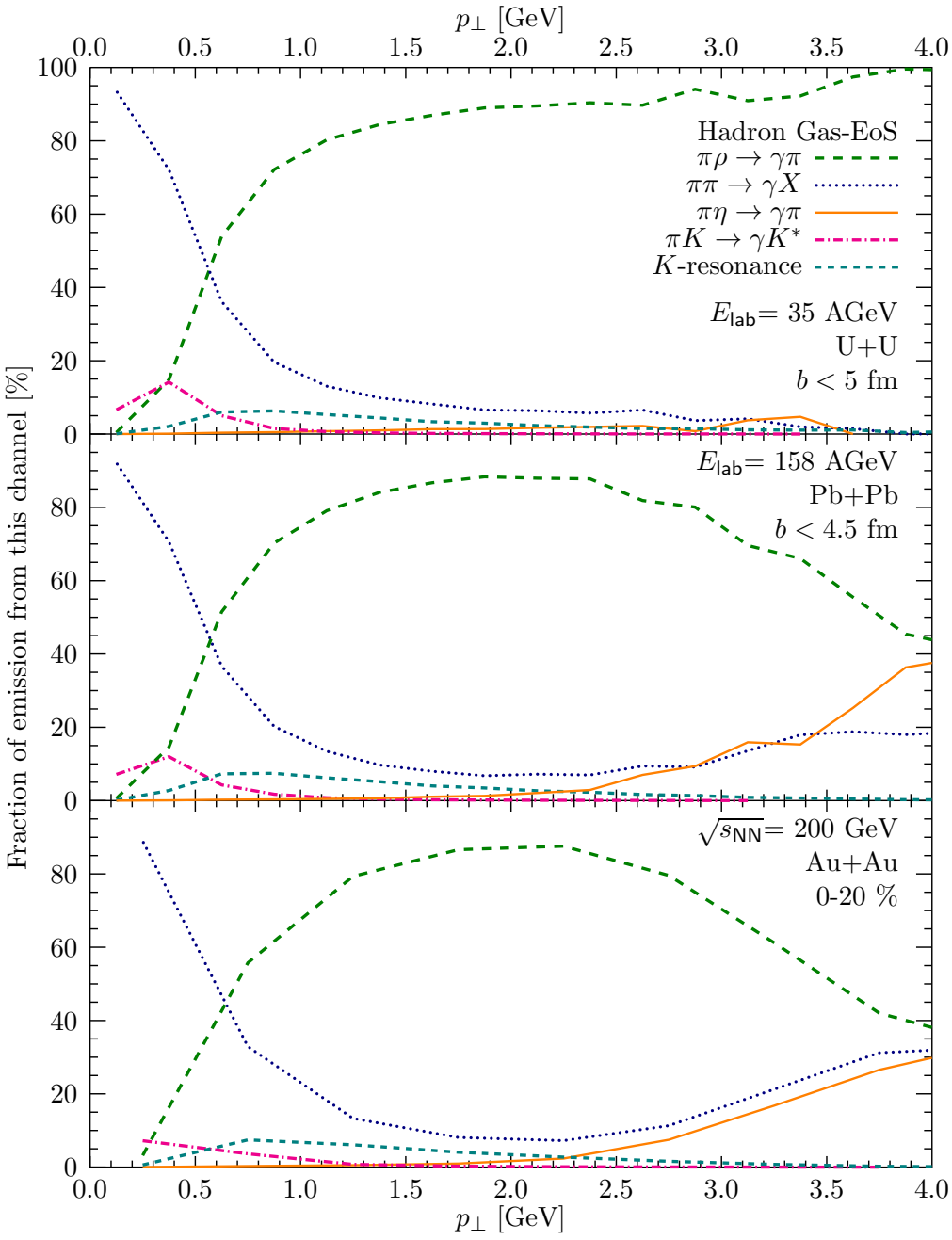

Figure 6.2: Relative contributions of the hadronic channels to the yield in hybrid calculations with HG-EoS in U+U-collisions at $E_{\mathsf{lab}} = 35$ AGeV (upper panel), Pb+Pb-collisions at $E_{\mathsf{lab}} = 158$ AGeV (middle panel) and Au+Au-collisions at $\sqrt{s_{\mathsf{NN}}} = 200$ GeV (lower panel). Both the contribution from the hydro phase and the transport phase are included. All channels have been summed over all charge combinations. Channel $\pi\pi \to \gamma X$ (dotted line) includes $X = \rho$, $X = \eta$ and $X = \gamma$, K-resonance includes all channels with a strange particle and a resonance in the initial state, i.e. $K\rho$-, $K^*\pi$- and K^*K-collisions.

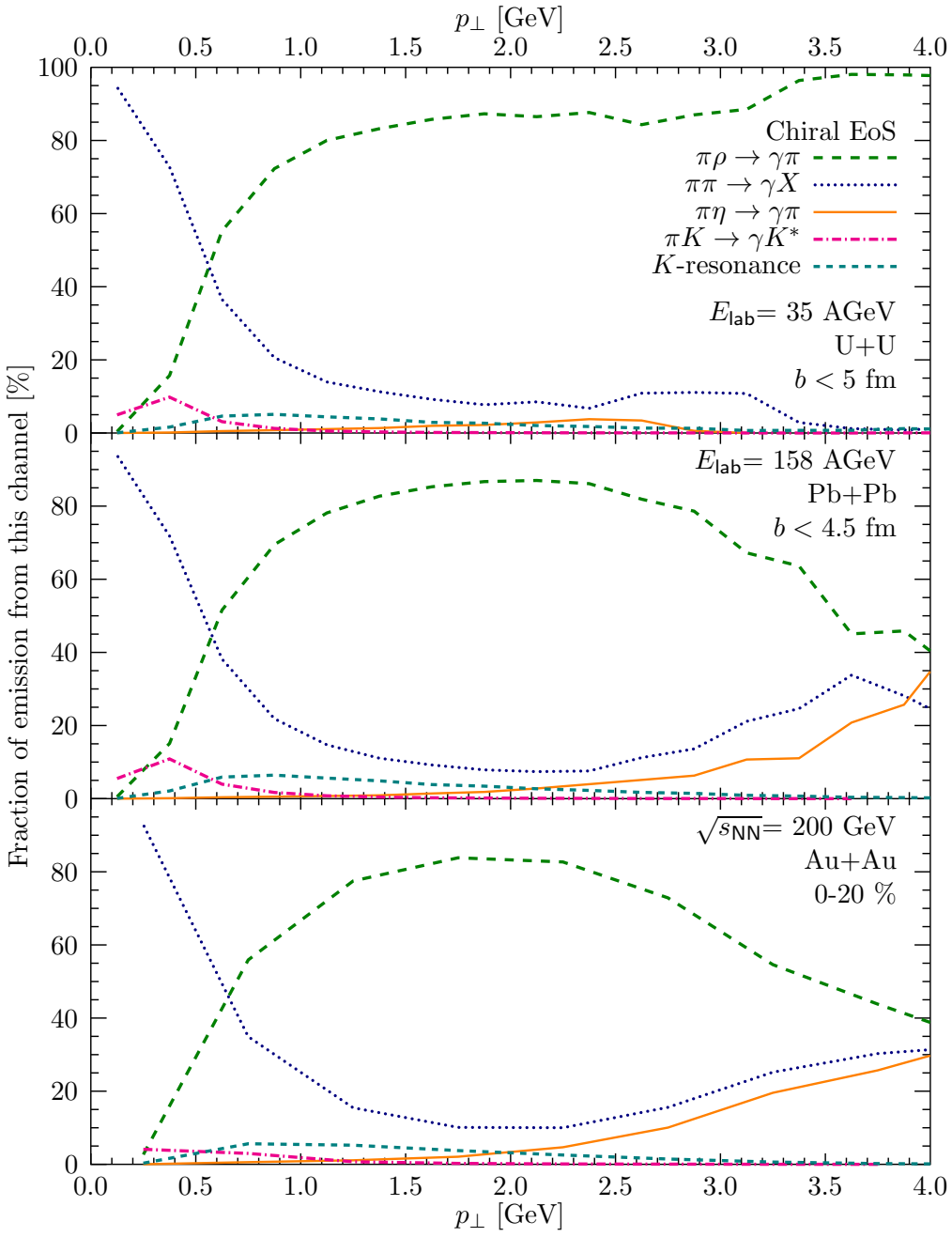

Figure 6.3: Relative contributions of the hadronic channels to the yield in hybrid calculations with χ-EoS in U+U-collisions at $E_{\mathsf{lab}} = 35$ AGeV (upper panel), Pb+Pb-collisions at $E_{\mathsf{lab}} = 158$ AGeV (middle panel) and Au+Au-collisions at $\sqrt{s_{\mathsf{NN}}} = 200$ GeV (lower panel). Both the contribution from the hydro phase and the transport phase are included. All channels have been summed over all charge combinations. Channel $\pi\pi \to \gamma X$ (dotted line) includes $X = \rho$, $X = \eta$ and $X = \gamma$, K-resonance includes all channels with a strange particle and a resonance in the initial state, i.e. $K\rho$-, $K^*\pi$- and K^*K-collisions.

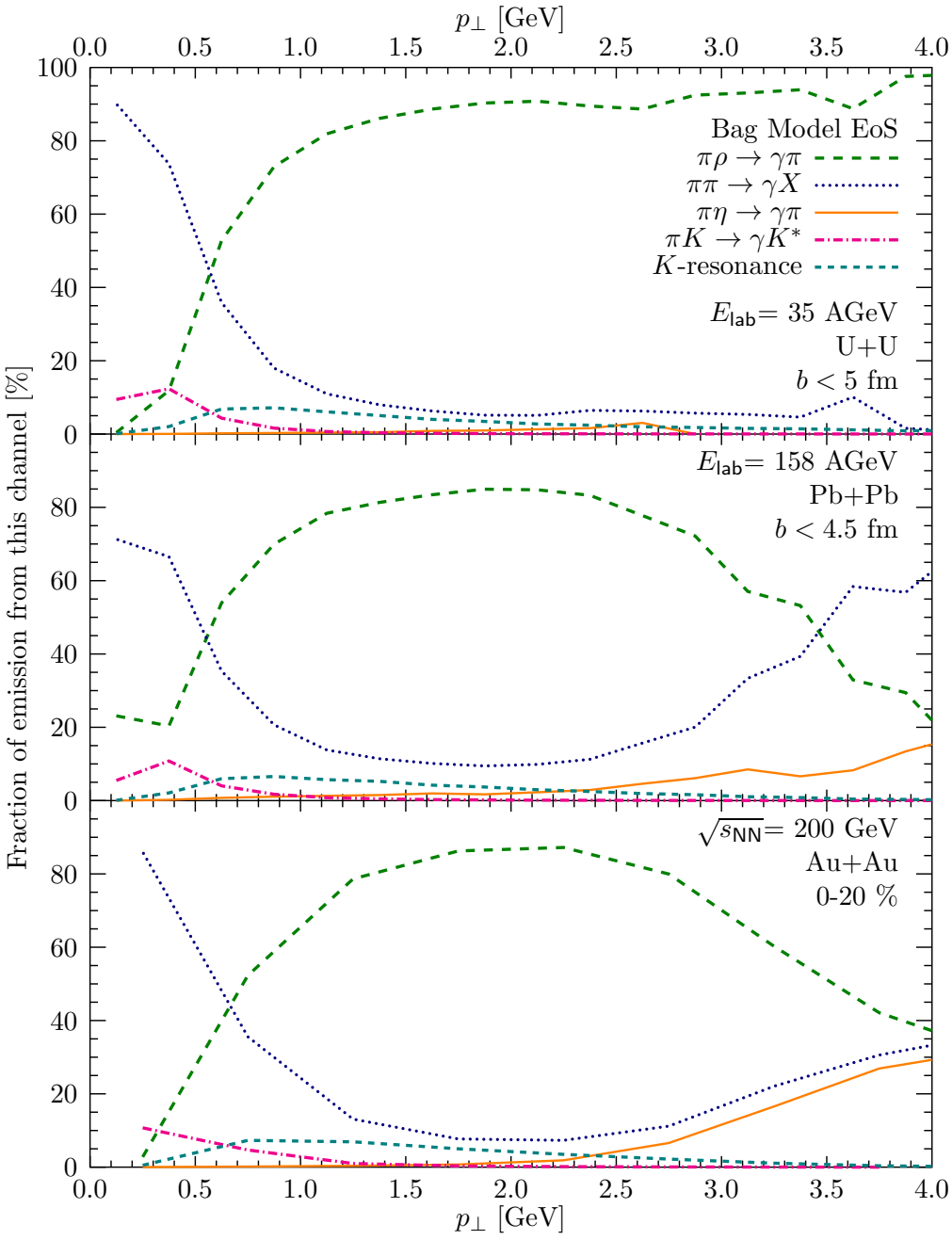

Figure 6.4: Relative contributions of the hadronic channels to the yield in hybrid calculations with BM-EoS in U+U-collisions at $E_{\mathsf{lab}} = 35$ AGeV (upper panel), Pb+Pb-collisions at $E_{\mathsf{lab}} = 158$ AGeV (middle panel) and Au+Au-collisions at $\sqrt{s_{\mathsf{NN}}} = 200$ GeV (lower panel). Both the contribution from the hydro phase and the transport phase are included. All channels have been summed over all charge combinations. Channel $\pi\pi \to \gamma X$ (dotted line) includes $X = \rho$, $X = \eta$ and $X = \gamma$, K-resonance includes all channels with a strange particle and a resonance in the initial state, i.e. $K\rho$-, $K^*\pi$- and K^*K-collisions.

in Figures 6.3 and 6.4, respectively.

With the exception of $\pi\eta$-collisions at high $p_\perp$, the combined relative contributions of the channels that are not common to both transport model and hydrodynamics are consistently below 10 %.

6.2 Partonic contribution

Investigating the relative contribution of the Quark-Gluon-Plasma photon emission can, naturally, only be done in calculations with BM-EoS or χ-EoS. In the following, we compare the relative contributions of prompt photon emission (not present at $E_{\mathsf{lab}} = 35$ AGeV), hadronic channels and Quark-Gluon-Plasma emission to the direct photon spectra.

Figure 6.5 shows the relative contributions of those channels for hybrid calculations with χ-EoS. At $E_{\mathsf{lab}} = 35$ AGeV, the hadronic contribution is about 15 % for $p_\perp = 0.5$ GeV and remains at this level even at high tranverse momenta. At higher beam energies $E_{\mathsf{lab}} = 158$ AGeV and $\sqrt{s_{\mathsf{NN}}} = 200$ GeV, the hadronic contribution drops to approximately 10 %, but rises at high $p_\perp$, coinciding with the increase of the $\pi\eta$- and $\pi\pi$-contribution in this momentum region (compare Figure 6.3). The fraction of prompt photons is constant at 30 % in the calculations at $E_{\mathsf{lab}} = 158$ AGeV for $p_\perp > 1.5$ AGeV, while it increases constantly in calculations at $\sqrt{s_{\mathsf{NN}}} = 200$ GeV where it dominates the spectra above transverse momenta of $p_\perp = 3.5$ GeV.

In calculations with BM-EoS, the picture is somewhat different (see Figure 6.6). At $E_{\mathsf{lab}} = 35$ AGeV, the QGP-contribution only amounts to about 55-75 % of the overall contribution, significantly less than in the χ-EoS calculations. Also at higher energies, the relative QGP-contribution is smaller than in calculations with χ-EoS, especially at intermediate transverse momenta $0.5 < p_\perp < 1.5$ GeV. In all cases, the decrease of the QGP-contribution is compensated by the increase of the hadronic contribution, so that the relative contribution of the prompt photons remains constant.

The large QGP contribution in calculations with the Chiral Equation of State can be understood if one considers the phase structures of both χ EoS and BM-EoS (see Figure 3.4 and 3.6). While the strong first order phase transition between a hadron gas and the quark-gluon plasma in the BM-EoS prolongs the lifetime of the hydrodynamic calculation, parts of the system that have frozen out and are already in the hadronic phase have no emission from a QGP phase. In the χ-EoS calculations, on the other hand, partonic emission from colder matter is still possible, so that cells that have cooled down below the phase transition but are not yet transferred to the transport calculation still contribute to the partonic part of the direct photon spectrum.

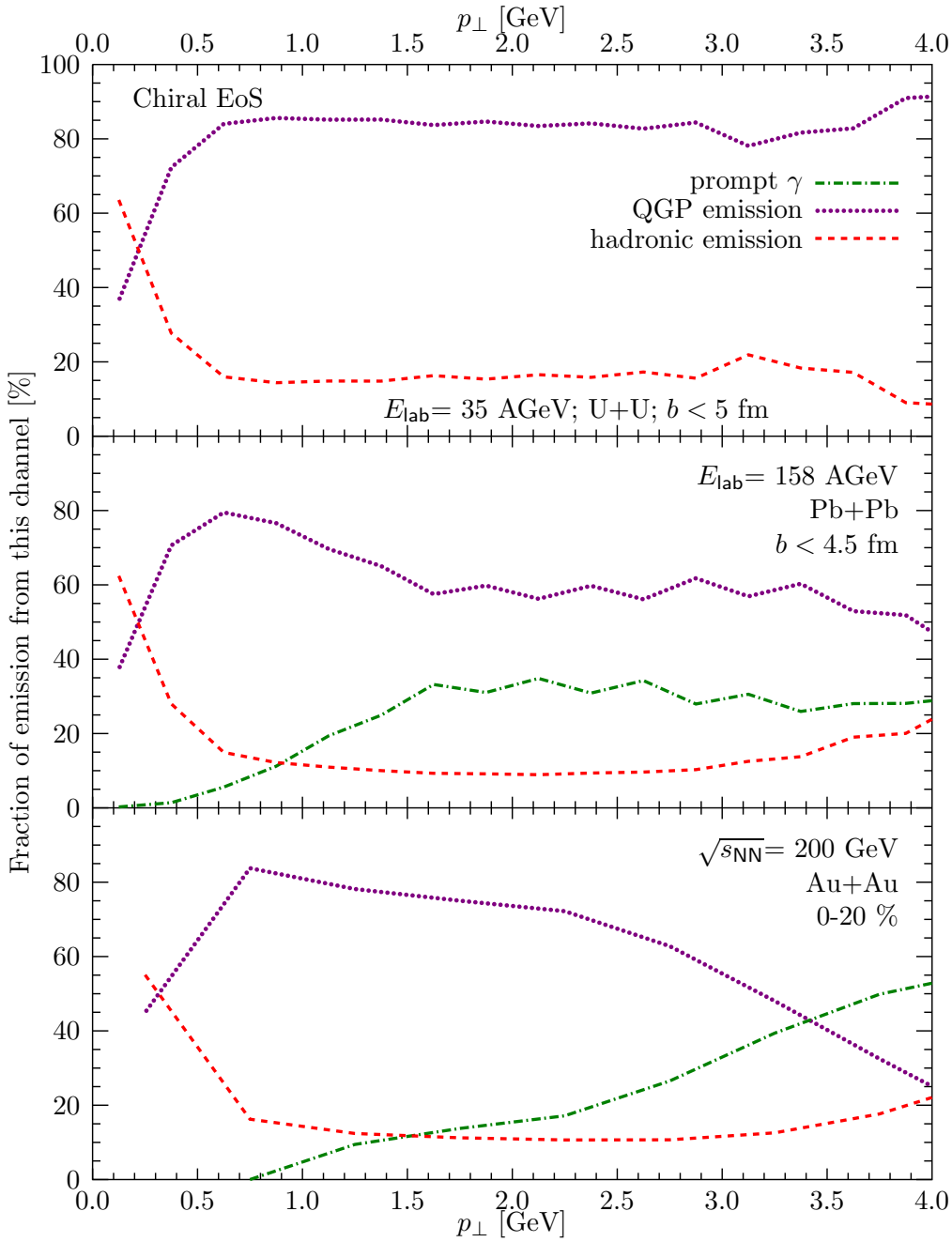

Figure 6.5: Relative contribution of QGP emission (dotted lines), hadronic emission (dashed line) and pQCD prompt photon emission (dash-dotted line) to the overall direct photon spectrum from hybrid calculations with χ-EoS. Top: U+U-collisions at $E_{\mathsf{lab}} = 35$ AGeV (prompt photon contribution negligible), $b < 5$ fm. Middle: Pb+Pb-collisions at $E_{\mathsf{lab}} = 158$ AGeV, $b < 4.5$ fm. Bottom: Au+Au-collisions at $\sqrt{s_{\mathsf{NN}}} = 200$ GeV, 0-20 % most central collisions.

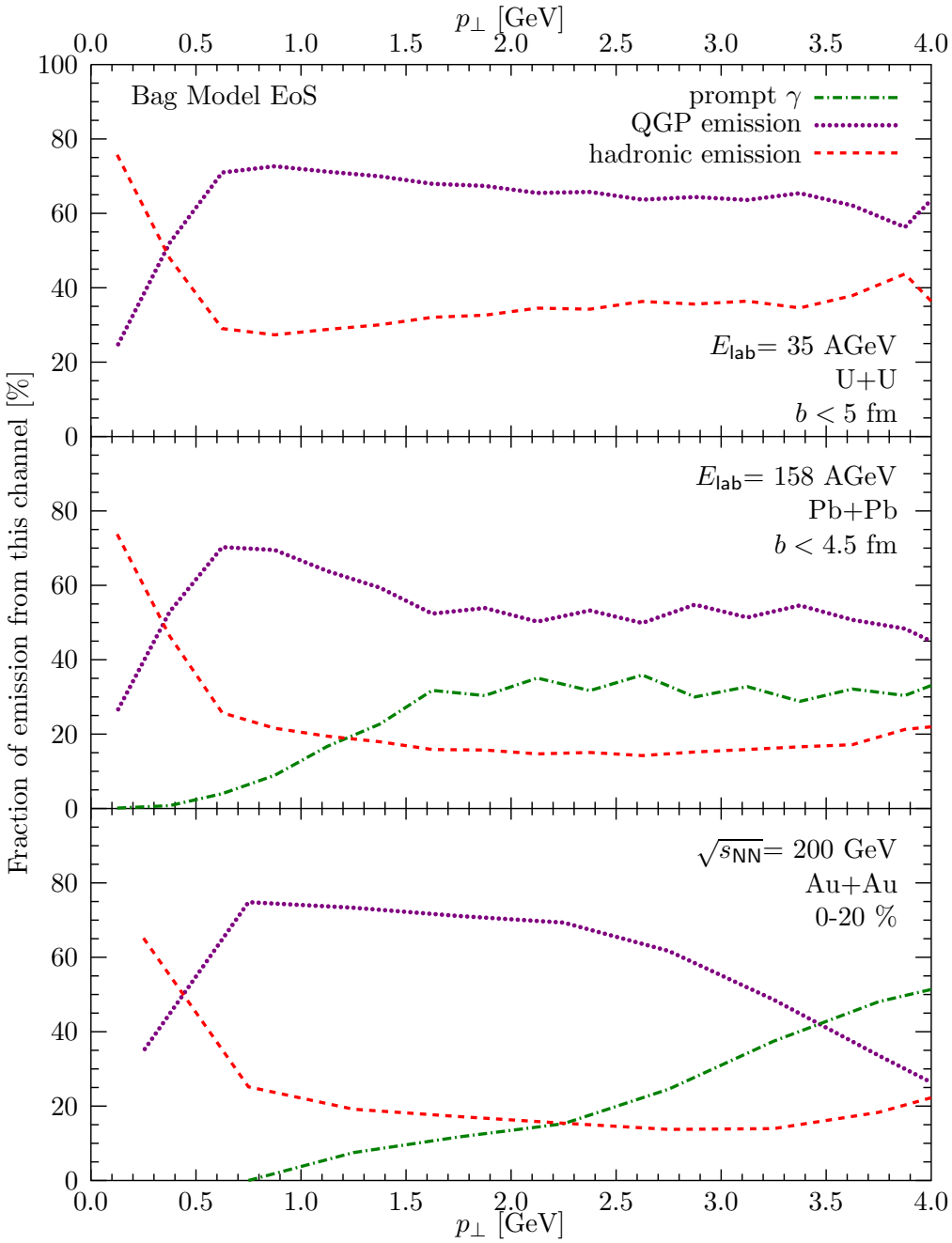

Figure 6.6: Relative contribution of QGP emission (dotted lines), hadronic emission (dashed line) and pQCD prompt photon emission (dash-dotted line) to the overall direct photon spectrum from hybrid calculations with BM-EoS. Top: U+U-collisions at $E_{\mathsf{lab}} = 35$ AGeV (prompt photon contribution negligible), $b < 5$ fm. Middle: Pb+Pb-collisions at $E_{\mathsf{lab}} = 158$ AGeV, $b < 4.5$ fm. Bottom: Au+Au-collisions at $\sqrt{s_{\mathsf{NN}}} = 200$ GeV, 0-20 % most central collisions.

Chapter 7

Time emission patterns

7.1 Emission stages

In the following Chapter, we will investigate the contribution of the three stages inherent in the model to the overall direct photon spectra: the early stage, which includes hadronic interaction, string dynamics and hard pQCD-scatterings before the system is transferred to the intermediate stage, the intermediate stage, and the late stage. In the hybrid calculations, all the intermediate stages contain only matter described by hydrodynamics. Matter that has been transferred to the transport calculation through the gradual transition scenario and matter that has not been transferred to the hydrodynamic description, like spectators at all energies and high rapidity $|y| > 2$ particles at RHIC energies, are not considered part of the intermediate stage. They are considered part of the late stage. When calculations with the isochronous transition scenario are done, only the spectators are present in the transport calculation parallel to the hydrodynamic calculation. In pure transport calculations, the intermediate stage is defined as beginning at the same time as in the hybrid calculations (which does not depend on the Equation of State used here), and it ends at the average ending time of the hydrodynamic phase in hybrid calculations with HG-EoS.

In calculations of the same system, but with different Equations of State, the early stage is described by the same model and therefore should give the same results. When investigating the influence of the different models, the relevant part is therefore always composed of the intermediate and late stages.

Calculations of uranium-uranium collisions at $E_{\mathsf{lab}} = 35$ AGeV are shown in Figure 7.1. The intermediate phase starts at $t_{\mathsf{start}} = 3.2$ fm for all calculations. In the transport calculations, it ends at $t_{\mathsf{end}}^{\mathsf{trans}} = 10.6$ fm, which is the ending time of the hybrid phase in HG-EoS calculations $\langle t_{\mathsf{end}}^{\mathsf{HG}} \rangle = 10.6$ fm. Hybrid calculations with χ-EoS take a little longer until the whole system is frozen out, $\langle t_{\mathsf{end}}^{\chi} \rangle = 12.4$ fm, and BM-EoS calculations are terminated at $\langle t_{\mathsf{end}}^{\mathsf{BM}} \rangle = 26.2$ fm. All photon emissions after this time contribute to the late stage emission. We show that the intermediate stage, which in the hybrid calculations is calculated

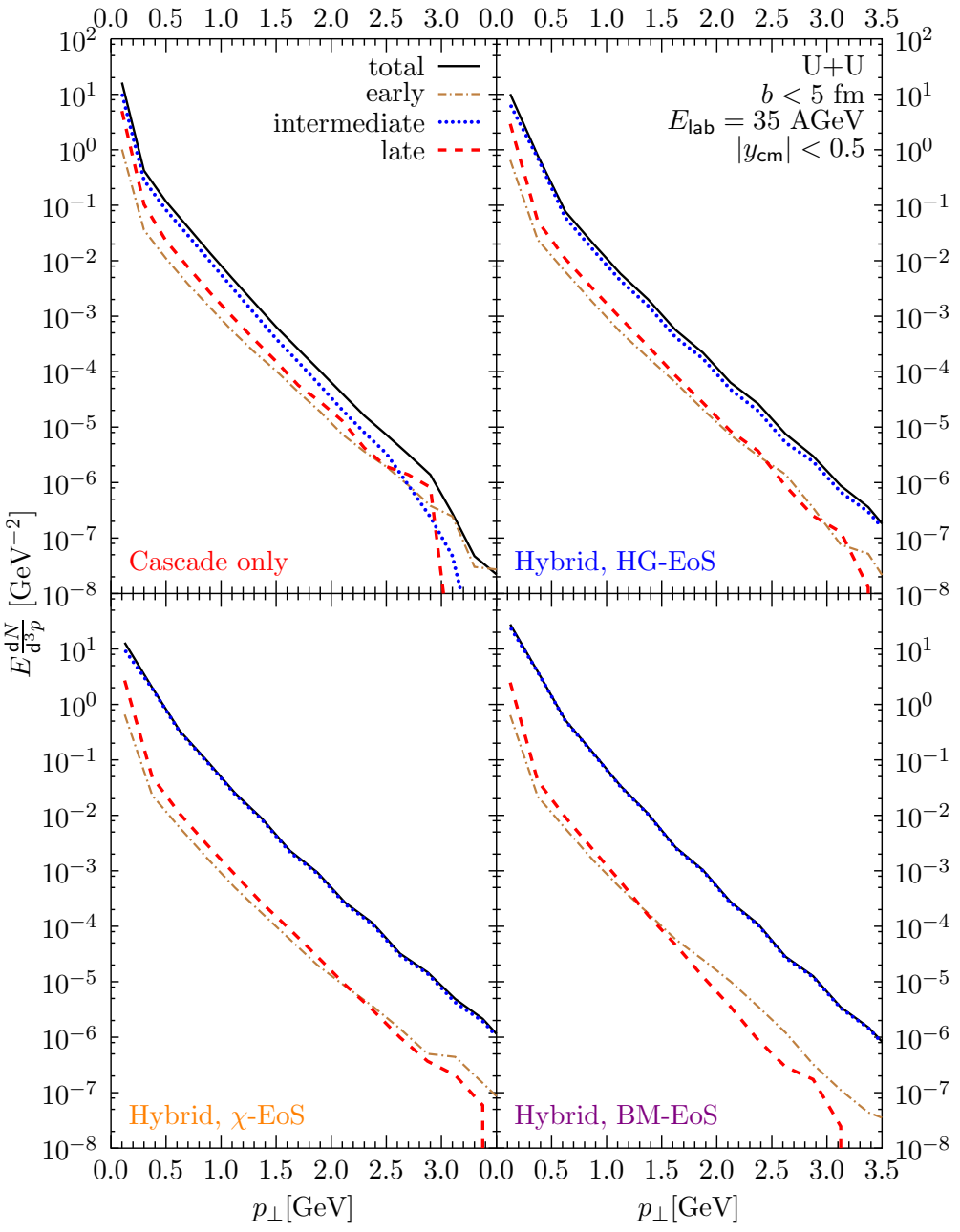

Figure 7.1: The contributions of the early (dash-dotted lines), intermediate (dotted lines) and late (dashed lines) stages to the overall direct photon spectra (solid lines) separately for all four variations of the model at $E_{\mathsf{lab}} = 35$ AGeV. Transport model calculations are in the top left, hybrid calculations with HG-EoS in the top right, χ-EoS hybrid calculations in the bottom left and BM-EoS hybrid calculations in the bottom right panel. The intermediate stage in the transport calculation is defined as $3.2 < t < 11$ fm.

with hydrodynamics, dominates the emission in all cases, although the excess of this stage is less significant in the hadronic calculations of pure transport and HG-EoS hybrid calculations. The contribution of the late stage, while in all cases much smaller than the intermediate stage contribution, is suppressed by a factor of ≈ 3 in the Bag Model EoS with respect to the other calculations.

Lead-lead collisions at $E_{\mathsf{lab}} = 158$ AGeV are shown for calculations with the standard gradual transition scenario with all Equations of State in Figure 7.2 and with the isochronous transition scenario with HG- and BM-EoS in Figure 7.3. The early stages ($t < 1.4$ fm) are shown in dash-dotted lines, the intermediate stages ($1.4 < t < 13.5$ fm for the transport model and HG-EoS calculations, $1.4 < t < 15.6$ fm for the χ-EoS calculations and $1.4 < t < 31$ fm for the Bag Model EoS calculations) are shown with dotted lines, and the subsequent late stage photon emission spectra are shown with dashed lines. At low and intermediate $p_\perp < 3$ GeV, the qualitative behaviour is very similar to the calculations at top FAIR energy $E_{\mathsf{lab}} = 35$ AGeV: the intermediate stage dominates the spectra, and its dominance is strongest in calculations with partonic emission (compare Figures 6.5 and 6.6). At high $p_\perp$, however, early stage contributions start to play a significant role. From the investigations in Section 4.2 (Figure 4.3), we can assert that this enhancement comes from the collisions of the leading particles in a string. Due to the small collision energy, these have not been present in the FAIR-calculations. The calculations with isochronous transition show a very good qualitative agreement with the spectra obtained from the calculations with gradual transition. This is mainly due to the dominant contribution of the intermediate (hydrodynamic) stage. In calculations with BM-EoS, the late stage contribution is suppressed by a factor larger than 4 at intermediate $p_\perp > 1$ GeV. A large part of the system that contributes to the late stage in the gradual scenario, but is treated hydrodynamically in the isochronous scenario, reduces the contribution of that stage. Since emission from this stage is small compared to the emission from hydrodynamics, the additional hydrodynamic emission does not significantly change its overall spectrum.

The data from the intermediate stage in transport calculations show a small deviation from a thermal spectrum at high $p_\perp$, which can be related to imperfect thermalisation of the system at the transition from the initial non-equilibrium state, which is forced to thermalisation at the transition to the hydrodynamic phase, but preserved when doing cascade-only calculations. However, Figure 7.2 suggests photon emission towards high transverse momenta from the intermediate stage is in any case strongly suppressed with respect to photon emission from the initial stage. It is therefore justified to neglect non-equilibrium effects from the intermediate phase in the hybrid model.

From all systems considered at RHIC energies, we show the contributions of the different stages for the 0-20 % most central gold-gold collisions at $\sqrt{s_{\mathsf{NN}}} = 200$ GeV. The significant change compared to the calculations at the top SPS energy $E_{\mathsf{lab}} = 158$ AGeV is that the late stage contribution is much larger than the early stage contribution below $p_\perp \approx 2.5$ GeV. However, the early stage

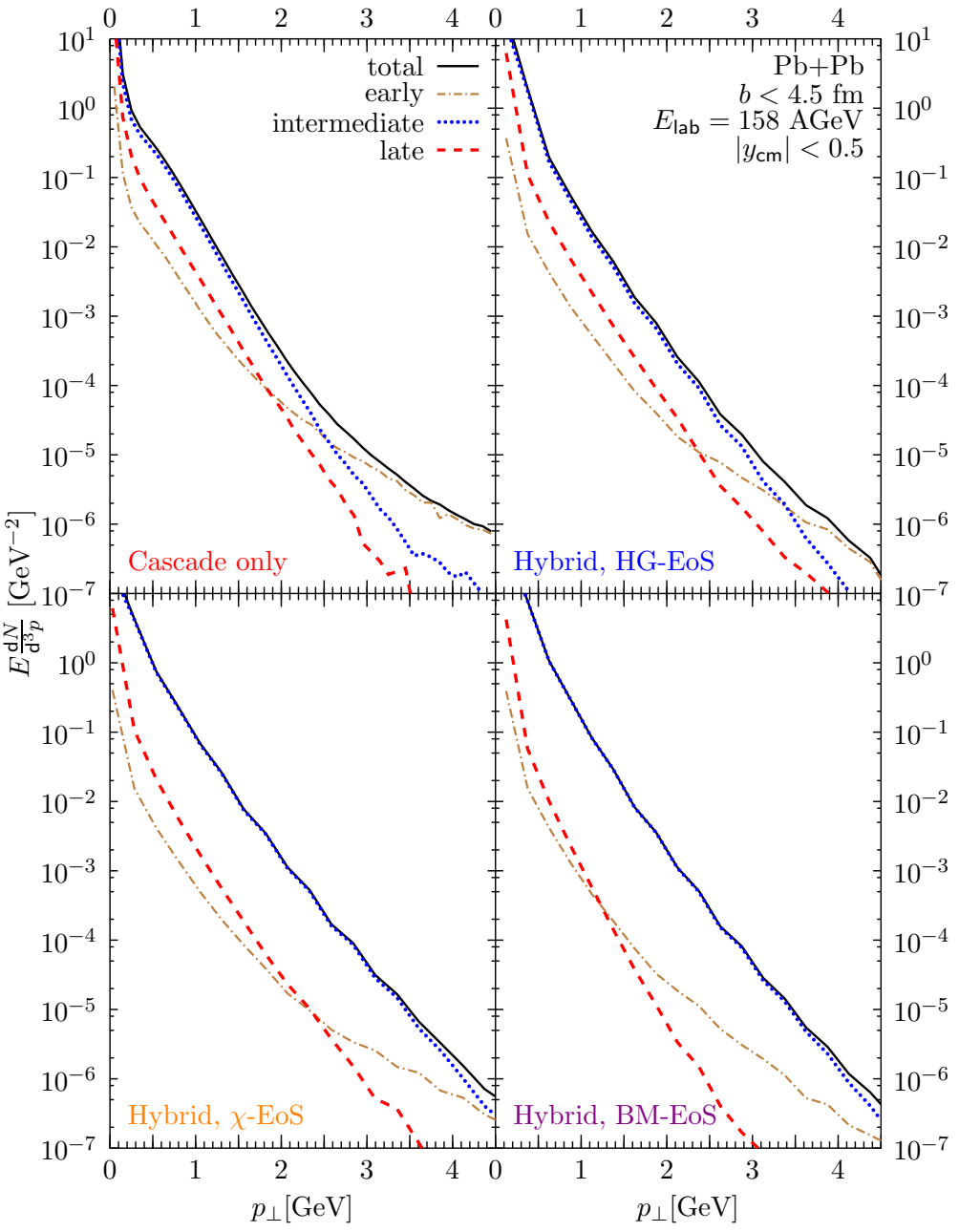

Figure 7.2: The contributions of the early (dash-dotted lines), intermediate (dotted lines) and late (dashed lines) stages to the overall direct photon spectra (solid lines) separately for all four variations of the model at $E_{\mathsf{lab}} = 158$ AGeV. Transport model calculations are in the top left, hybrid calculations with HG-EoS in the top right, χ-EoS hybrid calculations in the bottom left and BM-EoS hybrid calculations in the bottom right panel. The intermediate stage in the transport calculation is defined as $1.4 < t < 13$ fm.

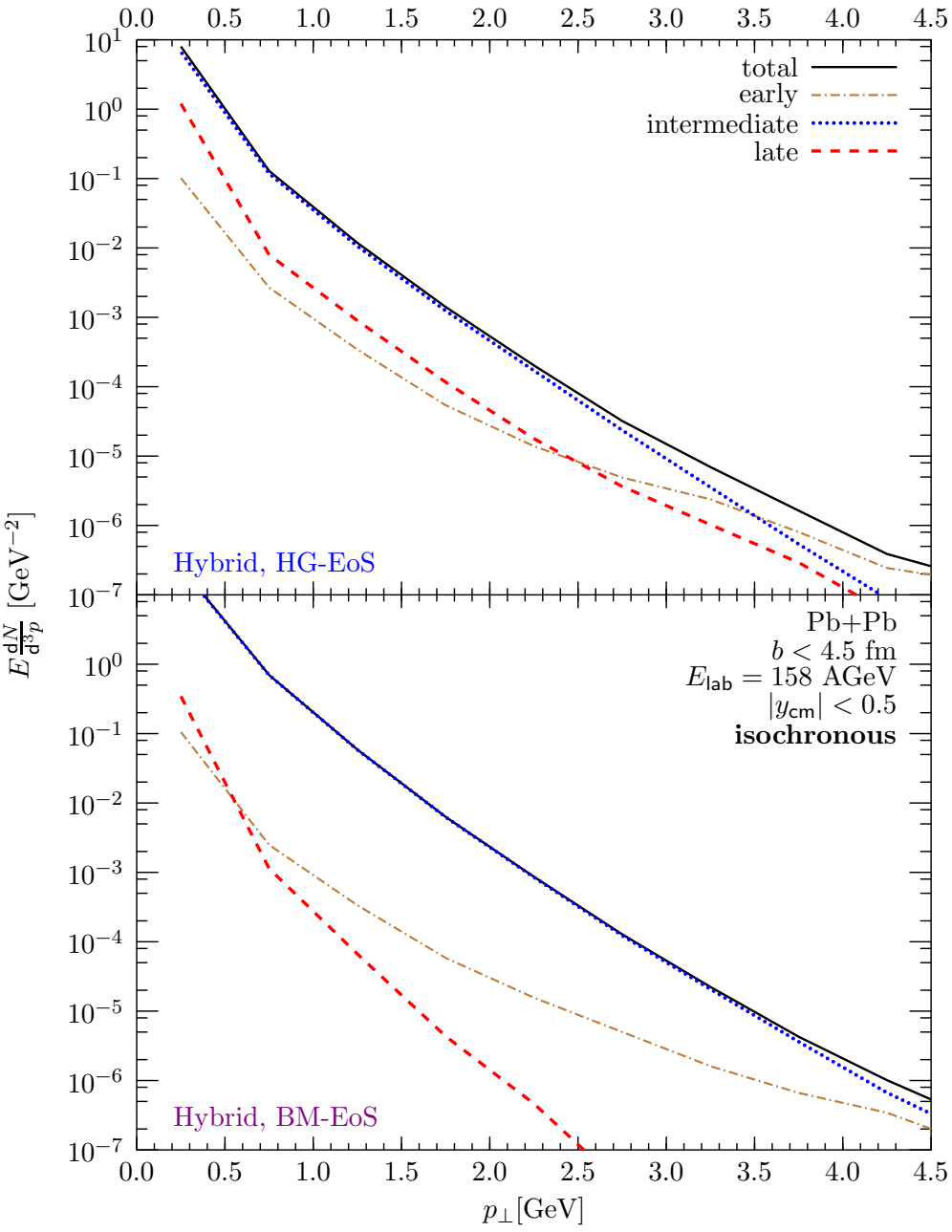

Figure 7.3: The contributions of the early (dash-dotted lines), intermediate (dotted lines) and late (dashed lines) stages to the overall direct photon spectra (solid lines) separately for HG-EoS (top) and BM-EoS (bottom) hybrid-calculations at $E_{\mathsf{lab}} = 158$ AGeV with isochronous transition scenario.

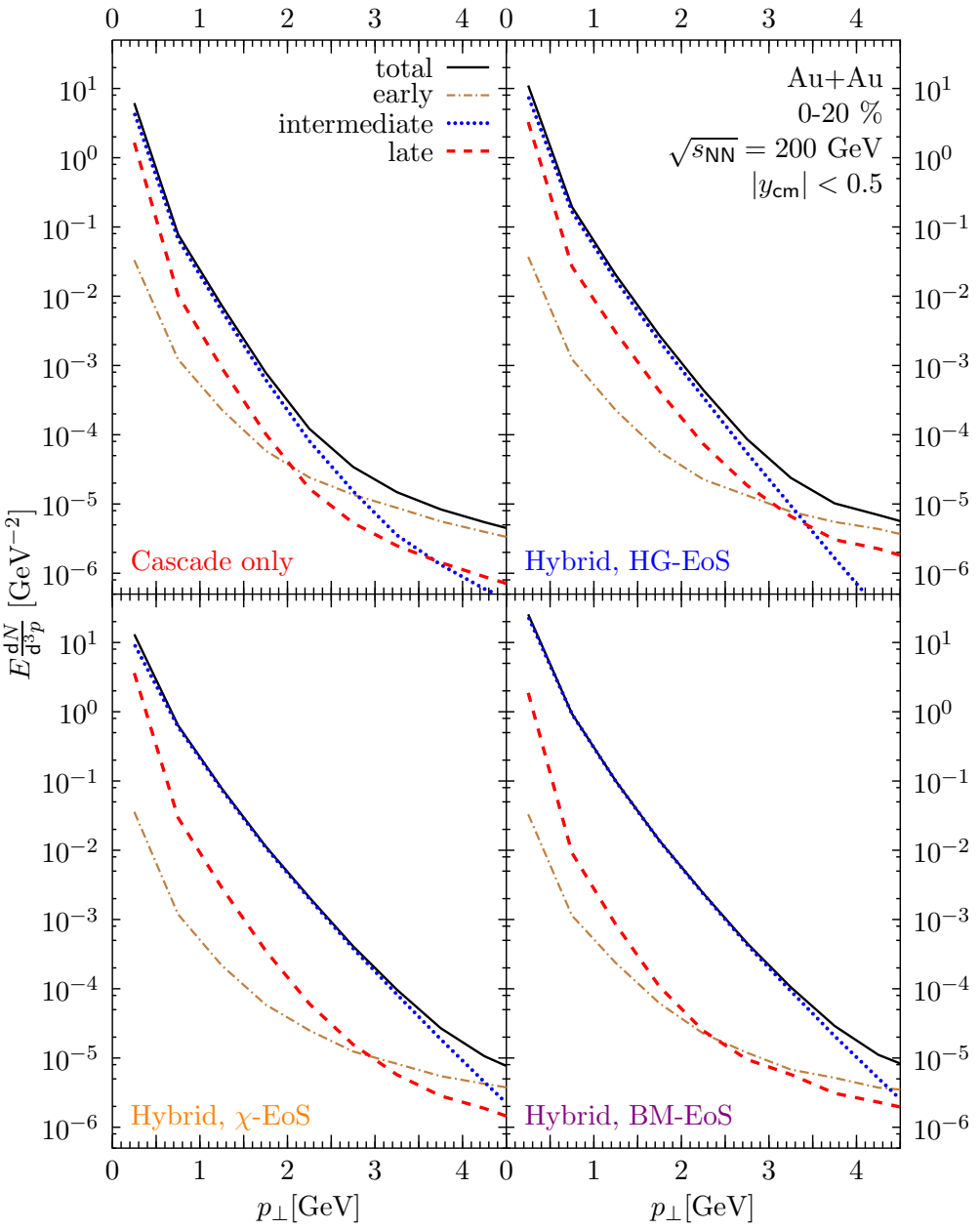

Figure 7.4: The contributions of the early (dash-dotted lines), intermediate (dotted lines) and late (dashed lines) stages to the overall direct photon spectra (solid lines) seperately for all four variation of the model in most central (0-20%) Au+Au-collisions at $\sqrt{s_{\mathsf{NN}}} = 200$ GeV. Transport model calculations are in the top left, hybrid calculations with HG-EoS in the top right, χ-EoS hybrid calculations in the bottom left and BM-EoS hybrid calculations in the bottom right panel. The intermediate stage in the transport calculation is defined as $0.6 < t < 14.3$ fm.

System	Energy ($E_{\mathsf{lab}}/\sqrt{s_{\mathsf{NN}}}$)	impact param.	t_{start} [fm]	$t_{\mathsf{end}}^{\mathsf{HG}}$ [fm]	t_{end}^{χ} [fm]	$t_{\mathsf{end}}^{\mathsf{BM}}$ [fm]
U+U	35 AGeV	< 5.0 fm	3.2	10.6	12.4	26.4
Pb+Pb	158 AGeV	< 4.5 fm	1.4	13.3	15.6	31.2
Au+Au	62.4 GeV	0-20 %	0.6	12.2	11.7	24.8
Au+Au	62.4 GeV	20-40 %	0.6	9.1	8.6	18.8
Cu+Cu	62.4 GeV	0-20 %	0.6	7.5	7.0	17.7
Cu+Cu	62.4 GeV	20-40 %	0.6	5.8	5.4	16.4
Au+Au	130 GeV	0-20 %	0.6	13.7	12.7	25.6
Au+Au	130 GeV	20-40 %	0.6	10.1	9.5	19.4
Cu+Cu	130 GeV	0-20 %	0.6	8.3	7.7	18.1
Cu+Cu	130 GeV	20-40 %	0.6	6.3	5.8	16.8
Au+Au	200 GeV	0-20 %	0.6	14.3	13.1	25.9
Au+Au	200 GeV	20-40 %	0.6	10.5	9.8	19.9
Cu+Cu	200 GeV	0-20 %	0.6	8.6	7.9	18.2
Cu+Cu	200 GeV	20-40 %	0.6	6.4	6.0	16.9

Table 7.1: Transition times for the transition from transport to hydrodynamics t_{start} and the time after which the complete system has been transfered back from the hydrodynamic calculation to the transport description t_{end} in hybrid model calculations.

($t < 0.6$ fm) is much shorter than in the calculations at lower energies. The late stages from hybrid model calculations has significant high-$p_\perp$ contributions, much like the early stages in RHIC- and SPS-systems. This can be attributed to scatterings of high-rapidity particles outside of the hydrodynamic region as well as to late scatterings with high transverse momenta. The comparison to the spectra from pure transport calculation (top left panel of Figure 7.4) shows that high-$p_\perp$ photons are indeed produced in the late stage after $\langle t_{\mathsf{end}}^{\mathsf{HG}} \rangle = 14.3$ fm. This behaviour is examined in more detail in Section 7.2.

An overview over the start- and ending times of the intermediate stage in the various calculations is given in Table 7.1. Along with the conventions used above, the ending time t_{end} is the time after which the complete system is described in transport theory again. While $t_{\mathsf{end}}^{\mathsf{BM}}$ is more than twice as big as $t_{\mathsf{end}}^{\mathsf{HG}}$ and t_{end}^{χ} for almost all systems, the difference between $t_{\mathsf{end}}^{\mathsf{HG}}$ and t_{end}^{χ} changes with beam energy: At FAIR- and SPS-energies, the hydrodynamic expansion with the Chiral Equation of State takes longer that that with the purely hadronic Hadron Gas EoS, while at RHIC energies, the χ-EoS leads to a more explosive expansion and dilutes faster.

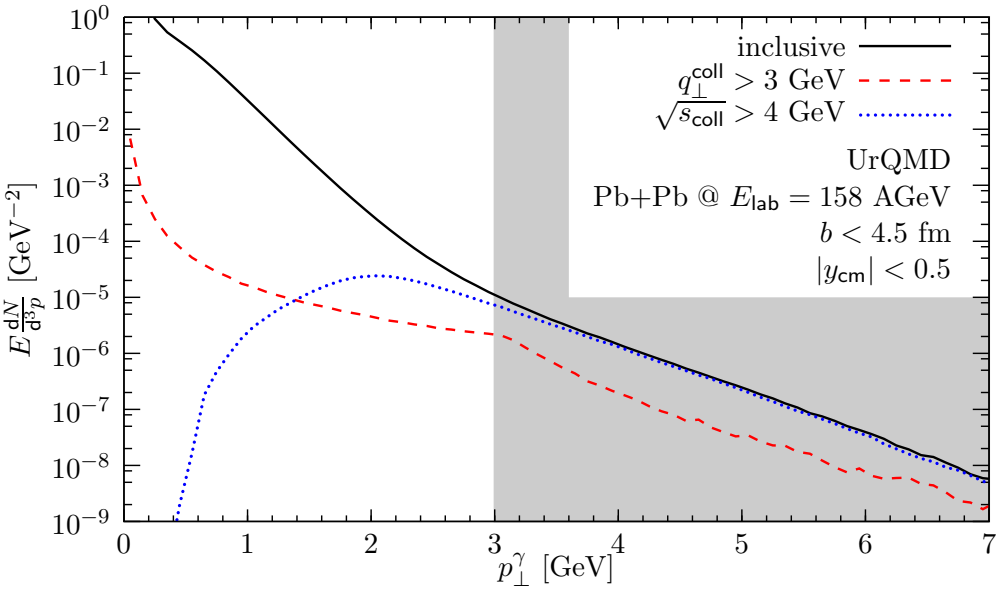

Figure 7.5: $p_\perp$-spectra for all photons (solid line), photons from boosted collisions (dotted line) and collisions with high center-of-mass energy (dashed line) at $E_{\mathsf{lab}} = 158$ AGeV. The shaded area indicates the range of the $p_\perp$-region used for the solid lines in Figures 7.6 and 7.7.

7.2 High-$p_\perp$ emission

To investigate the major sources for photons to the transverse momentum spectrum and to explore the sensitivity to the different reaction stages, we investigate the origin of the change of slope of the spectra at high transverse momenta $p_\perp \approx 3$ GeV that emerges in calculations at top SPS-energy $E_{\mathsf{lab}} = 158$ AGeV and RHIC-energies. Figure 7.5 shows that the spectrum exhibits two separate exponential parts, one with a low slope parameter T_{slope} at low momenta, and a bigger T_{slope} at higher $p_\perp$. The emission does not follow a power-law at high $p_\perp$. In Figures 7.5, 7.6 and 7.7, we take a closer look at this kinematic regime with pure transport calculations of central lead-lead collisions at $E_{\mathsf{lab}} = 158$ AGeV. Two processes may contribute to high $p_\perp$-photons: (I) collisions with a large $\sqrt{s_{\mathsf{coll}}}$ in elementary reactions (i.e. early stage collisions) and (II) collisions of particles with large transverse flow $q_\perp^{\mathsf{coll}}$ but rather small $\sqrt{s_{\mathsf{coll}}}$ (i.e. late stage collisions). To disentangle these effects, we determine the contributions of scatterings with high center-of-mass energy $\sqrt{s_{\mathsf{coll}}} > 4$ GeV and high center-of-mass transverse momentum $q_\perp^{\mathsf{coll}} > 3$ GeV. Figure 7.5 shows the transverse momentum spectrum of photons split up into the two contributions. Nearly all photons at high transverse momenta (shaded area) come from collisions with high center-of-mass energies, whereas the contribution of high center-of-mass transverse momenta only shows a trivial structure at $p_\perp \approx q_\perp^{\mathsf{threshold}} = 3$ GeV.

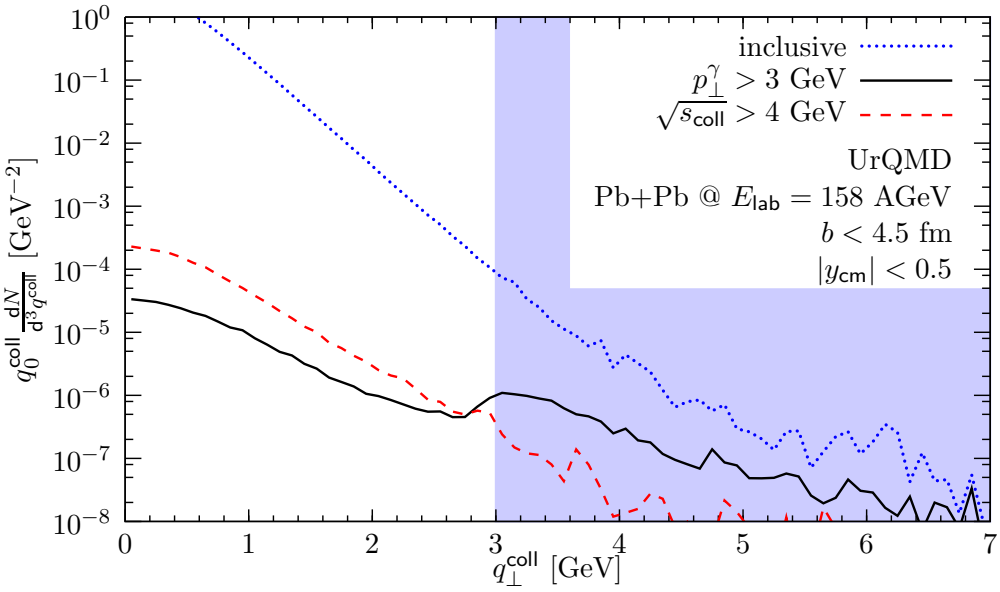

Figure 7.6: Number of photons as function of the transverse center-of-mass momentum of the elementary collision $q_\perp^{\mathsf{coll}}$. We show all photons (dotted line), photons that have high transverse momentum (solid line) and photons from collisions with high center-of-mass energy (dashed line) at $E_{\mathsf{lab}} = 158$ AGeV. The shaded area indicates the range of the $q_\perp^{\mathsf{coll}}$-region used for the dotted lines in Figures 7.5 and 7.7.

One cross-check for Figure 7.5 is shown in Figure 7.6. Here, we observe that the collision spectrum is exponential. Only at high transverse boosts, a deviation from an exponential spectrum can be seen. This indicates that most photons with high transverse momentum come from unboosted collisions with $q_\perp^{\mathsf{coll}} < 1$ GeV. The center-of-mass energy and transverse momentum of a collision show no correlation.

The latter can be seen in Figure 7.7, where the photon production rate is shown as a function of the center-of-mass energy of the individual collisions. The figure confirms the notion that most photons with high transverse momenta come from collisions with high center-of-mass energies. It is worthwhile to observe, however, that starting at $\sqrt{s_{\mathsf{coll}}} = 7$ GeV, each elementary collision produces essentially only photons with transverse momenta $p_\perp > 3$ GeV.

The distribution of center-of-mass energies also shows that the vast majority of collisions happen around the ρ- and a_1-pole masses.

7.3 Emission times

Since emission of direct photons happens throughout the heavy-ion collision, it is prudent to look at the emission times of photons. For U+U-collisions at top

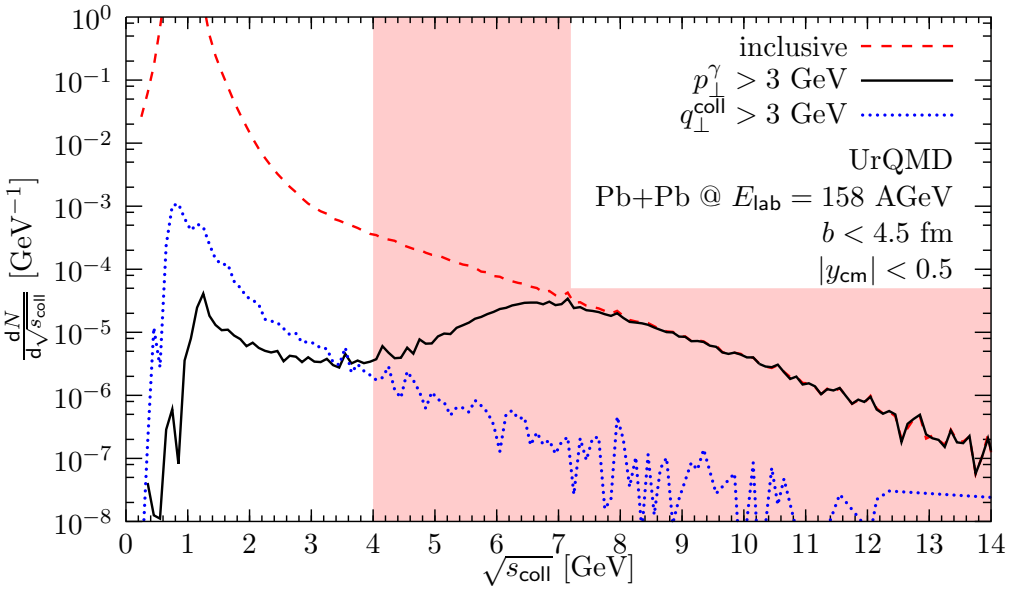

Figure 7.7: Number of photons as a function of the center-of-mass energy of the elementary collision $\sqrt{s_{\text{coll}}}$. We show all photons (dashed line), photons with high transverse momentum (solid line) and photons from collisions with high transverse center-of-mass momentum (dashed line) at $E_{\text{lab}} = 158$ AGeV. The shaded area shows the $\sqrt{s_{\text{coll}}}$-region used for the dashed lines in Figures 7.5 and 7.6.

FAIR energy $E_{\text{lab}} = 35$ AGeV, this analysis is shown in Figure 7.8, showing the average emission time of direct photons plotted against their transverse momentum for the two most abundant channels in cascade-only calculations $\pi\pi \to \gamma X$ and $\pi\rho \to \gamma\pi$. We can see that the average emission time is nearly constant at about $\langle t_{\text{emission}} \rangle \approx 7.6$ fm over the whole $p_\perp$-range. It is interesting to note that at intermediate $p_\perp$ direct photons from $\pi\pi$-scatterings have a significantly lower average emission time $\langle t_{\pi\pi} \rangle \approx 4$ fm than those coming from $\pi\rho$-collisions.

The time evolution of direct photon emission in Figure 7.9 shows that at intermediate transverse momentum $1.5 < p_\perp < 2.5$ GeV the emission has two peaks, one after roughly 3 fm and the other one at 8 fm. The average emission time in this momentum region is $\langle t(p_\perp \approx 2 \text{ GeV}) \rangle = 7.6$ fm. The two-peak structure coincides with the large difference in the average emission times between the two channels $\pi\pi \to \gamma X$ and $\pi\rho \to \gamma\pi$ already discussed in Chapter 6. Indeed, photons from $\pi\pi$-scatterings do not contribute to the later peak. At high transverse momentum, $2.5 < p_\perp < 3.5$ GeV, no significant peak at $t > 5$ fm is present, but the tail of the distribution is still large enough to have the average emission time as high as $\langle t(p_\perp \approx 3 \text{ GeV}) \rangle = 6.4$ fm. At very low $p_\perp < 0.5$ GeV, the emission is dominated by $\pi\pi$-scatterings, and is symmetrically centered around its average value of $\langle t(p_\perp \approx 0 \text{ GeV}) \rangle = 8.8$ fm, as is the $\pi\rho$-dominated photon

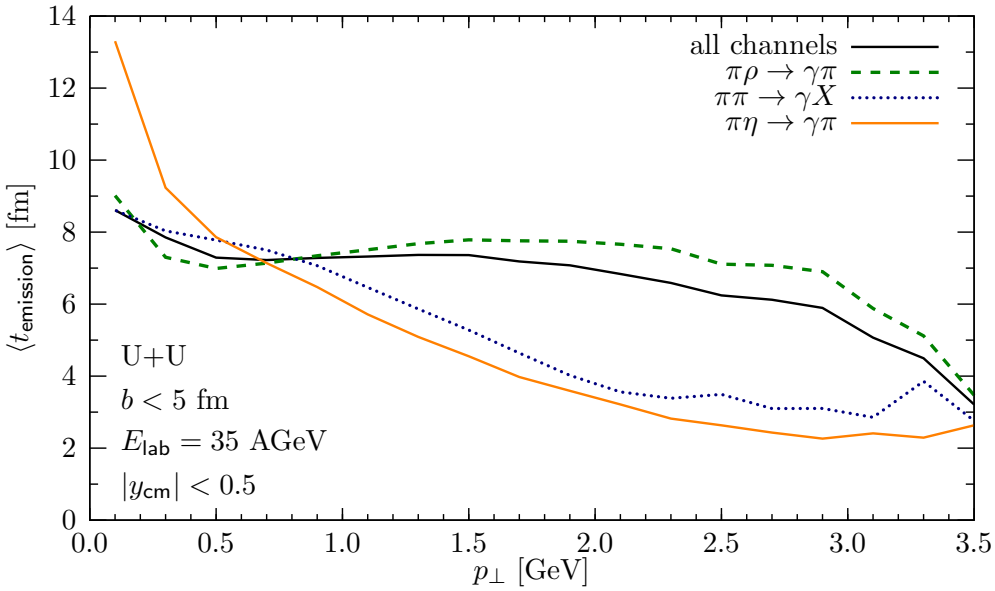

Figure 7.8: Average emission time of direct photons in cascade calculations of central uranium-uranium collisions at $E_{\mathsf{lab}} = 35$ AGeV as function of transverse photon momentum for all channels (dark solid line), $\pi\rho$-collisions (dashed line), $\pi\pi$-collisions (dotted line) and $\pi\eta$-collisions (light solid line).

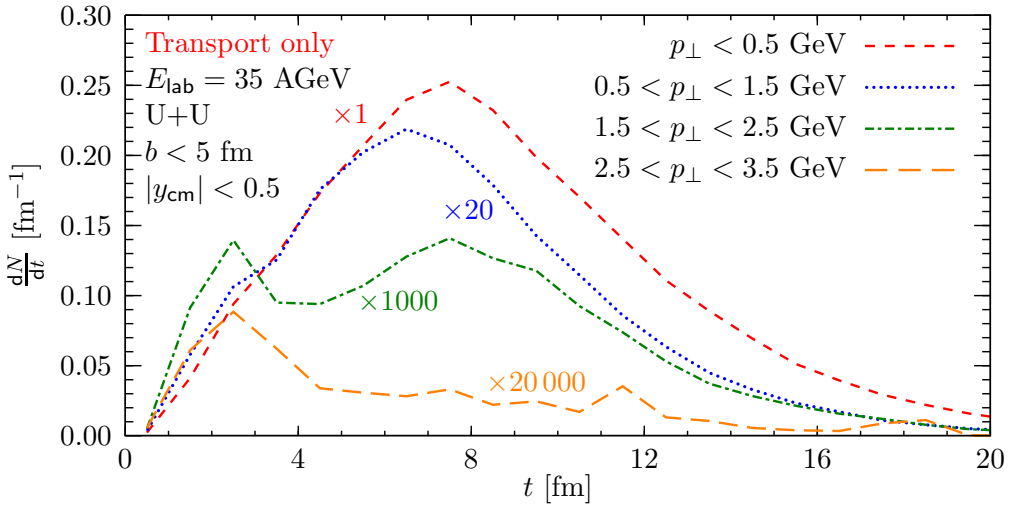

Figure 7.9: UrQMD calculation of central uranium-uranium collisions at $E_{\mathsf{lab}} = 35$ AGeV. Emission time distribution of photons in the momentum ranges $p_\perp < 0.5$ GeV (dashed line), $0.5 < p_\perp < 1.5$ GeV (dotted line, scaled by 20), $1.5 < p_\perp < 2.5$ GeV (dash-dotted line, scaled by 1000) and $2.5 < p_\perp < 3.5$ GeV (long dashed line, scaled by 20000).

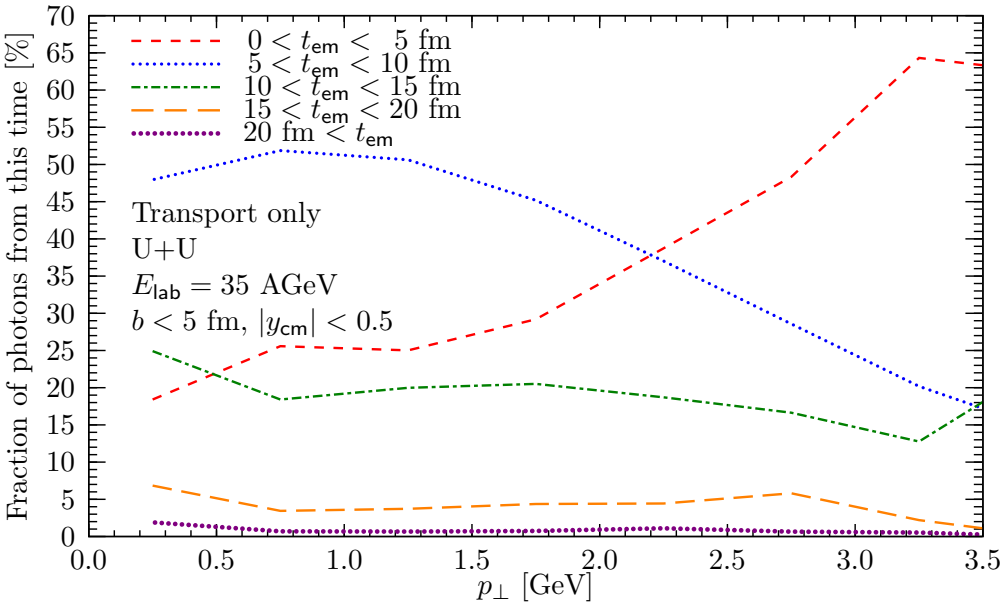

Figure 7.10: Fraction of photons that are emitted from $0 < t < 5$ fm (dashed line), $5 < t < 10$ fm (dotted line), $10 < t < 15$ fm (dash-dotted line), $15 < t < 20$ fm and $t > 20$ fm (short-dotted line) as a function of transverse momentum in UrQMD-calculations of uranium-uranium collisions at $E_{lab} = 35$ AGeV.

emission at low transverse momentum $0.5 < p_\perp < 1.5$ GeV, whose average time is $\langle t(p_\perp \approx 1 \text{ GeV}) \rangle = 7.6$ fm.

When looking at the relative contributions of the different emission times t_{em} to the direct photon yield as a function of direct photon transverse momentum in Figure 7.10, we can assert the picture presented above. At low transverse momenta $p_\perp < 2$ GeV, emission from $5 < t_{em} < 10$ fm (dotted line) dominates and constitutes about 50 % of the overall contribution. At higher $p_\perp > 2.5$ GeV, however, emission from the very early stages of the collision starts to dominate. The contribution of photons emitted earlier than $t_{em} = 5$ fm contribute more than 60 % to the direct photon spectrum at $p_\perp > 3$ GeV.

The same analysis is also done on calculations of Pb+Pb-collisions at $E_{lab} = 158$ AGeV. Figure 7.11 shows the average emission times of photons as a function of the transverse momentum for the various channels. As in the calculations for FAIR-energies discussed above, the average emission time stays at a constant level of about $\langle t_{emission} \rangle \approx 8$ fm over a very broad momentum range, $0.5 < p_\perp < 2.3$ GeV. Again, this coincides with the region where the process $\pi\rho \to \gamma\pi$ dominates. Only at high transverse momenta, the early times dominate. This is consistent with the findings in Section 7.2, that the spectrum clearly shows two different temperatures, one in the region below $p_\perp = 2.5$ GeV and a different temperature above $p_\perp > 3$ GeV. It also explains why the spectral contributions from $\pi\pi \to \gamma X$ and $\pi\eta$-collisions show a much flatter slope already at $p_\perp \approx$

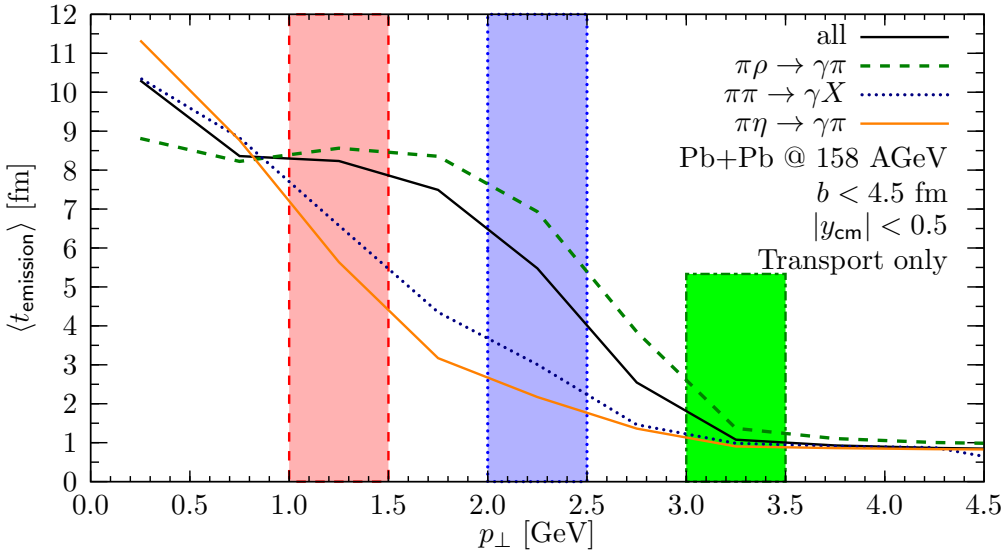

Figure 7.11: UrQMD calculation. Average photon emission times as a function of the transverse momentum for all photons, $\pi\rho$-, $\pi\pi$- and $\pi\eta$-processes (dark solid, dashed, dotted and light solid line, respectively) in central Pb+Pb-collisions at $E_{\mathsf{lab}} = 158$ AGeV. The shaded areas correspond to the $p_\perp$-regions used for the curves shown in Figure 7.12.

2 GeV. At late times, when the average center-of-mass energy of the individual scatterings $\sqrt{s_{\mathsf{coll}}}$ has decreased, photons are predominantly produced at low transverse momenta.

In Figure 7.12, we show the emission time distribution of photons in various $p_\perp$-bins for the $\pi\rho \to \gamma\pi$-processes in the same system. It is interesting to see that at all transverse momenta, there is an initial flash of photons emitted at very early times $t \approx 1$ fm. In the low $p_\perp$-bin $1 < p_\perp < 1.5$ GeV, a very strong contribution from the bulk emission in the hot and dense stage between $t = 4$ fm and $t = 12$ fm raises the average emission time. In the intermediate $p_\perp$-region $2 < p_\perp < 2.5$ GeV, the bulk contribution is greatly reduced and shines less bright than the initial flash. In the highest $p_\perp$-region $3 < p_\perp < 3.5$ GeV, the late bulk contribution is small and the initial stage dominates. However, one should note that due to the long lifetime of the intermediate stage, the average emission times are shifted to higher values. When looking at the relative contribution of different time spans in Figure 7.13, a significant difference to the analysis of photon emission patterns expected at FAIR (U+U at $E_{\mathsf{lab}} = 35$ AGeV) can be seen: early scatterings ($t < 5$ fm) contribute almost 100 % of the photons from hadronic channels at $p_\perp > 3$ GeV, while later processes cease to dominate already at $p_\perp = 1.5$ GeV.

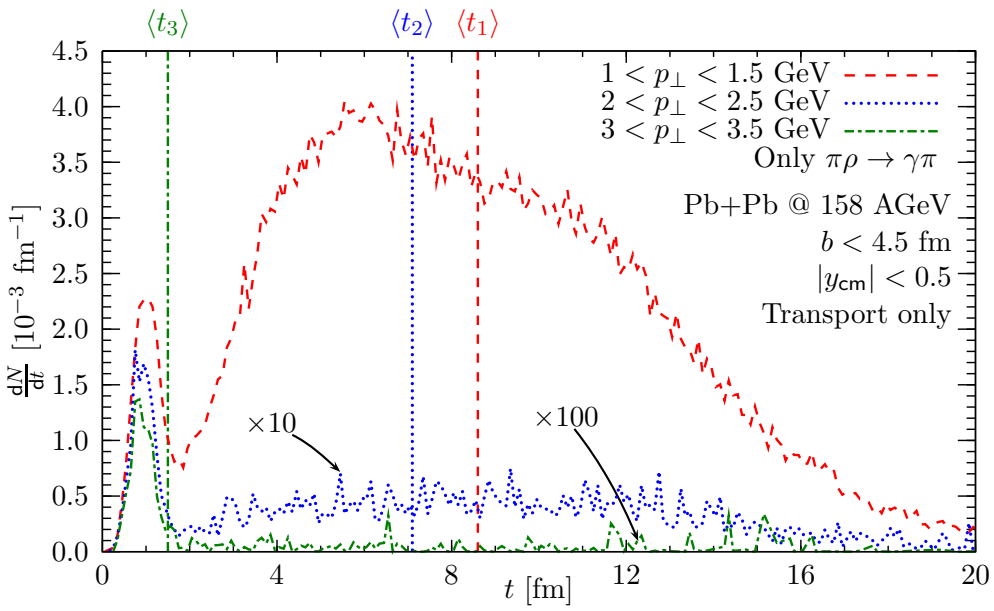

Figure 7.12: UrQMD calculation of central lead-lead collisions at $E_{\mathsf{lab}} = 158$ AGeV. Emission time distribution of photons from $\pi\rho$-scatterings for the different photon transverse momentum regions indicated in Figure 7.11. The vertical lines indicate the average emission time in the corresponding $p_\perp$-bin.

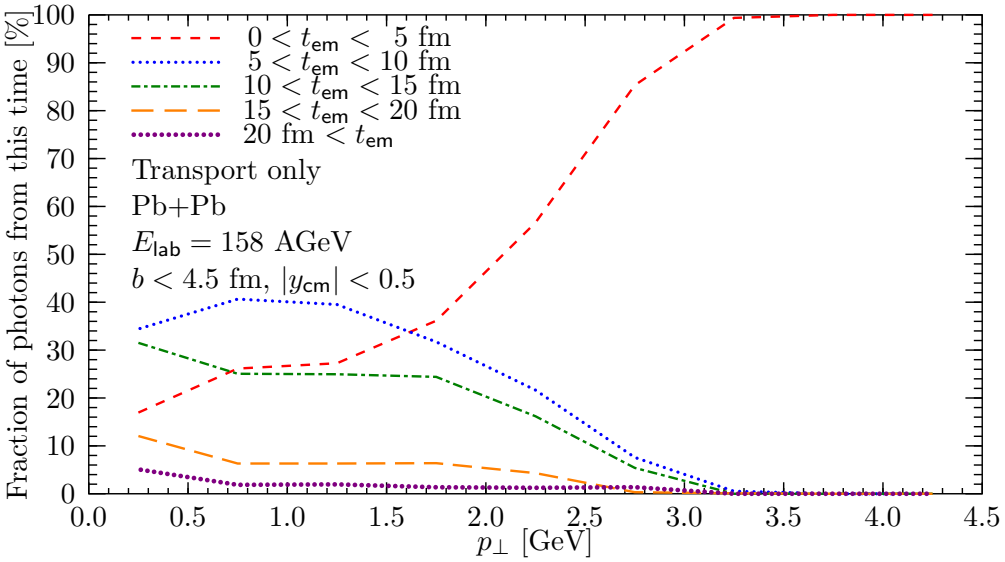

Figure 7.13: Fraction of photons that are emitted from $0 < t < 5$ fm (dashed line), $5 < t < 10$ fm (dotted line), $10 < t < 15$ fm (dash-dotted line), $15 < t < 20$ fm (long dashed line) and $t > 20$ fm (short-dotted line) as a function of transverse momentum in UrQMD-calculations of lead-lead collisions at $E_{\mathsf{lab}} = 158$ AGeV.

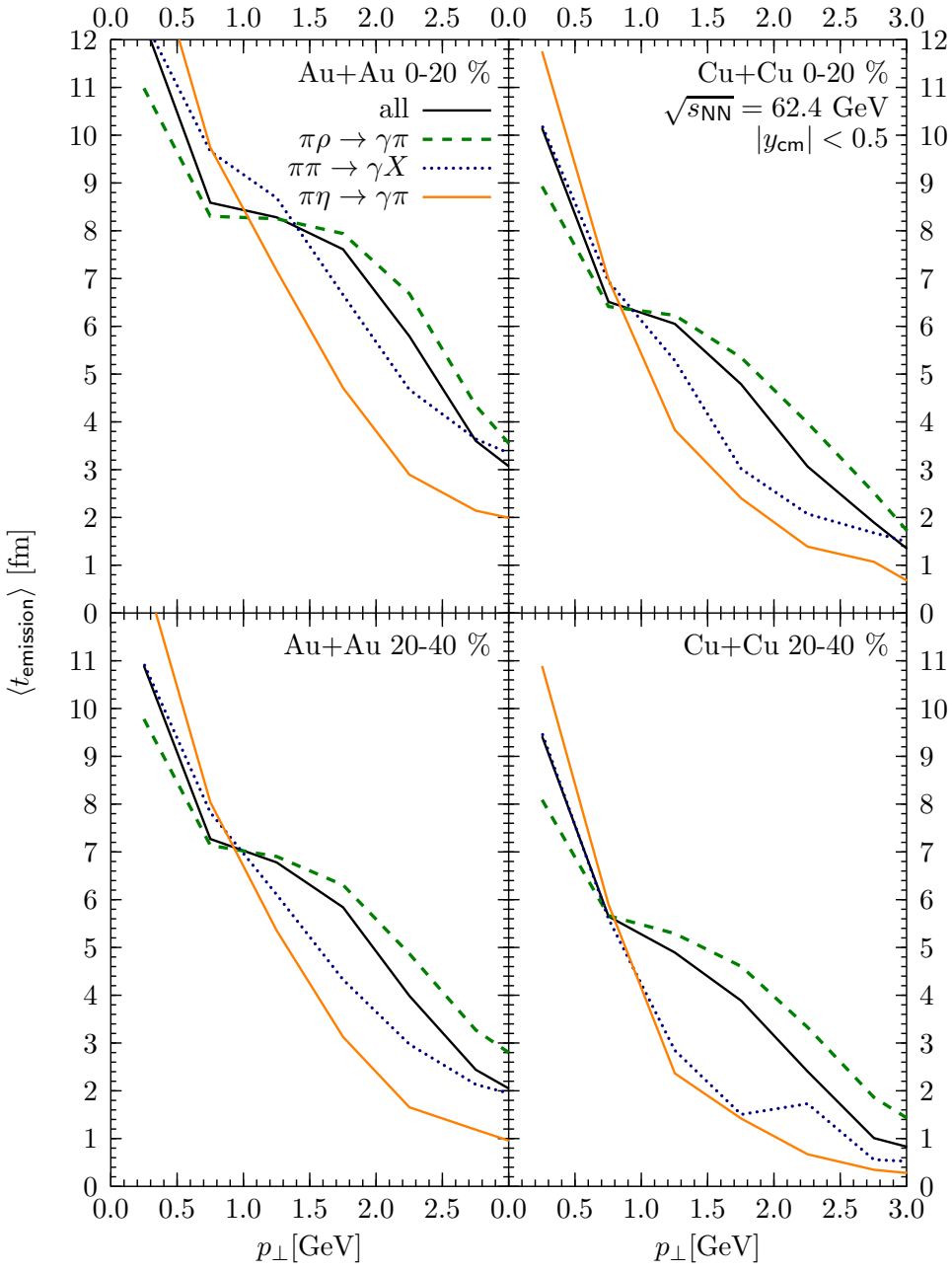

Figure 7.14: Average emission time of direct photons in cascade calculations of central (0-20 %, upper panels) and mid-central (20-40 %, lower panels) Au+Au-collisions (left panels) and Cu+Cu-collisions (right panels) at $\sqrt{s_{\mathsf{NN}}} = 62.4$ GeV as function of transverse photon momentum for all channels (dark solid line), $\pi\pi$-collisions (dotted line), $\pi\rho$-collisions (dashed line) and $\pi\eta$-collisions (light solid line).

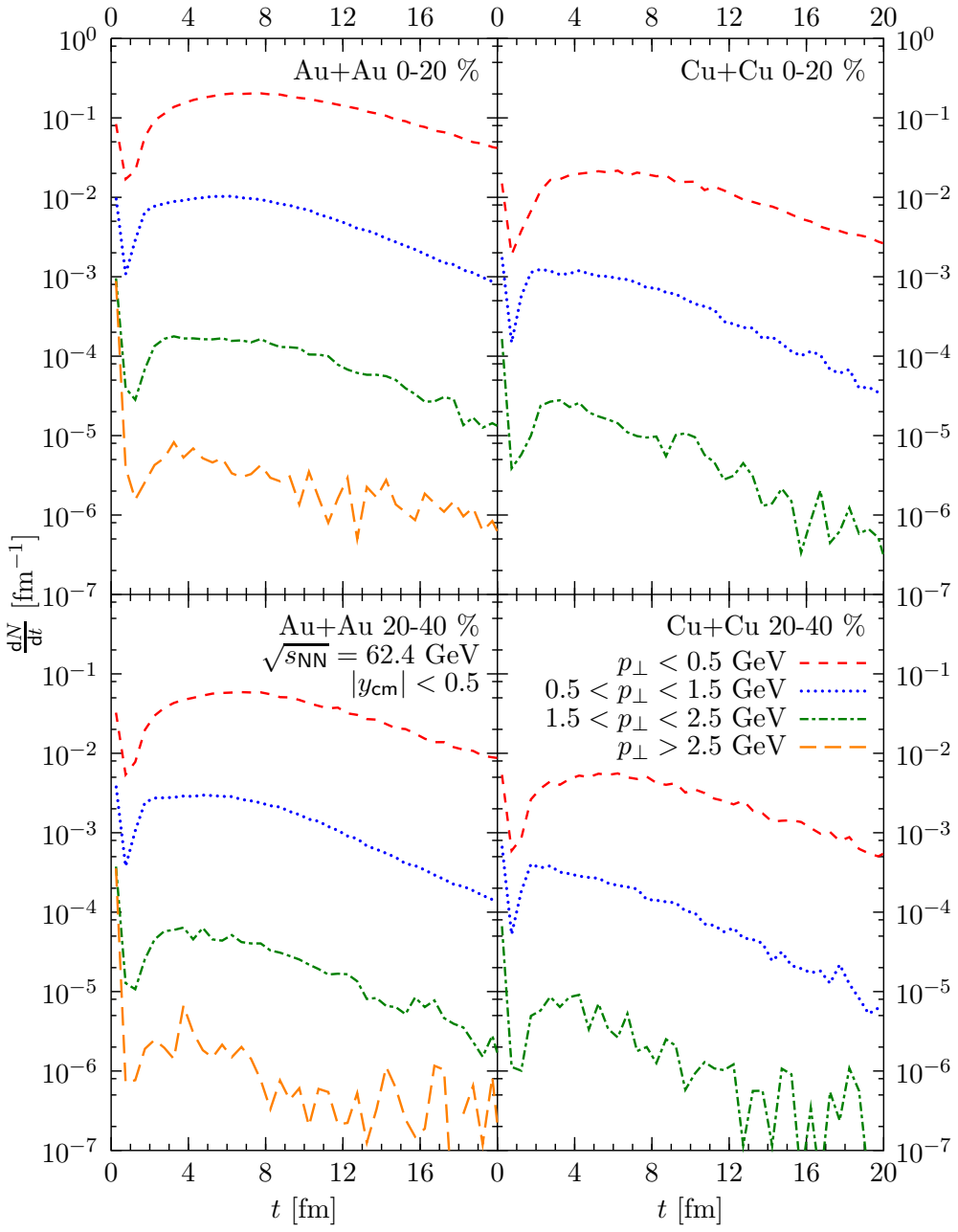

Figure 7.15: UrQMD calculation of central (0-20 %, upper panels) and mid-central (20-40 %, lower panels) Au+Au-collisions (left panels) and Cu+Cu-collisions (right panels) at $\sqrt{s_{NN}} = 62.4$ GeV. Emission time distribution of photons in the momentum ranges $p_\perp < 0.5$ GeV (dashed line), $0.5 < p_\perp < 1.5$ GeV (dotted line), $1.5 < p_\perp < 2.5$ GeV (dash-dotted line) and $p_\perp > 2.5$ GeV (long-dashed line).

At RHIC energies, we investigate the emission patterns at three different energies $\sqrt{s_{\mathsf{NN}}} = 62.4$ GeV, $\sqrt{s_{\mathsf{NN}}} = 130$ GeV and $\sqrt{s_{\mathsf{NN}}} = 200$ GeV. At each energy, we compare the results of Au+Au-collisions and Cu+Cu-collisions for the 0-20 % most central and 20-40 % most central collisions.

At $\sqrt{s_{\mathsf{NN}}} = 62.4$ GeV, the average emission time is between 4 and 8 fm for intermediate and low $p_\perp$ and drops to lower $\langle t_{\mathsf{emission}} \rangle$ at $p_\perp > 2.5$ GeV, see Figure 7.14. The behaviour of the different channels is very similar to that at lower energies, with the $\pi\rho$-collisions producing high- and intermediate $p_\perp$-photons significantly later than both $\pi\pi$- and $\pi\eta$-collisions. A clear decrease in the average emission times from central to mid-central collisions and from Au+Au- to Cu+Cu-collisions is visible, as should be expected. Despite the high average emission time, photons at high $p_\perp > 2.5$ GeV are dominantly emitted at very early stages (see Figure 7.15). Photon emission from the first 5 fm of the collision dominates above $p_\perp = 1$ GeV in central and above $p_\perp = 0.5$ GeV in mid-central collisions, as can be seen in Figure 7.16. After that, only soft collisions contribute to the direct photon spectra.

In gold-gold collisions at $\sqrt{s_{\mathsf{NN}}} = 130$ GeV, late $\pi\pi$-collisions contribute to the direct photon yield (see Figure 7.17). About 10 % of the photons at $p_\perp \approx 4$ GeV come from collisions that happen later than $t_{\mathsf{emission}} = 5$ fm (Figure 7.19). As in investigations at lower initial collision energy, direct photon emission comes either from very early collisions, where the baryon number density is high (see Chapter 8) or from late stages, where the baryon number density is rather small, but very few photons are emitted in between at $t \approx 1$ fm, where intermediate baryon number densities are expected, see Figure 7.18.

In collisions at the highest RHIC-energy $\sqrt{s_{\mathsf{NN}}} = 200$ GeV, the trend continues: the average emission time in gold-gold collisions (left panels in Figure 7.20) stays constant at about $\langle t_{\mathsf{emission}} \rangle = 7-8$ fm. The average emission time is shifted by very late $\pi\pi$-collisions that produce significant amounts of high-$p_\perp$ photons after $t_{\mathsf{emission}} = 20$ fm. This behaviour is also visible in central copper-copper collisions, but not in mid-central Cu+Cu. The life-time/system size ordering that has been discussed for collisions at $\sqrt{s_{\mathsf{NN}}} = 62.4$ GeV is also visible here. The time evolution of photon emission at different $p_\perp$(see Figure 7.21) is qualitatively very similar to the other cases, but the relative contributions of the early spark and later emissions is shifted towards the late emission at all systems and throughout the whole $p_\perp$-range. This reflects in Figure 7.22, where the relative contribution of early collisions to the complete direct photon spectra is shown to be no larger than 80 % in central gold-gold collisions even at $p_\perp = 4.5$ GeV. The contribution of early stage collisions is also decreased at mid-central gold-gold collisions and in copper-copper collisions with respect to the early stage contributions seen at lower initial collision energies. Moreover, emission from very late collisions ($t_{\mathsf{emission}} > 30$ fm) contributes significantly (in the order of 5 %) even to the spectrum at high-$p_\perp$, which is not the case for lower initial collision energies.

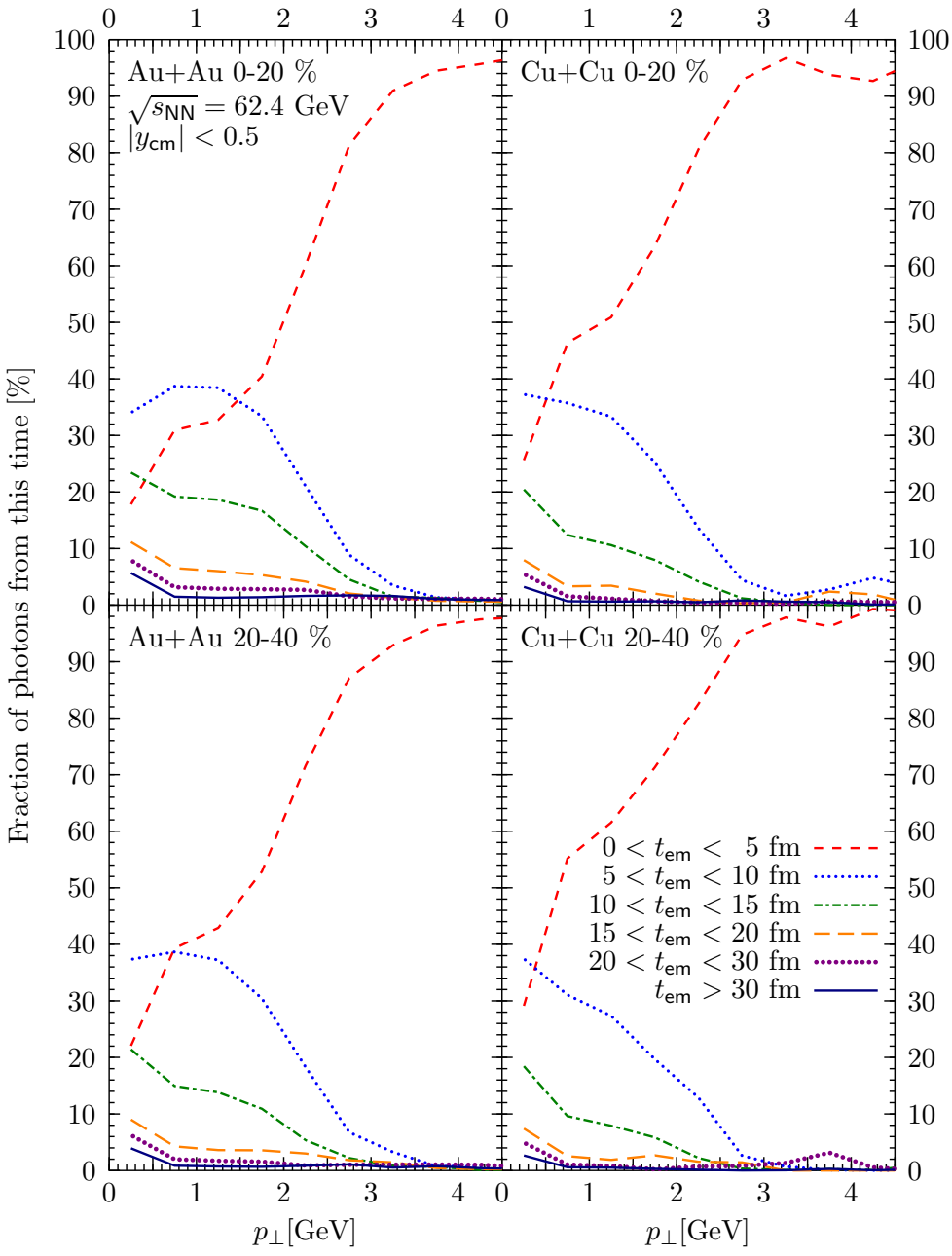

Figure 7.16: Fraction of photons that are emitted from $0 < t < 5$ fm (dashed line), $5 < t < 10$ fm (dotted line), $10 < t < 15$ fm (dash-dotted line), $15 < t < 20$ fm (long dashed line), $20 < t < 30$ fm (short-dotted line) and $t > 30$ fm (solid line) as a function of transverse momentum in UrQMD-calculations of gold-gold collisions (left panels) and copper-copper collisions (right panels) for central (0-20 %, upper panels) and mid-central (20-40 %, lower panels) collisions at $\sqrt{s_{NN}} = 62.4$ GeV.

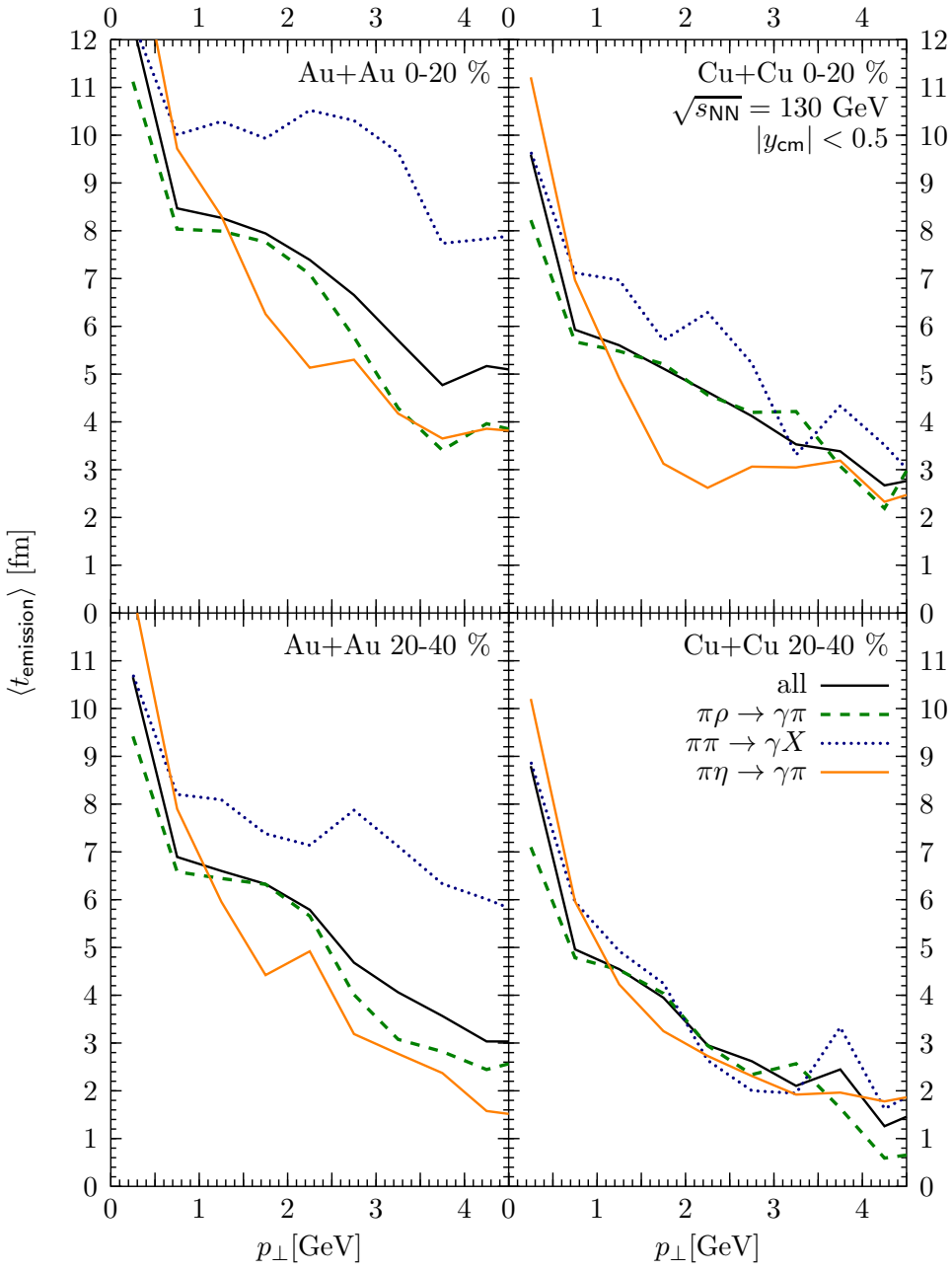

Figure 7.17: Average emission time of direct photons in cascade calculations of central (0-20 %, upper panels) and mid-central (20-40 %, lower panels) Au+Au-collisions (left panels) and Cu+Cu-collisions (right panels) at $\sqrt{s_{\mathsf{NN}}} = 130$ GeV as function of transverse photon momentum for all channels (dark solid line), $\pi\pi$-collisions (dotted line), $\pi\rho$-collisions (dashed line) and $\pi\eta$-collisions (light solid line).

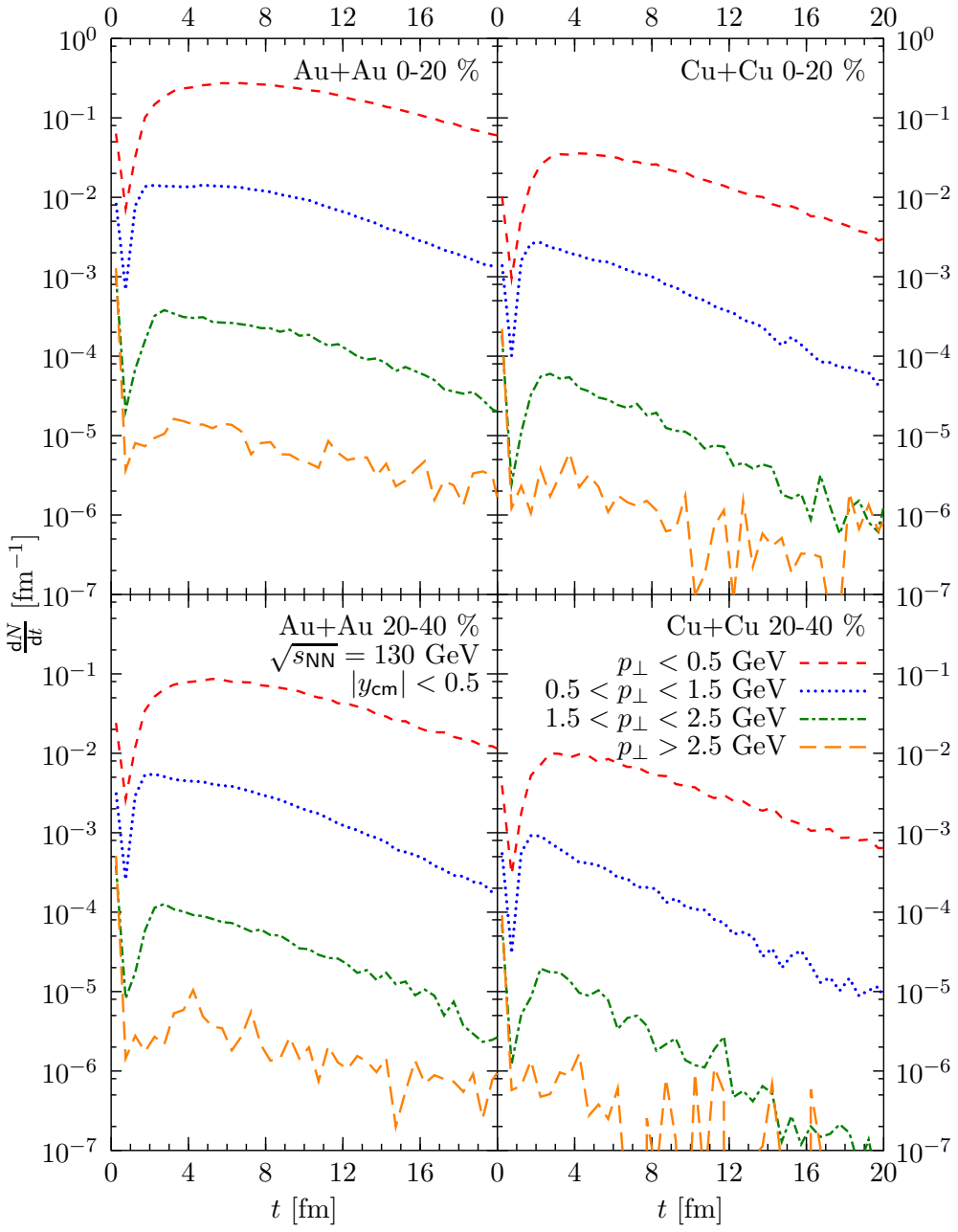

Figure 7.18: UrQMD calculation of central (0-20 %, upper panels) and mid-central (20-40 %, lower panels) Au+Au-collisions (left panels) and Cu+Cu-collisions (right panels) at $\sqrt{s_{NN}} = 130$ GeV. Emission time distribution of photons in the momentum ranges $p_\perp < 0.5$ GeV (dashed line), $0.5 < p_\perp < 1.5$ GeV (dotted line), $1.5 < p_\perp < 2.5$ GeV (dash-dotted line) and $p_\perp > 2.5$ GeV (long-dashed line).

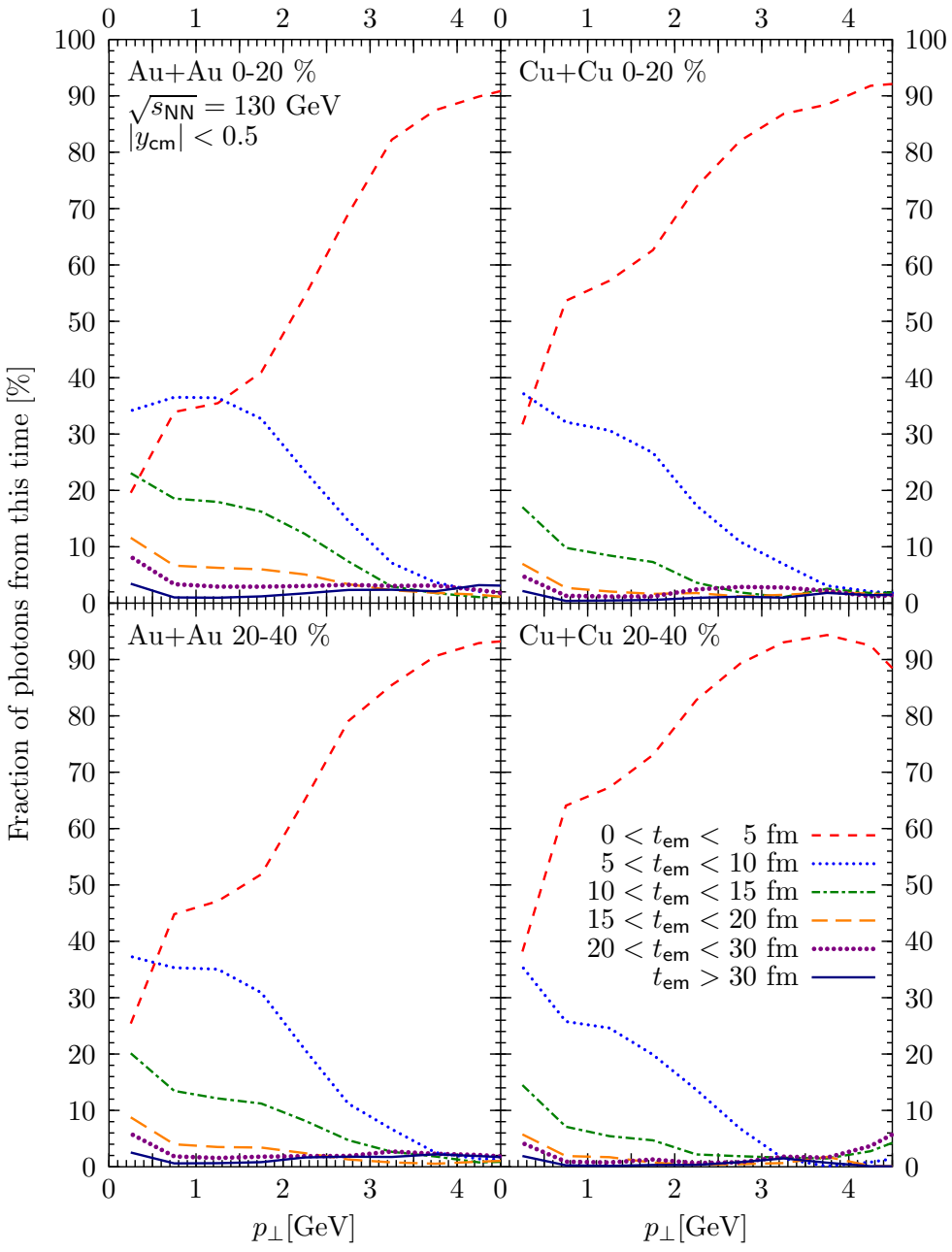

Figure 7.19: Fraction of photons that are emitted from $0 < t < 5$ fm (dashed line), $5 < t < 10$ fm (dotted line), $10 < t < 15$ fm (dash-dotted line), $15 < t < 20$ fm (long dashed line), $20 < t < 30$ fm (short-dotted line) and $t > 30$ fm (solid line) as a function of transverse momentum in UrQMD-calculations of gold-gold collisions (left panels) and copper-copper collisions (right panels) for central (0-20 %, upper panels) and mid-central (20-40 %, lower panels) collisions at $\sqrt{s_{NN}} = 130$ GeV.

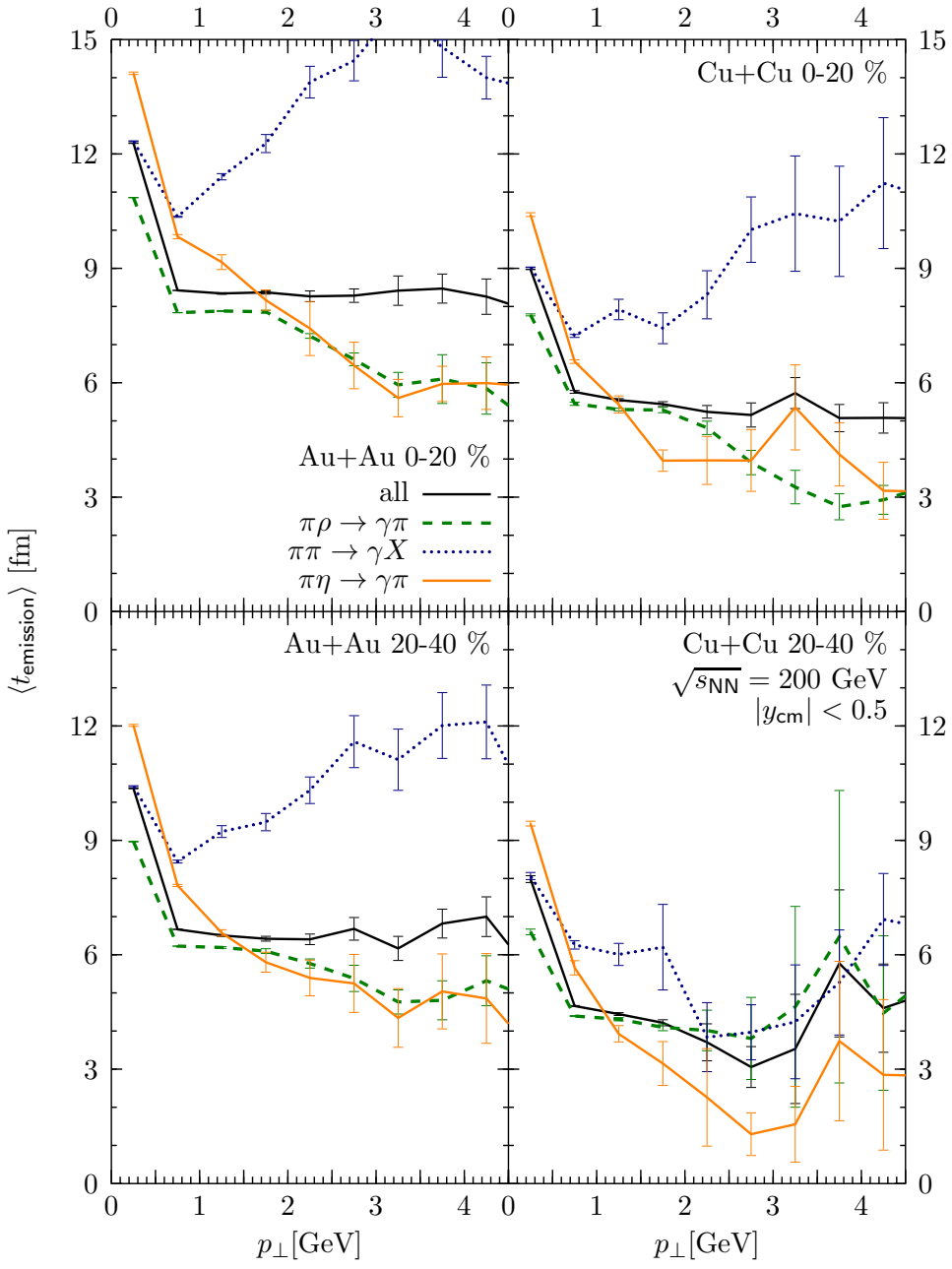

Figure 7.20: Average emission time of direct photons in cascade calculations of central (0-20 %, upper panels) and mid-central (20-40 %, lower panels) Au+Au-collisions (left panels) and Cu+Cu-collisions (right panels) at $\sqrt{s_{NN}} = 200$ GeV as function of transverse photon momentum for all channels (dark solid line), $\pi\pi$-collisions (dotted line), $\pi\rho$-collisions (dashed line) and $\pi\eta$-collisions (light solid line).

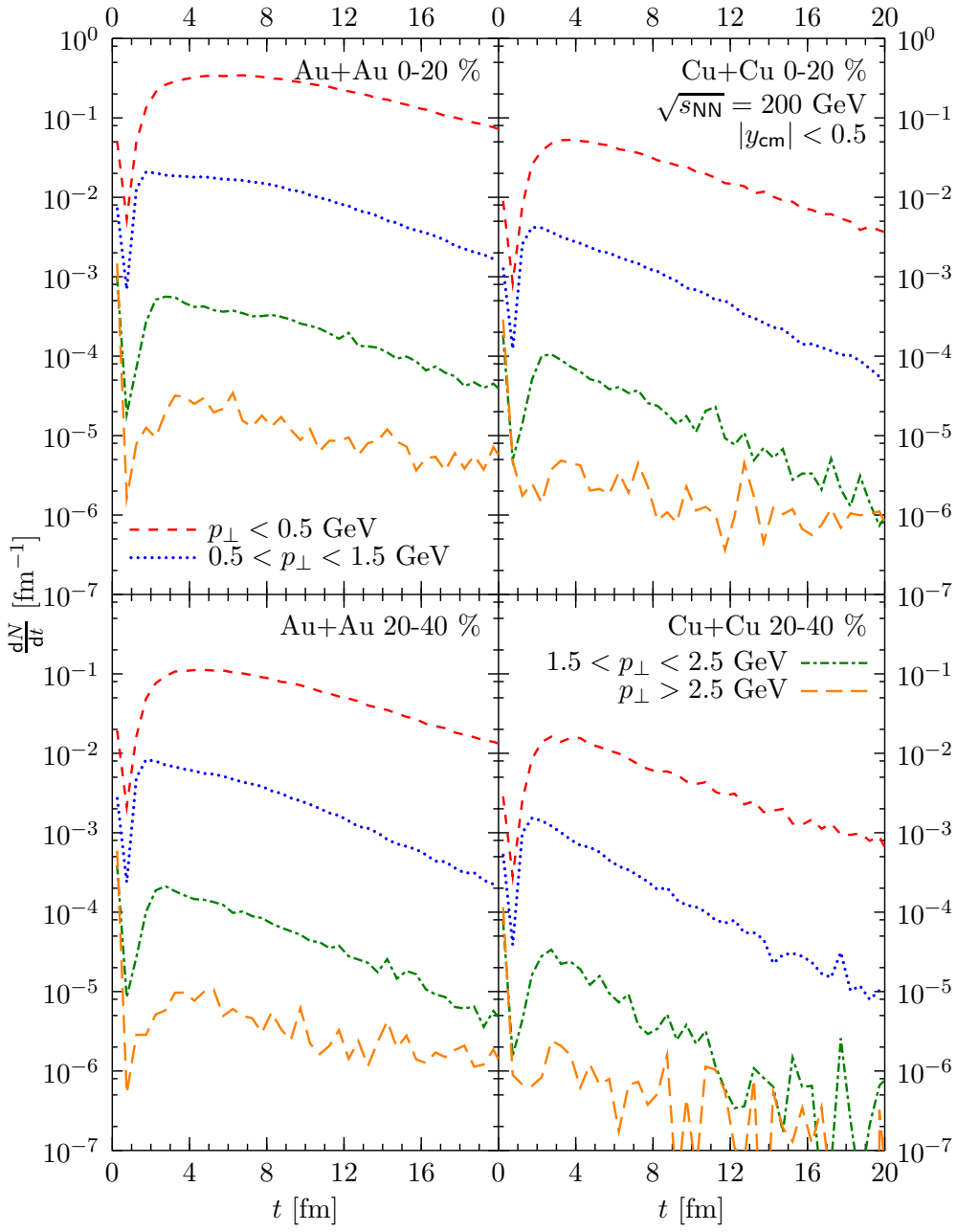

Figure 7.21: UrQMD calculation of central (0-20 %, upper panels) and mid-central (20-40 %, lower panels) Au+Au-collisions (left panels) and Cu+Cu-collisions (right panels) at $\sqrt{s_{NN}} = 200$ GeV. Emission time distribution of photons in the momentum ranges $p_\perp < 0.5$ GeV (dashed line), $0.5 < p_\perp < 1.5$ GeV (dotted line), $1.5 < p_\perp < 2.5$ GeV (dash-dotted line) and $p_\perp > 2.5$ GeV (long-dashed line).

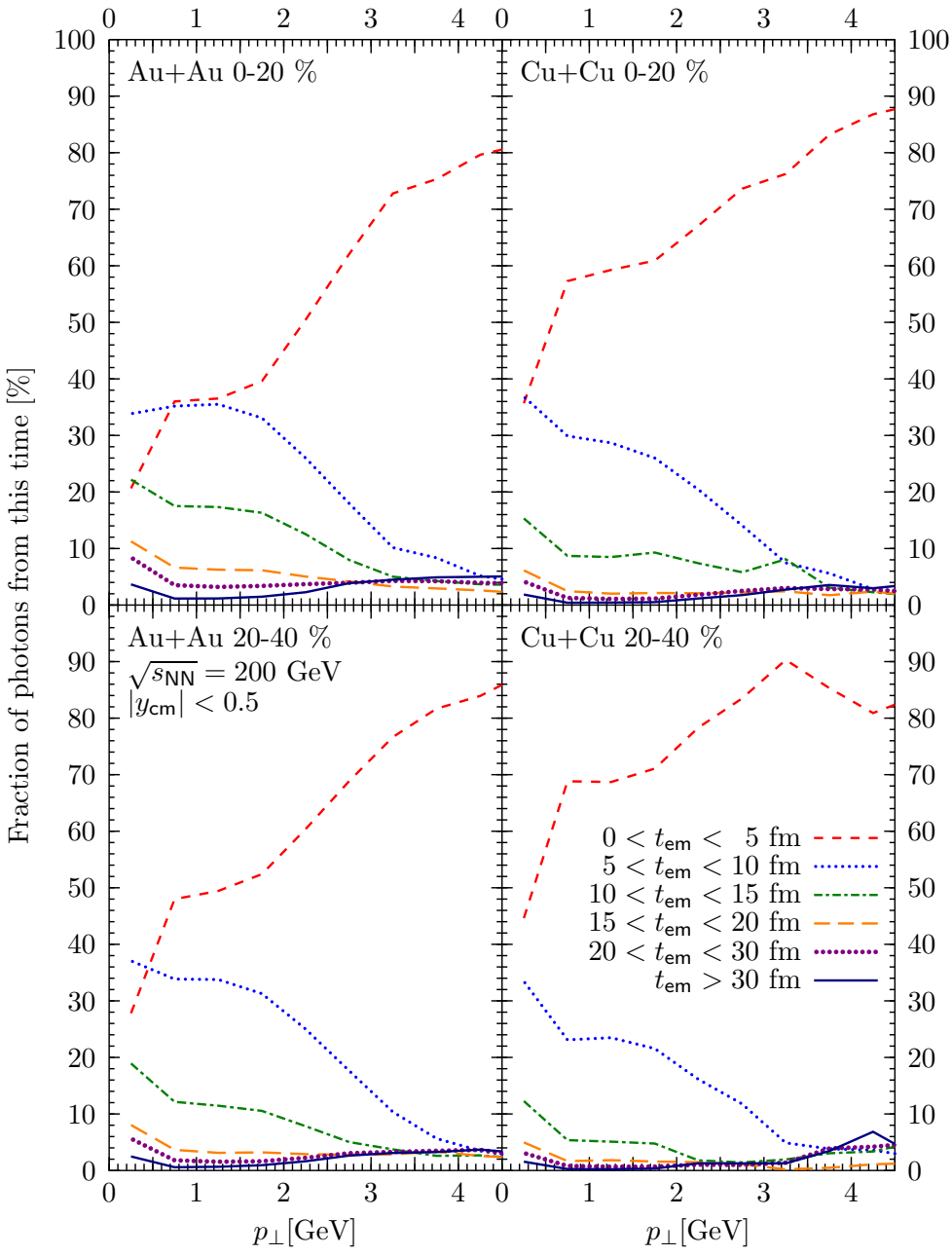

Figure 7.22: Fraction of photons that are emitted from $0 < t < 5$ fm (dashed line), $5 < t < 10$ fm (dotted line), $10 < t < 15$ fm (dash-dotted line), $15 < t < 20$ fm (long dashed line), $20 < t < 30$ fm (short-dotted line) and $t > 30$ fm (solid line) as a function of transverse momentum in UrQMD-calculations of gold-gold collisions (left panels) and copper-copper collisions (right panels) for central (0-20 %, upper panels) and mid-central (20-40 %, lower panels) collisions at $\sqrt{s_{NN}} = 200$ GeV.

Chapter 8

Baryon number density

One of the assumptions that is made in the extraction of both scattering cross-sections and thermal rates is that vacuum spectral functions can be used for the mesons. This means implicitly that the baryochemical potential μ_B and the baryon number density ρ_B at the points of photon emission are small. In the following Chapter, we will investigate this assumption in cascade calculations. The distribution of direct photons as a function of emission point baryon number density is examined for all direct photons and for photons in a given transverse momentum range.

Figure 8.1 shows the distribution of direct photons against the baryon number density ρ_B at their emission point in central U+U-collisions at $E_\mathsf{lab} = 35$ AGeV for various $p_\perp$-ranges. The baryon number density is given in units of the nuclear ground state baryon number density $\rho_0 = 0.16$ fm^{-3}. We note that the largest amount of photons is emitted from regions with low baryon number density $\rho_\mathsf{B} < 0.3\rho_0$. At higher $p_\perp$, the ratio between high-density photons and photons from low-density regions is higher, but the emission is still dominated by the later low-density part.

In Figure 8.2, we show the same analysis for central Pb+Pb-collisions at $E_\mathsf{lab} = 158$ AGeV. Here, photons are emitted at up to $\rho_\mathsf{B} \approx 2.8\rho_0$, and photons with transverse momenta higher than $p_\perp^\gamma = 3$ GeV are dominantly emitted from regions between $\rho_0 < \rho_\mathsf{B} < 2\rho_0$. This corresponds to early emission times, where a big fraction of the system is occupied by the lorentz-contracted nuclei, see Figure 7.12.

At RHIC-energies from $\sqrt{s_\mathsf{NN}} = 62.4$ GeV to $\sqrt{s_\mathsf{NN}} = 200$ GeV, the trend continues. While the overall spectrum is still completely dominated by emission from dilute regions $\rho_\mathsf{B} < 0.5\rho_0$, high-$p_\perp$ photons are emitted from dense regions. In Figures 8.3, 8.4 and 8.5, the distribution of photons with $3.5 < p_\perp < 4.5$ GeV and $p_\perp > 4.5$ GeV are shown separately in addition to the distributions at lower $p_\perp$. We find that in all of the systems at RHIC (gold-gold collisions and copper-copper collisions, central and mid-central collisions, $\sqrt{s_\mathsf{NN}} = 62.4$ GeV, $\sqrt{s_\mathsf{NN}} = 130$ GeV and $\sqrt{s_\mathsf{NN}} = 200$ GeV), photons with transverse momenta

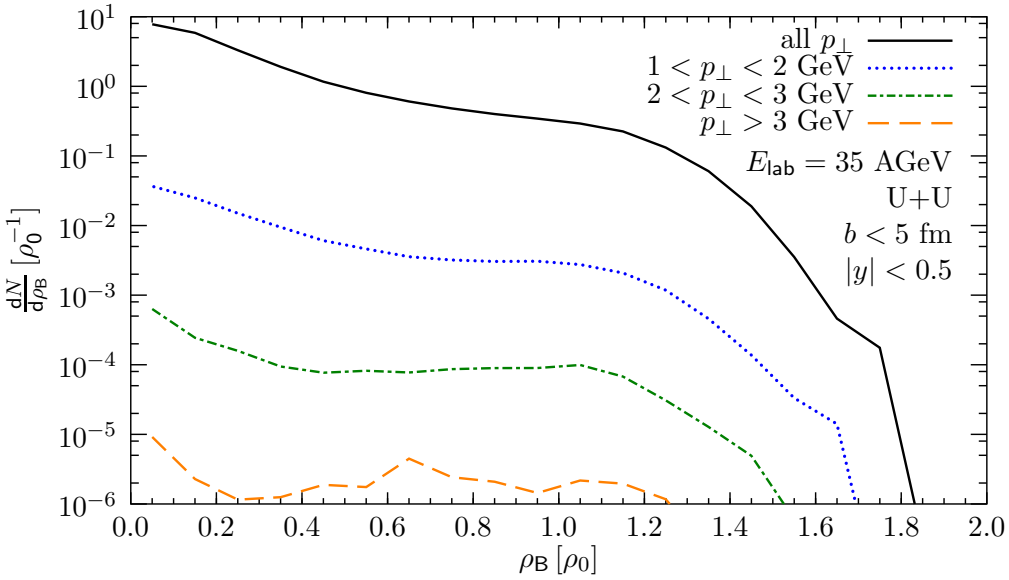

Figure 8.1: Distribution of direct photons against the baryon number density ρ_B at the emission point for cascade calculations of central U+U-collisions at $E_\mathsf{lab} = 35$ AGeV for all photons (solid line), for photons with $1 < p_\perp < 2$ GeV (dotted line), $2 < p_\perp < 3$ GeV (dash-dotted line) and $p_\perp > 3$ GeV (long-dashed line).

$p_\perp^\gamma > 2$ GeV are emitted in significant parts from regions with high baryon number densities. At $\sqrt{s_\mathsf{NN}} = 62.4$ GeV (see Figure 8.3), the density region that is accessible at high $p_\perp$ is $2\rho_0 < \rho_\mathsf{B} < 7\rho_0$. Photon emission from densities with even higher density is suppressed.

Densities up to $15\rho_0$ can be seen in central collisions at $\sqrt{s_\mathsf{NN}} = 130$ GeV, when triggering on photons with transverse momenta larger than $p_\perp \approx 2.5$ GeV, see Figure 8.4. The distribution of photons among the densities is rather insensible to the exact value of the photon transverse momentum above this value.

The highest energy – $\sqrt{s_\mathsf{NN}} = 200$ GeV – has the highest reach in density. In collisions of gold nuclei, photons are emitted from regions with baryon number densities as high as $\rho_\mathsf{B} = 25\rho_0$, and in copper-copper collisions, the emission comes from up to $\rho_\mathsf{B} = 22\rho_0$. The major part of the photons at high transverse momenta $p_\perp > 3$ GeV comes from $5\rho_0 < \rho_\mathsf{B} < 20\rho_0$.

In all systems at RHIC, the density-distributions of high-$p_\perp$ photons show a dip at intermediate baryon number densities and maxima at very low and rather high densities. At lower $p_\perp$, this dip is not present, so that the high-density part has no maximum anymore. As in the case of SPS-collisions, the maximum at high densities can be attributed to very early scatterings, when the nucleons from the initial nuclei are still very close to each other and are non-thermalised sources for a very high baryon number density. Photons from low-

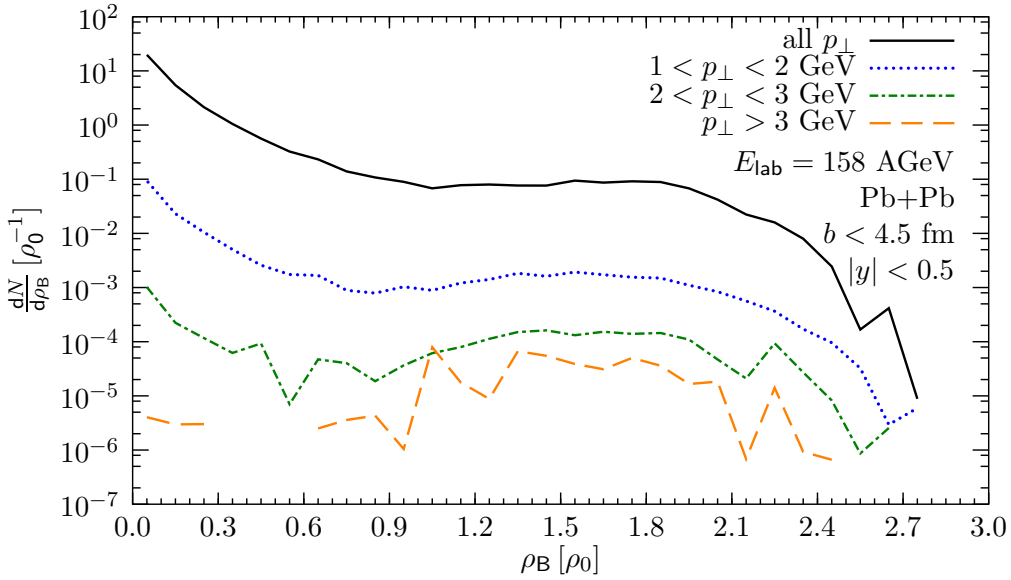

Figure 8.2: Distribution of direct photons against the baryon number density ρ_B at the emission point for cascade calculations of central Pb+Pb-collisions at $E_{\mathsf{lab}} = 158$ AGeV for all photons (solid line), for photons with $1 < p_\perp < 2$ GeV (dotted line), $2 < p_\perp < 3$ GeV (dash-dotted line) and $p_\perp > 3$ GeV (long-dashed line).

density regions, however, come from later parts of the evolution, when the initial nuclei have passed through each other and the resulting thermalised fireball evolves in regions of small chemical potential and therefore also small baryon number densities.

Concluding, we find that the bulk of photons (i.e. low-$p_\perp$ photons) are emitted dominantly from regions with very low net baryon densities $\rho_\mathsf{B} \ll 1\rho_0$. At low collision energies, even high-$p_\perp$ photons are not dominantly emitted from regions in which spectral functions of the mesons should be affected too much, and at RHIC-energies, high-$p_\perp$ photons are emitted from a non-thermalised system with very high net baryon number density at which the behaviour of meson spectral functions is completely unknown. Therefore, the use of vacuum spectral functions should not affect the final spectra by too much.

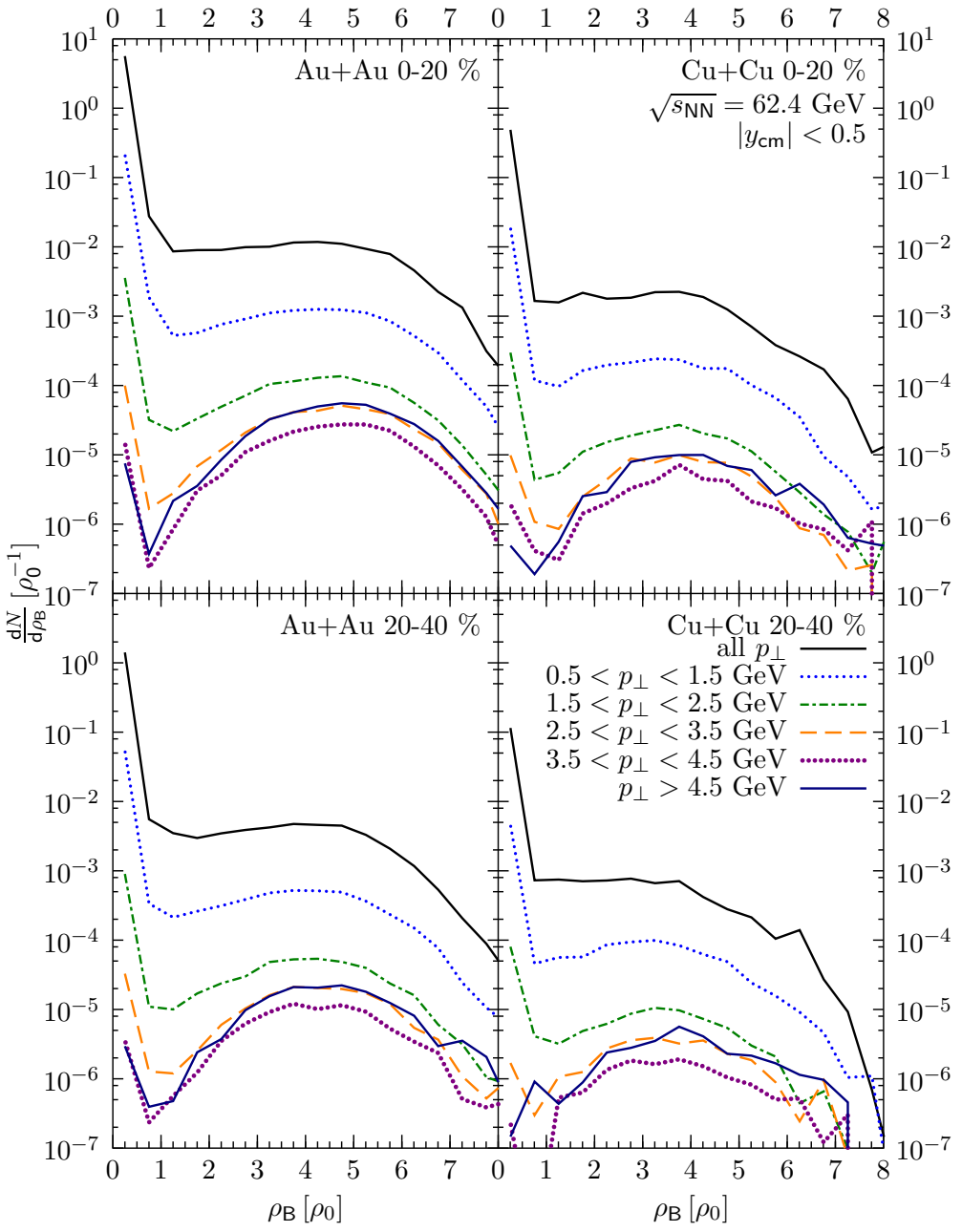

Figure 8.3: Distribution of direct photons against baryon number density ρ_B at the emission point for cascade calculations of central (0-20 %, upper panels) and mid-central (20-40 %, lower panels) Au+Au- (left panels) and Cu+Cu-collisions (right panels) at $\sqrt{s_{NN}} = 62.4$ GeV for all photons (upper solid line), for photons with $0.5 < p_\perp < 1.5$ GeV (dotted line), $1.5 < p_\perp < 2.5$ GeV (dash-dotted line), $2.5 < p_\perp < 3.5$ GeV (long-dashed line), $3.5 < p_\perp < 4.5$ GeV (short-dotted line) and $p_\perp > 4.5$ GeV (lower solid line).

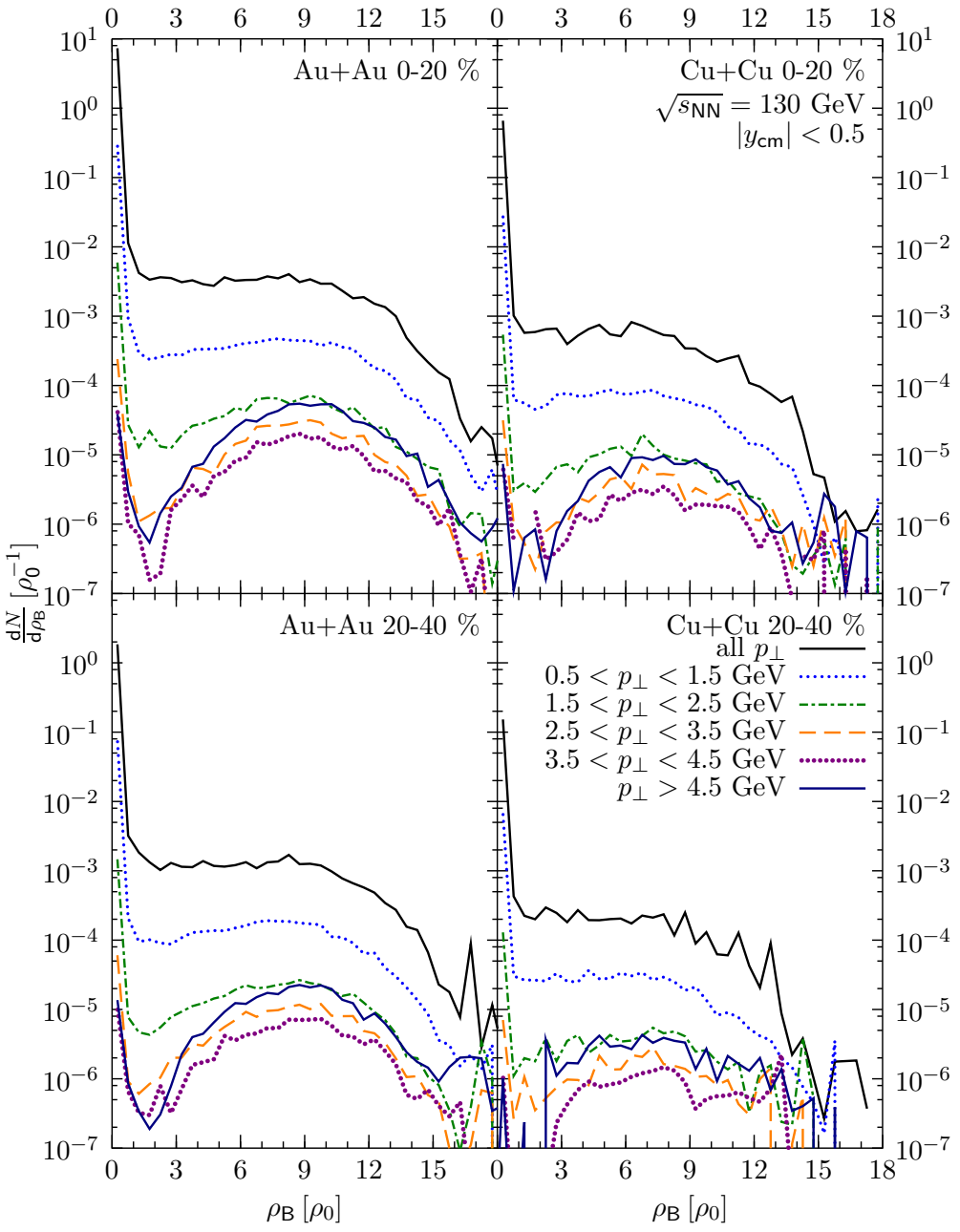

Figure 8.4: Distribution of direct photons against baryon number density ρ_B at the emission point for cascade calculations of central (0-20 %, upper panels) and mid-central (20-40 %, lower panels) Au+Au- (left panels) and Cu+Cu-collisions (right panels) at $\sqrt{s_{\mathsf{NN}}} = 130$ GeV for all photons (upper solid line), for photons with $0.5 < p_\perp < 1.5$ GeV (dotted line), $1.5 < p_\perp < 2.5$ GeV (dash-dotted line), $2.5 < p_\perp < 3.5$ GeV (long-dashed line), $3.5 < p_\perp < 4.5$ GeV (short-dotted line) and $p_\perp > 4.5$ GeV (lower solid line).

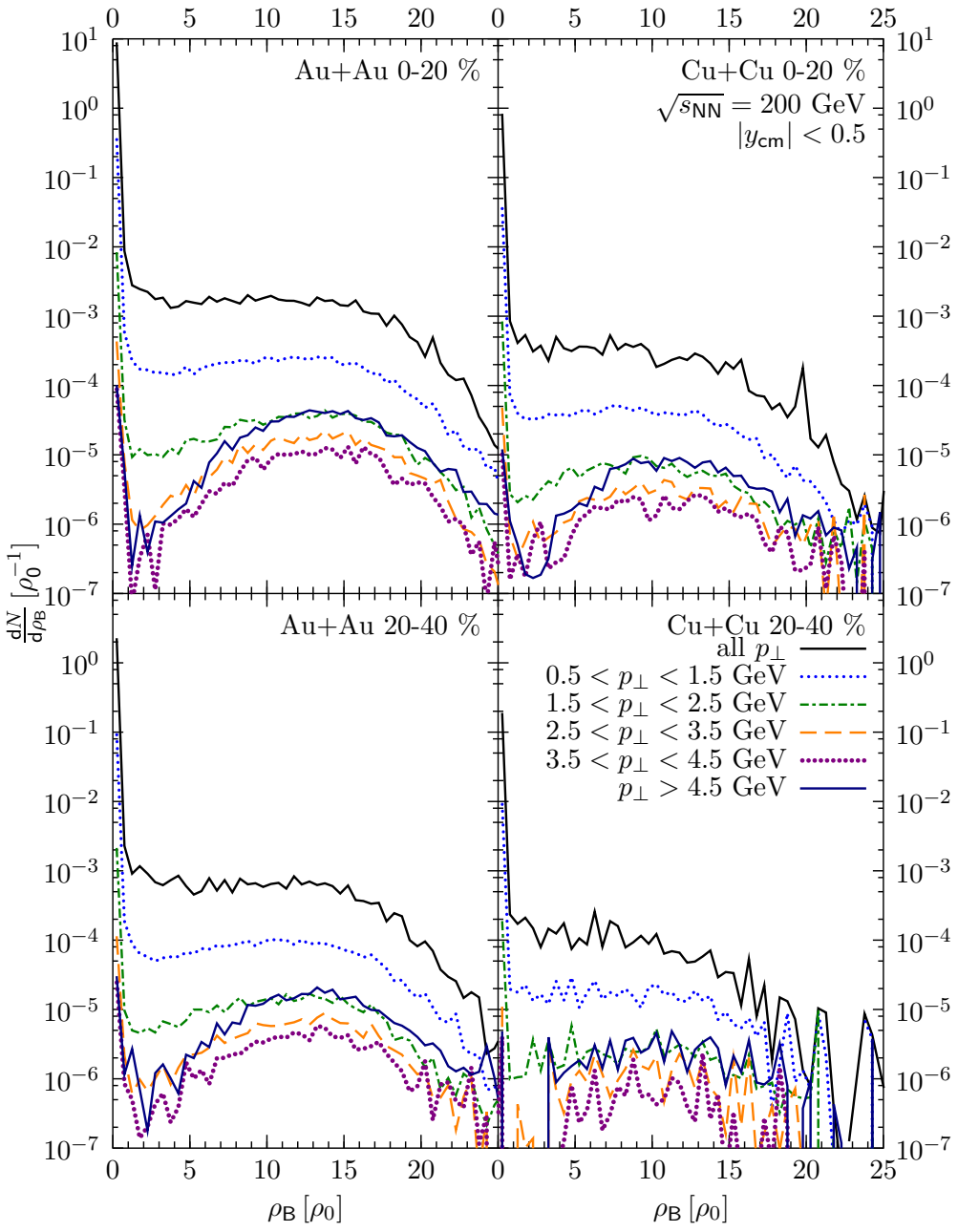

Figure 8.5: Distribution of direct photons against baryon number density ρ_B at the emission point for cascade calculations of central (0-20 %, upper panels) and mid-central (20-40 %, lower panels) Au+Au- (left panels) and Cu+Cu-collisions (right panels) at $\sqrt{s_{NN}} = 200$ GeV for all photons (upper solid line), for photons with $0.5 < p_\perp < 1.5$ GeV (dotted line), $1.5 < p_\perp < 2.5$ GeV (dash-dotted line), $2.5 < p_\perp < 3.5$ GeV (long-dashed line), $3.5 < p_\perp < 4.5$ GeV (short-dotted line) and $p_\perp > 4.5$ GeV (lower solid line).

Chapter 9

Summary

In the present work, direct photon emission from heavy-ion collisions has been calculated and compared to available experimental data. Three different models have been combined to extract direct photons from different environments in a heavy-ion collision: Thermal photons from partonic and hadronic matter have been extracted from relativistic, non-viscous 3+1-dimensional hydrodynamic calculations. Thermal and non-thermal photons from hadronic interactions have been calculated from relativistic transport theory. Prompt photons from pQCD interactions in primordial nucleon-nucleon scatterings have been taken from [Tur04] and [Gor93] to allow for comparison to experimental data. The impact of different physics assumptions about the thermalized matter has been studied. In pure transport calculations, a viscous hadron gas is present. This is juxtaposed with ideal gases of hadrons with vacuum properties, hadrons which undergo a chiral and deconfinement phase transition and with a system that has a strong first-order phase transition to a deconfined ideal gas of quarks and gluons in the hybrid model calculations with the various Equations of State.

The models used for the determination of photons from both hydrodynamic and transport calculations have been elucidated and their numerical properties tested. The origin of direct photons, itemised by emission stage, emission time, channel and baryon number density, has been investigated for various systems, as have the transverse momentum spectra and elliptic flow patterns of direct photons.

The differences of photon emission rates from a thermalized transport box and the hadronic photon emission rates that are used in hydrodynamic calculations are found to be very similar, as are the spectra from calculations of heavy-ion collisions with transport model and hybrid model with hadronic Equation of State. Taking into account the full (vacuum) spectral function of the ρ-meson decreases the direct photon emission by approximately 10 % at low photon transverse momentum. The numerical investigations show that the parameter with the largest impact on the direct photon spectra is the time at

which the hydrodynamic description is started. Its variation shows deviations of one to two orders of magnitude. In the regime that can be considered physical, however, the variation is less than a factor of 3. Other parameters change the direct photon yield by up to approximately 20 %.

In all systems that have been considered – heavy-ion collisions at $E_{\mathsf{lab}} = 35$ AGeV, $E_{\mathsf{lab}} = 158$ AGeV, $\sqrt{s_{\mathsf{NN}}} = 62.4$ GeV, $\sqrt{s_{\mathsf{NN}}} = 130$ GeV and $\sqrt{s_{\mathsf{NN}}} = 200$ GeV – thermal emission from a system with partonic degrees of freedom is greatly enhanced over that from hadronic systems, while the difference between the direct photon yields from a viscous and a non-viscous hadronic system (transport vs. hydrodynamics) is found to be very small.

Predictions for direct photon emission in central U+U-collisions at $E_{\mathsf{lab}} = 35$ AGeV have been made. Since non-soft photon sources are very much suppressed at this energy, experimental results should very easily be able to distinguish between a medium that is entirely hadronic and a system that undergoes a phase transition from partonic to hadronic matter.

In the case of lead-lead collisions at $E_{\mathsf{lab}} = 158$ AGeV, the situation is not so clear. In central collisions, the complete direct photon spectra including prompt photons seem to favour hadronic emission sources, while the partonic calculations only slightly overpredict the data. In peripheral collisions at the same energy, the hadronic contribution is more than one order of magnitude smaller than the prompt photon contribution, which fits the available experimental data. A similar picture presents itself at higher energies. At RHIC energies, however, the difference between transport calculations and hadronic hybrid model calculations is largest. Hybrid model calculations with partonic degrees of freedom can describe the experimental results in gold-gold collisions at $\sqrt{s_{\mathsf{NN}}} = 200$ GeV.

The elliptic flow component of direct photon emission is found to be consistently positive at small transverse momenta. This means that the initial photon emission from a non-flowing medium does not completely overshine the emission patterns from later stages. High-$p_\perp$ photons, however, do dominantly come from the beginning of a heavy-ion collision and therefore do not carry the directed information of an evolving medium.

The relative contributions of hadronic channels, thermal partonic emission and prompt photons show a decrease of the hadronic contribution with increasing energy, as was expected for a system that thermalizes farther inside the deconfined phase. Prompt photons become the dominant source of direct photon emission only at high $p_\perp$ at RHIC energies, while at SPS it is subleading to the thermal emission from a QGP in the complete experimentally resolvable $p_\perp$-range. Of the hadronic channels, thermal $\pi\rho$-scatterings are the biggest source of direct photons at all but very low $p_\perp$, where due to the collision kinematics $\pi\pi$-collisions produce more photons.

The detailed analyses of direct photon origins consistently show that the intermediate stage of a heavy-ion reaction dominates the direct photon spectra at low and intermediate $p_\perp$, while early emission dominates the high-$p_\perp$-part of the spectra. Early emission is at high initial collision energies (RHIC-systems)

connected to significantly higher baryon number densities than the later bulk emission. At lower energies (SPS and FAIR), the ratio of photons from low baryon densities and from high baryon densities decreases at high $p_\perp$, but is much higher at low $p_\perp$. In this region, at RHIC about three orders of magnitude lie between the photon yield from low- to high baryon number densities, while at FAIR, it is merely one order of magnitude.

In conclusion, this first detailed investigation of direct photon emission from a hybrid model including every significant source of direct photon emission shows that the measured direct photon spectra at RHIC unambiguously show signs of a partonic medium, while the situation at SPS is less clear. The predictions for FAIR will give a clear distinction between hadronic and partonic emission, and the detailed analysis performed in this work can give hints as to what measurements can be made to extract information about the hot and dense stages of a heavy-ion collision.

Appendix A

Kinetic variables in $2 \leftrightarrow 2$ scatterings

A.1 Mandelstam variables

Figure A.1 shows a schematic view of scatterings with two incoming and two outgoing particles. The Mandelstam variables s, t and u are defined as

$$s = (p_1 + p_2)^2 = (p_3 + p_4)^2 \quad , \tag{A.1a}$$

$$t = (p_1 - p_3)^2 = (p_2 - p_4)^2 \quad , \tag{A.1b}$$

$$u = (p_1 - p_4)^2 = (p_2 - p_3)^2 \quad , \tag{A.1c}$$

and their sum is

$$s + t + u = m_1^2 + m_2^2 + m_3^2 + m_4^2 \quad . \tag{A.1d}$$

From these variables, various quantities in the center-of-mass frame cm can be expressed. The cm-frame is defined as the frame in which the total three-momentum of the incoming (and therefore also the outgoing) particles vanish:

$$\vec{p}_1 + \vec{p}_2 = \vec{p}_3 + \vec{p}_4 = \vec{0} \quad , \tag{A.2}$$

$$\vec{p}_1 = -\vec{p}_2 = \vec{p}_{\mathsf{cm}} \tag{A.3}$$

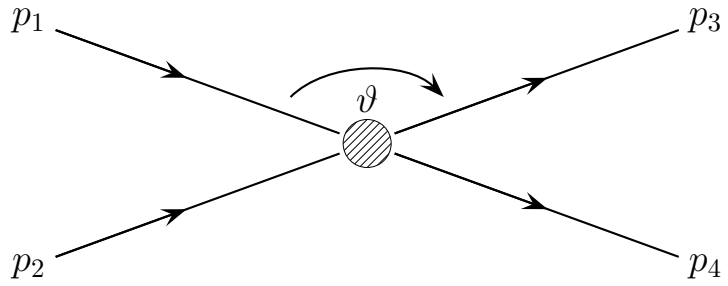

Figure A.1: Schematic view of the kinetic variables in a $2 \leftrightarrow 2$-scattering.

With the relativistic relation between mass m, energy E and momentum p, $E = \sqrt{m^2 + p^2}$, we can relate E_1^{cm} and E_2^{cm}:

$$E_2^{\mathsf{cm}} = \sqrt{m_2^2 + p_{\mathsf{cm}}^2} = \sqrt{m_2^2 + E_1^{\mathsf{cm}\,2} - m_1^2} \quad . \tag{A.4}$$

From this (and the according relations between E_3 and E_4), it follows that

$$E_1^{\mathsf{cm}} = \frac{s + m_1^2 - m_2^2}{2\sqrt{s}} \quad , \tag{A.5a}$$

$$E_2^{\mathsf{cm}} = \frac{s + m_2^2 - m_1^2}{2\sqrt{s}} \quad , \tag{A.5b}$$

$$E_3^{\mathsf{cm}} = \frac{s + m_3^2 - m_4^2}{2\sqrt{s}} \quad , \tag{A.5c}$$

$$E_4^{\mathsf{cm}} = \frac{s + m_4^2 - m_3^2}{2\sqrt{s}} \quad , \tag{A.5d}$$

$$E_1^{\mathsf{cm}} + E_2^{\mathsf{cm}} = \sqrt{s} \quad , \tag{A.5e}$$

$$E_1^{\mathsf{cm}} - E_3^{\mathsf{cm}} = \frac{m_1^2 - m_2^2 - m_3^2 + m_4^2}{2\sqrt{s}} \quad , \tag{A.5f}$$

$$E_1^{\mathsf{cm}} - E_4^{\mathsf{cm}} = \frac{m_1^2 - m_2^2 + m_3^2 - m_4^2}{2\sqrt{s}} \quad , \tag{A.5g}$$

Equation (A.5f) leads us to t:

$$\begin{aligned} t &= (p_1 - p_3)^2 \\ &= (E_1 - E_3)^2 - (\vec{p}_1 - \vec{p}_3)^2 \\ &= \left(\frac{m_1^2 - m_2^2 - m_3^2 + m_4^2}{2\sqrt{s}} \right)^2 - \left(\sqrt{E_1^{\mathsf{cm}} - m_1^2} - \sqrt{E_3^{\mathsf{cm}} - m_1^3} \right)^2 \\ &\quad - 4 p_1^{\mathsf{cm}} p_3^{\mathsf{cm}} \sin^2 \left(\frac{\vartheta_{\mathsf{cm}}}{2} \right) \quad . \end{aligned} \tag{A.6}$$

We can read off the smallest and largest possible value for t from Equation (A.6):

$$\begin{aligned} t_{\mathsf{min}} = t_+ = &\left(\frac{m_1^2 - m_2^2 - m_3^2 + m_4^2}{2\sqrt{s}} \right)^2 \\ &- \left(\sqrt{\frac{(s + m_1^2 - m_2^2)^2}{4s} - m_1^2} + \sqrt{\frac{(s + m_3^2 - m_4^2)^2}{4s} - m_3^2} \right)^2 \quad , \end{aligned} \tag{A.7}$$

$$\begin{aligned} t_{\mathsf{max}} = t_- = &\left(\frac{m_1^2 - m_2^2 - m_3^2 + m_4^2}{2\sqrt{s}} \right)^2 \\ &- \left(\sqrt{\frac{(s + m_1^2 - m_2^2)^2}{4s} - m_1^2} - \sqrt{\frac{(s + m_3^2 - m_4^2)^2}{4s} - m_3^2} \right)^2 \quad . \end{aligned} \tag{A.8}$$

Note that the sign in the name of $t_\pm$ corresponds to the sign in the brackets, so that $t_{\mathsf{min}} = t_+$ and $t_{\mathsf{max}} = t_-$.

In the cases we are interested in $m_3 = m_\gamma = 0$. Thus, the equations simplify to

$$t_\pm = \left(\frac{m_1^2 - m_2^2 + m_4^2}{2\sqrt{s}}\right) - \left\{\sqrt{\frac{(s + m_1^2 - m_2^2)^2}{4s} - m_1^2} \pm \frac{s - m_4^2}{2\sqrt{s}}\right\}^2 \quad . \tag{A.9}$$

The angle between particles 1 and 3 in the cm-frame can be derived from Equation (A.6):

$$\cos\vartheta = \frac{t - m_1^2 + 2E_1^{\mathsf{cm}}\omega}{2p^{\mathsf{cm}}\omega} \quad , \tag{A.10}$$

where ω is the energy of the photon in the cm-frame

$$\omega = E_3^{\mathsf{cm}} = \frac{s - m_4^2}{2\sqrt{s}} \quad . \tag{A.11}$$

Since Equation (A.1d) connects t and u, all of the above calculations can also be done for u and $u_\pm$ with very similar results.

In Section 3.5, the differential cross-sections from Equation (3.23) have been analytically integrated over t in order to calculate the total electromagnetic cross-section listed in Equation (3.26):

$$\sigma_{\mathsf{em}} = \int_{t_+}^{t_-} \frac{\mathsf{d}\sigma}{\mathsf{d}t}\mathsf{d}t \quad . \tag{A.12}$$

For the spherically symmetric cross-section of the process $\pi\rho \to a_1 \to \gamma\pi$, however, the procedure is reversed, since the total cross-section is given:

$$\frac{\mathsf{d}\sigma}{\mathsf{d}t} = \underbrace{\frac{\mathsf{d}\sigma}{\mathsf{d}\cos\vartheta}}_{\sigma/2}\underbrace{\frac{\mathsf{d}\cos\vartheta}{\mathsf{d}t}}_{1/2p_{\mathsf{cm}}\omega} = \frac{\sigma}{4p_{\mathsf{cm}}\omega} \tag{A.13}$$

A.2 Lorentz-Transformations

When photon emission is calculated from a collision, the photon momentum $k^\mu = (\omega, \vec{k})$ is first calculated in the cm-frame and then boosted to the calculational frame. In the first step, the incoming momenta p_1^μ and p_2^μ are transformed into the cm-frame and then rotated in two steps so that the momentum of particle 1 points in positive z-direction.

The velocity four-vector u^μ used in the Lorentz-transformation is calculated from the four-momenta of the incoming particles:

$$U^\mu = \frac{1}{\sqrt{s}}\left(p_1^\mu + p_2^\mu\right) \tag{A.14}$$

$$u^\mu = \left(U^0, -U^i\right) \quad . \tag{A.15}$$

Equation (A.15) is defined in such a way that the transformation ends in the rest frame of the collision and does not double its boost. The Lorentz transformation itself can be expressed as a matrix multiplication acting on the initial four-vector $x^{\mu\prime} = \Lambda^{\mu}{}_{\nu} x^{\nu}$ in terms of the rapidity vector $\vec{\eta} = (\eta_1, \eta_2, \eta_3)$ with $\eta = |\vec{\eta}| = \frac{1}{2}\log\left(\frac{1+\beta}{1-\beta}\right)$ or the velocity $\vec{\beta}$ with $\gamma = \sqrt{1-\beta^2}^{-1}$:

$$\begin{array}{rcccccl} \Lambda^0{}_0 & = & \cosh(\eta) & = & \gamma & = & u^0 \\ \Lambda^0{}_i & = & \frac{\eta_i}{\eta}\sinh(\eta) & = & \beta_i\gamma & = & u^i \\ \Lambda^i{}_j & = & \delta^i{}_j + \frac{\eta^i\eta_j}{\eta^2}(\cosh(\eta)-1) & = & \delta^i{}_j + \frac{\beta^i\beta_j}{\beta^2}(\gamma-1) & & \\ & & & = & \delta^i{}_j + \frac{u^i u_j}{u^2}\left(u^0-1\right) & & \end{array} \quad . \tag{A.16}$$

The transformations can be reformulated to reduce the numerical effort:

$$\vec{x}\,' = \vec{x} + \vec{\beta}\left[\gamma\left(\frac{\gamma\vec{\beta}\vec{x}}{1+\gamma} + x_0\right)\right] \quad , \tag{A.17a}$$

$$x^{0\prime} = \gamma\left(x_0 + \vec{\beta}\vec{x}\right) \quad . \tag{A.17b}$$

The center-of-mass momenta of the two particles $\pm\vec{p}\,'$ are then rotated in the first step so that they are in the y-z-plane (see Figure A.2):

$$\begin{pmatrix} 0 \\ p''_y \\ p''_z \end{pmatrix} = \begin{pmatrix} \frac{p'_y}{\sqrt{{p'_x}^2+{p'_y}^2}} & -\frac{p'_x}{\sqrt{{p'_x}^2+{p'_y}^2}} & 0 \\ \frac{p'_x}{\sqrt{{p'_x}^2+{p'_y}^2}} & \frac{p'_y}{\sqrt{{p'_x}^2+{p'_y}^2}} & 0 \\ 0 & 0 & 1 \end{pmatrix} \begin{pmatrix} p'_x \\ p'_y \\ p'_z \end{pmatrix} \quad , \tag{A.18}$$

and then a second rotation is done which rotates the momenta to the z-axis

$$\begin{pmatrix} 0 \\ 0 \\ p'''_z \end{pmatrix} = \begin{pmatrix} 1 & 0 & 0 \\ 0 & \frac{p'_z}{\sqrt{{p'_x}^2+{p'_y}^2+{p'_z}^2}} & -\frac{p''_y}{\sqrt{{p'_x}^2+{p'_y}^2+{p'_z}^2}} \\ 0 & \frac{p''_y}{\sqrt{{p'_x}^2+{p'_y}^2+{p'_z}^2}} & \frac{p'_z}{\sqrt{{p'_x}^2+{p'_y}^2+{p'_z}^2}} \end{pmatrix} \begin{pmatrix} 0 \\ p''_y \\ p''_z \end{pmatrix} \quad . \tag{A.19}$$

In the coordinate system $'''$, the photon momentum $\vec{k}\,'''$ is created. The polar angle $\cos\vartheta$ is calculated from the Mandelstam variable t (see Equation (A.10)) and the azimuthal angle $\varphi \in [0; 2\pi)$ is selected randomly from a flat distribution. Then, the transformations are reversed, i.e. $\vec{k}\,''$ is calculated from a rotation of $\vec{k}\,'''$ around the x-axis with $-\phi'$, $\vec{k}\,'$ is the result of a rotation of $\vec{k}\,''$ around the z-axis with $-\phi$ and k^μ is obtained from a Lorentz-transformation of $(|\vec{k}\,'|, \vec{k}\,')$ with U^μ.

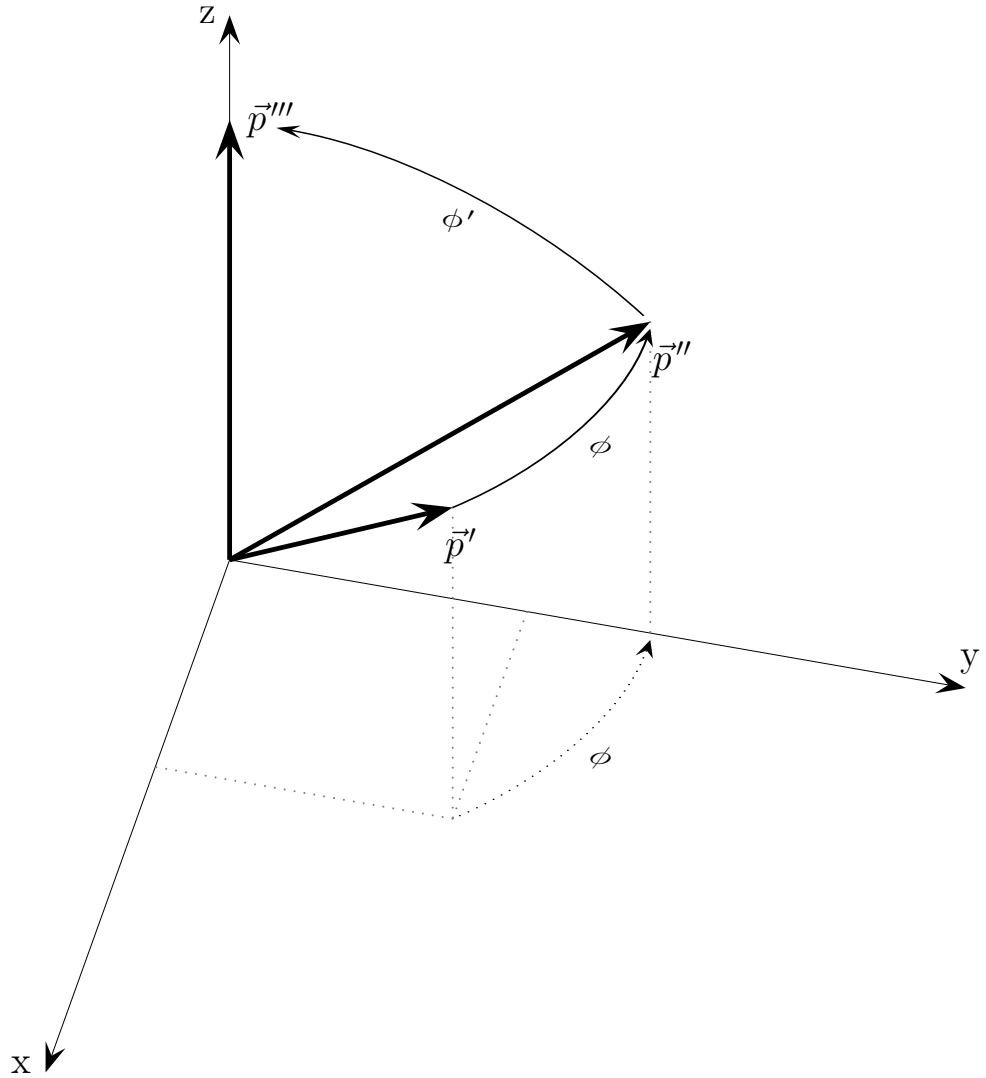

Figure A.2: Rotation of the momenta. First, a rotation around the z-axis with the angle ϕ transfers $\vec{p}'$ to $\vec{p}''$, then a rotation around the x-axis with ϕ' transforms $\vec{p}''$ to $\vec{p}'''$.

Appendix B

Photons from Hydrodynamics

All cells in the hydrodynamic phase that have not yet been transferred to the transport phase (in the case of the gradual transition) are considered for photon emission. The rates given in Section 3.5.2 need to be generalised to a moving coordinate system by replacing $E \to p^\mu u_\mu$. Because of this transformation, no obvious symmetries can be used to sample them. The most thorough possibility is to sample the complete momentum space for every cell,

$$N^\gamma(p_x, p_y, p_z) = \sum_{a=1}^{\frac{T}{\Delta t}} \sum_{i=1}^{\frac{L_x}{\Delta L}} \sum_{j=1}^{\frac{L_y}{\Delta L}} \sum_{k=1}^{\frac{L_z}{\Delta L}} R\left(T(x^\mu_{\mathsf{ijk}})\right) \Delta L^3 \Delta t \Delta p^3 \quad , \tag{B.1}$$

which requires about 10^{10} calculations of every rate per time step. In order to reduce the numerical cost of the calculation, several simplifications can be made. Due to the large number of cells and time steps, only every fifth time step is considered. Also, cold cells with $T < 30$ MeV are not considered, because the integrated photon yield from those cells is negligible.

Instead of sampling the complete phase space, each cell populates only one cell in phase space. This can be thought of as every cell emitting one fractional photon, much like every microscopic collision produces one fractional photon in the case of the cascade calculation. The fraction that goes into that phase space cell corresponds to the integrated yield of photons from that cell

$$N^\gamma = \Delta L^3 \, \Delta t \int \frac{d^3p}{E} \, R(E,T) \quad . \tag{B.2}$$

N^γ is Lorentz-invariant and can therefore be calculated in the rest frame and even be tabellised with justifiable effort.

However, the determination of the exact momentum needs more work. It is not possible to find closed algebraic expressions for the maxima of all rates with arbitrary velocity and temperatures, so that the application of a three-dimensional rejection method algorithm is highly discouraged.

It is well known [Coo74] that a boosted particle distribution cannot be achieved by generating particles in the rest frame and boosting them. However,

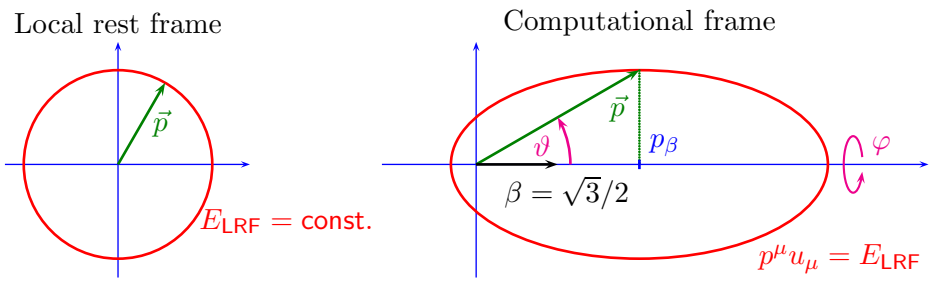

Figure B.1: Possible choices for $\vec{p}$ with a given local rest frame energy E_{LRF} for resting cells (left) and moving cells (right). The figure rotates around φ (in the x, y-plain).

the distributions of local rest frame energies E_{LRF} are obviously not affected by a Lorentz transformation and can be used to find the momentum distribution in the calculational frame. In a general frame, the role of the local rest frame energy E_{LRF} is transferred to the four-product of the cell's velocity and the particle's momentum $\Lambda = p_\mu u^\mu = E_{\mathsf{LRF}}$. If $p_\mu u^\mu$ is considered an independent variable, it can be fixed by a simple, one-dimensional rejection method algorithm from

$$\frac{1}{4\pi}\frac{\mathsf{d}N}{\mathsf{d}\Lambda} = \Lambda \; E\frac{\mathsf{d}N}{d^3p}\bigg|_{E=\Lambda} \quad . \tag{B.3}$$

The remaining task is to find a momentum $\vec{p}$ so that

$$p^\mu u_\mu = \Lambda \tag{B.4}$$

$$\frac{\Lambda}{\gamma} = p - \vec{\beta}\vec{p} = p(1 - \beta\cos\vartheta) \tag{B.5}$$

is fulfilled. In the last step, ϑ has been introduced as the angle between $\vec{p}$ and β. With the formulation in Equation (B.5), the number of independent variables from Equation (B.4) has been reduced from three to two. The remaining variable – the azimuthal angle φ – can be chosen freely. Solving Equation (B.5) for p one encounters the definition of an ellipsoid

$$p = \frac{\Lambda/\gamma}{1 - \beta\cos\vartheta} = \frac{\Lambda'}{1 - \beta\cos\vartheta} \quad . \tag{B.6}$$

Figure B.1 visualises the ellipsoid for a resting cell and a cell that moves with $\beta = \sqrt{3}/2$.

From the fact that the rates depend only on $\Lambda = p_\mu u^\mu$ it is clear that every Λ is equally probable. This translates to every surface element $\mathsf{d}A$ on the ellipsoid being equally probable:

$$\frac{\mathsf{d}N}{\mathsf{d}A(\vartheta,\varphi)} = \frac{N}{A} = \text{const.} \quad . \tag{B.7}$$

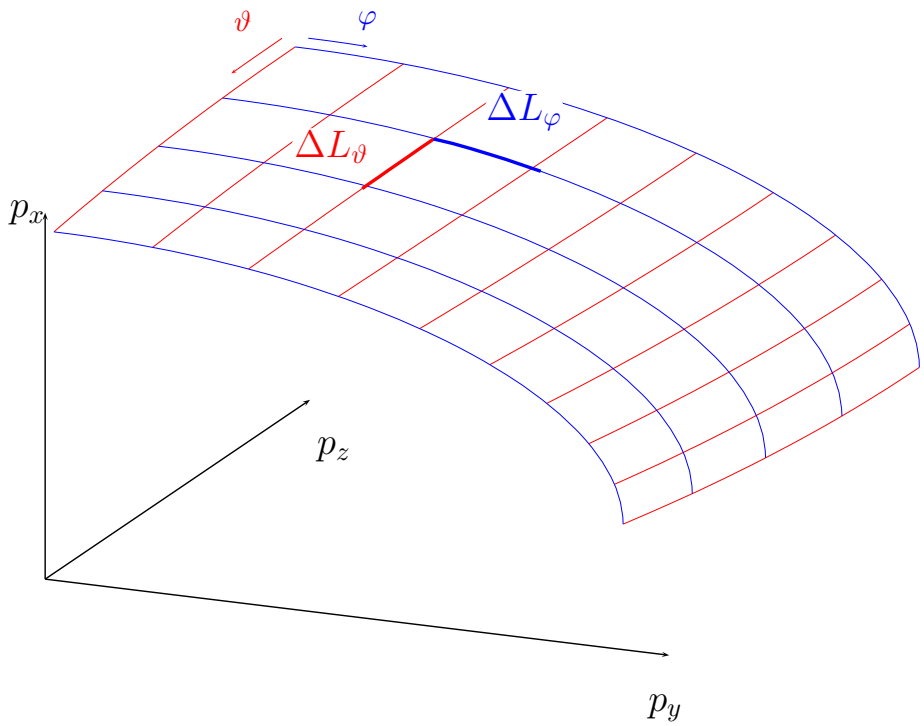

Figure B.2: Small excerpt from the surface of the $p^\mu u_\mu$-ellipsoid with the length elements ΔL_ϑ and ΔL_φ.

The surface element can be expressed in terms of the angles (compare Figure B.2) as

$$\mathsf{d}A = \mathsf{d}L_\varphi \mathsf{d}L_\vartheta \tag{B.8a}$$

$$\mathsf{d}L_\varphi = p(\vartheta)\sin\vartheta \mathsf{d}\varphi \tag{B.8b}$$

$$\begin{aligned}\mathsf{d}L_\vartheta &= \sqrt{p(\vartheta)^2 \mathsf{d}\vartheta^2 + \mathsf{d}p(\vartheta)^2} \\ &= \sqrt{p(\vartheta)^2 + \left(\frac{\partial p}{\partial \vartheta}\right)^2}\mathsf{d}\vartheta\end{aligned} \tag{B.8c}$$

$$\mathsf{d}A = p(\vartheta)\sin\vartheta\sqrt{p(\vartheta)^2 + \left(\frac{\partial p}{\partial \vartheta}\right)^2}\mathsf{d}\vartheta\mathsf{d}\varphi \quad . \tag{B.8d}$$

From Equation (B.8) and

$$\frac{\partial p}{\partial \vartheta} = -\frac{p^2}{\Lambda'}\beta\sin\vartheta \tag{B.9}$$

we can derive the distribution of ϑ:

$$\frac{\mathsf{d}N}{\mathsf{d}\vartheta} = 2\pi\frac{N}{A}p^2\sin\vartheta\sqrt{1+\left(\frac{p}{\Lambda'}\right)^2\beta^2\sin^2\vartheta} \quad , \tag{B.10a}$$

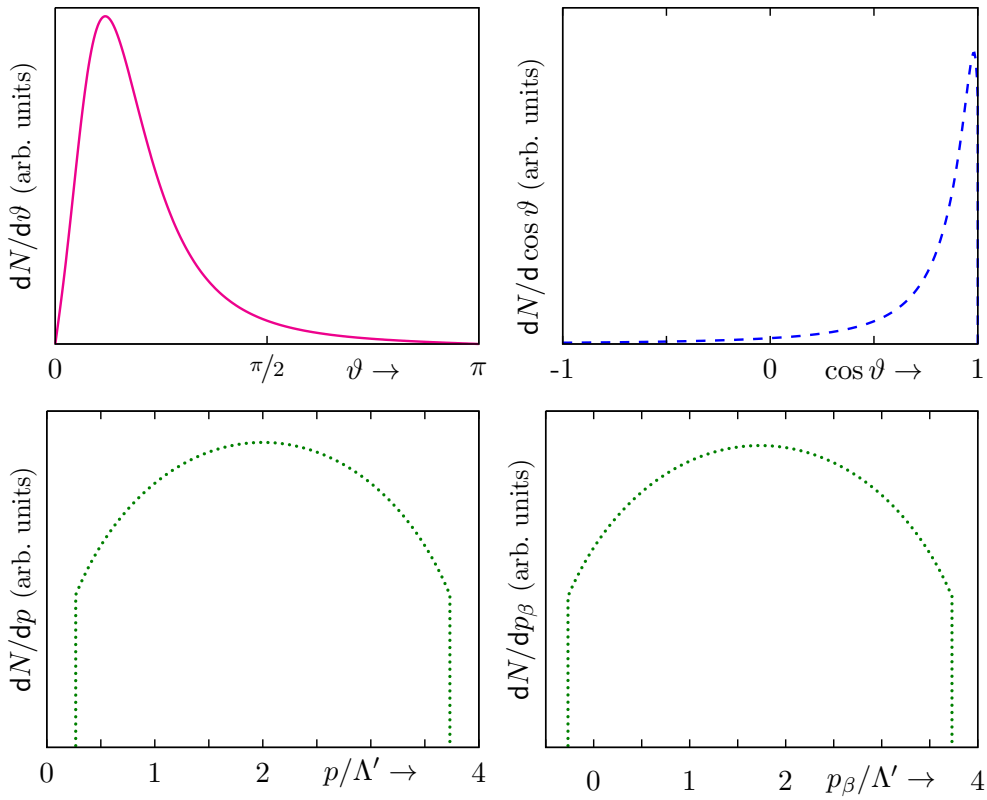

Figure B.3: The distributions of the angle ϑ (upper left), $\cos\vartheta$ (upper right) and the momenta p (lower left) and p_β (lower right) on an $p^\mu u_\mu$-ellipsoid with $\beta = \sqrt{3}/2$.

which can be reformulated to the distributions of momenta p or the momentum component along the direction of β p_β:

$$\frac{\mathrm{d}N}{\mathrm{d}p} = 2\pi \frac{N}{A\beta} \sqrt{p\left(p\beta^2 - p + 2\Lambda'\right)} \quad , \tag{B.10b}$$

$$\frac{\mathrm{d}N}{\mathrm{d}p_\beta} = 2\pi \frac{N}{A} \sqrt{\Lambda'^2 + \beta^2\left((\Lambda' + \beta p_\beta)^2 - p_\beta^2\right)} \quad . \tag{B.10c}$$

The resulting distributions for $\beta = \sqrt{3}/2$ are shown in Figure B.3. For an efficient choice of the variable the ratio between the integral of the distribution and the smallest rectangle that includes the function, the Monte-Carlo efficiency ϵ_{MC}, must be large, because the average number of tries with the rejection method is $\langle N_{\mathsf{rej}} \rangle = 1/\epsilon_{\mathsf{MC}}$. Figure B.4 shows ϵ_{MC} for the four variables as a function of the fluid cell velocity. For all β, the sampling of momenta is more efficient than the sampling of the angle. For the sampling of p, however, the division by β (see Equation (B.10b)) is inconvenient, so that the choice used in this work is to sample p_β.

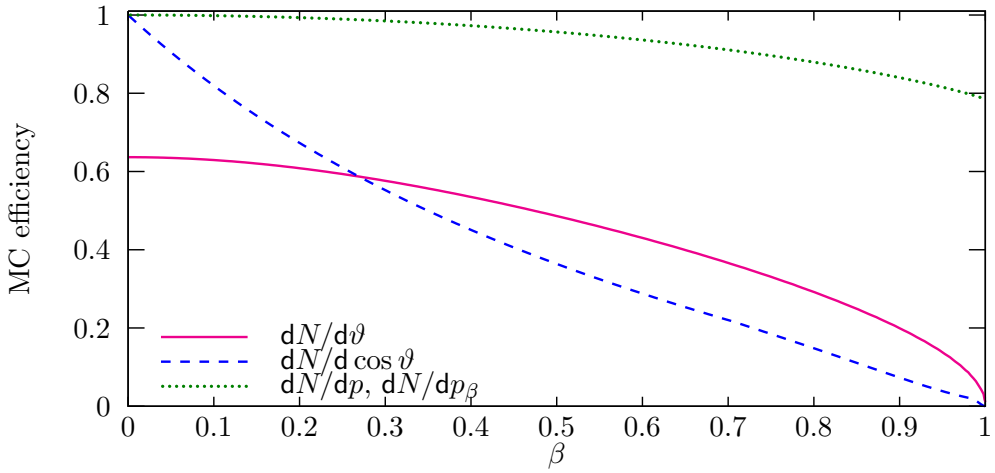

Figure B.4: Monte-Carlo efficiency ϵ_{MC} as a function of fluid velocity for a rejection method sampling of ϑ, $\cos\vartheta$, p and p_β. The efficiencies of p and p_β are equal.

Appendix C

Conventions and Units

In every specialised field of physics (and I suppose of every other science) there is bound to be a multitude of conventions that are not used or even known outside. The same applies to heavy-ion physics. This Chapter aims at giving a short overview over and motivation for the conventions that are used throughout this thesis.

C.1 Natural Units

In modern physics, several connections between physical quantities have been discovered that were not obvious when those quantities had been introduced into the sciences. Among these were a) the space-time correspondence inherent in special relativity, b) the wavelength-momentum correspondence that is a central part of quantum mechanics and c) the observation that temperature is the macroscopic result of microscopic particle energies. Any of those correspondences connects two physical parameters with a natural constant which, for convenience, is set to one and thereby dropped from all equations:

$$x = ct \quad , \tag{C.1a}$$

$$k = \hbar p \quad , \tag{C.1b}$$

$$E = k_{\mathsf{B}} T \quad , \tag{C.1c}$$

with $c = 2.99792458 \cdot 10^{8}\,\mathsf{m/s}$ being the speed of light, $\hbar \approx 1.055 \cdot 10^{-34}\,\mathsf{Js}$ the Planck constant and $k_{\mathsf{B}} \approx 1.381 \cdot 10^{-23}\,\mathsf{J/K}$ the Boltzmann constant.

By this choice, the system of four basic units for length, time, mass and temperature is reduced to one independent unit. For better compatibility with units that are known from macroscopic physics, two units are used which can be transformed into each other by the following relation

$$1 = \hbar c = 197.33\ \mathsf{MeV\ fm} \quad . \tag{C.2}$$

Usually, space-like quantities like length and time are given in Femtometer (or *fermi*) 1 fm = 10^{-15} m, while energy-like quantities like energy, momentum,

mass and temperature are given in Megaelectronvolt 1 MeV $= 10^6$ eV $= 1.602 \cdot 10^{-13}$ J (or Giga- and Teraelectronvolt, where better suited).

The rule of thumb for extracting the value of a quantity in SI-units is very simple: Take the value in natural units and multiply natural constants in such a way that the units match the units in the SI-system. This procedure is unique and can easily be done.

By using different, but not independent units, disambiguities are bound to occure. Most prominently, this happens for densities, frequencies and wavelengths, where the intuitive definition introduces inverse length scales. In this work, densities are always given in mixed units, e.g., the unit for energy density is $[\varepsilon] = \mathsf{MeV}/\mathsf{fm}^3$.

C.2 Einstein notation

In this work, scalar products of relativistic vectors are given with an implicit summation over the indices (also known as the Einstein notation). Additionally, a centered multiplication dot denotes the same. I.e., with the metric tensor $g_{\mu\nu} = g^{\mu\nu} = \mathsf{diag}\,(1, -1, -1, -1)$, the product reads

$$p^\mu u_\mu \overset{\mathsf{def}}{=} \sum_{\mu=0}^{3} g_{\mu\nu} p^\mu u^\nu = (p \cdot u) \quad . \tag{C.3}$$

The relativistic four-vectors are defined such that the time-like component carries the index $\mu = 0$. The derivation operator is given as ∂_μ in covariant notation and as $\left(\partial_t, \vec{\nabla}\right)$ in non-covariant relations.

C.3 Coordinate systems and indices

Unless otherwise noted, the coordinate system used in this thesis is such that the heavy ions travel in z-direction and the impact vector $\vec{b}$ that connects the centers of both nuclei is in the x/z-plane. The coordinate system is at rest in the center-of-mass system of the collision and has its origin at the time of the first nucleon-nucleon collision and at the center of mass of the nuclei (or where that would be if the nuclei's densities were continuous). The primary use of variables is that of a polar system in the x/y-plane, in the transverse component (index $\perp$) and the azimuthal angle φ, and for velocity and momentum, the z-direction is usually given in the rapidity y or pseudorapidity η, which in the case of photons is the same:

$$y = \frac{1}{2} \ln\left(\frac{1+\beta_z}{1-\beta_z}\right) = \frac{1}{2} \ln\left(\frac{E+p_z}{E-p_z}\right) \tag{C.4}$$

$$\eta = \frac{1}{2} \ln\left(\frac{\beta+\beta_z}{\beta-\beta_z}\right) = \frac{1}{2} \ln\left(\frac{p+p_z}{p-p_z}\right) \quad . \tag{C.5}$$

Nucleus	A	$\sqrt{s_{\mathsf{NN}}}$ [GeV]	$\sqrt{s}$ [TeV]	E_{lab} [TeV]	E_{lab} [AGeV]	Accelerator
U	238	8.16	1.941	8.330	35.0	FAIR
Pb	208	17.24	3.586	32.864	158.0	SPS
Cu	63	62.4	3.931	130.731	2075.1	RHIC
Au	197	62.4	12.292	408.794	2075.1	RHIC
Cu	63	130.0	8.190	567.508	9008.1	RHIC
Au	197	130.0	25.610	1774.588	9008.1	RHIC
Cu	63	200.0	12.600	1343.254	21321.5	RHIC
Au	197	200.0	39.400	4200.334	21321.5	RHIC

Table C.1: Conversions between E_{lab} and $\sqrt{s_{\mathsf{NN}}}$ for the systems most common in this work. Usually, in fixed-target experiments (FAIR and SPS), E_{lab} is given, while in collider experiments (RHIC), $\sqrt{s_{\mathsf{NN}}}$ is listed.

C.4 Accelerator parameters

In order to compare heavy-ion reactions with different nuclei, the total energy of the nuclei is usually given in the energy per nucleon times the number of nucleons A. The latter is included into the unit. Therefore, a lead-lead collision with $E_{\mathsf{lab}} = 158$ AGeV actually means that one nucleus has the energy $E_{\mathsf{lab}} = 158 \times 208$ GeV $= 32864$ GeV. In systems that are experimentally probed with fixed-target experiments, the energy of the projectile nucleus in the laboratory frame E_{lab} is usually given, while in collider experiments, the center-of-mass energy of a nucleon-nucleon-pair $\sqrt{s_{\mathsf{NN}}}$ is given. The relation between E_{lab} and $\sqrt{s_{\mathsf{NN}}}$ is given by

$$\sqrt{s_{\mathsf{NN}}} = \sqrt{2\frac{E_{\mathsf{lab}}}{A} m_{\mathsf{N}} + m_{\mathsf{N}}^2} \tag{C.6}$$

$$E_{\mathsf{lab}} = \frac{A}{2}\left(\frac{\left(\sqrt{s_{\mathsf{NN}}}\right)^2}{m_{\mathsf{N}}} - m_{\mathsf{N}}\right) \quad , \tag{C.7}$$

where $m_{\mathsf{N}} = 0.938$ GeV is the mass of a nucleon. In Table C.1, the values in the different representations can be looked up for the systems most commonly used in this thesis.

Appendix D

Bibliography

[ALICE08] P. Crochet [ALICE Collaboration], "The ALICE experiment at the LHC," Phys. Part. Nucl. **39** (2008) 1074.

[Ams08] C. Amsler *et al.* [Particle Data Group], "Review of particle physics," Phys. Lett. B **667** (2008) 1.

[And83] B. Anderson, G. Gustafson, B. Söderberg: Z. Phys. **C20** (1983) 317

[And86] B. Anderson, G. Gustafson, B. Söderberg: Nucl. Phys. **B264** (1986) 29

[Aok06] Y. Aoki, G. Endrodi, Z. Fodor, S. D. Katz and K. K. Szabó, "The order of the quantum chromodynamics transition predicted by the standard model of particle physics," Nature **443** (2006) 675 [arXiv:hep-lat/0611014].

[Apa99] L. Apanasevich *et al.*, "k_T effects in direct photon production," Phys. Rev. D **59** (1999) 074007 [arXiv:hep-ph/9808467].

[Arl03] F. Arleo *et al.*, "Photon physics in heavy ion collisions at the LHC," arXiv:hep-ph/0311131.

[Arn01] P. B. Arnold, G. D. Moore and L. G. Yaffe, "Photon emission from quark gluon plasma: Complete leading order results," JHEP **0112** (2001) 009 [arXiv:hep-ph/0111107].

[Aur87] P. Aurenche, R. Baier, M. Fontannaz and D. Schiff, "Dealing with ambiguities in higher order QCD predictions for large p(t) processes involving real photons," Nucl. Phys. B **286** (1987) 509.

[Aur87a] P. Aurenche, R. Baier, A. Douiri, M. Fontannaz and D. Schiff, "Scheme Invariant Higher Order QCD Predictions for Large p(t) Photoproduction Reactions," Nucl. Phys. B **286** (1987) 553.

[Aur88] P. Aurenche, R. Baier, M. Fontannaz and D. Schiff, "Prompt Photon Production At Large P(T) Scheme Invariant QCD Predictions And Comparison With Experiment," Nucl. Phys. B **297** (1988) 661.

[Aur98] P. Aurenche, F. Gelis, R. Kobes and H. Zaraket, "Bremsstrahlung and photon production in thermal QCD," Phys. Rev. D **58** (1998) 085003 [arXiv:hep-ph/9804224].

[Aur99] P. Aurenche, M. Fontannaz, J. P. Guillet, B. A. Kniehl, E. Pilon and M. Werlen, "A critical phenomenological study of inclusive photon production in hadronic collisions," Eur. Phys. J. C **9** (1999) 107 [arXiv:hep-ph/9811382].

[Aur00] P. Aurenche, F. Gelis and H. Zaraket, "KLN theorem, magnetic mass, and thermal photon production," Phys. Rev. D **61** (2000) 116001 [arXiv:hep-ph/9911367].

[BRAHMS05] I. Arsene *et al.* [BRAHMS Collaboration], "Quark Gluon Plasma an Color Glass Condensate at RHIC? The perspective from the BRAHMS experiment," Nucl. Phys. A **757** (2005) 1 [arXiv:nucl-ex/0410020].

[Bac05] B. B. Back *et al.*, "The PHOBOS perspective on discoveries at RHIC," Nucl. Phys. A **757** (2005) 28 [arXiv:nucl-ex/0410022].

[Bai92] R. Baier, H. Nakkagawa, A. Niégawa and K. Redlich, "Production rate of hard thermal photons and screening of quark mass singularity," Z. Phys. C **53** (1992) 433.

[Bai97] R. Baier, Y. L. Dokshitzer, A. H. Müller, S. Peigné and D. Schiff, "Radiative energy loss of high energy quarks and gluons in a finite-volume quark-gluon plasma," Nucl. Phys. B **483** (1997) 291 [arXiv:hep-ph/9607355].

[Bai97a] R. Baier, Y. L. Dokshitzer, A. H. Müller, S. Peigné and D. Schiff, "Radiative energy loss and p(T)-broadening of high energy partons in nuclei," Nucl. Phys. B **484** (1997) 265 [arXiv:hep-ph/9608322].

[Bai06] R. Baier, P. Romatschke and U. A. Wiedemann, "Dissipative hydrodynamics and heavy ion collisions," Phys. Rev. C **73** (2006) 064903 [arXiv:hep-ph/0602249].

[Bar01] H. W. Barz and B. Kampfer, "The role of three-body collisions in Phi meson production processes near threshold," Nucl. Phys. A **683** (2001) 594 [arXiv:nucl-th/0005063].

[Bas98] S. A. Bass *et al.*, "Microscopic models for ultrarelativistic heavy ion collisions," Prog. Part. Nucl. Phys. **41** (1998) 255 [Prog. Part. Nucl. Phys. **41** (1998) 225] [arXiv:nucl-th/9803035].

[Bas99] S. A. Bass, M. Gyulassy, H. Stöcker and W. Greiner, "Signatures of quark-gluon-plasma formation in high energy heavy-ion collisions: A critical review," J. Phys. G **25** (1999) R1 [arXiv:hep-ph/9810281].

[Bas07] S. A. Bass, T. Renk and D. K. Srivastava, "Photon production in the parton cascade model," Nucl. Phys. A **783** (2007) 367.

[Bäu09] B. Bäuchle and M. Bleicher, "Direct photon emission from hadronic sources: Hydrodynamics vs. Transport theory," Eur. Phys. J. C **62** (2009) 75 [arXiv:0810.0488 [nucl-th]].

[Bäu10] B. Bäuchle and M. Bleicher, "Hybrid model calculations of direct photons in high-energy nuclear collisions," Phys. Rev. C **81** (2010) 044904 [arXiv:0905.4678 [hep-ph]].

[Bäu10a] B. Bäuchle and M. Bleicher, "Direct photon calculations in heavy-ion collisions at $\sqrt{s_{\mathsf{NN}}} = 62.4 - 200$ AGeV in a (3+1) dimensional hybrid approach," arXiv:1008.2332 [nucl-th].

[Bäu10b] B. Bäuchle and M. Bleicher, "Transport and hydrodynamic calculations of direct photons at FAIR," arXiv:1008.2338 [nucl-th].

[Bäu10c] B. Bäuchle and M. Bleicher, "Direct photon emission in Heavy Ion Collisions from Microscopic Transport Theory and Fluid Dynamics," arXiv:1003.5454 [nucl-th].

[Bäu10d] B. Bäuchle and M. Bleicher, "Calculations of direct photon emission in Heavy Ion Collisions at $\sqrt{s_{\mathsf{NN}}} = 200$ GeV," J. Phys. Conf. Ser. **230** (2010) 012033 [arXiv:1008.1866 [nucl-th]].

[Bäu10e] B. Bäuchle and M. Bleicher, "Direct Photons from a Hybrid Approach – Exploring the parameter space," arXiv:1008.1862 [nucl-th].

[Bel98] M. Belkacem *et al.*, "Equation of state, spectra and composition of hot and dense infinite hadronic matter in a microscopic transport model," Phys. Rev. C **58** (1998) 1727 [arXiv:nucl-th/9804058].

[Ble99] M. Bleicher *et al.*, "Relativistic hadron hadron collisions in the ultra-relativistic quantum molecular dynamics model," J. Phys. G **25** (1999) 1859 [arXiv:hep-ph/9909407].

[Ble07] J. Bleibel, G. Burau, A. Fässler and C. Fuchs, "Pseudorapidity shape of elliptic flow as signature for fast equilibration in relativistic heavy-ion collisions at energies up to sqrt(s) = 200-GeV," Phys. Rev. C **76** (2007) 024912 [arXiv:nucl-th/0610021].

[Ble08] J. Bleibel, G. Burau and C. Fuchs, "Anisotropic flow in Pb+Pb collisions at LHC from the quark gluon string model with parton rearrangement," Phys. Lett. B **659** (2008) 520 [arXiv:0711.3366 [nucl-th]].

[Bor73] J.P. Boris, D.L. Book, "Flux corrected transport i: SHASTA a fluid algorithm that works," J. Comput. Phys. **11** (1973) 38-69

[Bor10] S. Borsanyi, Z. Fodor, C. Hölbling, S. D. Katz, S. Krieg, C. Ratti and K. K. Szabó, "Is there still any Tc mystery in lattice QCD? Results with physical masses in the continuum limit III," JHEP **1009** (2010) 073 [arXiv:1005.3508 [hep-lat]].

[Bra08] E. L. Bratkovskaya, S. M. Kiselev and G. B. Sharkov, "Direct photon production from hadronic sources in high-energy heavy-ion collisions," Phys. Rev. C **78** (2008) 034905 [arXiv:0806.3465 [nucl-th]].

[Bro91] G. E. Brown and M. Rho, "Scaling effective Lagrangians in a dense medium," Phys. Rev. Lett. **66** (1991) 2720.

[Bur05] G. Burau, J. Bleibel, C. Fuchs, A. Fässler, L. V. Bravina and E. E. Zabrodin, "Anisotropic flow of charged and identified hadrons in the quark-gluon string model for Au + Au collisions at s(NN)**(1/2) = 200-GeV," Phys. Rev. C **71** (2005) 054905 [arXiv:nucl-th/0411117].

[Büs10] H. Büsching: *private communication*

[CBM05] C. Höhne [CBM Collaboration], "The Compressed Baryonic Matter Experiment At The Future Accelerator Facility In Darmstadt," Nucl. Phys. A **749** (2005) 141.

[CERES96] R. Baur *et al.* [CERES Collaboration], "Search for direct photons from S - Au collisions at 200-GeV/u," Z. Phys. C **71** (1996) 571.

[CMS10] [CMS collaboration] "Observation of Long-Range Near-Side Angular Correlations in Proton-Proton Collisions at the LHC," arXiv:1009.4122 [hep-ex].

[Cas02] W. Cassing, "Antibaryon production in hot and dense nuclear matter," Nucl. Phys. A **700** (2002) 618 [arXiv:nucl-th/0105069].

[Cle85] J. Cleymans and K. Redlich, "Lattice QCD And The Hydrodynamic Expansion Of The Quark - Gluon Plasma," Bielefeld (1985)

[Cle93] J. Cleymans and H. Satz, "Thermal hadron production in high-energy heavy ion collisions," Z. Phys. C **57** (1993) 135 [arXiv:hep-ph/9207204].

[Cle98] J. Cleymans and K. Redlich, "Unified description of freeze-out parameters in relativistic heavy ion collisions," Phys. Rev. Lett. **81** (1998) 5284 [arXiv:nucl-th/9808030].

[Cle06] J. Cleymans, H. Öschler, K. Redlich and S. Wheaton, "Status of chemical freeze-out," J. Phys. G **32** (2006) S165 [arXiv:hep-ph/0607164].

[Coo74] F. Cooper and G. Frye, "Comment On The Single Particle Distribution In The Hydrodynamic And Statistical Thermodynamic Models Of Multiparticle Production," Phys. Rev. D **10** (1974) 186.

[De08] P. de Forcrand and O. Philipsen, "The curvature of the critical surface $(m_{ud}, m_s)^{crit}(\mu)$: a progress report," PoS **LATTICE2008** (2008) 208 [arXiv:0811.3858 [hep-lat]].

[Dre70] S. D. Drell and T. M. Yan, "Massive Lepton Pair Production In Hadron-Hadron Collisions At High-Energies," Phys. Rev. Lett. **25** (1970) 316 [Erratum-ibid. **25** (1970) 902].

[Dum95] A. Dumitru, U. Katscher, J. A. Maruhn, H. Stoecker, W. Greiner and D. H. Rischke, "Thermal Photons As A Measure For The Rapidity Dependence Of The Temperature," Z. Phys. A **353** (1995) 187 [arXiv:hep-ph/9503347].

[Dum97] A.B. Dumitru: Dissertation, Universität Frankfurt (1997)

[Dum98] A. Dumitru, M. Bleicher, S. A. Bass, C. Spieles, L. Neise, H. Stöcker and W. Greiner, "Nonthermal direct photons in Pb + Pb at 160-A-GeV from microscopic transport theory," Phys. Rev. C **57** (1998) 3271 [arXiv:hep-ph/9709487].

[Dum06] A. Dumitru, L. Portugal and D. Zschiesche, "Inhomogeneous freeze-out in relativistic heavy-ion collisions," Phys. Rev. C **73** (2006) 024902 [arXiv:nucl-th/0511084].

[Dus08] K. Dusling and D. Teaney, "Simulating elliptic flow with viscous hydrodynamics," Phys. Rev. C **77** (2008) 034905 [arXiv:0710.5932 [nucl-th]].

[Dus09] K. Dusling and I. Zahed, "Thermal photons from heavy ion collisions: A spectral function approach," arXiv:0911.2426 [nucl-th].

[Dus10] K. Dusling, "Photons as a viscometer of heavy ion collisions," Nucl. Phys. A **839** (2010) 70 [arXiv:0903.1764 [nucl-th]].

[Ehe95] W. Ehehalt and W. Cassing, "Relativistic Transport Approach For Nucleus-Nucleus Collisions Based On A Njl Lagrangian," arXiv:hep-ph/9507274.

[Ehe96] W. Ehehalt and W. Cassing, "Relativistic transport approach for nucleus nucleus collisions from SIS to SPS energies," Nucl. Phys. A **602** (1996) 449.

[Fei76] E. L. Feinberg, "Direct Production Of Photons And Dileptons In Thermodynamical Models Of Multiple Hadron Production," Nuovo Cim. A **34** (1976) 391.

[Fro07] E. Frodermann, R. Chatterjee and U. Heinz, "Evolution of pion HBT radii from RHIC to LHC – Predictions from ideal hydrodynamics," J. Phys. G **34** (2007) 2249 [arXiv:0707.1898 [nucl-th]].

[Gal02] C. Gale, "Direct photons and thermal dileptons: A theoretical review," Nucl. Phys. A **698** (2002) 143 [arXiv:hep-ph/0104235].

[Gal09] C. Gale, "Photon Production in Hot and Dense Strongly Interacting Matter," arXiv:0904.2184 [hep-ph].

[Gei97] K. Geiger, "VNI 3.1: MC-simulation program to study high-energy particle collisions in QCD by space-time evolution of parton-cascades and parton-hadron conversion," Comput. Phys. Commun. **104** (1997) 70 [arXiv:hep-ph/9701226].

[Gol60] G. Goldhaber, S. Goldhaber, W. Y. Lee and A. Pais, "Influence of Bose-Einstein statistics on the antiproton proton annihilation process," Phys. Rev. **120** (1960) 300.

[Gor93] L. E. Gordon and W. Vogelsang, "Polarized and unpolarized prompt photon production beyond the leading order," Phys. Rev. D **48** (1993) 3136.

[Grä09] G. Gräf: Diploma thesis, Universität Frankfurt (2009)

[Gyu00] M. Gyulassy, P. Levai and I. Vitev, "Jet quenching in thin quark-gluon plasmas. I: Formalism," Nucl. Phys. B **571** (2000) 197 [arXiv:hep-ph/9907461].

[HELIOS90] T. Akesson *et al.* [HELIOS collaboration], "Inclusive photon production in p A and A-A collisions at 200-GeV/u," Z. Phys. C **46** (1990) 369.

[Hal82] F. Halzen and H. C. Liu, "Experimental Signatures Of Phase Transition To Quark Matter In High-Energy Collisions Of Nuclei," Phys. Rev. D **25** (1982) 1842.

[Han56] R. Hanbury Brown and R. Q. Twiss, "A Test of a new type of stellar interferometer on Sirius," Nature **178** (1956) 1046.

[Har96] J. W. Harris and B. Müller, "The search for the quark-gluon plasma," Ann. Rev. Nucl. Part. Sci. **46** (1996) 71 [arXiv:hep-ph/9602235].

[Hir02] T. Hirano, "Is early thermalization achieved only near midrapidity in Au + Au collisions at sNN =130 GeV?," Phys. Rev. C **65** (2002) 011901 [arXiv:nucl-th/0108004].

[Huo02] P. Huovinen, P. V. Ruuskanen and S. S. Rasanen, "Photon emission in heavy ion collisions at the CERN SPS," Phys. Lett. B **535** (2002) 109 [arXiv:nucl-th/0111052].

[Huo02a] P. Huovinen, M. Belkacem, P. J. Ellis and J. I. Kapusta, "Dileptons and photons from coarse-grained microscopic dynamics and hydrodynamics compared to experimental data," Phys. Rev. C **66** (2002) 014903 [arXiv:nucl-th/0203023].

[Hus95] J. Huston, E. Kovacs, S. Kuhlmann, H. L. Lai, J. F. Owens and W. K. Tung, "A Global QCD study of direct photon production," Phys. Rev. D **51** (1995) 6139 [arXiv:hep-ph/9501230].

[Hwa85] R. C. Hwa and K. Kajantie, "Diagnosing Quark Matter By Measuring The Total Entropy And The Photon Or Dilepton Emission Rates," Phys. Rev. D **32** (1985) 1109.

[Ian03] E. Iancu and R. Venugopalan, "The color glass condensate and high energy scattering in QCD," arXiv:hep-ph/0303204.

[Kap91] J. I. Kapusta, P. Lichard and D. Seibert, "High-Energy Photons From Quark - Gluon Plasma Versus Hot Hadronic Gas," Phys. Rev. D **44** (1991) 2774 [Erratum-ibid. D **47** (1993) 4171].

[Kat88] M. Kataja, "Three-dimensional hydrodynamics of ultrarelativistic heavy ion collisions," Z. Phys. C **38** (1988) 419.

[Kol03] P. F. Kolb and U. W. Heinz, "Hydrodynamic description of ultrarelativistic heavy-ion collisions," arXiv:nucl-th/0305084.

[Lar07] A. B. Larionov, O. Buss, K. Gallmeister and U. Mosel, "Three-body collisions in Boltzmann-Uehling-Uhlenbeck theory," Phys. Rev. C **76** (2007) 044909 [arXiv:0704.1785 [nucl-th]].

[Li97] G. Q. Li, G. E. Brown, C. Gale and C. M. Ko, "Electromagnetic probes of dense matter in relativistic heavy-ion collisions," arXiv:nucl-th/9712048.

[Li09] Q. f. Li, J. Steinheimer, H. Petersen, M. Bleicher and H. Stöcker, "Effects of a phase transition on HBT correlations in an integrated

Boltzmann+Hydrodynamics approach," Phys. Lett. B **674** (2009) 111 [arXiv:0812.0375 [nucl-th]].

[Lic95] P. Lichard, "Formalism for dilepton production via virtual photon bremsstrahlung in hadronic reactions," Phys. Rev. D **51** (1995) 6017 [arXiv:hep-ph/9812211].

[Lin05] Z. W. Lin, C. M. Ko, B. A. Li, B. Zhang and S. Pal, "A multi-phase transport model for relativistic heavy ion collisions," Phys. Rev. C **72** (2005) 064901 [arXiv:nucl-th/0411110].

[Liu09] F. M. Liu, T. Hirano, K. Werner and Y. Zhu, "Jet quenching and direct photon production," J. Phys. G **36** (2009) 064072 [arXiv:0811.0666 [hep-ph]].

[Liu09a] F. M. Liu, T. Hirano, K. Werner and Y. Zhu, "Elliptic flow of thermal photons in Au+Au collisions at $\sqrt{s_{NN}} = 200$ GeV," Phys. Rev. C **80** (2009) 034905 [arXiv:0902.1303 [hep-ph]].

[Liu09b] F. M. Liu and K. Werner, "A Systematic Study on Direct Photon Production from Central Heavy Ion Collisions," J. Phys. G **36** (2009) 035101 [arXiv:0712.3619 [hep-ph]].

[Mcl86] L. D. McLerran, M. Kataja, P. V. Ruuskanen and H. von Gersdorff, "Studies of the Hydrodynamical Evolution of Matter Produced in Fluctuations in p anti-p Collisions and in Ultrarelativistic Nuclear Collisions. 2. Transverse Momentum Distributions," Phys. Rev. D **34** (1986) 2755.

[Mcl07] L. McLerran and R. D. Pisarski, "Phases of Cold, Dense Quarks at Large N_c," Nucl. Phys. A **796** (2007) 83 [arXiv:0706.2191 [hep-ph]].

[Mol05] D. Molnar and P. Huovinen, "Dissipation and elliptic flow at RHIC," Phys. Rev. Lett. **94** (2005) 012302 [arXiv:nucl-th/0404065].

[NA49-08] C. Alt *et al.* [NA49 Collaboration], "Pion and kaon production in central Pb+Pb collisions at 20A and 30A GeV: Evidence for the onset of deconfinement," Phys. Rev. C **77** (2008) 024903 [arXiv:0710.0118 [nucl-ex]].

[NA61-07] A. Laszlo *et al.* [NA61 Collaboration], "Na61/Shine at the CERN SPS," PoS C **POD07** (2007) 054 [arXiv:0709.1867 [nucl-ex]].

[Non07] C. Nonaka and S. A. Bass, "Space-time evolution of bulk QCD matter," Phys. Rev. C **75** (2007) 014902 [arXiv:nucl-th/0607018].

[Owe87] J. F. Owens, "Large Momentum Transfer Production Of Direct Photons, Jets, And Particles," Rev. Mod. Phys. **59** (1987) 465.

[PHENIX03] S. S. Adler *et al.* [PHENIX Collaboration], "Suppressed pi0 production at large transverse momentum in central Au + Au collisions at s(NN)**(1/2) = 200-GeV," Phys. Rev. Lett. **91** (2003) 072301 [arXiv:nucl-ex/0304022].

[PHENIX04] S. S. Adler *et al.* [PHENIX Collaboration], "High p_T charged hadron suppression in Au + Au collisions at $\sqrt{s}_{NN} = 200$ GeV," Phys. Rev. C **69** (2004) 034910 [arXiv:nucl-ex/0308006].

[PHENIX05] K. Adcox *et al.* [PHENIX Collaboration], "Formation of dense partonic matter in relativistic nucleus nucleus collisions at RHIC: Experimental evaluation by the PHENIX collaboration," Nucl. Phys. A **757** (2005) 184 [arXiv:nucl-ex/0410003].

[PHENIX05a] S. S. Adler *et al.* [PHENIX Collaboration], "Mid-rapidity direct-photon production in p^+p collisions at $\sqrt{s} = 200$-GeV," Phys. Rev. D **71** (2005) 071102 [arXiv:hep-ex/0502006].

[PHENIX05b] S. S. Adler *et al.* [PHENIX Collaboration], "Centrality dependence of direct photon production in s(NN)**(1/2) = 200-GeV Au + Au collisions," Phys. Rev. Lett. **94** (2005) 232301 [arXiv:nucl-ex/0503003].

[PHENIX06] S. S. Adler *et al.* [PHENIX Collaboration], "Measurement of identified pi0 and inclusive photon v(2) and implication to the direct photon production in s(NN)**(1/2) = 200-GeV Au + Au collisions," Phys. Rev. Lett. **96** (2006) 032302 [arXiv:nucl-ex/0508019].

[PHENIX07] S. S. Adler *et al.* [PHENIX Collaboration], "Measurement of direct photon production in p + p collisions at s**(1/2) = 200-GeV," Phys. Rev. Lett. **98** (2007) 012002 [arXiv:hep-ex/0609031].

[PHENIX09] A. Adare *et al.* [PHENIX Collaboration], "Photon-Hadron Jet Correlations in p+p and Au+Au Collisions at sqrt(s_NN) = 200 GeV," Phys. Rev. C **80** (2009) 024908 [arXiv:0903.3399 [nucl-ex]].

[PHENIX10] A. Adare *et al.* [PHENIX Collaboration], "Enhanced production of direct photons in Au+Au collisions at sqrt(s_NN)=200 GeV and implications for the initial temperature," Phys. Rev. Lett. **104** (2010) 132301 [arXiv:0804.4168 [nucl-ex]].

[PHENIX10a] A. Adare *et al.* [PHENIX Collaboration], "Detailed Measurement Of The E^+E^- Pair Continuum In $P+P$ And Au+Au Collisions At $\sqrt{s_{nn}} = 200$ Gev And Implications For Direct Photon Production," Phys. Rev. C **81** (2010) 034911 [arXiv:0912.0244 [nucl-ex]].

[PHENIX10b] A. Adare *et al.* [PHENIX Collaboration], "High p_T Direct Photon and π^0 Triggered Azimuthal Jet Correlations in sqrt(s)=200 GeV p+p Collisions," arXiv:1006.1347 [hep-ex].

[Pap99] P. Papazoglou, D. Zschiesche, S. Schramm, J. Schaffner-Bielich, H. Stöcker and W. Greiner, "Nuclei in a chiral SU(3) model," Phys. Rev. C **59** (1999) 411 [arXiv:nucl-th/9806087].

[Pap00] G. Papp, P. Levai and G. I. Fai, "Saturating Cronin effect in ultrarelativistic proton nucleus collisions," Phys. Rev. C **61** (2000) 021902 [arXiv:nucl-th/9903012].

[Pet08] H. Petersen, J. Steinheimer, G. Burau, M. Bleicher and H. Stöcker, "A Fully Integrated Transport Approach to Heavy Ion Reactions with an Intermediate Hydrodynamic Stage," Phys. Rev. C **78** (2008) 044901 [arXiv:0806.1695 [nucl-th]].

[Pet08a] H. Petersen, M. Bleicher, S. A. Bass and H. Stöcker, "UrQMD-2.3 - Changes and Comparisons," arXiv:0805.0567 [hep-ph].

[Pet09] H. Petersen: Dissertation, Universität Frankfurt (2009)

[Pet09a] H. Petersen, M. Mitrovski, T. Schuster and M. Bleicher, "Centrality and system size dependence of (multi-strange) hyperons at 40A and 158A GeV: A comparison between a binary collision and a Boltzmann+hydrodynamic hybrid model," Phys. Rev. C **80** (2009) 054910 [arXiv:0903.0396 [hep-ph]].

[Pet09b] H. Petersen, J. Steinheimer, M. Bleicher and H. Stöcker, "$< m_T >$ excitation function: Freeze-out and equation of state dependence," J. Phys. G **36** (2009) 055104 [arXiv:0902.4866 [nucl-th]].

[Pet09c] H. Petersen, J. Steinheimer, G. Burau and M. Bleicher, "Elliptic flow in an integrated (3+1)d microscopic + macroscopic approach with fluctuating initial conditions," Eur. Phys. J. C **62** (2009) 31.

[Ris95] D. H. Rischke, Y. Pursun and J. A. Maruhn, "Relativistic hydrodynamics for heavy ion collisions. 2. Compression of nuclear matter and the phase transition to the quark - gluon plasma," Nucl. Phys. A **595** (1995) 383 [Erratum-ibid. A **596** (1996) 717] [arXiv:nucl-th/9504021].

[Ris95a] D. H. Rischke, S. Bernard and J. A. Maruhn, "Relativistic hydrodynamics for heavy ion collisions. 1. General aspects and expansion into vacuum," Nucl. Phys. A **595** (1995) 346 [arXiv:nucl-th/9504018].

[Ris04] D. H. Rischke, "The quark-gluon plasma in equilibrium," Prog. Part. Nucl. Phys. **52** (2004) 197 [arXiv:nucl-th/0305030].

[STAR05] J. Adams *et al.* [STAR Collaboration], "Experimental and theoretical challenges in the search for the quark gluon plasma: The STAR collaboration's critical assessment of the evidence from RHIC collisions," Nucl. Phys. A **757** (2005) 102 [arXiv:nucl-ex/0501009].

[STAR09] H. Caines [STAR Collaboration], "The RHIC Beam Energy Scan - STAR'S Perspective," arXiv:0906.0305 [nucl-ex].

[STAR09a] B. I. Abelev *et al.* [STAR Collaboration], "Studying Parton Energy Loss in Heavy-Ion Collisions via Direct-Photon and Charged-Particle Azimuthal Correlations," arXiv:0912.1871 [nucl-ex].

[STAR10] M. M. Aggarwal *et al.* [STAR Collaboration], "An Experimental Exploration of the QCD Phase Diagram: The Search for the Critical Point and the Onset of De-confinement," arXiv:1007.2613 [nucl-ex].

[San10] E. Santini, H. Petersen and M. Bleicher, "Phi meson production in In-In collisions at $E_{\rm lab}$=158A GeV: evidence for relics of a thermal phase," Phys. Lett. B **687** (2010) 320 [arXiv:0909.4657 [nucl-th]].

[Sch93] Th. Schönnfeld: Dissertation, Universität Frankfurt (1993)

[Sch06] D. Schumacher, S. Vogel and M. Bleicher, "Theoretical analysis of dilepton spectra in heavy ion collisions at GSI-FAIR energies," Acta Phys. Hung. A **27** (2006) 451 [arXiv:nucl-th/0608041].

[Shu78] E. V. Shuryak, "Quark-Gluon Plasma And Hadronic Production Of Leptons, Photons And Psions," Phys. Lett. B **78** (1978) 150 [Sov. J. Nucl. Phys. **28** (1978) 408] [Yad. Fiz. **28** (1978) 796].

[Shu10] E. Shuryak, "Comments on the CMS discovery of the 'Ridge' in High Multiplicity pp collisions at LHC," arXiv:1009.4635 [hep-ph].

[Sin83] B. Sinha, "Universal Signals Of Quark - Gluon Plasma," Phys. Lett. B **128** (1983) 91.

[Sjö06] T. Sjöstrand, S. Mrenna and P. Z. Skands, "PYTHIA 6.4 Physics and Manual," JHEP **0605** (2006) 026 [arXiv:hep-ph/0603175].

[Son08] H. Song and U. W. Heinz, "Multiplicity scaling in ideal and viscous hydrodynamics," Phys. Rev. C **78** (2008) 024902 [arXiv:0805.1756 [nucl-th]].

[Sri91] D. K. Srivastava and B. Sinha, "Signals of quark - gluon plasma: Dimuons and photons through a window of invariant mass filter," Phys. Lett. B **261** (1991) 1.

[Sri92] D. K. Srivastava, B. Sinha, M. Gyulassy and X. N. Wang, "Equilibrium versus nonequilibrium photons in a nucleus-nucleus collision at RHIC energies," Phys. Lett. B **276** (1992) 285.

[Sri92a] D. K. Srivastava, J. Alam, S. Chakrabarty, S. Raha and B. Sinha, "Boost noninvariant hydrodynamics in ultrarelativistic heavy ion collisions," Phys. Lett. B **278** (1992) 225.

[Sri96] D. K. Srivastava, B. Sinha and T. C. Awes, "Photon pairs from relativistic heavy ion collisions and the quark hadron phase transition," Phys. Lett. B **387** (1996) 21.

[Sri98] D. K. Srivastava and K. Geiger, "Flash of photons from the early stage of heavy-ion collisions," Phys. Rev. C **58** (1998) 1734 [arXiv:nucl-th/9802034].

[Sri01] D. K. Srivastava and B. Sinha, "Radiation of single photons from Pb + Pb collisions at the CERN SPS and quark hadron phase transition," Phys. Rev. C **64** (2001) 034902 [arXiv:nucl-th/0006018].

[Sta86] G. Staadt, W. Greiner and J. Rafelski, "Photons From Strange Quark Annihilation In Quark - Gluon Plasma," Phys. Rev. D **33** (1986) 66.

[Ste09] J. Steinheimer, M. Mitrovski, T. Schuster, H. Petersen, M. Bleicher and H. Stöcker, "Strangeness fluctuations and MEMO production at FAIR," Phys. Lett. B **676** (2009) 126 [arXiv:0811.4077 [hep-ph]].

[Ste09a] J. Steinheimer, V. Dexheimer, H. Petersen, M. Bleicher, S. Schramm and H. Stöcker, "Hydrodynamics with a chiral hadronic equation of state including quark degrees of freedom," arXiv:0905.3099 [hep-ph].

[Ste09b] J. Steinheimer, S. Schramm and H. Stöcker, "An effective chiral Hadron-Quark Equation of State Part I: Zero baryochemical potential," arXiv:0909.4421 [hep-ph].

[Ste10] J. Steinheimer, *private communication*

[Tur04] S. Turbide, R. Rapp and C. Gale, "Hadronic production of thermal photons," Phys. Rev. C **69** (2004) 014903 [arXiv:hep-ph/0308085].

[Tur05] S. Turbide, C. Gale, S. Jeon and G. D. Moore, "Energy loss of leading hadrons and direct photon production in evolving quark-gluon plasma," Phys. Rev. C **72** (2005) 014906 [arXiv:hep-ph/0502248].

[Vog08] S. Vogel, H. Petersen, K. Schmidt, E. Santini, C. Sturm, J. Aichelin and M. Bleicher, "How sensitive are di-leptons from rho mesons to the high baryon density region?," Phys. Rev. C **78** (2008) 044909 [arXiv:0710.4463 [hep-ph]].

[Von86] H. Von Gersdorff, L. D. McLerran, M. Kataja and P. V. Ruuskanen, "Studies Of The Hydrodynamic Evolution Of Matter Produced In Fluctuations In Anti-P P Collisions And In Ultrarelativistic Nuclear Collisions," Phys. Rev. D **34** (1986) 794.

[WA80-91] R. Albrecht *et al.* [WA80 Collaboration], "Upper limit for thermal direct photon production in heavy ion collisions at 60-A/GeV and 200-A/GeV," Z. Phys. C **51** (1991) 1.

[WA80-96] R. Albrecht *et al.* [WA80 Collaboration], "Limits on the production of direct photons in 200-A/GeV S-32 + Au collisions," Phys. Rev. Lett. **76** (1996) 3506.

[WA93-94] Y. P. Viyogi *et al.* [WA93 Collaboration], "Photon multiplicity measurements in nucleus-nucleus collisions at 200-A/GeV," Nucl. Phys. A **566** (1994) 623C.

[WA98-00] M. M. Aggarwal *et al.* [WA98 Collaboration], "Direct photon production in 158-A-GeV Pb-208 + Pb-208 collisions," arXiv:nucl-ex/0006007.

[WA98-00a] M. M. Aggarwal *et al.* [WA98 Collaboration], "Observation of direct photons in central 158-A-GeV Pb-208 + Pb-208 collisions," Phys. Rev. Lett. **85** (2000) 3595 [arXiv:nucl-ex/0006008].

[WA98-04] M. M. Aggarwal *et al.* [WA98 Collaboration], "Interferometry of direct photons in central Pb-208 + Pb-208 collisions at 158-A-GeV," Phys. Rev. Lett. **93** (2004) 022301 [arXiv:nucl-ex/0310022].

[Wan92] X. N. Wang and M. Gyulassy, "Gluon shadowing and jet quenching in A + A collisions at s**(1/2) = 200-GeV," Phys. Rev. Lett. **68** (1992) 1480.

[Win96] L.A. Winckelmann: Dissertation, Universität Frankfurt (1996); Verlag Harri Deutsch, Frankfurt (1996)

[Won84] C. Y. Wong, "Initial Energy Density Of Quark Gluon Plasma In Relativistic Heavy Ion Collisions," Phys. Rev. D **30** (1984) 961.

[Won98] C. Y. Wong and H. Wang, "Effects of parton intrinsic transverse momentum on photon production in hard-scattering processes," Phys. Rev. C **58** (1998) 376 [arXiv:hep-ph/9802378].

[Xio92] L. Xiong, E. V. Shuryak and G. E. Brown, "Photon production through A1 resonance in high-energy heavy ion collisions," Phys. Rev. D **46** (1992) 3798 [arXiv:hep-ph/9208206].

[Xu05] Z. Xu and C. Greiner, "Thermalization of gluons in ultrarelativistic heavy ion collisions by including three-body interactions in a parton cascade," Phys. Rev. C **71** (2005) 064901 [arXiv:hep-ph/0406278].

[Zaj84] W. A. Zajc *et al.*, "Two-pion correlations in heavy ion collisions," Phys. Rev. C **29** (1984) 2173.

[Zsc02] D. Zschiesche, S. Schramm, J. Schaffner-Bielich, H. Stoecker and W. Greiner, "Particle ratios at RHIC: Effective hadron masses and chemical freeze-out," Phys. Lett. B **547** (2002) 7 [arXiv:nucl-th/0209022].

Appendix E

Acknowledgements

Now that I have almost finished this thesis, I have a lot of half-begun lists of who I must under no circumstances forget to mention in my Acknowledgements. Since most of these lists are somewhere in my head and since I am very sure that at least some important people are on neither list, I am bound to forget *someone*. My sincerest apologies to the forgotten helpers.

One person who supported me in innumerable ways during the last 40 months deserves first mention. My supervisor Marcus Bleicher has tought me a great many things, helped me along the way and supported me in every respect. Thank you for the trust you put in me, thank you for every advice on my thesis, on my life and on my future. Thank you especially for accepting my involvement in Fachschafts-things.

Despite his time at the institue being very limited, Horst Stöcker has been a great source of inspiration and support for me since I started studying physics seven years ago. I am not sure if I will ever understand the trust he puts in me and my abilities as a physicist, but it always leaves me feeling better nonetheless. Thank you for the opportunity to organise the introduction of a huge e-Learning project that accompanied more than twenty lectures so far and provided help to thousands of students.

Even though sometimes during a PhD meals may be irregular, occasionally even students have to eat, drink, go out, have fun, possibly even go on vacation and visit conferences, and all of that usually has one requirement: money. I am grateful for the support the Deutsche Telekom Stiftung offered. Not only the direct support via scholarship or travel money was very important to me, but also the interdisciplinary character of the foundation that allows to meet people from different fields of research.

In both the Helmholtz Research School for Quark Matter Studies and the Helmholtz Graduate School for Hadron and Ion Research the concept of a graduate school for the graduate students is made alive. The lecture weeks and soft-skill courses I was allowed to attend were an incredibly rich source of knowledge, both about science, about my fellow students and about me. I am happy to be

a part of both programmes.

Thank you, Henner Büsching, not only for those programmes, but also for your advice and support in questions concerning photons, and thank you for joining my PhD committee. Thank you to Christoph Blume, Rene Bellwied, Hans-Christian Bösing, Stefan Bathe and Klaus Reygers for experimental clarifications and discussions about my photons. Thank you to all my revisors: Martin, Elvira, Gunnar, Thomas, Johannes, Christoph and Luisa. If there are strange formulations in this thesis, it is not for their lack of trying, but because of my stubbornness.

Thank you to all of my colleagues: Elvira, Christoph and Marlene, all of who shared my office for quite some time, and whose company I enjoyed very much. Thanks also go to rest of the group: Jan, Gunnar, Sascha, Katharina, Daniel, George, Hannah, Thomas B and Thomas L all helped me at one point or another.

Thanks to Xela, Fritz, Stuck, Guido, Christian, Thomas and all others who helped me with my IT-problems.

Thank you to everyone who has been in the Fachschaft in the last years and accepted my company there: Johannes, Stefan, Berit, Eva, Alex, Fritz, Sophie, Janet, Marc, Dominik, Fritz, Thomas, Stuck, Patricia, Martin, Ulli, Viola, Könich, Marco, Philipp, Carola, Jonas, Miriam, Margret, Rita, Zuzana, Simay, Christina, Daniela, Rike, Dex, Franz, and everyone else, and the people around the Fachschaft: Lena, Fips, Christian, Andi and the others.

I am happy to be a member of the Frankfurt Music School's guitar orchestra and I am grateful for the many evenings in the Mainufer that have spinned off my friendship to Stefan Salm. I have yet to find a better way of recreation than the hours and hours of music, but then again, why would I want anything else?

Thanks also go to Hannah, and to Johannes and Rike for giving me a home when other places became ... unavailable.

Thank you to everyone who helped me with my everyday problems: Gabi, who never hesitated to help me with any administrative questions and with personal advice, and especially my very best friends Johannes, Luisa, Ulli and Stefan.

In closing, I would like to mention the life-long support I have received from my family. My UKS Melanie has shared many a nice experience with me, and my parents Marieluise and Peter have supported me all my life. Without their help, I would most probably sweep streets right now.

```
^[:w^M:make! ps^M:q^M
```

Appendix F

Zusammenfassung

In der vorliegenden Arbeit werden verschiedene Modelle benutzt, um die Emission von direkten Photonen aus Schwerionenkollisionen vorherzusagen.

F.1 Einführung

Schwerionenkollisionen stellen die einzige Methode dar, kollektive Eigenschaften stark wechselwirkender (Kern-)Materie in kontrollierten Experimenten zu untersuchen. Die Kenntnisse, die sich daraus über das Phasendiagramm stark wechselwirkender Materie gewinnen lassen, sind zum Beispiel wichtig, um genauere Rückschlüsse auf die ersten Millisekunden nach dem Urknall ziehen zu können. Bei hohen Temperaturen wird erwartet, dass der Farbeinschluss, der Quarks und Gluonen zu Hadronen zusammenbindet, aufgehoben ist und Quarks und Gluonen frei sind. Den Übergang zu diesem sogenannten Quark-Gluonen-Plasma will man in den Kollisionen von relativistisch beschleunigten Atomkernen (Schwerionen) erzeugen und nachweisen. Die Untersuchungen von heißer und/oder dichter Kernmaterie steht allerdings vor schwierigen Herausforderungen: Die experimentellen Möglichkeiten beschränken sich darauf, ein System (den Feuerball) zu erschaffen, das nur etwa 10^{-22} Sekunden lang existiert, bevor es durch die Expansion ins Vakuum zu stark ausgedünnt ist und nur noch als einzelne Teilchen beschrieben werden kann. Messbar sind also nur die Zerfallsprodukte, die von dem Feuerball emittiert werden. Von diesen sind weder orts- noch zeitaufgelöste Messungen möglich, da sowohl die Zeitskalen als auch die typischen Längenskalen einer Kollision mit ca. 10^{-14} Metern weit unterhalb aller direkt messbaren Größenordnungen liegen. Lediglich die Spezies, Impuls- und Energieinformationen der Teilchen sind daher bekannt.

Auch die theoretische Behandlung der starken Wechselwirkung wird durch die spezielle Struktur der zugrundeliegenden Theorie, der Quantenchromodynamik, erschwert. Die störungstheoretische Behandlung von QCD-Prozessen ist nur bei hohen Impulsüberträgen möglich, da die Kopplungskonstante bei niedrigen Impulsüberträgen zu groß wird. Der einzig gangbare Weg ist daher,

effektive Modelle zu entwickeln, die die Raum-Zeit-Entwicklung der Materie mit den Impulsspektren der Teilchen verbinden.

Die Teilchen, die aus einer Schwerionenkollision emittiert werden, streuen meistens bis in die späten Phasen der Reaktion, da sie recht große Wechselwirkungsquerschnitte haben. Dadurch gehen etwaige direkte Informationen über den heißesten und dichtesten Teil verloren. Unter verschiedenen Ansätzen, wie man dieses Problem lösen kann und doch Informationen aus der frühen Phase gewinnen kann, ist die Idee, Teilchen zu betrachten, die kleine Wechselwirkungsquerschnitte haben. Mit diesem Ansatz beschränkt man sich auf Teilchen, die nur elektromagnetisch wechselwirken, wie Photonen. Mit kleinen Wechselwirkungsquerschnitten einher geht allerdings auch ein kleiner Produktionsquerschnitt, sodass diese Teilchen in der Flut der hadronischen Teilchen schwer zu isolieren und messen sind.

Die besondere Schwierigkeit bei Photonen ist, dass sie größtenteils in Mesonzerfällen weit außerhalb der Kollisionszone erzeugt werden. Die experimentelle Herausforderung ist nun, den Anteil der im Feuerball erzeugten Photonen herauszufinden. Diese Photonen werden als direkte Photonen (im Gegensatz zu Zerfallsphotonen) bezeichnet. In Kapitel 2 werden alle gängigen Vorangehensweisen an diese Problematik kurz erläutert.

F.2 Das Modell

Direkte Photonen werden in dieser Arbeit vor dem Hintergrund einer Kern-Kern-Kollision errechnet. Zwei verschiedene Modelle für die hadronische Entwicklung der Reaktion werden benutzt und in Kapitel 3 ausführlich beschrieben.

Zum einen wird das in Frankfurt entwickelte hadronische ultrarelativistische Transportmodell UrQMD (Ultra-relativistic Quantum Molecular Dynamics) angewendet, das jedes einzelne Teilchen beschreibt und jede Wechselwirkung explizit berechnet. Die Freiheitsgrade dieses Modelles sind Mesonen und Baryonen, außerdem kann es bei hohen Energien Farbflussröhren (Strings) nach dem LUND-String-Modell erzeugen und zerfallen lassen. Eine der Annahmen für das UrQMD-Modell ist, dass die Teilchen eine große mittlere freie Weglänge haben, sodass einzelne Streuungen inkohärent sind. In sehr dichter Materie ist daher die Anwendbarkeit von UrQMD eingeschränkt.

Zum anderen wird eine Erweiterung des Modells benutzt, in der die heiße und dichte Phase mittels Hydrodynamik beschrieben wird. Hier wird über die einzelnen Teilchen gemittelt und nur noch deren statistische Verteilung betrachtet. Dieses Vorgehen ist nur möglich, wenn die Materie in lokalem thermischem Gleichgewicht und dicht genug ist. Dadurch begrenzt sich die Anwendbarkeit der Hydrodynamik auf den Zeitraum von der Thermalisierung des Feuerballs bis die Materie zu weit ausgedünnt ist. Ein Vorteil ist aber, dass man auch den Phasenübergang zwischen zwei Materieformen leicht beschreiben kann.

Das Hybridmodell, das hier Anwendung findet, kombiniert nun die Vorteile

aus Transporttheorie und Hydrodynamik, indem es eine anfängliche Transportphase an eine hydrodynamische Phase ankoppelt, der wieder eine Transportphase folgt. Für die hydrodynamische Phase stehen drei verschiedene Zustandsgleichungen zur Verfügung: Die Hadron Gas-Zustandsgleichung hat die gleichen Freiheitsgrade wie UrQMD. Rechnungen mit dieser erlauben somit, Unterschiede, die nur durch die geänderte kinetische Beschreibung auftreten, zu betrachten. In Rechnungen mit der Chiralen Zustandsgleichung hingegen existiert ein Phasenübergang, in dem die Hadronen ihre chiralen Massen verlieren (chiraler Phasenübergang) und zugleich der Farbeinschluss aufgehoben wird. Beide Phasenübergänge koinzidieren hier und werden als Cross-over beschrieben. Die dritte Zustandsgleichung (Bag Model) hat einen Phasenübergang erster Ordnung mit großer latenter Wärme von einem massiven Hadronengas hin zu einem Plasma aus masselosen Quarks und Gluonen. Details zu den Zustandsgleichungen sind dem Abschnitt 3.4 zu entnehmen.

Die Übergänge zwischen den drei Phasen des Hybridmodelles bedürfen eingehender Betrachtung: Im ersten Schritt werden die Impulse, Energien und Baryonzahlen der einzelnen Teilchen in Impuls-, Energie- und Baryondichten umgerechnet und diese Dichten dann als Anfangsbedingungen für die Hydrodynamik verwendet. Das System wird dabei ad hoc ins thermische Gleichgewicht gebracht. Im zweiten Übergang werden die Dichten über mehrere Schritte wieder in Teilchen umgewandelt. Das Hybridmodell und die Übergänge werden in Abschnitt 3.3 vorgestellt.

Aus jeder Kollision in der Transportphase und jeder numerischen Zelle in der Hydrodynamikphase wird nun Photonenemission berechnet. Die Wechselwirkungsquerschnitte werden ausgewertet und die Anzahl Photonen, die im Schnitt aus einer solchen Kollision ausgesandt wird, berechnet. Im hydrodynamischen Teil werden thermische Raten zur Berechnung verwendet. Aus jeder Ortsraumzelle wird eine Impulsraumzelle mit der durchschnittlichen Anzahl an Photonen von dieser Zelle populiert, die Verteilung in den Impulsraum erfolgt dabei anhand der in das Ruhesystem der Ortsraumzelle transformierten thermischen Rate. Genauere Ausführungen über den Emissionsmechanismus sind in Abschnitt 3.5 zu finden.

F.3 Ergebnisse

Kapitel 4 ist numerischen Tests des Modells gewidmet. Thermische Photonenemission aus dem Transportmodell wird mit den thermischen Raten in den hydrodynamischen Rechnungen verglichen und für kompatibel befunden. Die Streuung von führenden Teilchen aus den Strings und die Photonenemission daraus wird untersucht. Hier zeigt sich, dass der größte Teil der Photonen bei hohem Transversalimpuls eben aus Streuungen dieser Art stammt. Die Produktion von ρ-Mesonen wird daraufhin erforscht, ob es eine signifikante Änderung gibt, wenn ρ-Mesonen nur mit der Polmasse oder auf der breiten Spektralfunk-

tion erzeugt werden. Der Effekt liegt bei einer Erhöhung der Spektren von ca. 10 % bei niedrigen Transversalimpulsen, wenn als Masse immer die Polmasse gewählt wird. Frühere Berechnungen von Photonenemissionen mit einer alten Version von UrQMD werden mit den vorliegenden Berechnungen verglichen. Es zeigt sich, dass die vorliegenden Spektren wesentlich niedriger sind. Diese Effekte können allerdings vollständig auf Verbesserungen in UrQMD zurückgeführt werden. Der Einfluss der Parameter, die durch die Übergänge im Hybridmodell auftreten, wird im Abschnitt 4.5 untersucht. Hier ist das Ergebnis, dass lediglich der Zeitpunkt des ersten Überganges eine signifikante Veränderung der Photonenspektren bewirkt.

In Kapitel 5 werden Ergebnisse für Transversalimpulsspektren von direkten Photonen für verschiedene Kollisionsenergien vorgestellt. Bei den kleinsten Energien, $E_{\mathsf{lab}} = 35$ AGeV, für die es noch keine experimentellen Daten gibt, ist eine sehr deutliche Aufspaltung der Spektren zwischen Rechnungen mit und ohne partonische Phase zu sehen. Die rein hadronischen Rechnungen (Transport-Rechnungen und Hybrid-Rechnungen mit Hadron Gas-Zustandsgleichung) liegen etwa einen Faktor sieben niedriger als Hybrid-Rechnungen mit den anderen Zustandsgleichungen. Experimentelle Daten sollten hier ohne Probleme zwischen den beiden Modellen unterscheiden können.

Im Falle von Kollisionen bei $E_{\mathsf{lab}} = 158$ AGeV ist der Vergleich mit Daten der WA98-Kollaboration nicht eindeutig. Die komplett hadronischen Rechnungen sind weiterhin niedriger als die teilweise partonischen Rechnungen. Mit der Addition von prompten Photonen, die in frühen Nukleon-Nukleon-Streuungen erzeugt werden, liegen jedoch die partonischen Rechnungen leicht über den Daten, während die hadronischen Rechnungen mit den Daten besser verträglich sind. Berechnungen für Gold-Gold-Kollisionen bei $\sqrt{s_{\mathsf{NN}}} = 200$ GeV und der Vergleich dieser mit Daten der PHENIX-Kollaboration zeigen jedoch eindeutig, dass ein rein hadronisches System die dort gemessenen Photonenspektren nicht erklären kann. Rechnungen mit partonischer Phase jedoch sind kompatibel mit den Messwerten. Bei anderen Systemen, die von der PHENIX-Kollaboration untersucht werden, ist das Verhältnis von Rechnungen mit rein hadronischer und teilweise partonischer Materie ähnlich, durch die Veröffentlichung von experimentellen Ergebnissen sollte hier leicht zwischen den beiden Modellen unterschieden werden können.

Anisotroper Fluss wird ebenfalls untersucht. In allen Systemen und mit allen Zustandsgleichungen, die untersucht werden, ergibt sich ein leicht positiver elliptischer Flusskoeffizient v_2 bei niedrigen Transversalimpulsen, bei niedrigen Energien jedoch sind die Rechnungen noch kompatibel mit $v_2 = 0$. Bei hohen Transversalimpulsen ist der elliptische Fluss in allen Rechnungen bei 0. In diesem Bereich überwiegt die Photonenemission aus frühen Nukleon-Nukleon-Kollisionen, deren Emission uniform im Azimuthalwinkel ist. Bei niedrigen Impulsen trägt jedoch die Strahlung aus dem thermalisierten, fließenden Medium bei, sodass die Flussmuster der hadronischen Materie auf die Photonen übertragen wird.

Detaillierte Untersuchungen der Photonenspektren folgen in den Kapiteln 6, 7 und 8. Zunächst werden die Beiträge der einzelnen Produktionskanäle zu den Spektren untersucht. Der Kanal $\pi\rho \to \gamma\pi$ stellt den größten hadronischen Beitrag bei mittleren Impulsen dar. Nur bei kleinen Impulsen überwiegt $\pi\pi \to \gamma\rho$, was aufgrund der Kinematik der beiden Prozesse leicht ersichtlich ist. Bei hohen Transversalimpulsen gibt es einen qualitativen Unterschied zwischen den Rechnungen bei $E_{\mathsf{lab}} = 35$ AGeV und denen bei höheren Energien: während im Niedrigenergiebereich das Verhalten von mittleren Impulsen auf hohe Impulse übertragen werden kann (also $\pi\rho$-Streuungen das Spektrum dominieren), tragen bei den höheren Energien die Streuungen $\pi\rho$, $\pi\pi$ und $\pi\eta$ zu etwa gleichen Teilen zum Spektrum bei.

Emission aus partonischen Prozessen – thermische Emission aus dem Quark-Gluon-Plasma oder prompte Photonen – wird ebenfalls untersucht. Die hadronischen Beiträge verlieren mit steigender Kollisionsenergie an Bedeutung, wie zu erwarten ist, da die Systeme bei höheren Energien weit in der partonischen Phase thermalisieren.

Kapitel 7 widmet sich der zeitlichen Aufteilung der Photonenemission. Die heiße und dichte Phase, die in den Hybrid-Rechnungen mit Hydrodynamik beschrieben wird, dominiert die Emission bei niedrigen und mittleren Transversalimpulsen in allen Rechnungen, am stärksten jedoch in Rechnungen mit partonischer Phase. Die Spektren bei hohen Transversalimpulsen werden von früher Emission dominiert.

Die Verteilung der direkten Photonen auf die Bayronendichte an ihrem Emissionspunkt, die in Kapitel 8 vorgestellt wird, zeigt, dass frühe Photonenemission mit höheren Dichten einhergeht als die spätere thermale Emission. Bei niedrigeren Energien ($E_{\mathsf{lab}} = 35$ AGeV und $E_{\mathsf{lab}} = 158$ AGeV) nimmt das Verhältnis der Photonenzahlen von hohen und niedrigen Dichten bei hohen Transversalimpulsen ab. Bei niedrigen Transversalimpulsen ist das Verhältnis etwa eine Größenordnung, während Photonen mit niedrigem Impuls bei RHIC etwa 1000 mal eher von niedrigen als von hohen Dichten kommt.

F.4 Schlussfolgerungen

Diese Arbeit stellt die erste detaillierte Untersuchung von direkten Photonen mit einem integrierten Hybridmodell dar. Alle signifikanten Quellen für direkte Photonenemission wurden berücksichtigt. Die Ergebnisse zeigen eine klare Präferenz für thermale partonische Emission bei RHIC, während eine klare Aussage aus dem Vergleich mit SPS-Daten nicht gezogen werden kann. Die Vorhersagen für FAIR werden es möglich machen, klar zwischen partonischen und (rein) hadronischen Medien zu unterscheiden. Die detaillierten Untersuchungen, die hier vorgestellt wurden, können dazu verwendet werden, festzulegen, welche experimentellen Rahmenbedingungen geschaffen werden müssen, um Information über die heiße, dichte Phase einer Schwerionenkollision extrahieren zu können.

Appendix G

Index

Big Bang Theory, 4
Boltzmann-equation, 17
bremsstrahlung, 11

cell size, 25
center-of-mass frame, 123
changing the grid, 25
chiral symmetry, 3
    Equation of State, 28
collision term, 17
colour charge, 3
compton scattering, 11
critical point, 4
critical temperature, 3

dileptons, 8
Drell-Yan process, 8

elliptic flow coefficient, 74
energy-momentum-tensor, 21
Equation of State, 22, 27–28
equilibrium
    local, 22

fireball, 5
    typical time scale, 5
flattening at high $p_\perp$, 52
flavour, 2
flux-corrected transport, 23
fm, 135
formation time, 20, 49
freeze-out, 25

gradual transition, 26
grid
    Eulerian grid, 23
    expansion, 25

hadron gas, 3
    Equation of State, 27
HBT, 14
heavy-ion experiments, 5
Hybrid model
    critical energy density, 57
    first transition, 24, 55
    second transition, 25, 55
    stages
        early stage, 24
        intermediate stage, 25
        late stage, 25
    start time, 24, 55
        minimal start time, 24
Hydro
    Eckart frame, 22
    Equations of Motion, 21
    ideal, 22
    Landau frame, 22
    SHASTA, 22

isochronous transition, 26

Lagrangian density
    a_1-photons, 39
    hydro-photons, 43

QCD, 3
transport-photons, 36

Mandelstam variables, 123
MeV, 136
momentum-ellipsoid, 130
Monte-Carlo efficiency, 132

participants, 5
particle number density, 21
phase structure, 3
Photons
channels
cascade, 37
hydro, 44
pQCD, 45
cross-sections, 38–41
experiments, 11
form factor, 43
measurement, 13
perturbative emission, 36
sources, 11
thermal rates, 43
$p^\mu u_\mu$-ellipsoid, 130
PYTHIA, 19

QCD, 2
Lagrangian density, 3
phase structure, 3
Quark-Gluon-Plasma, 3

rapidity, 136
rejection algorithm, 130

spectators, 5, 25
start time, 24

test particles, 17
transverse momentum, 136

UrQMD, 18
box calculations, 49
old calculations, 52
v1.0, 54
v1.3, 54
v3.3, 23

virtual photons, 14

Appendix H

Lebenslauf

H.1 Meine Akademischen Lehrer

- Dr. Andronic
- Dr. Büsching
- PD Dr. Bruls
- PD Dr. Podlech
- Prof. Dr. Bliedtner
- Prof. Dr. Greiner
- Prof. Dr. Blume
- Prof. Dr. Rischke
- Prof. Dr. Siemsen
- Prof. Dr. Appelshäuser
- Prof. Dr. Roskos
- Prof. Dr. Ströbele
- Prof. Dr. Stöcker
- Prof. Dr. Jacoby
- Prof. Dr. Stroth
- Prof. Dr. Baumeister
- Prof. Dr. Peters
- Prof. Dr. Kohlbesen
- Prof. Dr. Csernai
- Prof. Dr. Bleicher
- Prof. Dr. Huth
- Prof. Dr. Lang

- Prof. Dr. Osland
- Prof. Dr. Dörner
- Prof. Dr. Schmidt

H.2 Lebenslauf

Name Björn Bäuchle
Adresse Brühlstraße 15, 60439 Frankfurt am Main, Deutschland
Geburtstag 22. Mai 1984
Geburtsort Frankfurt am Main, Deutschland
Nationalität Deutsch
Familienstand ledig

1990-1994 Grundschule: Michael-Grzimek-Schule, Frankfurt am Main

1994-2003 Gymnasium: Ziehenschule, Frankfurt am Main

Juni 2003 Abitur

Oktober 2003 Beginn des Studiums im Fach Physik an der Johann Wolfgang Goethe-Universität in Frankfurt am Main

14. März 2005 Vordiplom

Mai 2006 - Juni 2007 Stipendiat der Studienstiftung des Deutschen Volkes

August 2006 - Juni 2007 Forschungsaufenthalt am IFT in Bergen, Norwegen

12. Juni 2007 Diplom. Titel der Arbeit ,,Mach Cones in Heavy Ion Collions"

1. Juli 2007 Annahme als Promotionsstudent in Physik an der Johann Wolfgang Goethe-Universität Frankfurt am Main.

Seit Juli 2007 Student der Frankfurt International Graduate School of Science (FIGSS) (Stipendiat Juli 2007 - Dezember 2007)

Seit Juli 2007 Student der Helmholtz Reasearch School for Quark Matter Studies (H-QM)

Seit Januar 2008 Stipendiat der Deutsche Telekom Stiftung

Seit Januar 2009 Student der Helmholtz Graduate School for Hadron and Ion Research (HGS-HIRe)